ESPOO 2007 VTT PUBLICATIONS 628

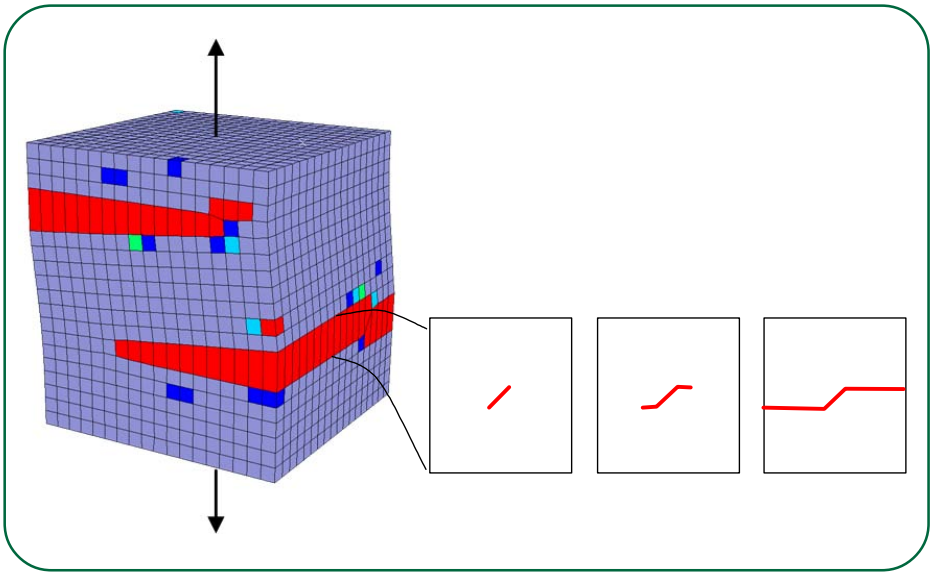

Kari Kolari

Damage mechanics model for brittle failure of transversely isotropic solids

Finite element implementation

VTT PUBLICATIONS 628

Damage mechanics model for brittle failure of transversely isotropic solids

Finite element implementation

Kari Kolari

Dissertation for the degree of Doctor of Science in Technology to be presented with due permission of the Department of Mechanical Engineering, for public examination and debate in Auditorium TU1 at Helsinki University of Technology (Espoo, Finland) on the 20th of April, 2007, at 12 noon.

ISBN 978-951-38-6995-3 (soft back ed.)
ISSN 1235-0621 (soft back ed.)

ISBN 978-951-38-6996-0 (URL: http://www.inf.vtt.fi/pdf/)
ISSN 1455-0849 (URL: http://www.inf.vtt.fi/pdf/)

JULKAISIJA – UTGIVARE – PUBLISHER

VTT, Vuorimiehentie 5, PL 2000, 02044 VTT
puh. vaihde (09) 4561, faksi (09) 456 4374

VTT, Bergsmansvägen 5, PB 2000, 02044 VTT
tel. växel (09) 4561, fax (09) 456 4374

VTT Technical Research Centre of Finland, Vuorimiehentie 5, P.O.Box 2000, FIN–02044 VTT, Finland
phone internat. + 358 9 4561, fax + 358 9 456 4374

VTT, Kemistintie 3, PL 1000, 02044 VTT
puh. vaihde 020 722 111, faksi 020 722 7007

VTT, Kemistvägen 3, PB 1000, 02044 VTT
tel. växel 020 722 111, fax 020 722 7007

VTT Technical Research Centre of Finland, Kemistintie 3, P.O. Box 1000, FI-02044 VTT, Finland
phone internat. +358 20 722 111, fax +358 20 722 7007

Edita Prima Oy, Helsinki 2007

Kolari, Kari. Damage mechanics model for brittle failure of transversely isotropic solids. Finite element implementation. [Transversaali-isotroopisen materiaalin haurasmurtuman mallintaminen vauriomekaniikan avulla. Implementointi elementtimenetelmään]. Espoo 2007. VTT Publications 628. 195 p. + app. 7 p.

Keywords failure mechanics, brittle failure, anisotropy, continuum mechanics, damage models, finite element analysis, solid materials, structural analysis, three-dimensional, transversal isotropy, wing crack

Abstract

A new continuum damage model, the wing crack damage (WCD) model, was developed for the analysis of brittle failure of transversely isotropic solids. Special attention was paid to the analysis of axial splitting under compression and tensile cracking under tension.

In addition to the WCD model a three-dimensional version of the damage model proposed by Murakami and Kamiya was enhanced and implemented in ABAQUS/Standard FE software.

The proposed WCD model is based on the use of the damage vector. The vector represents both the normal direction of the surface of the plane crack and the size of the damaged area. Damaging induces anisotropy in an originally transversely isotropic material. The evolution equations for damage are motivated by the wing crack growth mechanism. The evolution is based on propagation of pre-existing damage.

The proposed model enables modelling of pre-existing cracks. The feature can be exploited in studying the effect of orientation and size distribution of pre-existing cracks on the failure of materials. The model was implemented in ABAQUS/Standard FE software as a user subroutine.

The unsymmetrical behaviour of cracked materials under tension and compression due to the opening and closure of cracks is taken into account in the proposed model. In the work it was shown that the widely used strain-based crack closure criteria cannot be reliably applied in a two- and three-dimensional

stress state. To attain a deformation localisation zone of finite width, a damage rate-dependent damage surface was introduced.

The validity of the proposed model was verified by testing it against five basic structures composed of known natural materials (ice, marble and concrete). The numerical simulations revealed the capability of the model in modelling brittle failure modes of transversely isotropic materials.

Kolari, Kari. Damage mechanics model for brittle failure of transversely isotropic solids. Finite element implementation. [Transversaali-isotroopisen materiaalin haurasmurtuman mallintaminen vauriomekaniikan avulla. Implementointi elementtimenetelmään]. Espoo 2007. VTT Publications 628. 195 s. + liitt. 7 s.

Avainsanat failure mechanics, brittle failure, anisotropy, continuum mechanics, damage models, finite element analysis, solid materials, structural analysis, three-dimensional, transversal isotropy, wing crack

Tiivistelmä

Tutkimuksessa on esitetty kaksi vauriomekaniikkaan (Continuum damage mechanics) perustuvaa materiaalimallia: Murakami Kamiyan (MK) malli, sekä uusi ”wing crak damage” -malli (WCD). Molemmat mallit on liitetty ABAQUS-elementtimenetelmäohjelmistoon UMAT-aliohjelmana.

Esitetty uusi WCD-malli on tarkoitettu transversaali-isotrooppisten materiaalien haurasmurtuman mallintamiseen. Erityistä huomiota on kiinnitetty yksiaksiaalisessa puristuksessa tapahtuvan kuormituksen kanssa yhdensuuntaisen halkeamisen sekä yksiaksiaalisessa vedossa tapahtuvan kuormitusta vastaan kohtisuorassa olevan säröytymisen mallintamiseen.

Esitetty WCD-malli perustuu ”vauriovektorin” käyttöön. Vauriovektori edustaa sekä tasomaisen särön normaalin suuntaa että vaurioituneen alueen kokoa. Vaurioitumisen vuoksi transversaali-isotrooppisesta materiaalista tulee anisotrooppista. Vaurion kasvumekanismi simuloi siipisärön (wing crack) kasvumekanismia.

Uusi WCD-malli mahdollistaa materiaalissa ennen kuormitusta olevien alkusäröjen mallintamisen. Piirrettä voidaan hyödyntää tutkittaessa alkusäröjen suunnan ja suuruuden vaikutusta materiaalin vaurioitumiseen.

Halkeilleen materiaalin epäsymmetrinen käyttäytyminen vedossa ja puristuksessa särön avautumisen ja sulkeutumisen vuoksi on otettu huomioon esitetyssä mallissa. Tutkimuksessa on osoitettu, että venymäperusteista sulkeutumiskriteeriä ei voida luotettavasti soveltaa kaksi- ja kolmiaksiaalisessa jännitystilassa.

Esitetyssä mallissa vauriopinta on vaurionopeuden funktio. Siksi muodonmuutosten paikallistumisvyöhykkeen leveys on äärellinen.

Esitetyn mallin pätevyys on todennettu testaamalla mallia viidessä eri kuormitustapauksessa käyttäen tunnettuja luonnonmateriaaleja (jää, betoni ja marmori). Numeeriset testit osoittivat mallin pätevyyden ja tehokkuuden transversaali-isotrooppisten materiaalien haurasmurtuman mallintamisessa.

Preface

The primary idea for the research reported in this thesis evolved from international and national projects focused on ice loads on offshore structures. The projects were supported by Tekes – Finnish Funding Agency for Technology and Innovation [project ARKI, Contract No. 40857/99], the European MAST-III project LOLEIF [Contract No. MAS3-CT-97-0098] and the European FP5 EESD project STRICE [Contract No. EVG1-CT-2000-00024].

I am grateful to my supervisor, Professor Mauri Määttänen, for his positive attitude and for granting me a position at the Helsinki University of Technology (TKK) for two years. Many thanks also to Professor Jukka Tuhkuri for his comments during the final revision of the thesis. I would like to thank the personnel at the Laboratory for Mechanics of Materials at TKK for the encouraging atmosphere.

I am also grateful to my ex-colleague Dr. Tuomo Kärnä for providing me with the opportunity to carry out research in the field of ice mechanics and dynamics. The idea for this report was hatched as we studied the modelling of brittle failure of natural ice.

I would like to thank my friend Dr. Reijo Kouhia from the Helsinki University of Technology for his advice during countless discussions and for his comments on the manuscripts of this work. I am also grateful to Dr. Kari Santaoja from the Helsinki University of Technology for his help concerning both theoretical and practical issues and for his precise comments on the manuscript. Many thanks also to M.Sc. Kalle Kanervo from the Helsinki University of Technology for the valuable discussions, especially in the field of mathematics.

I would like to thank all my colleagues at VTT for their support and care. I am grateful to Lic.Sc. Heli Koukkari and to Dr. Matti Kokkala for making my two year stay at the Helsinki University of Technology possible. I am indebted to my colleagues Dr. Jaakko Heinonen and Dr. Lasse Makkonen for the discussions on material failure. I would like to thank VTT for their financial support for revising the manuscript. Many thanks also to M.Sc. Eila Lehmus for supporting the finalisation of the thesis.

I am grateful for the preliminary reviewers of the thesis, Prof. (emeritus) Martti Mikkola from the Helsinki University of Technology and PhD Péter Ván from the Department of Theoretical Physics, KFKI Research Institute for Particle and Nuclear Physics of the Hungarian Academy of Sciences, for their constructive comments.

I would also like to thank B.Sc. Adelaide Lönnberg for her proficient work with the English text of this work. I am grateful to Ms. Erja Schlesier for her accurate work finalising the format of the thesis.

Finally, I would like to express my deep gratitude to Dr. Anna Kronlöf for her encouragement and patience, and for her invaluable help with the structure of this work.

Contents

List of symbols

Greek

α	internal state variable corresponding to plastic hardening
δ_{ij}	Kronecker delta
ε_{ij}	total strain tensor
$\varepsilon^{\parallel}$	shear (strain) traction, parallel to the crack plane
ε^{N}	normal (strain) traction, perpendicular to the crack plane
ε_{ij}^{eff}	effective strain
ε_{ij}^{e}	elastic strain tensor
ε_{ij}^{p}	plastic strain tensor
$\hat{\varepsilon}_{(i)}$	principal strains
ε_{ij}^{*}	modified strain tensor
$\hat{\varepsilon}_{ij}^{*}$	modified strain tensor expressed in principal strain coordinate system
η	viscosity parameter
$\eta_1, \eta_2, \eta_3, \eta_4$	material constants
γ	power of dissipation
γ^{d}	power of dissipation, damage part
γ^{p}	power of dissipation, plastic part
κ	internal state variable corresponding to damage hardening
λ	multiplier, Lamé constant
λ^{d}	damage multiplier
λ^{p}	plasticity multiplier
μ	Lamé constant
$\mu_{R,C}$	residual shear modulus under compression
$\mu_{R,T}$	residual shear modulus under tension
ν, ν_{ij}	Poisson's ratio
ω	scaling factor
Ω_i	direction of the damage vector increment in WCD model

$\phi_{(i)}$	principal value of integrity tensor
ϕ_{ij}	integrity tensor
$\psi\ , \psi^d, \psi^e, \psi^p$	Helmholtz free energy
ρ	density
σ_c	compressive strength
σ_{ij}	Cauchy stress tensor
σ_u	ultimate stress
σ_t	tensile strength
$\sigma^{\parallel}$	shear (stress) traction, parallel to the crack plane
σ^N	normal (stress) traction, perpendicular to the crack plane
σ_{ij}^{eff}	effective stress tensor
σ_{ij}^*	stress tensor corresponding to the modified strain tensor ε_{ij}^*
σ^{TR}	threshold traction
ξ	stiffness reduction factor for fully damaged model with passive crack
ζ	material parameter (concerning unilateral behaviour)

Small caps

a	material parameter defining damage surface
h	internar (linear) “hardening” coefficient
$(\mathbf{i}_1, \mathbf{i}_2, \mathbf{i}_3)$	Cartesian basis
k_{ij}	diagonal operator which modifies principal strains to take account of the crack activation/deactivation
$m_{\parallel D0\parallel}$	mean of the pre-existing damage vector length
m_{Dk}	mean of the pre-existing damage vector component *k*
x_1, x_3, x_3	
n_k, $\mathbf{n}$	unit normal vector
s	entropy per unit volume, standard deviation
$s_{\parallel D0\parallel}$	standard deviation of pre-existing damage vector length
s_{Dk}	standard deviation of pre-existing damage vector component *k*

x_0	material parameter defining damage surface
x_1, x_3, x_3	coordinates of rectangular Cartesian coordinate system
x_1', x_3', x_3'	coordinates of local coordinate system defined by damage vector
z_0	material parameter defining damage surface

Capital

A	surface area
A_D	damaged surface area
B	conjugate force corresponding to damage variable κ
B_0	material parameter
B_{ijkl}	projection tensor
c	material parameter
C_{ijkl}, $[\mathbf{C}]$	constitutive tensor, constitutive matrix
$[\mathbf{C}']$	constitutive matrix in local, damage coordinate system
D	scalar damage variable
$D_i, \mathbf{D}$	damage vector
$D_{(i)}$	principal values of the second order damage tensor D_{ij}
D_{ij}	damage tensor
E	Young's Modulus
E_{ij}	Young's Modulus for transversely isotropic material
F	yield surface, damage surface
F^d	damage surface
F^p	yield surface
G	plastic potential, damage potential
G^d	damage potential
G^p	plastic potential
G_F	fracture energy (J / m^2)
G_{ij}	shear modulus for transversely isotropic material
$H()$	Heaviside step function
K_{ijkl}	secant stiffness tensor
$[\mathbf{K}]$	secant stiffness matrix

$[\mathbf{K}']$	secant stiffness matrix in local, damage coordinate system
K^t_{ijkl}	material Jacobian tensor (tangent stiffness)
L_{ijkl}	damage characteristic tensor
$M_i, \mathbf{M}$	vector parallel to symmetry axis of transversely isotropic material
M_{ij}	second order tensor related to material symmetry axis M_i
M_{ijkl}	damage effect tensor
Q_{ij}	rotation tensor
R	material parameter defining damage surface
T	absolute temperature
Y_{ij}, $[\mathbf{Y}]$	conjugate force tensor and matrix corresponding to damage tensor D_{ij}
Y^{eq}	equivalent damage conjugate force
W, W_D	elastic strain energy

Math

$\{\,\}$	column matrix
$[\,]$	matrix
$\|\ \|$	norm of vector
$\mathbf{a} \parallel \mathbf{b}$	vector $\mathbf{a}$ and $\mathbf{b}$ are parallel
$\dot{a}$	time derivative: $\dot{a} = \dfrac{\partial a}{\partial t}$
M^{-1}_{ij}	inverse of M_{ij}
$\dfrac{\partial W}{\{\partial \mathbf{x}\}}$	represents $\left\{\dfrac{\partial W}{\partial x_1}, \dfrac{\partial W}{\partial x_2}, \ldots, \dfrac{\partial W}{\partial x_n}\right\}$ where W is a scalar function of $x_1, x_2, \ldots, x_n$
$[\ ]^T$	matrix transpose
$[\ ]_{ij}$	component of matrix, *i* refers to row number and *j* to column number

Abbreviations

CDM	Continuum damage mechanics
FE	Finite element
FEA	Finite element analysis
FEM	Finite element method
MK	Damage model proposed by Murakami and Kamiya (1997)
RVE	Representative volume element
WCD	Wing crack damage model

1. Introduction

One of the greatest challenges in material failure analysis is the modelling of brittle failure in continuum mechanics. Rock, concrete and ceramics are well known and widely used examples of brittle materials. Formation and unstable growth of (micro)cracks due to the material inhomogeneities and external force is considered to be the mechanism of brittle failure (Nemat-Nasser and Horii, 1984).

The finite element method (FEM) is a widely used tool in structural analysis. The elements used in the FE analysis of structures are based on the theory of continuum mechanics. FEM is therefore not well suited to crack propagation analysis, as crack propagation induces geometrical discontinuity in the medium. Despite the contradiction, tools for brittle failure analysis are needed in FEM.

The effects of discontinuities have been modelled in FEM using e.g. higher order shape functions or enrichment functions. In elemental enrichment methods, additional internal discontinuous degrees of freedom are applied at the element level. Implementation in commercial FE software would therefore require programming of new elements, whereas classical continuum mechanics based approaches (e.g. damage mechanics, smeared cracking) can be implemented without element-level modifications.

1.1 Objectives

Axial splitting is known to be the most likely failure mode under uniaxial compression of brittle materials. Despite its generality, commercial FE software does not provide proper tools for splitting failure analysis. Murakami and Kamiya (1997) have proposed a method for the modelling of brittle failure. The method is based on continuum damage mechanics (CDM) and has proved to be promising in axial splitting analysis as shown by Skrzypek and Kuna-Ciskal (2003). The method also takes into account the crack activation-deactivation process due to crack closure and opening.

This work focused on the modelling of brittle failure based on the continuum damage mechanics approach. The two fundamental objectives (A and B) were:

A. To enhance applicability of the damage mechanics approach proposed by Murakami and Kamiya (1997) for modelling brittle failure in 3D space as follows:

    1. Implement a 3D version of the Murakami and Kamiya model (MK model) in the ABAQUS/Standard FE software.
    2. Identify the weaknesses and strengths of the MK model and amend potential weaknesses.
    3. Study whether the MK model could be modified for analysis of transversely isotropic materials.

B. To introduce a new *wing crack damage* (WCD) model for modelling pre-existing crack evolution under shear and tension and to implement the model in the ABAQUS/Standard FE software as follows:

    1. Damage evolution simulates wing crack growth.
    2. Damaging introduces anisotropy.
    3. Distribution, size and orientation of pre-existing defects can be modelled.
    4. The model can be applied in uniaxial splitting and tensile failure mode analysis (see Fig 3.2 c, e).
    5. Initially transversely isotropic materials can be analysed.
    6. The upper limit of the damage variable is well defined.
    7. Damage activation/deactivation corresponding to open and closed microcracks is taken into account.
    8. Constitutive equations are derived independently of the direction of principal strain.

C. To implement the rate-dependent strength model in the wing crack damage model.

1.2 Scope

This work concentrated on the modelling of axial splitting and tensile failure of brittle material. Because of the extensive nature of the subject, only a limited scope of applications was covered.

The failure was assumed to be brittle, i.e. plastic dissipation was assumed to be negligible. Shear and crushing failure were outside the scope of this work.

Although crack initiation, propagation and wing crack formation are the mechanisms behind axial splitting failure, the model in this study was not based on micromechanics. The approach was phenomenological, although it was motivated by micromechanical mechanisms.

Material dependent parameters that define rate dependency are needed for practical applications. These material parameter studies were outside the scope of this work. The rate-dependent model was applied to reduce mesh sensitivity.

The effect of rate-dependent softening on the mesh sensitivity was studied using numerical examples with coarse and fine mesh. More detailed studies were outside the scope of this work.

Crack activation and deactivation due to the opening and closing crack were taken into account in this study. However, frictional sliding of crack surfaces was not studied.

Material damaging is known to affect the apparent Poisson's ratio and induce volume change in the material. The phenomenon was neglected in this study.

The size, distribution and orientation of initial flaws such as voids and cracks etc. are known to affect the strength of specimens. However, the flaw distribution studies were outside the scope of this study.

2. Mathematical notation

2.1 Tensor notation

Vectors are denoted in bold type. The vector $\mathbf{u}$ has the following representation:

$$\mathbf{u} = u_1\mathbf{i}_1 + u_2\mathbf{i}_2 + u_3\mathbf{i}_3 \tag{2.1}$$

where the vectors $\mathbf{i}_1$, $\mathbf{i}_2$ and $\mathbf{i}_3$ are unit base vectors of the rectangular Cartesian basis shown in Fig. 2.1. Using summation convention the vector in Eq. (2.1) can be written as

$$\mathbf{u} = u_i\mathbf{i}_i \tag{2.2}$$

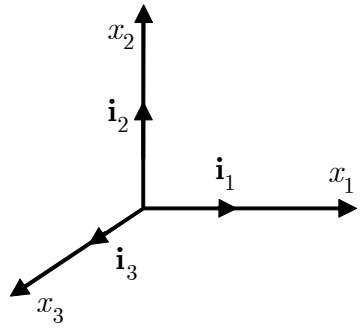

Figure 2.1. Rectangular Cartesian coordinate axes.

Index notation is used throughout this study. Thus e.g. the inner product of the vectors $\mathbf{u}$ and $\mathbf{v}$ is written as

$$\mathbf{u} \cdot \mathbf{v} = u_k v_k \tag{2.3}$$

The summation indexes are subscripted. Summation over superscripted letters is not done. Superscript is used to represent tensor features, e.g. the total strain tensor is ε_{ij} while the total elastic strain is ε_{ij}^e. Not all the subscripted letters are summation indexes. Only lowercase letters are considered as summation indexes. Some parameters like compressive strength σ_c are subscripted with lowercase letters.

All vectors and tensors refer to the same basis unless stated otherwise; therefore only components are written in this text. The components of tensors are called tensors. Similarly, components of vectors are called vectors. Both index (e.g. u_k) and boldface notation ($\mathbf{u}$) is used to represent vectors.

Similarly to Eq. (2.3), the inner product M_{kn} of the two tensors ε_{ij} and A_{ij} is written as

$$M_{kn} = \sigma_{kl} A_{ln} \tag{2.4}$$

which, written with the base vectors, reads

$$\begin{aligned} M_{kn}\mathbf{i}_k\mathbf{i}_n &= \sigma_{kl}\mathbf{i}_k\mathbf{i}_l \cdot A_{mn}\mathbf{i}_m\mathbf{i}_n \\ &= \sigma_{kl}A_{ln}\mathbf{i}_k\mathbf{i}_n \end{aligned} \tag{2.5}$$

2.2 Matrix notation

Index notation of stress tensors σ_{ij} and strain tensors ε_{ij} is used throughout this study. Because the finite element applications require the use of matrix notation, the notation is also used in this study. The column matrix of elastic strains ε^e_{ij} reads

$$\begin{aligned} \{\boldsymbol{\varepsilon}^e\} &= \{\varepsilon^e_{11}, \varepsilon^e_{22}, \varepsilon^e_{33}, 2\varepsilon^e_{12}, 2\varepsilon^e_{13}, 2\varepsilon^e_{23}\}^T \\ &= \{\varepsilon^e_1, \varepsilon^e_2, \varepsilon^e_3, \varepsilon^e_4, \varepsilon^e_5, \varepsilon^e_6\}^T \end{aligned} \tag{2.6}$$

where the order of the shear strains is the same as used in ABAQUS/Standard (ABAQUS, 2003) FE software. Although row and column matrices are not real vectors, also row and column matrices are called vectors in this text.

The stress vector is given in the following form:

$$\begin{aligned} \{\boldsymbol{\sigma}\} &= \{\sigma_{11}, \sigma_{22}, \sigma_{33}, \sigma_{12}, \sigma_{13}, \sigma_{23}\}^T \\ &= \{\sigma_1, \sigma_2, \sigma_3, \sigma_4, \sigma_5, \sigma_6\}^T \end{aligned} \tag{2.7}$$

Hooke's law defining the relation between stresses and strains is

$$\sigma_{ij} = C^{e}_{ijkl}\varepsilon^{e}_{kl} \tag{2.8}$$

where C^{e}_{ijkl} is the constitutive tensor. Eq. (2.8) in matrix notation is given in the following form:

$$\{\boldsymbol{\sigma}\} = [\mathbf{C}^{e}]\{\boldsymbol{\varepsilon}^{e}\} \tag{2.9}$$

where $[\mathbf{C}^{e}]$ is the constitutive matrix.

The second order, symmetric damage tensor D_{ij} and the thermodynamic force Y_{ij} corresponding to the damage tensor have a vector notation similar to Eq. (2.6) and (2.7):

$$\begin{aligned}\{\mathbf{D}\} &= \{D_{11}, D_{22}, D_{33}, 2D_{12}, 2D_{13}, 2D_{23}\}^{T}\\ \{\mathbf{Y}\} &= \{Y_{11}, Y_{22}, Y_{33}, Y_{12}, Y_{13}, Y_{23}\}^{T}\end{aligned} \tag{2.10}$$

Thus the inner product of $\{\mathbf{D}\}$ and $\{\mathbf{Y}\}$ is

$$\{\mathbf{D}\}^{T}\{\mathbf{Y}\} = D_{ij}Y_{ij} \tag{2.11}$$

where $\{\mathbf{D}\}^{T}$ is the transpose of $\{\mathbf{D}\}$.

3. Literature review

3.1 Brittle failure and axial splitting

Fracture of metals is often characterised by some amount of plastic hardening, whereas in the fracture of brittle materials like rock, concrete and many other materials, “plastic flow is next to nonexistent” (Bazant, 2002). The definition of ductile and brittle failure is usually based on the amount of plastic strain; “The damage is called brittle when a crack is initiated at the mesoscale without a large amount of plastic strain” (Lemaitre, 1992, p. 4). The order of magnitude given by Lemaitre (1992) is:

$$\frac{\varepsilon^p}{\varepsilon^e} < 1 \tag{3.1}$$

where ε^p is the uniaxial plastic strain and ε^e is the elastic strain. Ductile and brittle behaviour are illustrated in Fig. 3.1. Brittle type behaviour is often divided into the following two subclasses:

a) Quasi-brittle behaviour
b) Brittle behaviour.

According to Bazant et al. (2004), quasi-brittle materials “(1) are incapable of purely plastic deformations, and (2) in normal use have a fracture process zone (FPZ) which is not negligible compared to structure size *D*. For a large enough *D*, every quasi-brittle structure becomes brittle.” This means that the definition quasi-brittle cannot be considered as a pure material property but depends on the specimen size; e.g. a concrete beam may be quasi-brittle whereas a large bridge made of the same material may be brittle.

Uniaxial compression and tension tests are the most common test setup in the definition of material strength parameters. The failure mode (or mechanism) information is as important as the strength values obtained from the test. The failure mode is needed in the verification of material models. Kendall (1978) classifies compression failure modes into three categories (see Fig 3.2): yielding, cone failure and axial splitting. The notion of compressive strength is useful only in the case of yielding (ibid). An example of a tensile strength test using

compressive force is the Brazilian test (Fig 3.2d). Although the external load is compression, the test itself is considered an indirect tensile test.

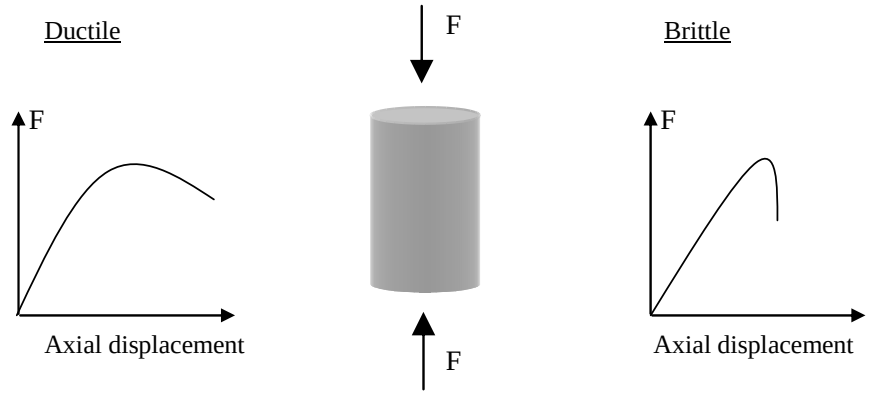

Figure 3.1. Illustration of ductile (left) and brittle (right) response under uniaxial compression.

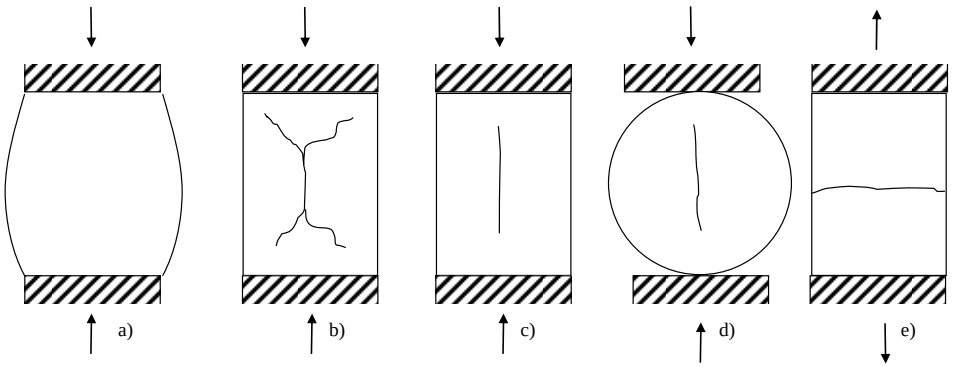

Figure 3.2. Compressive and tensile failure modes: a) plastic yielding, b) cone failure, c) axial splitting, d) disk or Brazilian, e) uniaxial tensile failure (a–c redrawn from Kendall (1978)).

The axial splitting shown in Fig. 3.2c characterises the macroscopic compressive failure mode of many brittle materials like concrete, rock, ceramics and sea ice. (Nemat-Nasser and Horii, 1984; Kuehn et al., 1992; Espinosa and Brar, 1995; Weiss and Schulson, 1995; Bhattacharya et al., 1998; Chen and Ravichandran, 2000; Sarva and Nemat-Nasser, 2001; Gupta and Bergstrom, 2002). The axial splitting failure mode is sometimes called slabbing (Ashby and Hallam, 1986).

Axial splitting is a complex failure mechanism. The splitting does not cause a global energy release, although energy is needed to form and propagate the splitting crack. As stated by Bazant and Planas (1998, p. 299), a splitting crack does not change the macroscopic stress field, whereas a transverse tensile crack causes a change in the macroscopic stress field as shown in Fig. 3.3. The axial splitting failure mechanism does not have a size effect because of the absence of a global energy release (ibid.).

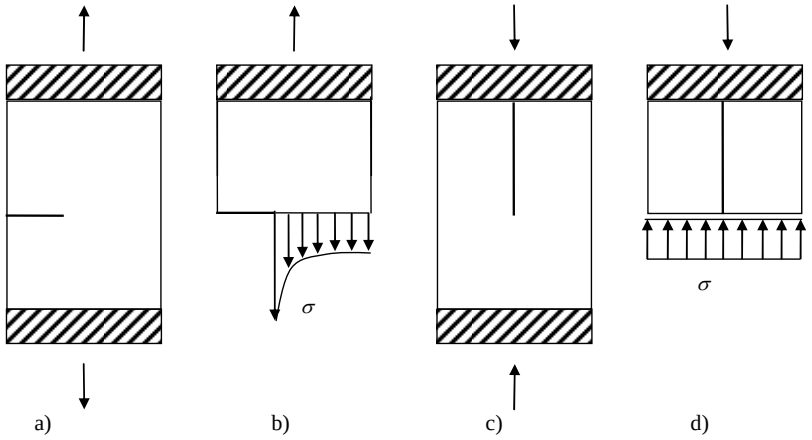

Figure 3.3. a) Tensile crack, b) macroscopic tensile stress field, c) axial splitting crack, d) macroscopic compressive stress field (redrawn from Bazant and Planas (1998, p. 299)).

3.2 Wing crack model

The failure mechanism of brittle materials under compression has been studied for decades. There are several models describing the mechanisms behind axial splitting; wing cracks are commonly accepted to be the one of the mechanisms. (Nemat-Nasser and Horii, 1984; Ashby and Hallam, 1986; Cannon et al., 1990). The notion “wing crack” was introduced in 1963 by Brace and Bombolakis (Nemat-Nasser and Horii, 1984; Renshaw and Schulson, 2001).

Axial splitting failure begins when a primary crack undergoes sliding, creating wing cracks at the tips of the primary crack (Fig 3.4). The failure occurs when series of wing cracks extend and finally link together and split the material. The

final failure mode consists of a series of longitudinal splits (Sanderson, 1988; Renshaw and Schulson, 2001).

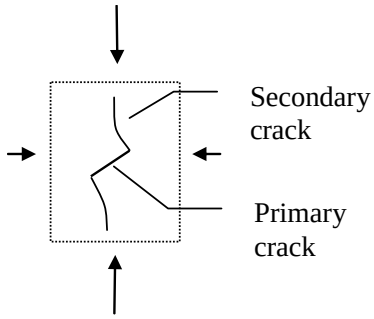

Figure 3.4. Wing crack formation; redrawn from (Renshaw and Schulson, 2001).

3.2.1 Wing crack initiation

Consider stresses near the tip of a crack in a homogeneous and isotropic plate. Radial σ_r, circumferential σ_θ and shear $\tau_{r\theta}$ stresses near the tip of the crack shown in Fig. 3.5a can be solved based on the theory of linear elasticity (for further details see e.g. Hellan (1984)). In the theory of fracture mechanics the stresses are given as a function of the stress intensity factors (SIFs) K_I, K_{II}, the radius r and the angle θ as follows (Hellan, 1984, p.10,13):

$$\begin{aligned}
\sigma_r &= \frac{1}{4}\left[\frac{K_I}{\sqrt{2\pi r}}\left(5\cos\frac{\theta}{2}-\cos\frac{3\theta}{2}\right)+\frac{K_{II}}{\sqrt{2\pi r}}\left(-5\sin\frac{\theta}{2}+3\sin\frac{3\theta}{2}\right)\right] \\
\sigma_\theta &= \frac{1}{4}\left[\frac{K_I}{\sqrt{2\pi r}}\left(3\cos\frac{\theta}{2}+\cos\frac{3\theta}{2}\right)-\frac{K_{II}}{\sqrt{2\pi r}}\left(3\sin\frac{\theta}{2}+3\sin\frac{3\theta}{2}\right)\right] \\
\tau_{r\theta} &= \frac{1}{4}\left[\frac{K_I}{\sqrt{2\pi r}}\left(\sin\frac{\theta}{2}+\sin\frac{3\theta}{2}\right)+\frac{K_{II}}{\sqrt{2\pi r}}\left(\cos\frac{\theta}{2}+3\cos\frac{3\theta}{2}\right)\right]
\end{aligned} \tag{3.2}$$

where the stress intensity factors K_I and K_{II} are functions of loading, the state of stress and the geometry of the crack.

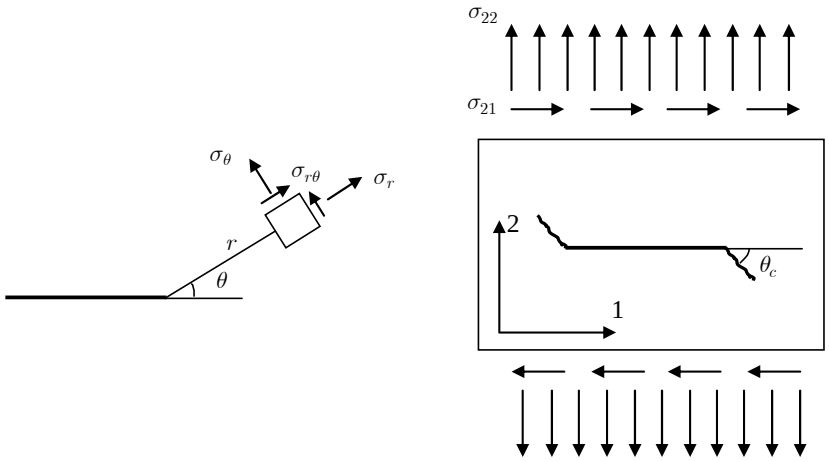

(a) (b)

Figure 3.5. Stresses near the tip of a crack (a) and the initiation of a new branch under tensile and shear loading (b).

When SIF exceeds the fracture toughness (K_{IC} in pure mode I) a crack starts to initiate. In 1963 Erdogan and Sih (Hellan, 1984, p. 158) investigated both the direction of growth and the initiation of growth under mixed mode loading. They proposed the following equations:

$$\begin{aligned} \sigma_\theta &= \frac{K_{IC}}{\sqrt{2\pi r}} \\ \tau_{r\theta} &= 0 \end{aligned} \tag{3.3}$$

where Eq. $(3.3)_2$ indicates the direction of growth. Substituting Eq. (3.2) in (3.3) the following equations are obtained:

$$\begin{aligned} K_I\left(3\cos\frac{\theta}{2}+\cos\frac{3\theta}{2}\right)-K_{II}\left(3\sin\frac{\theta}{2}+3\sin\frac{3\theta}{2}\right) &= 4K_{IC} \\ K_I\left(\sin\frac{\theta}{2}+\sin\frac{3\theta}{2}\right)+K_{II}\left(\cos\frac{\theta}{2}+3\cos\frac{3\theta}{2}\right) &= 0 \end{aligned} \tag{3.4}$$

The kinking angle θ_c shown in Fig. 3.5b and the relationship between K_I and K_{II} in mixed mode can be solved from (3.4). Under pure shear loading ($K_I = 0$) the kinking angle $\theta_c \approx 70.6°$. Determination of the kinking angle for anisotropic material is a more demanding task and outside the scope of this work.

3.2.2 Modelling wing cracks under compression

Brittle materials like rocks and ice are assumed to contain small sized cracks that propagate under compression. As described earlier, the wing crack mechanism is a model describing the propagation of these cracks. A stress intensity factor (SIF) is required to estimate the initiation of wing crack growth. The frictional sliding of a primary crack has been found to be important in these models, therefore the coefficient of friction μ is taken into account in the determination of SIF.

The sliding crack approach has been widely analysed in the literature (e.g. Cotterell and Rice, 1980; Nemat-Nasser and Horii, 1982; Steif, 1984; Ashby and Hallam, 1986; Horii and Nemat-Nasser, 1986). Lehner and Kachanov (1996) have summarised differences among the proposed models. The models are based on the theory of fracture mechanics. The basic idea in these models is that a wing crack (or a "branched crack") is loaded by "splitting" forces induced by frictional sliding of the primary crack. Stress intensity factors K_I and K_{II} are derived for the crack based on orientation, length, loading etc. When the stress intensity factors K_I and K_{II} are known, the propagation of the crack can be analysed similar to the theory of fracture mechanics. In a pure mode I propagation starts when $K_I = K_{IC}$.

A representative crack of Nemat-Nasser and Horii (Nemat-Nasser and Horii, 1984; Horii and Nemat-Nasser, 1986) is shown in Fig. 3.6b. In their model the stress intensity factors are defined as follows (ibid.):

$$\begin{aligned} K_I &= \frac{F\sin(\phi)}{\sqrt{\pi l}} \\ K_{II} &= \frac{-F\cos(\phi)}{\sqrt{\pi l}} \end{aligned} \tag{3.5}$$

where the force is defined as follows:

$$\begin{aligned} F = -a[&(\sigma_{11}-\sigma_{22})\sin(2\gamma) \\ &-2\tau_c + \mu[\sigma_{11}+\sigma_{22}-(\sigma_{11}-\sigma_{22})\cos(2\gamma)]] \end{aligned} \tag{3.6}$$

where τ_c is the cohesive stress, μ is the coefficient of friction and γ is the inclination angle of the primary crack.

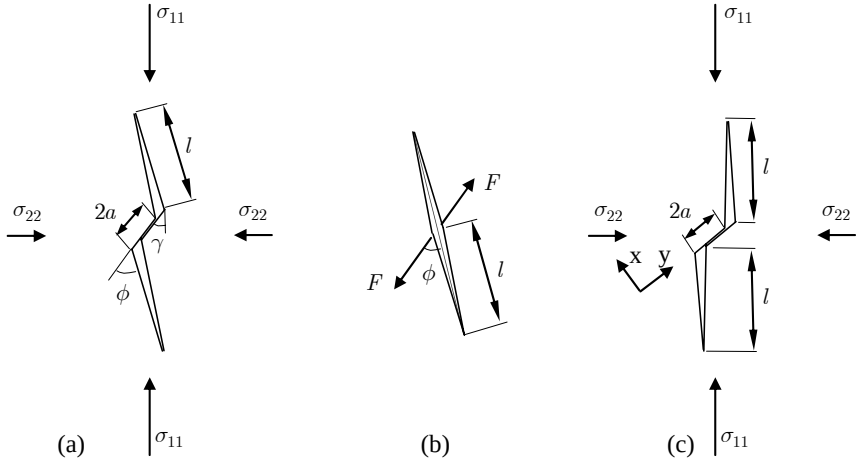

Figure 3.6. a) Idealised wing crack; b) representative tension crack of Horii and Nemat-Nasser (1986) and c) the model of Ashby and Hallam (1986).

In the model of Ashby and Hallam (1986) a wing crack is assumed to grow parallel to the axial loading as shown in Fig. 3.6c. The SIF applied in the analysis of crack growth is the following (Ashby and Hallam, 1986, Eq. (A36)):

$$K_I = \frac{\sqrt{\pi a}}{(1+L)^{3/2}}\left[\frac{2}{\sqrt{3}}(\sigma_{xy} + \mu\sigma_{xx}) + 2.5\sigma_2 L\right]\left[0.4L + \frac{1}{(1+L)^{1/2}}\right] \quad (3.7)$$

where σ_{xy} and σ_{xx} are the stresses in local coordinate system shown in Fig. 3.6c (σ_{xx} is positive under compression) and $L = l/a$ is the undimensional length.

3.3 Continuum mechanics based brittle failure analysis

There are two practical requirements which material failure models have to meet. Firstly, the model must be able to predict correct macroscopic stress and strain state at failure (e.g. in uniaxial compression test simulation, the model should give a similar force displacement diagram to that obtained in the tests). Secondly, the predicted failure mechanism must fit the mechanism found in the experiments. In practice, mathematical failure models seldom wholly fulfil both criteria.

One of the objectives of this work was to introduce material models capable of predicting the axial split failure mode along the loading direction under compression and tensile cracking perpendicular to the loading direction under tension (see Fig. 3.2). The second requirement was that the model should be able to take into account damage activation and deactivation corresponding to open and closed microcracks (the activation/deactivation process is often called the unilateral effect).

3.3.1 Discontinuity models and FEA

Although various methods have been introduced in modelling discontinuities in FEA, only a brief review of the classical (continuum) discontinuity models is given in this section.

The concepts used in FEA for modelling discontinuities due to material failure can be divided into the following two branches (Oliver and Huespe, 2004):

- Discrete approaches, which are based on the modelling of cohesive surfaces between continuum elements. The cohesive surface is ruled by the traction-separation law.
- Continuum approaches based on the classical continuum mechanics (e.g. smeared cracking, damage mechanics) or enriched continuum (e.g. gradient enrichment, non-local models).

In 1958, Kachanov introduced the concept of effective stress (Lemaitre and Chaboche, 1990). It can be considered as a starting point for new types of approaches like the smeared crack and the damage mechanics concept.

In the damage mechanics concept, loss of stiffness can be considered to be a consequence of randomly distributed microcracks. The loss can be macroscopically measured and characterised by a single damage variable. Depending on the type of damage, scalar *D*, vector $\mathbf{D}$ or tensor (D_{ij}, D_{ijkl}) variables can be used. Damage vectors and tensors have been introduced to take into account anisotropic stiffness degradation.

The basic phenomenological difference between the theory of plasticity and continuum damage mechanics (CDM) is that in the theory of plasticity inelastic deformation induces irreversible strains, while in CDM, material damaging reduces the elastic stiffness as illustrated in Fig. 3.7. The distinction between the mechanisms could be simplified as follows: In plasticity theory the irreversible strains are created by dislocation movement, while in CDM the damage is caused by breaking of atomic bonds or debonding because of crack initiation.

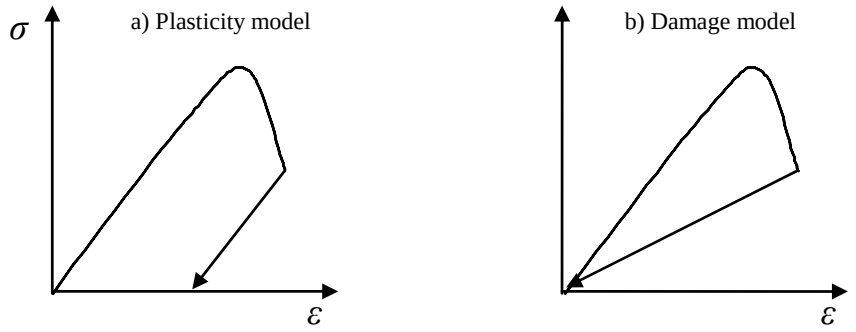

Figure 3.7. Stress-strain response of strain softening material; a) plasticity model, b) damage model.

The *smeared crack* and *discrete crack* concepts were introduced in the 1960s (Rots and Blaauwendraad, 1989). Both concepts have been specially developed for brittle failure analysis in FEM.

In the early days of the *discrete crack* approach, the crack was modelled by separating element edges when the separation criterion was fulfilled. Before the separation, element edges were tied together with interface elements. The crack propagation path was determined beforehand.

The *smeared crack* approach has been implemented in several commercial FE software applications. Physically the smeared crack concept can be considered as a representation of series of microcracks. In the smeared crack approach, the direction of crack formation is usually defined by the maximum tensile principal stress. The crack is formed along the plane normal to the stress. When the crack is formed, a local coordinate system is fixed to the crack such that one of the coordinates points in the direction normal to the crack surface. An orthotropic

stress-strain law is then fixed to the local coordinate system, usually with a strain-softening feature. Three versions of the smeared crack approach exist:

a) Fixed crack
b) Multiple fixed crack
c) Rotating crack.

In the fixed crack approach the crack growth direction does not change with the varying loading direction, whereas in the rotating crack approach the crack orientation follows the principal tensile stress. The fixed crack approach tends to give an "overly stiff response" (Guzina et al., 1995). In the multiple crack approach a new crack is formed when the principal stress rotation increment exceeds a threshold value (Ohmenhauser et al., 1999).

In 1976 Hillerborg pioneered the *fictitious crack model* (Hillerborg et al., 1976; Bazant and Planas, 1998; Cotterell, 2002; Elices et al., 2002). When the fictitious crack approach is used to model a pre-existing crack, the mathematical formalism is identical to that for the cohesive crack approach (Bazant and Planas, 1998, p. 158). In the fictitious crack model the cohesive stress σ_c is given as a function of the crack opening w (Fig 3.8). The function $\sigma_{COH}(w)$ is called the softening function, which is a material property, and it can be related to the fracture energy G_F as follows:

$$G_F = \int_0^{w_c} \sigma_{COH}(w)\,\mathrm{d}w \tag{3.8}$$

where w_c is the critical crack opening. Based on the fracture energy and tensile strength the so-called characteristic length l_{ch} can be derived (Elices et al., 2002) as follows:

$$l_{ch} = \frac{E\,G_F}{(\sigma_t)^2} \tag{3.9}$$

where *E* is Young's modulus and σ_t is the tensile strength. The characteristic length is an inverse measure of the material brittleness: the smaller l_{ch} is, the more brittle the material (Elices et al., 2002). Although the fictitious crack approach is attractive, the drawback is that usually the cracking zone has to be

modelled using cohesive elements, i.e. the crack propagation path has to be defined in advance. Recently the fictitious crack model has been implemented in FE programs (Ruiz et al., 2001; Li and Siegmund, 2002; Planas et al., 2003; Shi, 2004).

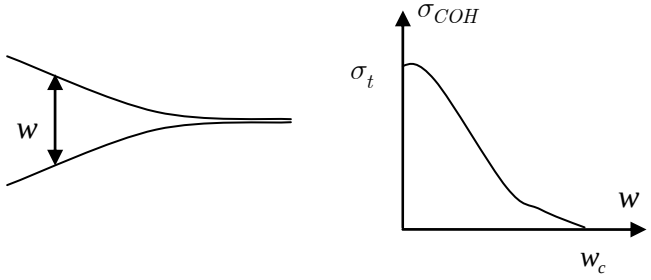

Figure 3.8. Fictitious crack approach.

The X-FEM approach has been developed based on the enrichment approach (Belytschko and Black, 1999; Sukumar et al., 2000). In this approach, discontinuous enrichment functions are added to the FE approximation to account for the presence of the crack. Work has recently been done to develop a strong discontinuity approach (SDA) (Oliver et al., 2002; Chaves, 2003) and a continuum strong discontinuity approach (CSDA) (Oliver and Huespe, 2004). In the CSDA, discontinuous kinematics and strain-softening constitutive laws are introduced into the continuum model, which "allows one to bridge both continuum and discrete approaches to material failure" (ibid.).

3.3.2 Plasticity theory

The theory of plasticity has been used in analysis of brittle failure. Although plastic deformations are negligible in brittle failure, plasticity theory can be applied from the phenomenological point of view. The phenomenological modelling of brittle failure requires the use of a strain-softening approach. As shown in Fig. 3.9, the sudden drop after peak stress can be modelled using the theory of plasticity (Kolari et al., 2002; Kolari et al., 2003). In conventional plasticity theory, the unilateral behaviour cannot be modelled.

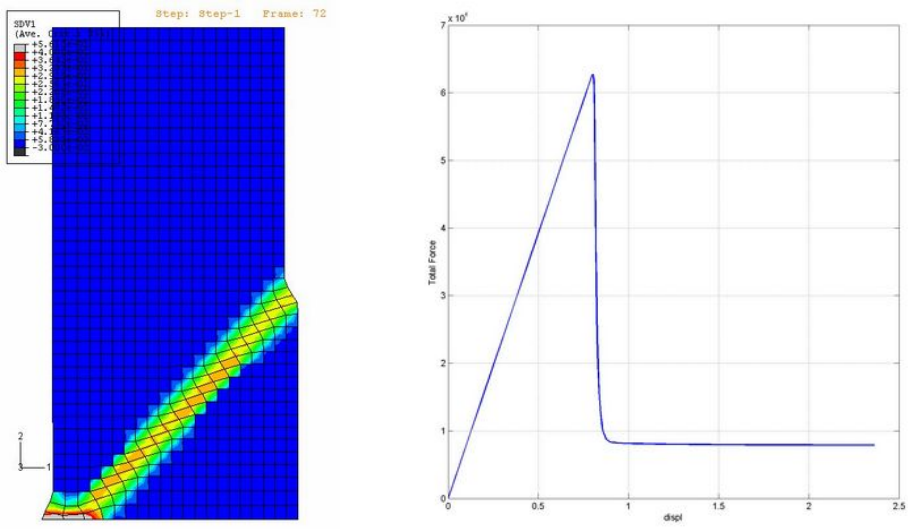

Figure 3.9. Failure mechanism and force-displacement diagram in a compression test simulation using a Perzyna-type strain-softening approach with von Mises-type plasticity model (Kolari et al., 2003; Kolari et al., 2004).

3.3.3 Axial splitting analysis in continuum mechanics

As discussed in the previous section, axial splitting failure is a result of crack formation and propagation processes. In nature, crack initiation starts from a material inhomogeneity or fault (Fig. 3.10a, b). When the specimen is modelled using continuum mechanics, the material is usually assumed to be homogeneous without any faults or discontinuities. Therefore, in the classical continuum models there are no voids or disturbances to initiate crack formation or growth.

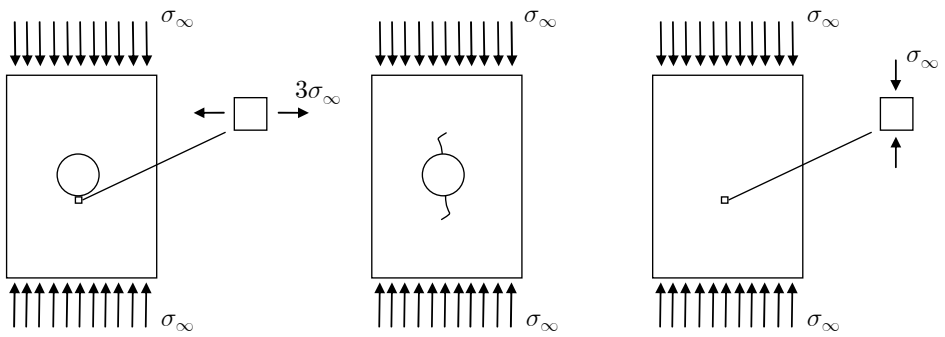

Figure 3.10. Stress state under axial compression. a–b) circular material fault inducing axial crack, c) stress state of undamaged and homogeneous material.

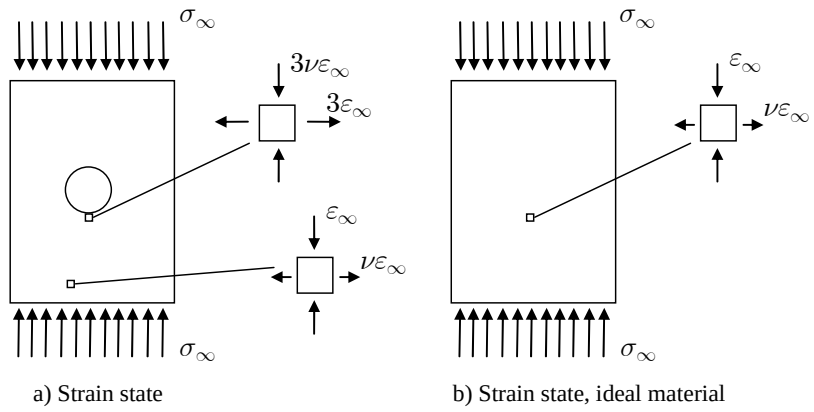

Figure 3.11. Strain state under axial compression: a) strain on the lower edge of the circular hole, b) strain state of undamaged and homogeneous material. ν is Poisson's ratio.

Failure criteria in continuum mechanics are often based on dissipation potentials (also called failure surface or yield surface). The evolution direction of failure is defined by the derivative of the potential with respect to the stress or strain tensor. The dissipation potential is a function of either stresses or strains. Stress-based dissipation potentials are commonly used, although stress-based dissipation potentials cannot be used when modelling axial splitting.

The uniaxial compression test shown in Figs. 3.10 and 3.11 illustrates the usefulness of the strain space-based formulation in axial splitting modelling. The

direction of damage evolution in the stress-based formulation is controlled by the stress state. It is common for the damage evolution of brittle materials to be based on the direction of maximum principal tensile stress, i.e. crack surfaces are assumed to be orthogonal to the direction of maximum principal tensile stress (Elices and Planas, 1996; Ohmenhauser et al., 1999; Oliver et al., 2003; Zolochevsky et al., 2005). However, there is no stress in the lateral direction, as shown in Fig. 3.10c. Therefore (to the author's knowledge), there are no stress-based failure evolution equations that give a correct evolution direction both under axial compression and under tension (see Figs 3.2c and 3.2e).

The direction of damage evolution in a strain-based formulation of brittle materials is often based on the direction of maximum principal tensile strain, i.e. crack surfaces are assumed to be orthogonal to the direction of maximum principal tensile strain. As shown in Fig. 3.11b, the tensile strain points in the lateral direction, thus the crack must be vertically oriented and modelling of axial splitting is possible.

3.4 Transversely isotropic elasticity

Material models can be divided into two categories: isotropic models and anisotropic models. A special class of anisotropy is transverse isotropy. A material is transversely isotropic when it has identical properties in one plane and different properties in the direction normal to the plane (see Fig. 3.12). Wood, some rocks, columnar ice, some ceramics and piezoelectric materials are examples of transversely isotropic materials (Zhu and Cescotto, 1995; Cazacu et al., 1998; Renshaw and Schulson, 2001; Lu and Shao, 2002; Litewka and Debinski, 2003).

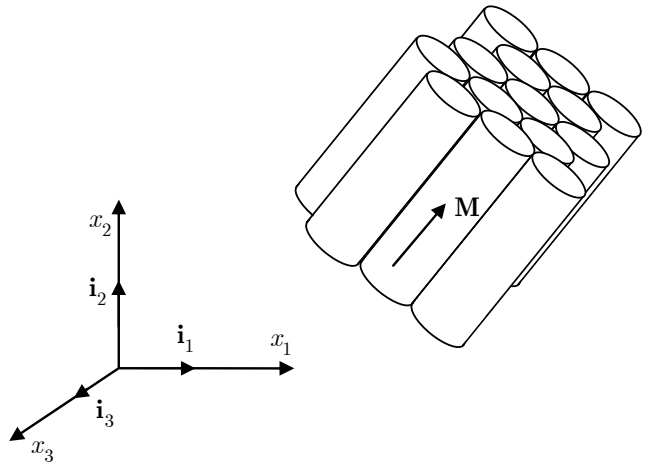

Figure 3.12. Material symmetry axis $\mathbf{M}$ *for transversely isotropic material.*

Elastic behaviour of transversely isotropic materials is described with five independent elastic constants, whereas only two are needed for isotropic materials. The most convenient way is to express the elastic strain energy using four of the following five independent invariants (Rogers, 1990):

$$\begin{aligned} J_1 &= \varepsilon^e_{kk} \\ J_2 &= \varepsilon^e_{kl}\varepsilon^e_{kl} \\ J_3 &= \varepsilon^e_{kl}\varepsilon^e_{lm}\varepsilon^e_{mk} \\ J_4 &= M_{kl}\varepsilon^e_{kl} \\ J_5 &= M_{km}\varepsilon^e_{ml}\varepsilon^e_{lk} \end{aligned} \tag{3.10}$$

The initial material symmetry is characterised by the second order tensor M_{ij}, which is defined as follows:

$$M_{ij} = M_i M_j \tag{3.11}$$

where M_i is the component of the unit vector $\mathbf{M}$ defining the material symmetry axis direction shown in Fig. 3.12. The strain energy density *W* for linear elastic transversely isotropic material is given as follows (Rogers, 1990):

$$W = \frac{1}{2}\lambda(J_1)^2 + \mu_T J_2 + \alpha J_4 J_1 + 2(\mu_L - \mu_T)J_5 + \beta(J_4)^2 \tag{3.12}$$

where μ_T and μ_L may be interpreted as shear moduli for simple shear, and λ, α and β are material constants.

If the symmetry axis $\mathbf{M}$ is parallel to the Cartesian base vector $\mathbf{i}_3$ shown in Fig 3.12, the material constants in Eq. (3.12) expressed using the conventional engineering constants are

$$
\begin{aligned}
\lambda &= \frac{\alpha - 2\,G_{12}\,\nu_{31}}{2\,\nu_{31} - 1} \\
\alpha &= \frac{2\,G_{21}\left[\left(E_{11}(E_{33} - E_{33}\,\nu_{31} + 2\,G_{12}\,(\nu_{31})^2)\right) - 2E_{33}G_{21}\right]}{E_{11}\left(E_{33} + 4G_{21}\,(\nu_{31})^2\right) - 4E_{33}G_{21}} \\
\beta &= \frac{E_{11}\left[(E_{33})^2 + 4G_{21}\,(G_{21} - 4G_{13}\,)(\nu_{31})^2 - 4E_{33}(G_{13} - G_{21}\nu_{31})\right]}{2E_{11}\left(E_{33} + 4G_{21}(\nu_{31})^2\right) - 8E_{33}G_{21}} \\
&\quad - \frac{4E_{33}G_{21}\,(E_{33} + G_{21} - 4G_{13}\,)}{2E_{11}\left(E_{33} + 4G_{21}(\nu_{31})^2\right) - 8E_{33}G_{21}} \\
\mu_T &= G_{21} = \frac{E_{11}}{2(1+\nu_{21})} \\
\mu_L &= G_{13}
\end{aligned}
\tag{3.13}
$$

where ν_{21} and ν_{31} are Poisson's ratios, G_{12} and G_{13} are shear moduli, E_{11} and E_{33} are Young's moduli in the directions 1 and 3, respectively. Poisson's ratios are defined as follows:

$$
\nu_{mp} = -\frac{\varepsilon_{pp}}{\varepsilon_{mm}} \text{ (no summ.)} \tag{3.14}
$$

where ε_{mm} is the strain in direction *m* under uniaxial compression and ε_{pp} is the corresponding strain in direction *p*.

3.5 Mesh sensitivity and strain softening

Mesh sensitivity and localisation are problems that arise in strain-softening applications. Mesh sensitivity means that beyond a critical load level all further deformations tend to localise in a small band. In finite element applications, the

band width is a function of the element mesh; the denser the mesh the smaller the band width. From the mathematical point of view, the localisation is caused by “loss of ellipticity of the underlying differential equations” (Kang and Willam, 2000). Mesh-independent solutions are difficult to obtain unless a length scale is introduced (ibid.). The use of rate-dependent solution methods like viscoplasticity introduces the length scale.

The mesh dependency can be illustrated with the simple tension spring example shown in Figs. 3.13–3.15 (Bazant and Planas, 1998). The system of springs consists of *n* springs having a total length of *L*. Each spring has an identical softening curve illustrated in Fig. 3.13. The tension test is force controlled. It can be assumed that one of the springs starts softening before the others. The situation is similar to the numerical applications where, due to round-off errors etc., the strains are not identical for all the springs. The displacement response is illustrated in Fig. 3.15. As shown in the figure, the end displacement approaches zero as the number of springs increases.

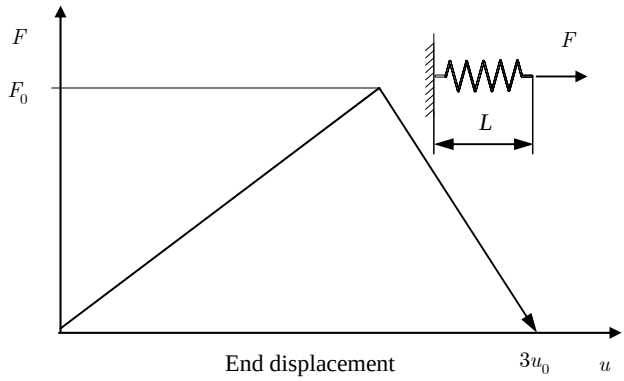

Figure 3.13. Softening curve for a single spring.

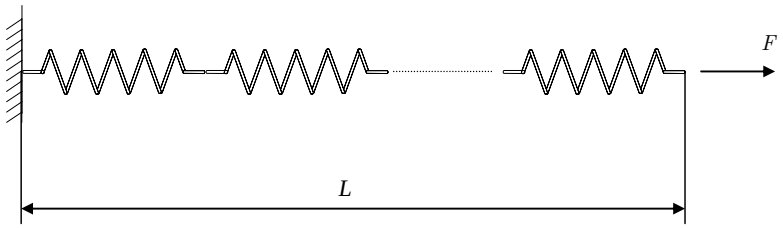

Figure 3.14. n-spring system.

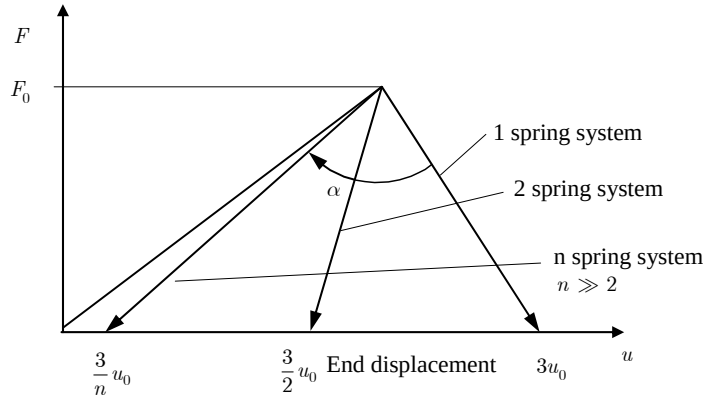

Figure 3.15. Load displacement diagram for softening the n-spring system (redrawn from Bazant and Planas (1998, p. 216)).

3.6 Damage mechanics approach

3.6.1 Thermodynamic basis for material damage theory

A brief review of the formulation of constitutive equations based on continuum thermodynamics is given in the following paragraphs, whereas more detailed presentations are given by Lemaitre and Chaboche (1990), Lemaitre (1992), Ristinmaa and Ottosen (1998), Santaoja (2001) and Olsson & Ristinmaa (2003).

According to Lemaitre and Chaboche (1990), the variables used in thermomechanics can be divided into two classes: a) observable variables, and b) internal variables. Common examples of observable state variables are the total strain ε_{ij} and the absolute temperature *T*, while the plastic strain ε_{ij}^p is an example of an internal variable.

The assumption of small strains is made. This allows a decomposition of total strain tensor ε_{ij} into the elastic part ε_{ij}^e and inelastic part ε_{ij}^p:

$$\varepsilon_{ij} = \varepsilon_{ij}^e + \varepsilon_{ij}^p \tag{3.15}$$

If damage and plasticity are assumed to be uncoupled, the Helmholtz free energy per unit mass ψ is (Zhu and Cescotto, 1995):

$$\psi = \psi^e(\varepsilon_{ij} - \varepsilon^p_{ij}, D_{ij}) + \psi^p(\alpha) + \psi^d(\kappa) \tag{3.16}$$

where ε^p_{ij}, D_{ij}, α and κ are internal state variables, $\psi^p(\alpha)$ is the free energy due to plastic hardening and $\psi^d(\kappa)$ is free energy due to damage hardening. The Clausius-Duhem inequality takes the following form in isothermal conditions (Olsson and Ristinmaa, 2003):

$$\gamma = -\rho\dot{\psi} + \sigma_{ij}\dot{\varepsilon}_{ij} \geq 0 \tag{3.17}$$

where γ is the power of dissipation and a dot denotes rate with respect to time, and ρ is the density. The thermodynamic conjugate forces corresponding to the internal variables are

$$\begin{aligned} \sigma_{ij} &= \rho\frac{\partial\psi}{\partial\varepsilon^e_{ij}}, \qquad & Y_{ij} &= -\rho\frac{\partial\psi}{\partial D_{ij}} \\ B &= \rho\frac{\partial\psi}{\partial\kappa}, \qquad & R &= \rho\frac{\partial\psi}{\partial\alpha} \end{aligned} \tag{3.18}$$

The sign convention in Eq. (3.18) is similar to the convention used by Murakami and Kamiya (1997). With Eqs. (3.16) and (3.18) we have the dissipation inequality from Eq. (3.17):

$$\begin{aligned} \gamma &= -\rho\frac{\partial\psi}{\partial(\varepsilon_{ij} - \varepsilon^p_{ij})}(\dot{\varepsilon}_{ij} - \dot{\varepsilon}^p_{ij}) - \rho\frac{\partial\psi}{\partial D_{ij}}\dot{D}_{ij} - \rho\frac{\partial\psi}{\partial\alpha}\dot{\alpha} \\ &\quad - \rho\frac{\partial\psi}{\partial\kappa}\dot{\kappa} + \sigma_{ij}\dot{\varepsilon}_{ij} \\ &= -\sigma_{ij}(\dot{\varepsilon}_{ij} - \dot{\varepsilon}^p_{ij}) + Y_{ij}\dot{D}_{ij} - R\dot{\alpha} - B\dot{\kappa} + \sigma_{ij}\dot{\varepsilon}_{ij} \\ &= \sigma_{ij}\dot{\varepsilon}^p_{ij} + Y_{ij}\dot{D}_{ij} - R\dot{\alpha} - B\dot{\kappa} \geq 0 \end{aligned} \tag{3.19}$$

The equation can be separated into two parts if dissipation due to damage and plasticity are uncoupled (see Eq. (3.16)).

$$\gamma = \gamma^p + \gamma^d \geq 0 \tag{3.20}$$

where

$$\begin{aligned} \gamma^p &= \sigma_{ij}\dot{\varepsilon}^p_{ij} - R\,\dot{\alpha} \geq 0 \\ \gamma^d &= Y_{ij}\dot{D}_{ij} - B\,\dot{\kappa} \geq 0 \end{aligned} \tag{3.21}$$

A condition that determines whether plastic and/or damage loading occur must be defined. These conditions are known as the yield surface and damage surface. The yield surface F^p and damage surface F^d are often given as a function of state variable D_{ij} and conjugate forces

$$\begin{aligned} F^p &= F^p(\sigma_{ij}, R) = 0 \\ F^d &= F^d(Y_{ij}, B) = 0 \end{aligned} \tag{3.22}$$

When

$$F^p = 0 \text{ or } F^d = 0 \tag{3.23}$$

plastic or damage response is possible. The response is elastic if the following condition is fulfilled:

$$F^p < 0 \text{ and } F^d < 0 \tag{3.24}$$

The thermodynamic formulation gives the thermodynamic forces and the dissipation inequality equation but does not give information about the evolution laws for internal variables. The only restriction imposed by continuum thermodynamics on the evolution laws is that the dissipation inequality of Eq. (3.21) must be fulfilled.

Evolution laws can be derived from the postulate of maximum dissipation using the definitions in Eqs. (3.22)–(3.24). The objective is to find stresses and forces for given thermodynamic fluxes $\dot{\varepsilon}^p_{ij}$, $\dot{\alpha}$, $\dot{D}_{ij}$ and $\dot{\kappa}$ such that the dissipation γ in Eq. (3.19) is maximised. The postulate of maximum dissipation leads to the following evolution laws (Zhu and Cescotto, 1995; Ristinmaa and Ottosen, 2000; Olsson and Ristinmaa, 2003):

$$
\begin{aligned}
\dot{D}_{ij} &= \dot{\lambda}^d \frac{\partial F^d}{\partial Y_{ij}} \\
\dot{\kappa} &= -\dot{\lambda}^d \frac{\partial F^d}{\partial B} \\
\dot{\varepsilon}^p_{ij} &= \dot{\lambda}^p \frac{\partial F^p}{\partial \sigma_{ij}} \\
\dot{\alpha}^p &= -\dot{\lambda}^p \frac{\partial F^p}{\partial R}
\end{aligned}
\tag{3.25}
$$

In Eq. (3.25) the parameters $\dot{\lambda}^d \geq 0$ and $\dot{\lambda}^p \geq 0$ are called consistency parameters. They are assumed to obey the Kuhn-Tucker consistency requirements (Olsson and Ristinmaa, 2003):

$$
\begin{aligned}
\dot{\lambda}^d &\geq 0, & \dot{\lambda}^p &\geq 0 \\
F^d &\leq 0, & F^p &\leq 0 \\
\dot{\lambda}^d F^d &= 0, & \dot{\lambda}^p F^p &= 0
\end{aligned}
\tag{3.26}
$$

In addition to condition (3.26), when $\dot{\lambda}^d \geq 0$ and $\dot{\lambda}^p \geq 0$ the consistency requirements must be satisfied (Olsson and Ristinmaa, 2003):

$$
\dot{F}^d = 0, \qquad \dot{F}^p = 0 \tag{3.27}
$$

In non-associative formulation the functions F^p and F^d in Eq. (3.25) are replaced by plastic potential function G^p and damage potential function G^d

$$
\begin{aligned}
G^p &= G^p(\sigma_{ij}, R) \\
G^d &= G^d(Y_{ij}, B)
\end{aligned}
\tag{3.28}
$$

The evolution laws are then

$$
\begin{aligned}
\dot{D}_{ij} &= \dot{\lambda}^d \frac{\partial G^d}{\partial Y_{ij}}, & \dot{\kappa} &= -\dot{\lambda}^d \frac{\partial G^d}{\partial B} \\
\dot{\varepsilon}^p_{ij} &= \dot{\lambda}^p \frac{\partial G^p}{\partial \sigma_{ij}}, & \dot{\alpha}^p &= -\dot{\lambda}^p \frac{\partial G^p}{\partial R}
\end{aligned}
\tag{3.29}
$$

The non-associated formulation reduces to associated formulation when $F^d = G^d$ and $F^p = G^p$. As stated by Ristinmaa and Ottosen (2000) and Santaoja (2001), the associated formulation fulfils the dissipation inequality if F is a convex function. When considering non-associated formulation it is more difficult to show that the dissipation inequality is fulfilled.

Edelen (1972) introduced requirements for the non-associated potential function such that the dissipation inequality is fulfilled. According to Lemaitre and Chaboche (1990, p. 193), the dissipation inequality in non-associated formulation is ensured if the potential function *G* "is convex and positive as soon as there is plastic flow and includes the origin".

3.6.2 Basis of damage mechanics

In models of continuum damage mechanics (CDM), damage can be considered as a macroscopic state variable that affects the macromechanical properties (stiffness degradation) of the material. Physically the loss of stiffness can be considered a consequence of distributed microcracks and microvoids.

Continuum mechanics deals with mathematical quantities that represent averages of a certain volume (Lemaitre, 1992, p. 3). The volume must be small enough to avoid high gradient smoothing, "but large enough to represent an average of the microprocesses" (ibid.). The volume is called "representative volume element" (RVE). The size of the RVE depends on the material. Lemaitre (1992, p. 3) gives the following scales for the RVE:

- metals and ceramics: $(0.1\ \text{mm})^3$
- wood: $(10\ \text{mm})^3$
- concrete: $(100\ \text{mm})^3$.

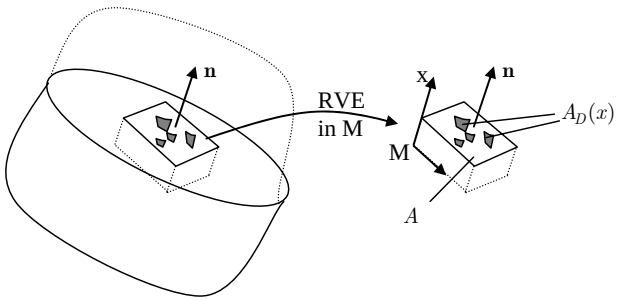

Figure 3.16. Definition of damage (Redrawn from Lemaitre (1992, p. 11)).

The concept of damage can be illustrated by considering the RVE at a point M shown in Fig. 3.16, where $\mathbf{n}$ is the surface normal to the intersection, *x* is the abscissa along the direction $\mathbf{n}$, A is the surface area, and A_D is the area of all microcracks and microcavities that lie on the intersection A. The value of the damage *D* attached to the point M in the direction $\mathbf{n}$ is

$$D(M, x, \mathbf{n}) = \frac{A_D(x)}{A} \tag{3.30}$$

As shown in Eq. (3.30), the damage *D* varies with *x*. A continuous variable over the RVE for its deterioration to failure is defined considering the plane that is most damaged:

$$D(M, \mathbf{n}) = \frac{\mathrm{Max}[A_D(x)]}{A} \tag{3.31}$$

Thus the value of the scalar damage variable depends on the point and direction considered. The value is in the range

$$0 \leq D < 1 \tag{3.32}$$

where the value of 0 corresponds to undamaged RVE material and the value of 1 to fully broken material.

In CDM, formulation of the constitutive equations is based one of the following two approaches:

- Strain equivalence principle approach
- Stress equivalence principle approach.

In the strain equivalence principle shown in Fig. 3.17, “any strain constitutive equation for damaged material may be derived in the same way as for a virgin material, except that the usual stress is replaced by the effective stress” (Lemaitre, 1992, p. 13). In the stress equivalence principle, the stress associated with the damaged state is the same as the stress obtained in the undamaged state under effective strain (fig. 3.18).

As stated by Simo and Ju (1987), the strain equivalence principle is naturally associated with a strain-based formulation of the constitutive equations while the stress equivalence principle corresponds to a stress-based formulation. In the strain-based formulation the elastic energy density is written as a function of strains, while in the stress-based formulation the complementary form is used.

The damage effect tensor M_{ijkl} defines the relation between the effective and nominal counterparts as follows (Voyiadjis and Park, 1997; Carol et al., 2001):

$$\begin{aligned} \sigma_{ij}^{eff} &= M_{ijkl}\sigma_{kl}, \qquad \sigma_{ij} = M_{ijkl}^{-1}\sigma_{kl}^{eff} \\ \varepsilon_{ij}^{eff} &= M_{ijkl}^{-1}\varepsilon_{kl}, \qquad \varepsilon_{ij} = M_{ijkl}\varepsilon_{kl}^{eff} \end{aligned} \tag{3.33}$$

where M_{ijkl}^{-1} is the inverse of M_{ijkl}. Depending on the form of the damage effect tensor M_{ijkl}, it is possible that the effective stress in Eq. (3.33) is non-symmetric. By contrast, the energy equivalence principle automatically induces symmetry in the secant stiffness tensor.

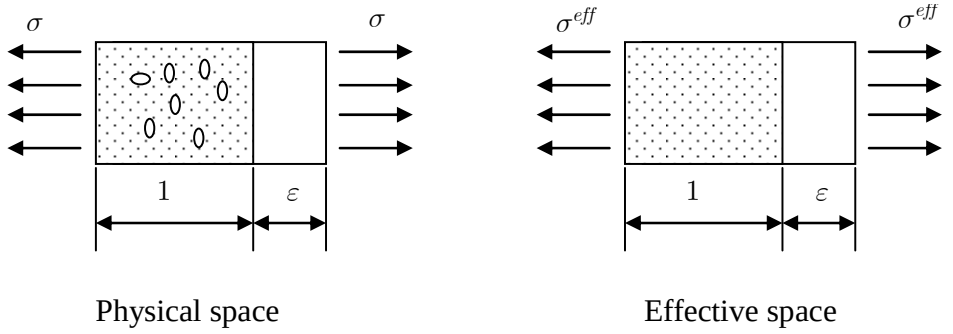

Figure 3.17. Effective stress concept and the hypothesis of strain equivalence (redrawn from Simo and Ju (1987)).

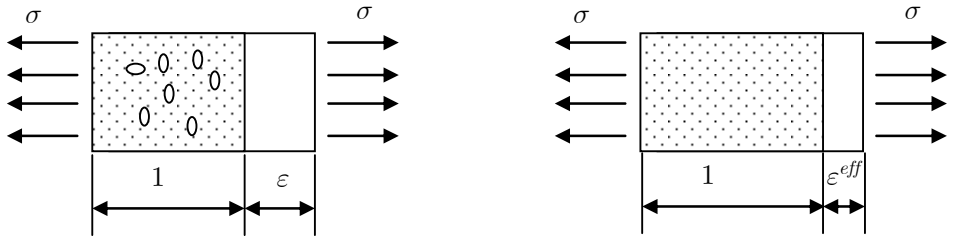

Physical space Effective space

Figure 3.18. Effective strain concept and the hypothesis of stress equivalence (redrawn from Simo and Ju (1987)).

3.6.2.1 Effective stress concept

The effective stress approach was introduced by Rabotnov 1968 (Lemaitre, 1992, p. 12). Consider the RVE shown in Fig. 3.19 loaded by a force **F**. The uniaxial stress due to the force is

$$\sigma = \frac{F}{A} \tag{3.34}$$

If the force is divided by the area that effectively resists the load ($A - A_D$), the result is the effective stress σ^{eff}:

$$\sigma^{eff} = \frac{F}{A - A_D} \tag{3.35}$$

Using the definition of damage given in Eqs. (3.30) and (3.31), Eq. (3.35) gives

$$\sigma^{eff} = \frac{\sigma}{1 - D} \tag{3.36}$$

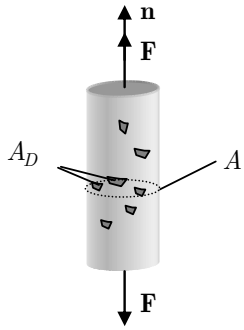

Figure 3.19. Damaged element (Redrawn from Lemaitre (1992, p. 12)).

The definition given in Eq. (3.35) is for the RVE under tension. Under compression the effective area resisting the load may be larger due to the closing defects. If all the defects close under compression, the effective stress is the same as the stress in the undamaged RVE.

3.6.2.2 Isotropic damage

The damage variable D introduced in Eq. (3.31) depends on the location and orientation of the RVE. If the damage is assumed to be isotropic, it has the same value in all directions and the scalar damage variable completely characterises the three-dimensional damage state:

$$D = \frac{A_D}{A} \tag{3.37}$$

The Hooke's law defining the relation between stresses and strains is

$$\sigma_{ij} = C^e_{ijkl}\varepsilon^e_{kl} \tag{3.38}$$

According to the effective stress concept introduced in Section 3.6.2, the stress in Eq. (3.38) can be replaced by the effective stress of Eq. (3.36):

$$\frac{\sigma_{ij}}{1-D} = C^e_{ijkl}\varepsilon^e_{kl} \tag{3.39}$$

from which the following stress-strain relation for isotropic damage is obtained:

$$\sigma_{ij} = (1 - D)\, C^{e}_{ijkl}\, \varepsilon^{e}_{kl} \tag{3.40}$$

3.6.2.3 Geometric second order damage tensor

When damage is anisotropic, the damage vector or tensor must be used instead of a scalar damage variable. Second, fourth and higher than fourth order tensors have been used to represent damage, but the physical meaning of higher than second order tensors may be difficult to understand. The effective stress concept in anisotropic damage is straightforward when a second order damage tensor is used. The second order damage tensor can be obtained from purely geometric analysis as shown in this section. The tensorial nature of damage has been widely studied (Leckie and Onat, 1981; Betten, 1983; Voyiadjis and Deliktas, 2000; Carol et al., 2001).

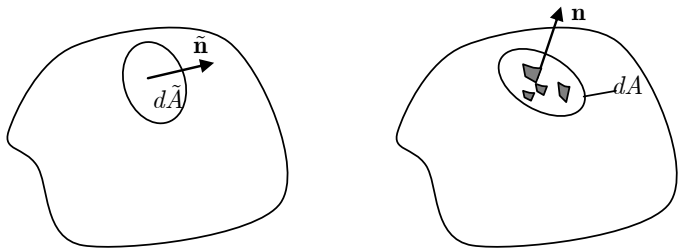

Undamaged configuration
Strain equivalent

Damaged configuration

Figure 3.20. Damaged and undamaged surface area (Redrawn from Lemaitre (1992, p. 61)).

Second order damage tensor D_{ij} can be derived from the surface area analogy as in Eq. (3.31). Let dA represent the surface area of the material in its current configuration, and n_j a unit normal to the area element as shown in Fig. 3.20, while $d\tilde{A}$ represents the strain-equivalent undamaged area and $\tilde{n}_j$ its normal, respectively. The relation between the damaged and undamaged and area elements is the following (Murakami, 1990; Lemaitre, 1992):

$$\tilde{n}_j d\tilde{A} = (\delta_{jk} - D_{jk}) n_k dA \tag{3.41}$$

The principal values $D_{(i)}$ of the damage tensor D_{ij} correspond to the reduction of the area of the tetrahedron as shown in Fig. 3.21.

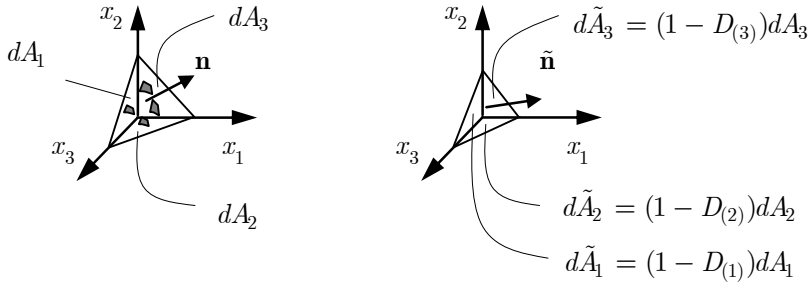

Figure 3.21. Damaged and strain equivalent undamaged configuration in principal coordinates of the damage tensor. (Redrawn from Lemaitre (1992, p. 61).

The force acting on the area is

$$\sigma_{ij}^{eff}\tilde{n}_j d\tilde{A} = \sigma_{ik} n_k dA \tag{3.42}$$

Using the definition in Eq. (3.41), Eq. (3.42) is written in the following form:

$$\sigma_{ij}^{eff}(\delta_{jk} - D_{jk}) = \sigma_{ik} \tag{3.43}$$

The tensor $\phi_{kj} = \delta_{kj} - D_{kj}$ is the continuity tensor, also called the integrity tensor (Valanis, 1990; Carol et al., 2001). Tensors ϕ_{ki} and D_{ki} share their principal axes and principal values and the principal values vary between 0 and 1 (Carol et al., 2001). Their principal values are related according to

$$D_{(i)} = 1 - \phi_{(i)} \tag{3.44}$$

where $D_{(i)}$ are the principal values of D_{ki} and $\phi_{(i)}$ are the principal values of ϕ_{ki}.

The effective stress tensor given in Eq. (3.43) could be defined by

$$\sigma_{ij}^{eff} = \sigma_{ik} a_{kj} \tag{3.45}$$

where a_{kj} is the inverse of $(\delta_{ik} - D_{ik})$ i.e. $(\delta_{ik} - D_{ik})a_{kj} = \delta_{ij}$.

Similar to Eq. (3.33), also Eq. (3.45) leads to a non-symmetric effective stress tensor. A number of symmetrisation forms have been proposed by researchers. Betten (1983) has proposed the following sum-type symmetrisation form:

$$\sigma_{ij}^{eff} = \frac{1}{2}\left[\sigma_{ik}a_{kj} + \sigma_{jk}a_{ki}\right] \tag{3.46}$$

The following product-type symmetrisation method has been proposed by Cordebois and Sidoroff at 1982 (Voyiadjis and Park, 1997; Voyiadjis and Deliktas, 2000):

$$\sigma_{ij}^{eff} = b_{ik}\sigma_{kl}b_{jl} \tag{3.47}$$

where b_{ik} defined in principal damage coordinate system is:

$$b_{ik} = \begin{bmatrix} \frac{1}{\sqrt{1-D_{(1)}}} & 0 & 0 \\ 0 & \frac{1}{\sqrt{1-D_{(2)}}} & 0 \\ 0 & 0 & \frac{1}{\sqrt{1-D_{(3)}}} \end{bmatrix} \tag{3.48}$$

Using the symmetrisation method of Eq. (3.47), the following form of the damage effect tensor M_{ijkl} in Eq. (3.33) can be obtained (Voyiadjis and Deliktas, 2000):

$$M_{ikjl} = b_{ik}b_{jl} \tag{3.49}$$

To illustrate the damage effect tensor M_{ijkl}, the tensor is written in matrix form. The inverse of the tensor written on the principal axis of the integrity tensor is (Carol et al., 2001)

$$[\mathbf{M}]^{-1} = \begin{bmatrix} \phi_{(1)} & 0 & 0 & 0 & 0 & 0 \\ 0 & \phi_{(2)} & 0 & 0 & 0 & 0 \\ 0 & 0 & \phi_{(3)} & 0 & 0 & 0 \\ 0 & 0 & 0 & \sqrt{\phi_{(1)}\phi_{(2)}} & 0 & 0 \\ 0 & 0 & 0 & 0 & \sqrt{\phi_{(1)}\phi_{(3)}} & 0 \\ 0 & 0 & 0 & 0 & 0 & \sqrt{\phi_{(2)}\phi_{(3)}} \end{bmatrix} \tag{3.50}$$

3.6.2.4 Phenomenological damage models

In the previous chapter, the derived second order damage tensor D_{ij} was based on the effective stress approach and the physical meaning of the tensor was based purely on the geometric analysis. The principal values $D_{(i)}$ of the damage tensor D_{ij} based on the effective stress concept are in the range $0 \leq D_{(i)} < 1$ (Carol et al., 2001).

There are number of models in which the damage tensor can be considered (only) as an internal state variable (Murakami and Kamiya, 1997; Halm and Dragon, 1998; Hayakawa et al., 1998; Challamel et al., 2005). These models are called "phenomenological damage models" in this study. In the phenomenological approach, a model formulation may be based on micro-mechanically motivated mechanisms, or the damage tensor may be considered only as an internal state variable affecting the stress-strain response without a micromechanical background. Therefore the physical meaning of the damage tensor might be difficult to understand. Also, the allowable range of principal values of the damage tensor may be indeterminate.

In the "phenomenological approach" the Helmholtz free energy $\psi(\varepsilon^e_{ij}, D_{ij})$ is often written using invariants based on the use of the damage tensor. For example, a combination of the basic invariants of elastic strain tensor ε^e_{ij} and damage tensor D_{ij} can be used (Murakami and Kamiya, 1997):

$$\begin{array}{lll} \varepsilon^e_{kk}\varepsilon^e_{ll}, & \varepsilon^e_{kl}\varepsilon^e_{kl}, & \varepsilon^e_{kk}\varepsilon^e_{ll}D_{mm}, \\ \varepsilon^e_{kk}\varepsilon^e_{ml}D_{ml}, & D_{km}\varepsilon^e_{ml}\varepsilon^e_{lk} & \varepsilon^e_{kl}\varepsilon^e_{kl}D_{mm} \end{array} \tag{3.51}$$

where only the invariants that are linear in D_{ij} are given. Using the invariants in Eq. (3.51) the Helmholtz free energy can be written as follows (Murakami and Kamiya, 1997):

$$\begin{aligned}\rho\psi^e &= \frac{1}{2}\lambda(\varepsilon^e_{kk})^2 + \mu\,\varepsilon^e_{kl}\varepsilon^e_{kl} + \eta_1 D_{kk}(\varepsilon^e_{ll})^2 + \eta_2 D_{kk}\varepsilon^e_{mn}\varepsilon^e_{nm} \\ &\quad + \eta_3\varepsilon^e_{kk}\varepsilon^e_{mn}D_{nm} + \eta_4\varepsilon^*_{kl}\varepsilon^*_{lm}D_{mk} \\ \rho\psi^d &= \frac{1}{2}h\,\kappa^2\end{aligned} \tag{3.52}$$

where ε^*_{ij} is the modified strain describing the crack closure effect, $\eta_1,\ldots,\eta_4$ and h are material constants, ρ is the density and κ is "internal scalar variable prescribing the development of damage."

3.7 Rate-dependent brittle damaging

The behaviour of most materials is known to be strain rate-dependent. Concrete and natural ice are examples of strain rate-dependent brittle materials (Lambert and Ross, 2000; Schulson, 2001). The rate dependency is verified experimentally using either the displacement-rate or force-rate controlled methods. In the experimental evaluation of strain-rate dependency, the effects of inertia forces should be carefully taken into account in order to avoid misleading results.

The strain rate is known to affect the material strength of viscoplastic materials. There are also results which indicate that the strength of brittle materials is strain-rate dependent, e.g. the strength of concrete and ceramics has been found to be higher when the strain rate is increased (Chen and Ravichandran, 2000; Koh et al., 2001; Georgin and Reynouard, 2003). In their studies of strength increase due to strain rate increase, Nard and Bailly (2000) suggested that the apparent compressive strength increase was a result of "inertial confinement". In numerical simulations, they remarked that introducing rate-dependent strength into the constitutive model was not necessary in order to take into account an experimental compressive strength increase. According to Georgin and Reynouard (2003), at strain rates below 1 s^{-1} the rate effect of concrete material is assumed to result from free water, while for rates over 10 s^{-1} it is assumed to result from the inertial confinement.

Although the mechanisms behind the strain rate dependency in brittle failure are not known, the rate dependency has been considered in this study. As discussed in Section 1.1, the objective concerning the rate effect was to implement the rate-dependent strength model in the wing crack damage model.

Rate-dependent solution methods introduce the length scale into the numerical model. The length scale eliminates the mesh sensitivity, which is known to be a problem in strain-softening material models.

3.7.1 Perzyna model

The commonly used Perzyna-type rate-dependent approach has been applied also in damage mechanics; e.g. Dube et al. (1996) proposed a model for isotropic rate-dependent damage of concrete using the Perzyna method. Challamel et al. (2005) have also proposed a Perzyna-type time-dependent equation for damage evolution. Challamel et al. have neither applied the rate dependency nor given any examples of rate-dependent damage. The Perzyna-type rate-dependent method is an example of an “overstress model”. In the Perzyna method, material strength increases with increasing rate.

In the Perzyna (1966) model the evolution law for plastic strains $\dot{\varepsilon}_{ij}^{p}$ is given in the following form:

$$\begin{aligned} \dot{\varepsilon}_{ij}^{p} &= \dot{\lambda}\frac{\partial F}{\partial \sigma_{ij}} \\ \dot{\kappa} &= \dot{\lambda}\frac{\partial F}{\partial B} \end{aligned} \tag{3.53}$$

where the consistency parameter is defined as non-negative function ϕ of a static yield function F and viscosity parameter η as follows:

$$\dot{\lambda} = \frac{\langle \phi(F) \rangle}{\eta} \tag{3.54}$$

where $\langle\ \rangle$ are McCauley brackets:

$$\langle x \rangle = \frac{1}{2}(x + |x|) \tag{3.55}$$

In 1995, Ponthot introduced “continuous” viscoplastic formulation (Carosio et al., 2000). In the formulation, Eq. (3.54) is transformed into the format of a rate-dependent yield condition:

$$\bar{F}(\sigma_{ij}, \lambda, \dot{\lambda}) = F(\sigma_{ij}, \lambda) - \phi^{-1}(\eta\dot{\lambda}) = 0 \tag{3.56}$$

where $\phi^{-1}(\eta\dot{\lambda})$ is inverse function of $\phi(F)$ in Eq.(3.54).

The viscoplastic consistency condition is then

$$\frac{\partial F}{\partial \sigma_{ij}}\dot{\sigma}_{ij} + \left(\frac{\partial F}{\partial \lambda} - \frac{\partial \phi^{-1}\left(\eta\dot{\lambda}\right)}{\partial \lambda}\right)\dot{\lambda} - \frac{\partial \phi^{-1}\left(\eta\dot{\lambda}\right)}{\partial \dot{\lambda}}\ddot{\lambda} = 0 \tag{3.57}$$

3.7.2 Consistent viscoplasticity

Wang (Wang et al., 1997; Wang, 1997) proposed a so-called consistency viscoplastic formulation where the rate-dependent yield surface was introduced in such way that Kuhn-Tucker conditions remain valid. In addition to time-dependent solutions, Wang’s formulation can be used to introduce a length scale into the model. In the approach, the proposed rate of state variables is included as an independent variable into the yield criteria:

$$F = F(\sigma_{ij}, \kappa, \dot{\kappa}) = 0 \tag{3.58}$$

The corresponding consistency condition is then

$$n_{ij}\dot{\sigma}_{ij} - h\dot{\kappa} - \xi\ddot{\kappa} = 0 \tag{3.59}$$

where the yield surface gradient n_{ij}, the hardening modulus h and the viscosity parameter ξ are defined as follows:

$$n_{ij} = \frac{\partial F}{\partial \sigma_{ij}}, \quad h = -\frac{\partial F}{\partial \kappa}, \quad \xi = -\frac{\partial F}{\partial \dot{\kappa}} \tag{3.60}$$

In the consistency approach, the yield surface can expand and shrink due to both the hardening and hardening rate effects.

As shown by Carosio et al. (2000) and Heeres et al. (2002), the consistency approach of Eq. (3.59) reduces to the Perzyna formulation of Eq. (3.57) when

$$\begin{aligned} \xi &= \frac{\partial \phi^{-1}(\dot{\lambda}\eta)}{\partial \dot{\lambda}} \\ \dot{\kappa} &= \dot{\lambda} \end{aligned} \tag{3.61}$$

3.7.2.1 Consistent viscoplasticity in damage mechanics

The damage surface is given as a function of the total elastic strain ε_{ij}^{e}, hardening variable κ and hardening variable rate $\dot{\kappa}$

$$F = F(\varepsilon_{ij}^{e}, \kappa, \dot{\kappa}) = 0 \tag{3.62}$$

The consistency condition is

$$\dot{F} = \frac{\partial F}{\partial \varepsilon_{ij}^{e}} \dot{\varepsilon}_{ij}^{e} + \frac{\partial F}{\partial \kappa} \dot{\kappa} + \frac{\partial F}{\partial \dot{\kappa}} \ddot{\kappa} = 0 \tag{3.63}$$

In finite element formulation, stresses and internal state variables are updated in integration points. The update starts from time *t* with the known variables: $\sigma_{ij}^{t}, \varepsilon_{ij}^{e,t}, \kappa^{t}$. In the update process the corresponding values at time $t + \Delta t$ are calculated: $\sigma_{ij}^{t+\Delta t}, \varepsilon_{ij}^{e,t+\Delta t}, \kappa^{t+\Delta t}$.

There are no plastic deformations in this approach, therefore the elastic strain tensor $\varepsilon_{ij}^{e,t+\Delta t}$ is known. The hardening variable κ is solved iteratively from the discretised consistency condition of the damage surface following the same procedure as Wang et al. (1997). The Newton-Raphson iteration process is used to solve the hardening variable κ. The consistency condition at iteration step *i* is:

$$F(\varepsilon_{ij}^{e},\kappa,\dot{\kappa}) \approx F^{(i)} + \frac{\partial F}{\partial \varepsilon_{ij}^{e}}\delta\varepsilon_{ij}^{e} + \frac{\partial F}{\partial \kappa}\delta\kappa + \frac{\partial F}{\partial \dot{\kappa}}\delta\dot{\kappa} = 0 \tag{3.64}$$

where $\delta\varepsilon_{ij}^{e}$ is the iterative strain increment, $\delta\kappa$ is the iterative hardening variable increment, $\delta\dot{\kappa}$ is the increment of the iterative hardening variable rate and $F^{(i)} = F(\varepsilon_{ij}^{e(i)},\kappa^{(i)},\dot{\kappa}^{(i)})$ is the *i*th residual of the damage function F at iteration step *i*. The variable κ is integrated by the Euler backward algorithm:

$$\begin{aligned} \delta\kappa^{(i)} &= \delta\dot{\kappa}\,\Delta t \\ \Delta\kappa^{(i)} &= \sum_{i}\delta\kappa^{(i)} \end{aligned} \tag{3.65}$$

where Δt is the time increment and $\Delta\kappa^{(i)}$ is the hardening variable increment. The updated hardening variable increment $\Delta\kappa$ when $F^{(i)} \approx 0$ is

$$\kappa^{t+\Delta t} = \kappa^{t} + \Delta\kappa \tag{3.66}$$

Using Eqs. (3.64) and (3.65) the consistency condition can be rewritten as

$$-F^{(i)} = \frac{\partial F}{\partial \varepsilon_{ij}^{e}}\delta\varepsilon_{ij}^{e} + \left(\frac{\partial F}{\partial \kappa} + \frac{\partial F}{\partial \dot{\kappa}}\frac{1}{\Delta t}\right)\delta\kappa \tag{3.67}$$

from which $\delta\kappa$ is obtained as follows:

$$\delta\kappa = -\left(\frac{\partial F}{\partial \kappa} + \frac{\partial F}{\partial \dot{\kappa}}\frac{1}{\Delta t}\right)^{-1}\left(F^{(i)} + \frac{\partial F}{\partial \varepsilon_{ij}^{e}}\delta\varepsilon_{ij}^{e}\right) \tag{3.68}$$

During local iteration the iterative strain increment $\delta\varepsilon_{ij}^{e}$ in Eq. (3.68) vanishes.

In incremental solution of equilibrium equations, the stress-strain relation must be formulated into incremental form. Assuming that the stress is a function of damage and elastic strain as follows:

$$\sigma_{ij} = \sigma_{ij}(\varepsilon_{kl}^{e}, D_{kl}) \tag{3.69}$$

the incremental form is obtained from Eq. (3.69) is

$$\delta\sigma_{ij} = \frac{\partial\sigma_{ij}}{\partial\varepsilon^e_{kl}}\delta\varepsilon^e_{kl} + \frac{\partial\sigma_{ij}}{\partial D_{kl}}\delta D_{kl} \tag{3.70}$$

In this study the hardening parameter equals the multiplier

$$\kappa = \lambda \tag{3.71}$$

Thus also $\delta\kappa = \delta\lambda$. The damage increment is obtained from $(3.29)_1$ as follows:

$$\begin{aligned} \delta D_{ij} &= \dot{D}_{ij}\Delta t \\ \delta\lambda &= \dot{\lambda}\Delta t \\ \delta D_{ij} &= \delta\lambda\frac{\partial G}{\partial Y_{ij}} \end{aligned} \tag{3.72}$$

Substituting Equations (3.71) and (3.72) into Eq. (3.70), the following for the stress increment is obtained:

$$\delta\sigma_{ij} = \frac{\partial\sigma_{ij}}{\partial\varepsilon^e_{kl}}\delta\varepsilon^e_{kl} + \frac{\partial\sigma_{ij}}{\partial D_{kl}}\frac{\partial G}{\partial Y_{kl}}\delta\kappa \tag{3.73}$$

Substitution of (3.68) into Eq. (3.73) gives the material Jacobian when the residual $F^{(i)}$ vanishes:

$$K^t_{ijkl} = \frac{\partial\sigma_{ij}}{\partial\varepsilon^e_{kl}} - \frac{1}{\dfrac{\partial F}{\partial\kappa} + \dfrac{\partial F}{\partial\dot{\kappa}}\dfrac{1}{\Delta t}}\frac{\partial\sigma_{ij}}{\partial D_{mp}}\frac{\partial G}{\partial Y_{mp}}\frac{\partial F}{\partial\varepsilon^e_{kl}} \tag{3.74}$$

3.8 Murakami Kamiya damage model

3.8.1 Objectives

In the continuum damage model of Murakami and Kamiya (1997) the damage evolution induces anisotropic stiffness degradation of initially isotropic material. Under uniaxial compression, the damage tensor evolution is mainly determined by the directions of principal tensile strain. Thus the approach enables modelling

of the axial splitting failure mode under compression. The model also produces the correct tensile failure mode (see Fig. 3.2e).

Besides the Murakami and Kamiya (1997) model there are several other models suitable for unilateral behaviour modelling (Florez-Lopez, 1995; Fremond and Nedjar, 1995; Papa, 1996; Vinet and Priou, 1997; Voyiadjis and Zolochevsky, 1998; Comi and Perego, 2001; Pensee et al., 2002; Gambarotta, 2004). As discussed in Section 3.3.3, stress-based failure surfaces are generally not suitable for modelling the axial splitting and tensile failure, because it is difficult to formulate a dissipation potential function whose derivative gives a correct damage evolution both under uniaxial compression and tension. Halm and Dragon (Halm and Dragon, 1998; Dragon et al., 2000; Halm et al., 2002) have introduced a damage model suitable for modelling the axial splitting and tensile failure, but as pointed out by Cormery and Welemane (2002) their method leads to non-uniqueness of free energy.

The Murakami and Kamiya (MK) model has promising features for modelling of quasi-brittle material. The model was recently studied by Skrzypek and Kuna-Ciskal (2003), and Kuna-Ciskal and Skrzypek (2004). They implemented the MK model in ABAQUS FE software but only for 2D problems. Challamel et al. (2005) introduced a modified MK model by changing the function controlling unilateral behaviour and simplifying the Helmholtz free energy equation.

The MK model was chosen as a basis for the brittle failure model development because of both its capability and simplicity. The MK model has the basic features needed: a unilateral feature and a splitting feature. The simplicity enables FE implementation. The experience of Skrzypek and Kuna-Ciskal (2003) with the MK model also encourages its choice.

As described in Section 1.1, the objective concerning the MK model was:

A. To enhance applicability of the damage mechanics approach proposed by Murakami and Kamiya (1997) for modelling brittle failure in 3D space as follows:

    1. Implement a 3D version of the Murakami and Kamiya model (MK model) in the ABAQUS/Standard FE software.

2. Identify the weaknesses and strengths of the MK model and amend potential weaknesses.
3. Study whether the MK model could be modified for analysis of transversely isotropic materials.

3.8.2 Murakami-Kamiya model

3.8.2.1 Helmholtz free energy

In the MK model the Helmholtz free energy per unit mass is expressed in the following form:

$$\begin{aligned}
\rho\psi &= \rho\psi^e + \rho\psi^d \\
\rho\psi^e &= \frac{1}{2}\lambda\,(\varepsilon^e_{kk})^2 + \mu\,\varepsilon^e_{kl}\varepsilon^e_{kl} + \eta_1\,D_{kk}(\varepsilon^e_{ll})^2 + \eta_2 D_{kk}\varepsilon^e_{mn}\varepsilon^e_{nm} \\
&\quad +\eta_3\varepsilon^e_{kk}\varepsilon^e_{mn}D_{nm} + \eta_4\varepsilon^*_{kl}\varepsilon^*_{lm}D_{mk} \\
\rho\psi^d &= \frac{1}{2}h\,\kappa^2
\end{aligned} \tag{3.75}$$

where ε^e_{ij} is the elastic strain tensor, ε^*_{ij} is modified strain describing the crack closure effect, λ and μ are lame constants, η_1, η_2, η_3 and η_4 are scalar material constants describing the damage surface, *h* is a material parameter, and κ is the scalar damage variable.

The modified strain in the principal strain coordinate system $\hat{\varepsilon}^*_{ij}$ can be represented using the following (Skrzypek and Kuna-Ciskal, 2003):

$$\hat{\varepsilon}^*_{(i)} = k_{(i)}\,\hat{\varepsilon}^e_{(i)}, \ \text{no summ.} \tag{3.76}$$

where $\hat{\varepsilon}^e_{(i)}$ is the principal strain and the function $k_{(i)}$ describes the crack closure effect as follows:

$$k_{(i)} = H(\hat{\varepsilon}^e_{(i)}) + \zeta\,H(-\hat{\varepsilon}^e_{(i)}) \tag{3.77}$$

where H is the Heaviside step function and ζ is a material constant describing the crack closure effect. When ζ = 1 the crack closure effect is neglected. The rotation of the strain tensor into principal coordinates can be expressed using the rotation tensor Q_{ij} as follows:

$$\begin{aligned} \hat{\varepsilon}^e_{ij} &= Q_{ki}\varepsilon^e_{kl}Q_{lj} \\ \varepsilon^e_{ij} &= Q_{ik}\hat{\varepsilon}^e_{kl}Q_{jl} \end{aligned} \tag{3.78}$$

where the rotation tensor has the following feature:

$$\delta_{ij} = Q_{ik}Q_{jk} \tag{3.79}$$

The expression of Eq. (3.76) can be written in the following form

$$\hat{\varepsilon}^*_{ij} = k_{ik}\,\hat{\varepsilon}^e_{kj} \tag{3.80}$$

where

$$\begin{aligned} k_{ij} &= 0, \quad \text{when} \quad i \neq j \\ \hat{\varepsilon}^e_{ij} &= 0, \quad \text{when} \quad i \neq j \\ k_{ii} &= k_{(i)}, \quad (\text{no summ.}) \\ \hat{\varepsilon}^e_{ii} &= \hat{\varepsilon}^e_{(i)}, \quad (\text{no summ.}) \end{aligned} \tag{3.81}$$

Using Eqs. (3.78) and (3.80) the modified strain tensor may be given as follows:

$$\begin{aligned} \varepsilon^*_{ij} &= Q_{ip}\hat{\varepsilon}^*_{pr}Q_{jr} \\ &= Q_{ip}(k_{pm}Q_{km}\varepsilon^e_{kl}Q_{lr})Q_{jr} \\ &= B_{ijkl}\varepsilon^e_{kl} \end{aligned} \tag{3.82}$$

where B_{ijkl} is the projection tensor.

3.8.2.2 Constitutive equations and damage evolution

Using the Helmholtz free energy per unit mass ψ in Eq. (3.75) the relation between stress and strain is obtained from $(3.18)_1$:

$$\begin{aligned}\sigma_{ij} &= \rho \frac{\partial \psi}{\partial \varepsilon^e_{ij}} \\ &= \lambda \varepsilon^e_{kk}\delta_{ij} + 2\mu\varepsilon^e_{ij} + [2\eta_1 D_{kk}\varepsilon^e_{ll} + \eta_3 \varepsilon^e_{kl} D_{lk}]\delta_{ij} + 2\eta_2 D_{kk}\varepsilon^e_{ij} \\ &+\eta_3 \varepsilon^e_{kk} D_{ji} + \eta_4 \left[\varepsilon^*_{lm} D_{mk} + D_{lm}\varepsilon^*_{mk} \right] \frac{\partial \varepsilon^*_{kl}}{\partial \varepsilon^e_{ij}}\end{aligned} \tag{3.83}$$

Substituting Eq. (3.82) into Eq. (3.83) the following formula is obtained:

$$\sigma_{ij} = K_{ijkl}\, \varepsilon^e_{kl} \tag{3.84}$$

where K_{ijkl} is the constitutive (secant stiffness) tensor as follows:

$$\begin{aligned}K_{ijkl} &= \lambda\delta_{kl}\delta_{ij} + 2\mu\delta_{ki}\delta_{jl} + 2\eta_1 D_{mm}\delta_{ij}\delta_{kl} + \eta_3\delta_{ij}D_{lk} \\ &+2\eta_2 D_{mm}\delta_{ik}\delta_{jl} + \eta_3 D_{ji}\delta_{kl} + \eta_4 \left[B_{rmkl} D_{mq} + D_{rm} B_{mqkl} \right] B_{qrij} \\ &= (\lambda + 2\eta_1 D_{mm})\delta_{ij}\delta_{kl} + 2(\mu + \eta_2 D_{mm})\delta_{ki}\delta_{jl} \\ &+\eta_3(\delta_{ij}D_{lk} + D_{ji}\delta_{kl}) + \eta_4 \left[B_{rmkl} D_{mq} + D_{rm} B_{mqkl} \right] B_{qrij}\end{aligned} \tag{3.85}$$

Using the matrix notation for stress and strain, Eq. (3.84) can be written in the following form:

$$\{\boldsymbol{\sigma}\} = [\mathbf{K}]\{\boldsymbol{\varepsilon}^e\} \tag{3.86}$$

where $[\mathbf{K}]$ is the secant stiffness matrix.

The associated variable (thermodynamic conjugate force) for damage is obtained from Eq. $(3.18)_2$:

$$-Y_{ij} = \rho \frac{\partial \psi}{\partial D_{ij}} = \left[\eta_1 (\varepsilon^e_{kk})^2 + \eta_2 \varepsilon^e_{kl}\varepsilon^e_{lk} \right]\delta_{ij} + \eta_3 \varepsilon^e_{kk}\varepsilon^e_{ji} + \eta_4 \varepsilon^*_{jl}\varepsilon^*_{li} \tag{3.87}$$

The force Y_{ij} represents energy release due to the development of damage at constant stress: $d\sigma_{ij} = 0$ (Lemaitre, 1992, p. 43; Murakami and Kamiya, 1997). Respectively, the associated variable for κ is obtained from $(3.18)_3$

$$B = \rho \frac{\partial \psi}{\partial \kappa} = h\kappa \tag{3.88}$$

For the damage evolution equations, a proper expression for the dissipation potential is needed. Murakami and Kamiya (1997) have expressed the dissipation potential (Damage Surface) as a function of thermodynamic conjugate forces *B* and Y_{ij} as follows:

$$F = Y^{eq} - (B_0 + B) = 0 \tag{3.89}$$

where

$$Y^{eq} = \sqrt{\frac{1}{2} Y_{ij} L_{ijkl} Y_{kl}} \tag{3.90}$$

The fourth order tensor L_{ijkl}, called a damage characteristic tensor (Zhu and Cescotto, 1995), is used to represent the anisotropic nature of damage growth. In general, the tensor L_{ijkl} can depend on the internal state variables and material orientation. According to Murakami and Kamiya (1997) the damage characteristic tensor for isotropic material is:

$$L_{ijkl} = \frac{1}{2}(\delta_{ik}\delta_{jl} + \delta_{il}\delta_{jk}) \tag{3.91}$$

In Eq. (3.89) B_0 is a constant representing the initial threshold of damage evolution (in plasticity theory B_0 corresponds to the yield stress). Substituting Eq. (3.91) into Eq. (3.90), the following form is obtained:

$$Y^{eq} = \sqrt{\frac{1}{4}(Y_{kl}Y_{kl} + Y_{lk}Y_{kl})} \tag{3.92}$$

Evolution equations for damage tensor D_{ij} and damage variable κ are based on the normality rule. From Eqs. $(3.25)_{1,2}$, (3.89) and (3.92) after some manipulation the following is obtained:

$$\dot{D}_{ij} = \dot{\lambda}^d \frac{\partial F}{\partial Y_{ij}} = \dot{\lambda}^d \frac{(Y_{ij} + Y_{ji})}{4\,Y^{eq}}$$
$$\dot{\kappa} = -\dot{\lambda}^d \frac{\partial F}{\partial B} = \dot{\lambda}^d \tag{3.93}$$

where $\dot{\lambda}^d$ is a multiplier which can be determined from the consistency condition given in Eq. (3.27):

$$\frac{\partial F}{\partial Y_{ij}} \dot{Y}_{ij} + \frac{\partial F}{\partial B} \dot{B} = 0 \tag{3.94}$$

The multiplier $\dot{\lambda}^d$ can be solved using Eqs. (3.88), (3.89) and (3.94):

$$\begin{aligned} \dot{\lambda}^d &= \frac{1}{\dfrac{\partial F}{\partial B}\dfrac{\partial B}{\partial \kappa}\dfrac{\partial F}{\partial B}} \frac{\partial F}{\partial Y_{ij}} \dot{Y}_{ij} \\ &= \frac{1}{\dfrac{\partial F}{\partial B}\dfrac{\partial B}{\partial \kappa}\dfrac{\partial F}{\partial B}} \frac{(Y_{ij} + Y_{ji})}{4Y^{eq}} \dot{Y}_{ij} \end{aligned} \tag{3.95}$$

The Y_{ij} is a function of strain. Thus from Eq. $(3.95)_1$ we have

$$\dot{\lambda}^d = \frac{1}{\dfrac{\partial F}{\partial B}\dfrac{\partial F}{\partial \kappa}\dfrac{\partial F}{\partial B}} \frac{\partial F}{\partial Y_{ij}} \frac{\partial Y_{ij}}{\partial \varepsilon^e_{kl}} \dot{\varepsilon}^e_{kl} \tag{3.96}$$

3.8.2.3 Material Jacobian

Eq. (3.83) gives the stress tensor as a function of the strain and the damage tensor. The tensor B_{ijkl} is a function of strains, therefore the equation is nonlinear in the strain and linear in the damage tensor. In numerical solution of nonlinear problems, a structural response is solved using incremental iterative methods like the Newton-Raphson method. The material Jacobian tensor (tangent stiffness at equilibrium) is needed in the global solution of state equations.

Using the relations given in Eqs. $(3.18)_1$ and $(3.18)_2$ the rate form for the stress tensor can be written as

$$\begin{aligned}\dot{\sigma}_{ij} &= \frac{\partial \sigma_{ij}}{\partial\, \varepsilon^e_{kl}}\,\dot{\varepsilon}^e_{kl} + \frac{\partial \sigma_{ij}}{\partial D_{kl}}\,\dot{D}_{kl} \\ &= \frac{\partial \sigma_{ij}}{\partial\, \varepsilon^e_{kl}}\,\dot{\varepsilon}^e_{kl} - \frac{\partial\, Y_{kl}}{\partial\, \varepsilon^e_{ij}}\,\dot{D}_{kl}\end{aligned} \tag{3.97}$$

Substituting Eq. (3.93) and Eq. (3.95) into Eq. (3.97) and noting that Y_{ij} is symmetric, the stress rate can be written as

$$\begin{aligned}\dot{\sigma}_{ij} &= \frac{\partial \sigma_{ij}}{\partial\, \varepsilon^e_{kl}}\,\dot{\varepsilon}^e_{kl} + \frac{\partial \sigma_{ij}}{\partial D_{kl}}\,\dot{\lambda}^d\,\frac{(Y_{kl} + Y_{kl})}{4\,Y^{eq}} \\ &= \left(\frac{\partial \sigma_{ij}}{\partial\, \varepsilon^e_{mn}} + \frac{Y_{kl} Y_{po}}{4\,(Y^{eq})^2}\,\frac{1}{\dfrac{\partial F}{\partial B}\dfrac{\partial B}{\partial \kappa}\dfrac{\partial F}{\partial B}}\,\frac{\partial \sigma_{ij}}{\partial D_{kl}}\,\frac{\partial\, Y_{op}}{\partial \varepsilon^e_{mn}} \right) \dot{\varepsilon}^e_{mn}\end{aligned} \tag{3.98}$$

Using the matrix notation described in Section 2.2, Eq. (3.98) can be written in the following form:

$$\{\dot{\boldsymbol{\sigma}}\} = [\mathbf{K}^t(\mathbf{D}, \boldsymbol{\varepsilon}^e)]\{\dot{\boldsymbol{\varepsilon}}^e\} \tag{3.99}$$

where $[\mathbf{K}^t(\mathbf{D}, \boldsymbol{\varepsilon}^e)]$ is the material Jacobian. The stress tensor derivatives in Eq. (3.98) are obtained from Eq. (3.83) as follows:

$$\begin{aligned}\frac{\partial \sigma_{ij}}{\partial D_{op}} &= \left[2\eta_1 \delta_{op} \varepsilon^e_{ll} + \eta_3 \varepsilon^e_{op}\right]\delta_{ij} + 2\eta_2 \delta_{op} \varepsilon^e_{ij} \\ &\quad + \eta_3 \varepsilon^e_{kk} \delta_{jo} \delta_{ip} + \eta_4 \left[\varepsilon^*_{lo} \delta_{pk} + \delta_{ol} \varepsilon^*_{pk}\right] \frac{\partial\, \varepsilon^*_{kl}}{\partial \varepsilon^e_{ij}}\end{aligned} \tag{3.100}$$

$$\begin{aligned}\frac{\partial \sigma_{ij}}{\partial \varepsilon^e_{op}} &= \lambda \delta_{op} \delta_{ij} + 2\mu \delta_{oi} \delta_{jp} + \left[2\eta_1 D_{kk} \delta_{op} + \eta_3 D_{po}\right]\delta_{ij} \\ &\quad + 2\eta_2 D_{kk} \delta_{oi} \delta_{jp} + \eta_3 \delta_{op} D_{ji} \\ &\quad + \eta_4 \left[\left(\frac{\varepsilon^*_{lm}}{\partial \varepsilon^e_{op}} D_{mk} + D_{lm} \frac{\varepsilon^*_{mk}}{\partial \varepsilon^e_{op}} \right) B_{klij} \right. \\ &\quad \left. + \left(\varepsilon^*_{lm} D_{mk} + D_{lm} \varepsilon^*_{mk} \right) \frac{\partial B_{klij}}{\partial \varepsilon^e_{op}} \right]\end{aligned} \tag{3.101}$$

All derivatives are straightforward to calculate in numerical application, apart from the derivatives of ε_{ij}^{*} and B_{ijkl} which are cumbersome also according to Skrzypek and Kuna-Ciskal (2003).

3.8.3 Damage in tension-compression cycles

Due to the axial splitting feature of the MK model, the stiffness degradation in the compression direction is small compared to the perpendicular direction. The degree of degradation depends on the constant ζ in Eq. (3.77). A higher value of ζ results in increasing damage in the compression strain direction. The response is illustrated in Fig. 3.22 for uniaxial loading cases. Under compression, major damage evolution occurs perpendicular to the direction of compression stress. The perpendicular damage evolution introduces the splitting failure mode. If compression is continued after rupture, the stress-strain response follows path No. 2) in Fig. 3.22.

The tension-compression cycle is illustrated in Fig. 3.23. The stiffness degradation in the tension direction coincides with the loading direction. The degree of degradation is limited by the secant matrix positive definiteness condition. If the material is "fully damaged" (ruptured) under tension as illustrated in Fig. 3.23, it will not suffer further damage in the compression cycle (path No. 4 in Fig. 3.23). If tension of the fully damaged material is continued after tensile rupture, the stress-strain response follows path No. 3) shown in Fig. 3.23. The coefficient K^{R} in Fig. 3.23 illustrates the residual stiffness of ruptured material.

Ruptured material behaves like softened elastic material, having different stiffness under compression and tension. Thus if a material is ruptured in a cyclic loading case, it is questionable whether the response is in a reliable range. Therefore, the MK damage model is not recommended for cyclic (compression-tension) loading cases where the material is considerably damaged. The behaviour in cyclic loading should be studied more carefully and modified before it can be reliably used in cyclic loading simulations.

Axial stiffness is recovered when the loading direction is changed from tension to compression.

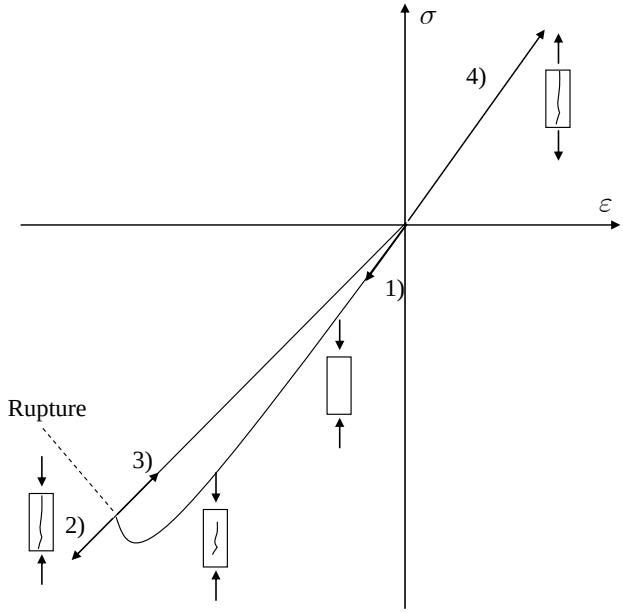

Figure 3.22. Illustration of uniaxial compression-tension cycle under displacement-controlled loading.

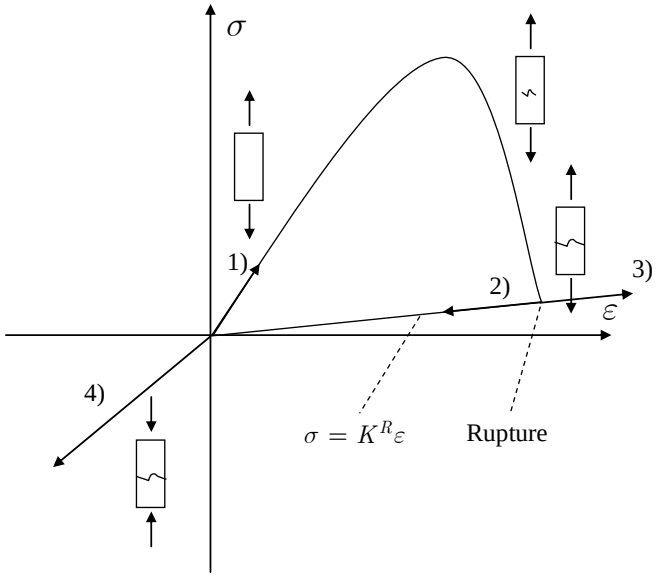

Figure 3.23. Illustration of uniaxial tension-compression cycle under displacement-controlled loading. K^R is the residual stiffness.

3.9 Conclusions of the literature review – remarks on the Murakami-Kamiya model

Axial splitting under compression and tensile cracking under tension are the failure modes studied in this work. One of the mechanisms behind the axial splitting failure mode is known as the wing crack mechanism.

Continuum damage models have been successfully applied in the analysis of brittle failure of materials. In these models, damage initiation is based on the use of the damage surface (cf. yield surface in the theory of plasticity). In order to model axial splitting, the surface is formulated based either on the strains or on the thermodynamic conjugate force corresponding to the damage tensor.

Due to damaging, the stiffness of the material is degraded. In continuum damage models the degradation is described by the strain softening approach. The strain softening applications are subject to mesh sensitivity and localisation problems. Rate-dependent solution methods can be applied to avoid mesh sensitivity problems, therefore the Perzyna and the consistency models have been introduced in Section 3.7. The consistency model was further formulated and an equation for the material Jacobian was introduced.

The approaches where the physical meaning of the damage tensor is indeterminate are called phenomenological approaches in this study (see 3.6.2.4). In the phenomenological approaches the upper limit of the damage tensor D_{ij} is often undefined. To ensure the positive definiteness of the strain energy density, the upper limit of damage must be well defined.

Many natural materials like ice, many rocks and ceramics are transversely isotropic. A strain energy equation for modelling the elastic behaviour of transversely isotropic materials was discussed in Section 3.4.

The unsymmetrical behaviour of cracked materials under tension and compression due to the opening and closure of cracks is called *unilateral behaviour*. Many continuum damage models for analysis of brittle damage take into account the unilateral behaviour. Either stress or strain-based methods are generally used.

Various continuum damage models capable of analysing axial splitting have been presented in the literature, but few of them have been verified by implementing them in FE software. The MK model was chosen as a starting point of this work due to its promising features and the encouraging results obtained by Skrzypek and Kuna-Ciskal (2003). They have implemented the MK model in ABAQUS/Standard FE software as a plane stress version.

Remarks on the Murakami-Kamiya model

The constitutive equations of the MK model are based on the theory of continuum thermodynamics. The damage evolution equations are derived similarly to the theory of plasticity. Because of the thermodynamic approach, the equations are well formed and theoretically consistent. As discussed in Section 1.1, one of the objectives was to implement a 3D version of the MK model in ABAQUS/Standard FE software. The following conclusions can be made concerning the applicability of the MK model:

1. The model is formulated in such way that it can be implemented in FE software.
2. The method for carrying out the derivative of the modified strain ε_{ij}^{*} must be introduced before successful 3D FE implementation.
3. A more general damage surface should be introduced to extend the model applicability to various materials.
4. A method to ensure positive definiteness of the secant stiffness during damage evolution must be introduced.
5. The derivative of the modified strain ε_{ij}^{*} is needed in the incremental formulation of FE applications. Skrzypek and Kuna-Ciskal (2003) proposed a simplified method which can be used in plane stress problems (2D). A new formulation is required for 3D applications.
6. The dissipation potential (damage/failure surface) given by Murakami and Kamiya (1997) is given as a function of the thermodynamic conjugate force Y_{ij}. The material constants were determined for concrete material in such way that the response in a uniaxial compression test can be simulated. The initial damage surface in the strain space is shown in Fig. 3.24. The original

damage surface of the MK model must be modified before the model can be used for various materials.

7. As described in Section 1.1, one of the objectives was to study whether the MK model could be modified for the analysis of transversely isotropic materials. Due to the shortcomings described above, it was decided that the MK model would not be modified for this purpose.

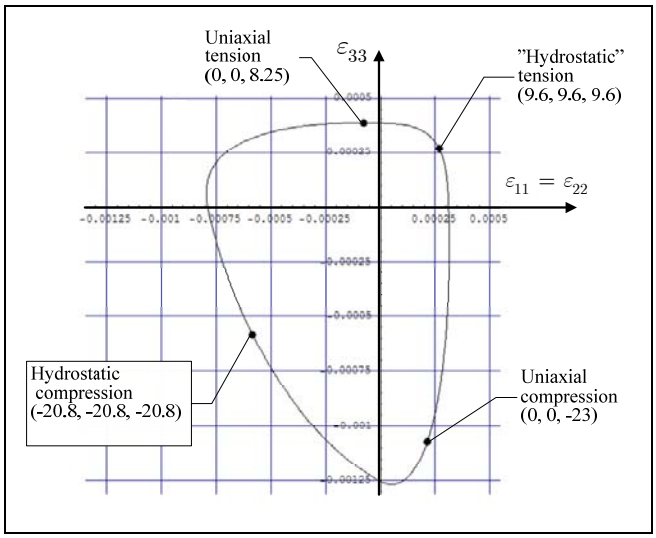

Figure 3.24. Damage surface of Murakami and Kamiya (1997) in principal strain space, when $\varepsilon_{11} = \varepsilon_{22}$*. The numbers in parentheses refer to the corresponding stress state in MPa.*

The MK model takes into account damage-induced anisotropy using the second order damage tensor D_{ij}. In the MK model the damage tensor is considered an internal state variable. As described in Section 3.6.2.4, the upper limit of the principal values of the damage tensor is not explicitly defined in these phenomenological approaches. If the upper limit is exceeded, the positive definiteness of the secant stiffness matrix is lost. Therefore, a method to determine the upper limit is needed.

In the MK model the crack opening closure criterion is based on the modified strain ε_{ij}^{*} although the criterion is not universally valid as described in Section 4.2. The opening criterion can be reliably applied only in uniaxial loading.

4. Formulation of the wing crack damage model

This work tested the hypothesis that the brittle failure phenomenon can be represented by a model, namely the *wing crack damage model* (WCD model), which has the following main features:

- Damage evolution simulates axial splitting under uniaxial compression as well as tensile cracking under tension
- The effect of orientation and size distribution of pre-existing cracks can be taken into account
- Initially transversely isotropic materials can be modelled as well, and

the model can be implemented in ABAQUS/Standard FE software.

4.1 Introduction to wing crack model formulation

Formulation of the wing crack damage model consists of the following Sections:

- Discussion of strain- and stress-based activation criteria, arriving at a conclusion on applying the stress-based criterion throughout the model formulation.
- Enhancement of phenomenological damage models such as the MK model.
- Detailed presentation of the principles of the new WCD model proposed in this work.
- Detailed presentation of the thermodynamic formulation of the proposed damage model.
- Directions for determination of material parameters.
- Condensed presentation of the main features of the proposed method and its applications.

4.2 Criticism of strain-based damage activation criteria

Due to the directionality of defects, damage is anisotropic in nature. In many brittle failure models, the stiffness normal to the crack surface direction is assumed to recover when the crack is fully closed (unilateral effect), while the stiffness is assumed to be considerably less than the undamaged material when the crack is open.

Damage is “activated” when the crack is open and “deactivated” (or passive) when the crack is closed. In this study, the expression “active/passive crack” is used as a synonym for “active/passive damage”.

The crack opening-closure criterion is called the unilateral condition. The condition defines whether the damage is active or passive. The closure criteria are based on either the stress or strain state. Different versions of strain-based criteria are used in damage mechanics, although the criteria considered here do not hold true in all loading conditions.

Chaboche (1993) has proposed both strain-based and stress-based methods for activation/deactivation criteria. According to the criterion, “the damage can be considered as fully active if the normal strain $\varepsilon^N = n_k \varepsilon_{kl} n_l$ associated to that direction[1] is positive” (ibid). The strain ε^N is the strain in the direction of the normal vector n_i. Thus the strain-based damage deactivation criterion of Chaboche is written as

$$\begin{aligned} \varepsilon^N &< 0 \\ \varepsilon^N &= n_k \varepsilon_{kl} n_l \end{aligned} \tag{4.1}$$

where n_k is the unit normal parallel to the principal direction of the damage tensor D_{ij}. When Eq. (4.1) holds, damage is inactivated and stiffness is recovered in the direction of vector n_i. The criterion of Eq. (4.1) holds true under the uniaxial compression and tension shown in Figs. 4.1a and 4.1b, where the crack plane is perpendicular to the loading.

[1] Chaboche refers to the principal direction of the damage tensor.

The stress-based crack closure criterion can be written using normal traction σ^N. The closure criterion reads:

$$\sigma^N = n_k \sigma_{kl} n_l < 0 \tag{4.2}$$

For isotropic material the traction in Eq. (4.2) can be written as a function of strains:

$$\begin{aligned} \sigma^N &= n_k(\lambda \varepsilon_{mm} \delta_{kl} + 2\mu \varepsilon_{kl}) n_l \\ &= \lambda \varepsilon_{mm} + 2\mu \varepsilon^N \end{aligned} \tag{4.3}$$

The contradiction in the strain-based criterion is that the normal strain ε^N given in Eq. (4.1) does not include information about the stress state, unless the stress state is uniaxial. Positive normal strain ε^N may occur due to either the tensile stress or the Poisson effect. Therefore, normal strain may be positive although the normal stress is negative.

To illustrate the contradiction, let us consider the case shown in Fig. 4.1c. After closure of the crack (II in Fig. 4.1b), the confined compression stress σ_{11} is increased while σ_{22} is constant. Damage in the state II shown in Fig. 4.1b is inactivated (both ε^N and σ^N are negative) i.e. stiffness parallel to $\mathbf{i}_2$ is recovered. The vector $\mathbf{n} = (0,1,0)$ represents the unit normal vector of the crack plane. Assuming that the material is homogeneous and isotropic, the Lamé constants λ and μ determine the material behaviour. It can be shown that the strain ε_{22} is

$$\varepsilon_{22} = \frac{2(\lambda + \mu)\sigma_{22} - \sigma_{11}\lambda}{2(3\lambda + 2\mu)\mu} \tag{4.4}$$

where tensile stresses are positive. The strain ε_{22} is positive if

$$\sigma_{11} < \frac{2(\lambda + \mu)}{\lambda} \sigma_{22} \tag{4.5}$$

When the confined compressive stress σ_{11} is increased, the normal strain ε^N becomes positive (III in Fig. 4.1c). According to Eq. (4.1) the damage should be

activated when $\varepsilon^N > 0$ i.e. the stiffness parallel to $\mathbf{i}_2$ should be degraded. However, the compressive stress σ_{22} shown in Fig. 4.1c is closing the crack. Therefore the stiffness should remain unchanged and the damage deactivated. If the damage were activated, the stiffness into the direction of σ_{22} would be degraded. Therefore the activation of damage due to positive strain ε^N under increasing confining stress would lead to an erroneous result.

In the example shown in Fig. 4.1c, the stress-based criterion of Eq. (4.2) gives

$$\sigma^N = n_k \sigma_{kl} n_l = \sigma_{22} < 0 \tag{4.6}$$

Therefore the damage remains deactivated.

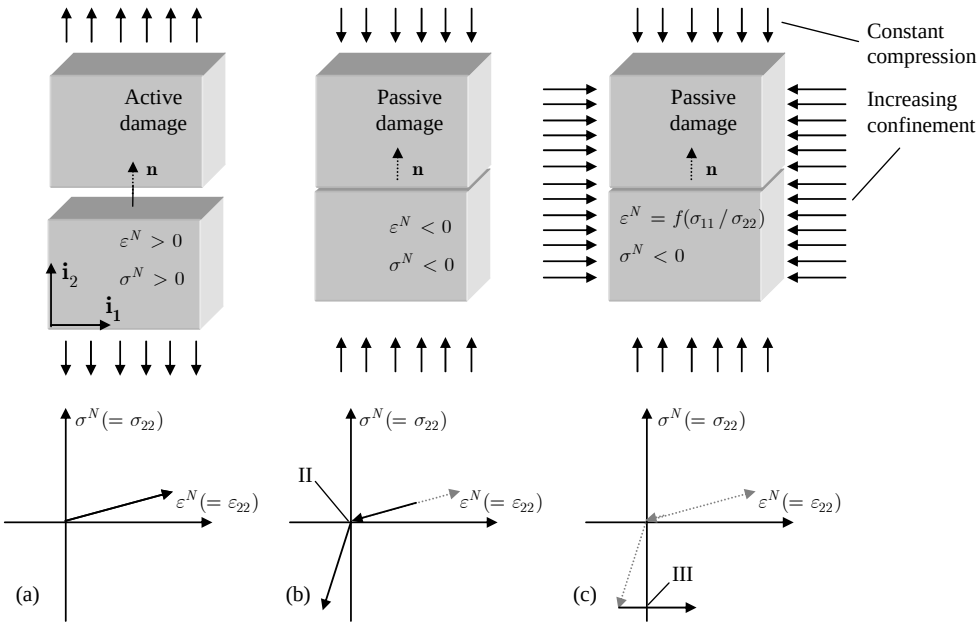

Figure 4.1. Sequential loading of a damaged sample.

The strain-based damage activation criterion given in Eq. (4.1) should be used only in uniaxial load cases, because it may lead to an erroneous result even in the simple biaxial load case illustrated in Fig. 4.1c. The stress-based criterion given in Eq. (4.2) should be used instead.

Another criterion for damage activation is based on the sign of principal strain (Murakami and Kamiya, 1997; Challamel et al., 2005). In the MK model described in Section 3.8, the "modified elastic strain tensor" was introduced to "represent the unilateral response of a damaged material" (Murakami and Kamiya, 1997). The idea in the method is that the damage is activated in the direction where the principal strain is positive. Nor does this criterion hold true in the confined compression test illustrated in Fig. 4.1c.

4.3 Enhancements for phenomenological damage models

Due to its undesirable features, the MK model was not developed further (see Section 3.9). The modifications proposed in Sections 4.3.2 and 4.3.3 are applicable both to the MK model and to most of the "phenomenological damage models" described in Section 3.6.2.4.

4.3.1 Introduction and objectives

Murakami and Kamiya (1997) introduced a continuum damage model based on the modified strain tensor ε_{ij}^{*}. The modified strain is the feature that makes the MK model attractive compared to other continuum damage models. The principal directions of the modified strain tensor determine the damage evolution "direction" and enable the axial splitting failure mode under uniaxial compression, as well as the tensile failure mode under uniaxial tension. In addition to the features described above, the crack opening/closure criterion is based on the modified strain tensor.

Despite these desirable features, the modified strain tensor ε_{ij}^{*} creates difficulties in the numerical implementation of the model. Firstly, the derivative of the modified strain tensor cannot be expressed explicitly; secondly, the opening/ closure criterion can be applied reliably only in the analysis of uniaxial loading.

The MK model is based on the use of a combination of invariants of the damage tensor D_{ij} and the elastic strain tensor ε_{ij}^{e}, as well as the modified strain tensor ε_{ij}^{*} (see Section 3.8.2.1). As described in Section 3.6.2.4, the rupture criterion

(upper limit of damage) in “phenomenological damage models” is undetermined and often neglected. The criterion is needed to ensure positive definiteness of the secant stiffness matrix.

The following subjects were studied:

- To ensure positive definiteness of the secant stiffness, a criterion for the upper limit of the damage tensor was introduced.
- Non-associated formulation with a strain-based failure surface was introduced to extend the applicability to various materials.
- A numerical derivative of the modified strain tensor ε^{*}_{ij} was introduced.

4.3.2 Rupture criterion

When damage is considered as isotropic, the effective stress σ^{eff}_{ij} is defined as described in Section 3.6.2.2:

$$\sigma^{eff}_{ij} = \frac{\sigma_{ij}}{1 - D} \tag{4.7}$$

where *D* must be in the range

$$0 \leq D < 1 \tag{4.8}$$

When damage tensor D_{ij} is used instead of a scalar damage variable, it is not obvious what the admissible state is for D_{ij}. Murakami and Kamiya (1997) imply that the “magnitude” of the damage variable might be limited to unity: “... [the] final fracture usually occurs before the magnitude of the damage variable $\|\mathbf{D}\|$ attains to the unity”. They do not determine how the magnitude is obtained for the second order tensor. In their numerical analyses, they have observed that a practical value for the rupture criterion of a damaged material could be the following:

$$D_{kk} \approx 0.4, \qquad (\text{no summ.}) \tag{4.9}$$

The numerical value of the rupture criterion defined in Eq. (4.9) depends on the material parameters η_1, η_2, η_3 and η_4. Kuna-Ciskal and Skrzypek (2004) have formulated a general criterion for rupture: "Loss of the positive definiteness of the tangent stiffness matrix is used as a failure criterion".

In the numerical application, Kuna-Ciskal and Skrzypek (2004) have degraded the stiffness of the failed element to zero when the failure criterion is fulfilled. They have also released the failed element from stress. Unfortunately there are drawbacks in the criterion itself and in the actions carried out for the failed element:

1. The actions (stiffness degradation to zero and release of integration point stress) might yield to ill-conditioning in the numerical model and to severe convergence problems.
2. By degrading the stiffness to zero the original idea of anisotropic unilateral damage in the MK model is lost.

The elastic strain energy density function W must be positive definite (Malvern, 1969, p. 292). The requirement is fulfilled when the secant stiffness matrix $[\mathbf{K}]$ is positive definite, i.e. all eigenvalues are positive. Therefore it is evident that the loss of the positive definiteness of the secant stiffness matrix can be used as a rupture criterion as proposed by Van (Van, 2001; Van and Vasarhelyi, 2001) in a more general context. The restrictions for material constants can be derived from the positive definiteness requirement as follows:

$$\det[\mathbf{K}] > 0 \tag{4.10}$$

A procedure to determine the allowable damage increment $\{\Delta\tilde{\mathbf{D}}\}$ is given here. In FE application damage at time $t + \Delta t$ is obtained as follows:

$$\{\mathbf{D}^{t+\Delta t}\} = \{\mathbf{D}^{t}\} + \{\Delta\mathbf{D}\} \tag{4.11}$$

where $\{\mathbf{D}^{t}\}$ is the damage vector before update and $\{\Delta\mathbf{D}\}$ is the damage increment obtained from the evolution equation $(3.25)_1$.

The admissible damage increment could be solved easily if the secant stiffness tensor were independent of strain, but it is not. An approximate solution to the problem can be found if the tensor B_{ijkl} in Eq. (3.85) is replaced by $\delta_{ik}\delta_{jl}$, which means that the unilateral feature of the model is neglected. When B_{ijkl} is replaced by $\delta_{ik}\delta_{jl}$ the secant stiffness matrix $[\mathbf{K}(\mathbf{D})]$ of Eq. (3.86) becomes a linear function of the damage tensor as follows:

$$[\mathbf{K}(\beta\mathbf{D})] = \beta[\mathbf{K}(\mathbf{D})] \tag{4.12}$$

where β is a scalar variable. In view of Eqs. (4.11) and (4.12), the secant stiffness at time $t + \Delta t$ can be written as

$$[\mathbf{K}(\mathbf{D}^{t+\Delta t})] = [\mathbf{K}(\mathbf{D}^{t})] + \beta[\Delta\mathbf{K}(\Delta\mathbf{D})] \tag{4.13}$$

where $[\mathbf{K}(\mathbf{D}^{t})]$ is the secant stiffness matrix before damage vector update and $[\Delta\mathbf{K}(\Delta\mathbf{D})]$ is the damage-induced part of the secant stiffness matrix which is a function of the damage increment $\{\Delta\mathbf{D}\}$ and β is a scalar multiplier.

Using Eqs. (4.10) and (4.13) the following rupture criterion is obtained:

$$\det\big([\mathbf{K}(\mathbf{D}^{t})] + \beta[\Delta\mathbf{K}(\Delta\mathbf{D})]\big) = 0 \tag{4.14}$$

Eq. (4.14) is similar to the solution of the generalised eigenproblem:

$$[\mathbf{K}(\mathbf{D}^{t})]\{\boldsymbol{\varphi}\}_k = -\beta_k[\Delta\mathbf{K}(\Delta\mathbf{D})]\{\boldsymbol{\varphi}\}_k, \quad \text{no summ.} \tag{4.15}$$

where $-\beta_k$ is the eigenvalue corresponding to the k:th eigenvector $\{\boldsymbol{\varphi}\}_k$. If β_1 ($\beta_k < \beta_{k+1}$) is less than 1.0, the damage increment $\Delta\mathbf{D}$ is inadmissible. The admissible increment is then

$$\{\Delta\tilde{\mathbf{D}}\} = \beta_1\,\{\Delta\mathbf{D}\} \tag{4.16}$$

In the specific case when only $D_{11} \neq 0$ and when the material parameters are the same as given by Murakami and Kamiya (1997), the critical value of 0.436 is obtained for D_{11} from Eq. (4.14). The obtained value is close to that of 0.4 proposed by Murakami and Kamiya.

A material is considered fully damaged when $\beta_1 \approx 0$, which means that damage evolution is not admissible: $\{\Delta\tilde{\mathbf{D}}\} = \{\mathbf{0}\}$. When the material is fully damaged the damage tensor remains constant and the last term in the material Jacobian in Eq. (3.97) becomes

$$\frac{\partial \sigma_{ij}}{\partial D_{kl}} dD_{kl} = 0 \tag{4.17}$$

Thus the material Jacobian equals the constitutive matrix of Eq. (3.85) when the material is fully damaged.

4.3.3 Damage surface

In damage mechanics models the damage surface is usually given as a function of thermodynamic conjugate forces, i.e. as a function of σ_{ij} or Y_{ij}. In the MK model the surface is based on the conjugate force Y_{ij}. Damage surfaces based on the force Y_{ij} are widely used and very often the surface is formulated in the following way (Zhu and Cescotto, 1995; Murakami and Kamiya, 1997; Halm and Dragon, 1998; Luo et al., 2003; Alliche, 2004; Challamel et al., 2005):

$$F = \sqrt{Y_{ij} L_{ijkl} Y_{kl}} - B(\kappa) = 0 \tag{4.18}$$

where the coefficient tensor L_{ijkl} is often taken as a symmetric unit tensor and $B(\kappa)$ defines the size of the damage surface.

The use of the conjugate force Y_{ij} is complex in the formation of a more general damage surface. Thus a non-associative formulation was proposed in this work. The damage surface is given as a function of the elastic strain ε^e_{ij} and damage rate $\dot{D}_{ij}$:

$$\begin{aligned} F &= F_0(\varepsilon^e_{ij}) - f(\dot{D}^{ekv}) - B(\kappa) = 0 \\ \dot{D}^{ekv} &= \sqrt{\dot{D}_{kl}\dot{D}_{kl}} \end{aligned} \tag{4.19}$$

The rate dependency was not implemented into the MK model. Damage tensor evolution is obtained using a potential function G that is similar to the MK model:

$$\dot{D}_{ij} = \dot{\lambda}\frac{\partial G}{\partial Y_{ij}}$$
$$G = \sqrt{Y_{ij}L_{ijkl}Y_{kl}} - B(\kappa) = 0 \tag{4.20}$$

The strain-based damage surface is commonly applied in damage mechanics (e.g. Fonseka and Krajcinovic, 1981; Simo and Ju, 1987). The proposed approach is non-associated because the damage surface *F* and the potential function *G* do not coincide. Therefore special attention must be paid to the dissipation inequality condition, which is not necessarily fulfilled as described in Section 3.6.1.

4.3.4 Derivative of modified elastic strain of the MK model

As described earlier, Skrzypek and Kuna-Ciskal (2003) and Kuna-Ciskal and Skrzypek (2004) have implemented a plane-stress version of the MK model in ABAQUS FE software. In their numerical examples they successfully analysed macrocrack propagation under tensile and compressive stress in the plane stress condition. To overcome the cumbersome derivatives in Eqs. (3.100) and (3.101), they introduced simplified equations for describing the modified elastic strain dependence of the elastic strain: $\varepsilon^{*}_{ij} = f(\varepsilon^{e}_{ij})$. The simplified equations are applicable only in the state of plane stress.

The modified strain ε^{*}_{ij} is obtained as follows (see Eq. (3.77)):

1. Define the principal strains $\hat{\varepsilon}^{e}_{(k)}$
2. Multiply those principal strains that have a negative sign by factor ζ to obtain modified strains $\hat{\varepsilon}^{*}_{(k)}$ in the principal coordinate system defined by elastic strain tensor
3. Rotate the modified principal strains back to the spatial coordinate system to obtain the modified strain ε^{*}_{ij}.

In the incremental formulation the following derivatives related to the modified strain are needed (see Eq. (3.101)):

$$\frac{\partial \varepsilon^{*}_{jm}}{\partial \varepsilon^{e}_{op}} \text{ and } \frac{\partial B_{ijkl}}{\partial \varepsilon^{e}_{op}} \tag{4.21}$$

The derivatives cannot be explicitly formulated; therefore the derivatives are obtained numerically starting from the definition of the derivative:

$$\frac{\partial f}{\partial x} = \lim_{\Delta x \to 0} \frac{f(x + \Delta x) - f(x)}{\Delta x} \tag{4.22}$$

Using the definition we can write the approximation for the derivatives at the beginning of the current time increment ($t + \Delta t$):

$$\begin{aligned} \frac{\partial \varepsilon^*_{jm}}{\partial \varepsilon^e_{op}} &\approx \frac{\varepsilon^*_{jm}(\varepsilon^{e,t}_{op} + \Delta\varepsilon^e) - \varepsilon^*_{jm}(\varepsilon^{e,t}_{op})}{\Delta\varepsilon^e} \\ \frac{\partial B_{ijkl}}{\partial \varepsilon^e_{op}} &\approx \frac{B_{ijkl}(\varepsilon^{e,t}_{op} + \Delta\varepsilon^e) - B_{ijkl}(\varepsilon^{e,t}_{op})}{\Delta\varepsilon^e} \end{aligned} \tag{4.23}$$

where $\varepsilon^{e,t}_{op}$ is the elastic strain at the beginning of the increment and $\Delta\varepsilon^e$ is the strain increment. Eq. (4.23) gives a numerical approximation of the derivative at the beginning of the increment, although the derivative at the end of the increment was needed.

The proposed method was implemented in ABAQUS/Standard software as a user material subroutine. The strain increment size $\Delta\varepsilon^e$ needed in the derivative evaluation is based on experience with numerical application of the MK method:

$$\Delta\varepsilon^e = \max(\Delta\varepsilon^e_{kl})/10 \tag{4.24}$$

4.4 Wing crack damage model for transversely isotropic solids

In this study a new continuum damage model for analysis of brittle transversely isotropic solids was proposed. Damaging was assumed to induce anisotropy. Although the approach is phenomenological, the model was motivated by the growth mechanism of wing cracks. Special attention was paid to the axial splitting failure mode under uniaxial compression and transverse tensile cracking under uniaxial tension.

4.4.1 Objectives and scope

Several damage models for brittle failure and anisotropic damaging have been proposed (e.g. Betten, 1986; Murakami, 1990; Chaboche, 1993; Murakami and Kamiya, 1997; Halm et al., 2002), but few of them have been implemented in FE software. Often the numerical examples given are simple and based on the numerical application of the constitutive equation in a uniaxial case. However, applicability of methods is best revealed using examples where the sample is under multiaxial stress and is modelled with several elements.

In anisotropic continuum damage models, often the second or fourth order tensor represents the damage, and the damage evolution is determined by the derivative of the damage potential surface. It is not known how to formulate the evolution equation for second and fourth order tensors such that the evolution of brittle failure modes is captured.

In brittle damage models, the direction of damage evolution is often based on the sign of principal stresses or strains (Simo and Ju, 1987; Chaboche, 1993; Murakami and Kamiya, 1997; Halm and Dragon, 1998). The principal values and directions may also be needed in the formulation of the Helmholtz free energy equation (Murakami and Kamiya, 1997; Halm and Dragon, 1998). An approach based on directions of principal tensile strain may introduce a projection tensor into the constitutive equations (see B_{ijkl} in Section 3.8.2.1). The use of the projection tensor may lead to cumbersome derivatives in incremental formulation of the stress-strain relation as stated in Section 3.9 and by Skrzypek and Kuna-Ciskal (2003).

In the model of Murakami and Kamiya (1997), principal directions and values of the strain tensor are used in the derivation of the "modified strain tensor" ε_{ij}^{*}. The tensor was introduced to take into account the unilateral condition of damage due to the opening and closure of microcracks. As shown in Section 4.2, the method based on the modified strain tensor approach cannot give correct information about the opening and closure of a crack in biaxial loading conditions. Therefore a new approach was introduced.

Due to the requirement for positive definite strain energy density discussed in Section 4.3.2, the constitutive stiffness matrix must be a positive definite in all

strain and damage states. Therefore a condition for the upper limit of the damage tensor should be well defined to ensure the positive definiteness. In the phenomenological approaches described in Section 3.6.2.4, the condition for positive definiteness is difficult to formulate explicitly and usually the condition is disregarded in these models.

It is well known that the mechanical strength and response of the solid are dependent on the orientation, distribution, size and type of the defects in its structure (Ashby and Hallam, 1986; Krajcinovic, 1989).

At this point, besides the items described above this work focused on the derivation of a new damage model having the following features (as described in Section 1.1):

1. Damage evolution simulates wing crack growth.
2. Damaging introduces anisotropy.
3. Distribution, size and orientation of pre-existing defects can be modelled.
4. The model can be applied in uniaxial splitting and tensile failure mode analysis (see Fig 3.2 c, e).
5. Initially transversely isotropic materials can be analysed.
6. The upper limit of the damage variable is well defined.
7. Damage activation/deactivation corresponding to open and closed microcracks is taken into account.
8. Constitutive equations are derived independently of the direction of principal strain.

The approach described in the following Sections (4.4.2–4.4.6) was based on the assumption of pre-existing cracks. As stated in Section 1.2, the flaw distribution studies were outside the scope of this study.

4.4.2 Presumptions

In the model formulation, special attention was paid to the axial splitting failure mode. The proposed “wing crack model” is based on the following presumptions:

1. Axial splitting occurs when a series of wing cracks link together to form an axial splitting crack (see Fig. 4.2).
2. A wing crack and a series of wing cracks can be approximated by a single plane crack.
3. Damage vector D_k represents the orientation and relative size of the plane crack (see Fig. 4.3).
4. Material rupture is taking place when the damage vector length equals 1 ($\sqrt{D_k D_k} = 1$).

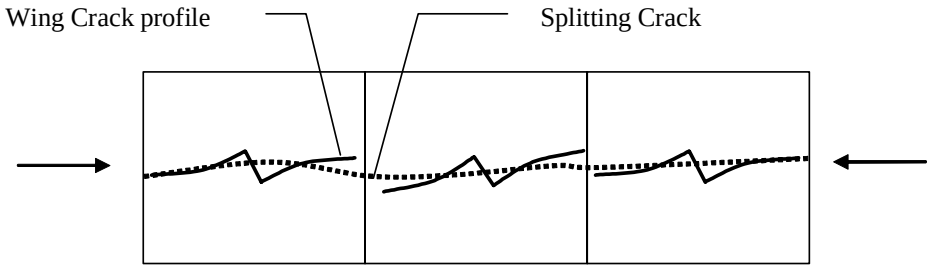

Figure 4.2. Schematic drawing of the proposed failure model (dashed line).

A number of damage vector-based models have been proposed (Davison and Stevens, 1973; Krajcinovic and Fonseka, 1981; Mikkola and Piila, 1984; Van, 2001), although the use of a second order damage tensor is more general. The damage vector D_k can be interpreted to represent an averaged normal direction of a series of microcracks (Van, 2001).

As shown by Leckie and Onat (1981), a damage vector is not appropriate for the representation of the distribution of voids (or cracks), while the use of a second order damage tensor enables representation of the crack distribution in the three orthogonal directions. In this study it is assumed that the element considered is small enough to contain very few plane cracks, and that the average orientation of the plane cracks is well defined by the damage vector.

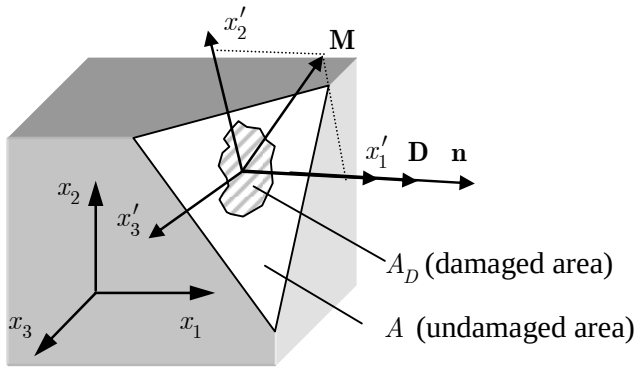

Figure 4.3. Global and local coordinate systems. The Local coordinate system is defined by the vectors **D** *and* **M**. *Vector* **M** *defines the material symmetry axis for a transversely isotropic material, while* **D** *is the damage vector.*

In the proposed model, the damage vector D_i represents both damage orientation and the relative size of the damage. The vector orientation is normal to the crack plane as shown in Fig. 4.3. The damaged area A_D and the damage vector are defined as follows:

$$\begin{aligned} A_D n_i &= A\, D_i \\ D_i &= \frac{A_D}{A}\, n_i \end{aligned} \tag{4.25}$$

where A is the undamaged area and n_i is the unit normal vector of the crack plane.

A single vector represents satisfactorily one plane crack or a series of parallel plane cracks. A kinked crack can be replaced by a representative straight crack as done by e.g. Basista and Gross (1989). When the straight crack is used to represent a wing crack, the result can only be a rough estimate of the real wing crack. In the proposed model it is assumed that the crack is formed of parallel plane surfaces and that the ratio of crack surface area projections shown in Fig. 4.4 is small:

$$\frac{A_2^p}{A_1^p} \ll 1 \tag{4.26}$$

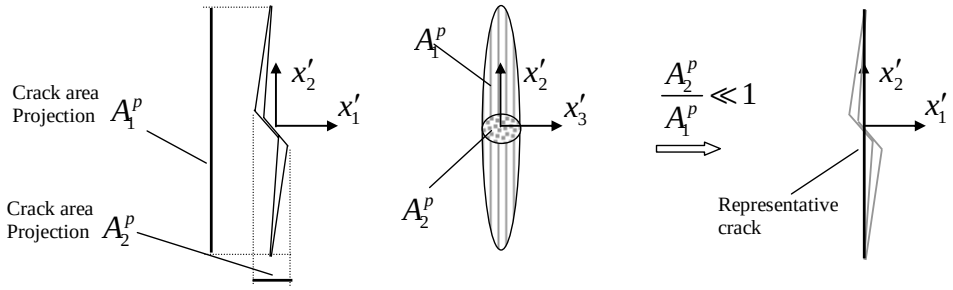

Figure 4.4. Actual wing crack and representative crack.

4.4.3 Basic concepts in the WCD approach

The basic idea in the WCD approach is to describe the behaviour of a cracked material with constitutive relation. The equations describing the relation are based on the known anisotropic material models.

To illustrate the WCD concept, the behaviour of initially isotropic, cracked material was considered in the damage coordinate system shown in Fig. 4.3. Consider a case when specimen rupture has taken place i.e. $\sqrt{D_k D_k} = 1$ as described earlier. The crack is idealised as a plane surface. The vector $\mathbf{n}$ in Fig. 4.5b is the unit normal of the crack surface.

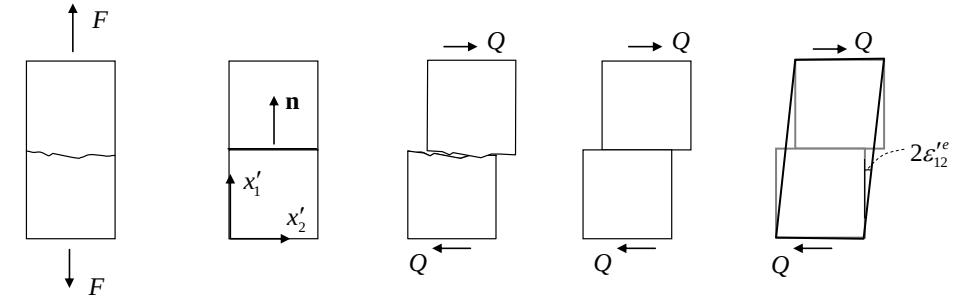

a) Tensile crack b) Idealised crack c) Sliding d) Idealised sliding e) Model

Figure 4.5. Behaviour of idealised crack model.

Shear behaviour

Assume there is no friction. The crack surfaces are then free of shear stresses ($\sigma'_{12} = \sigma'_{13} = 0$) during sliding of the surfaces as illustrated in Figs 4.5d and 4.6. In this study the stiffness corresponding to the nonzero stresses ($\sigma'_{22}, \sigma'_{23}, \sigma'_{33}$) was assumed to remain unchanged.

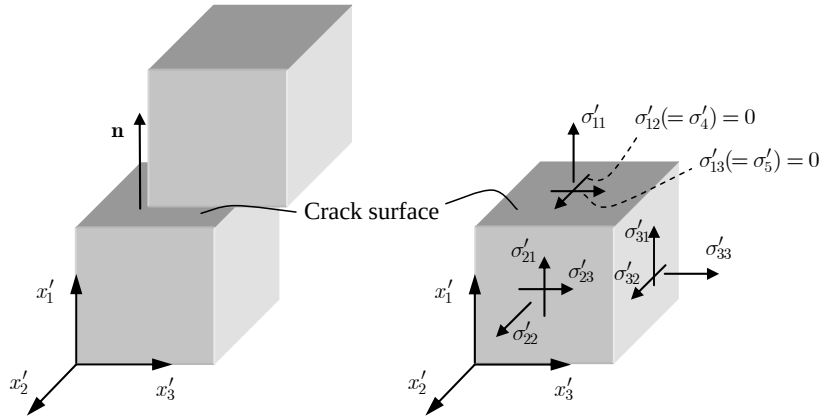

Figure 4.6. Sliding of the crack surfaces and stresses on the crack surface expressed in the damage coordinate system (see Fig. 4.3).

In the model, shear strains ε'^e_{12} and ε'^e_{13} represent sliding (see Fig 4.5e). When sliding is frictionless the shear strains ($\varepsilon'^e_{12}, \varepsilon'^e_{13}$) must not induce stresses. Therefore the constitutive relation of ruptured material must be such that the nonzero stresses are independent of the shear strains ($\varepsilon'^e_{12}, \varepsilon'^e_{13}$). In isotropic material model the condition is fulfilled when the shear modulus μ_R corresponding to the shear stresses σ'_{12} and σ'_{13} equals zero ($\mu_R = 0$).

Active crack

The crack surface of an open crack was assumed to be free of normal stress; $\sigma'_{11} = 0$, therefore the nonzero stresses are: $\sigma'_{22}, \sigma'_{23}$ and σ'_{33}. The stress state corresponds to the plane state of stress. In the model the stiffness corresponding to the stress σ'_{11} was assumed to be zero. The strain ε'^e_{11} represents opening of the crack. Therefore the following conditions must be fulfilled:

1. Normal and shear stresses ($\sigma'_{11}, \sigma'_{12}, \sigma'_{13}$) vanish on the crack surface.

2. Normal and shear strains ($\varepsilon'^{e}_{11}, \varepsilon'^{e}_{12}, \varepsilon'^{e}_{13}$) do not affect the stress state.
3. The stresses in plane $x'_2 - x'_3$ ($\sigma'_{22}, \sigma'_{23}, \sigma'_{33}$, see Fig. 4.6) are determined as in the plane stress state.
4. The stiffness in the direction of the nonzero stresses ($\sigma'_{22}, \sigma'_{23}, \sigma'_{33}$) remains unchanged.

Passive crack

When a crack is closed due to compressive stress the stiffness corresponding to the stress σ'_{11} was assumed to be the same as for virgin material. The following conditions must be fulfilled for a passive crack:

1. Shear stresses ($\sigma'_{12}, \sigma'_{13}$) vanish on the crack surface.
2. Shear strains ($\varepsilon'^{e}_{12}, \varepsilon'^{e}_{13}$) do not affect the stress state.
3. The stiffness in the direction of the nonzero stresses ($\sigma'_{11}, \sigma'_{22}, \sigma'_{23}, \sigma'_{33}$) remains unchanged.

As stated above, normal and shear stresses vanish on the crack surface when the crack is open. The condition of vanishing shear and axial stress has also been applied e.g. by Valanis (1990). The condition can be expressed using the shear traction $\sigma^{\|}$ and the normal tractions σ^{N} (shown in Fig 4.7) related to the damage orientation. The tractions are obtained as follows (Kachanov, 1982):

$$\begin{aligned} \sigma^{N} &= n_k \sigma_{kl} n_l = 0 \\ \sigma^{\|}_{k} &= \sigma_{kl} n_l \text{ - } \sigma^{N} n_k = 0 \end{aligned} \tag{4.27}$$

where n_{k} is the unit vector component in the direction of the damage vector defined as follows:

$$n_k = \frac{D_k}{\sqrt{D_m D_m}} \tag{4.28}$$

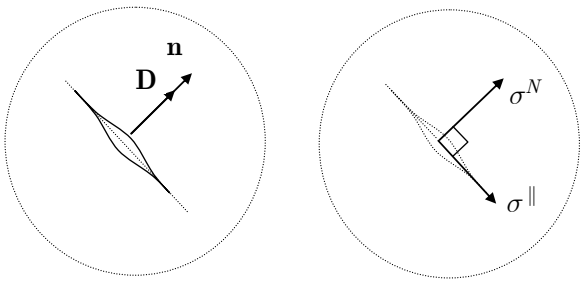

Figure 4.7. Crack orientation given by the damage vector (a). Normal and shear tractions (b).

The WCD model

The features described above were attained by applying the constitutive relation of transversely isotropic material described in Section 3.4. Vector $\mathbf{n}$ represents material symmetry axis. Based on Eq. (3.12) the following expression for the strain energy density was introduced:

$$W_D = \frac{1}{2}\lambda\varepsilon^e_{kk}\varepsilon^e_{ll} + \mu\varepsilon^e_{kl}\varepsilon^e_{kl} + \sqrt{D_m D_m}\left[\lambda_D\varepsilon^e_{kk}\varepsilon^e_{ll} + \mu_D n_k n_i \varepsilon^e_{ij}\varepsilon^e_{jk} + \alpha_D n_k n_l \varepsilon^e_{kl}\varepsilon^e_{ii} + \beta_D(n_k n_l \varepsilon^e_{kl})^2\right] \tag{4.29}$$

$$n_i = \frac{D_i}{\sqrt{D_k D_k}}$$

where the four unknown parameters ($\lambda_D, \mu_D, \alpha_D, \beta_D$) can be solved for active and passive crack using the conditions described in this section. Lamé constants (λ, μ) describe the behaviour of isotropic material.

The stress tensor is obtained from the following equation:

$$\sigma'_{ij} = \frac{\partial W_D}{\partial \varepsilon'^e_{ij}} \tag{4.30}$$

where ε'^e_{ij} is the strain tensor in the damage coordinate system.

The parameters for an active crack, when rupture has taken place ($\sqrt{D_k D_k} = 1$), can be solved from Eqs. (4.29) and (4.30). When the conditions described earlier in this section are fulfilled, the following parameters are obtained:

$$\begin{aligned} \alpha_D &= -\frac{2\lambda\mu}{\lambda+2\mu} \qquad & \beta_D &= \frac{2\mu(\lambda+\mu)}{\lambda+2\mu} \\ \lambda_D &= -\frac{\lambda^2}{\lambda+2\mu} \qquad & \mu_D &= -2\mu \end{aligned} \tag{4.31}$$

For a passive crack ($\sigma'_{11} \neq 0$) the parameters are respectively:

$$\begin{aligned} \alpha_D &= 0 \qquad & \beta_D &= 2\mu \\ \lambda_D &= 0 \qquad & \mu_D &= -2\mu \end{aligned} \tag{4.32}$$

Stiffness matrices for both active and passive cracks are shown in Figs. 4.8a and 4.8b.

a) Passive crack

$$[\mathbf{K}'] = \begin{bmatrix} \lambda+2\mu & \lambda & \lambda & 0 & 0 & 0 \\ & \lambda+2\mu & \lambda & 0 & 0 & 0 \\ & & \lambda+2\mu & 0 & 0 & 0 \\ & & & 0 & 0 & 0 \\ & \textit{symm.} & & & 0 & 0 \\ & & & & & \mu \end{bmatrix} \Longrightarrow$$

c) Transversal damage; $0 < \xi \leq 1$

$$[\mathbf{K}'] = \xi \begin{bmatrix} \lambda+2\mu & \lambda & \lambda & 0 & 0 & 0 \\ & \lambda+2\mu & \lambda & 0 & 0 & 0 \\ & & \lambda+2\mu & 0 & 0 & 0 \\ & & & 0 & 0 & 0 \\ & \textit{symm.} & & & 0 & 0 \\ & & & & & \mu \end{bmatrix}$$

b) Active crack

$$[\mathbf{K}'] = \begin{bmatrix} 0 & 0 & 0 & 0 & 0 & 0 \\ & \frac{4\mu(\lambda+\mu)}{\lambda+2\mu} & \frac{2\lambda\mu}{\lambda+2\mu} & 0 & 0 & 0 \\ & & \frac{4\mu(\lambda+\mu)}{\lambda+2\mu} & 0 & 0 & 0 \\ & & & 0 & 0 & 0 \\ & \textit{symm.} & & & 0 & 0 \\ & & & & & \mu \end{bmatrix} \Longrightarrow$$

$$[\mathbf{K}'] = \xi \begin{bmatrix} 0 & 0 & 0 & 0 & 0 & 0 \\ & \frac{4\mu(\lambda+\mu)}{\lambda+2\mu} & \frac{2\lambda\mu}{\lambda+2\mu} & 0 & 0 & 0 \\ & & \frac{4\mu(\lambda+\mu)}{\lambda+2\mu} & 0 & 0 & 0 \\ & & & 0 & 0 & 0 \\ & \textit{symm.} & & & 0 & 0 \\ & & & & & \mu \end{bmatrix}$$

Figure 4.8. Stiffness matrix of ruptured material in the damage coordinate system ($\mathbf{n} \parallel \mathbf{i}_1$). Parameter ξ describes the effect of transversal damage.

Transversal damaging

The idea in the proposed approach is that damaging degrades the shear stiffness in the crack plane and the "normal stiffness" when the crack is active. It means that the stiffness of the split specimen in the direction of the axial load shown in Fig. 4.9 is the same as the stiffness of the undamaged specimen. If in addition to splitting other failure mechanisms are present, the stiffness in the loading direction (i.e. transversal to the vector $\mathbf{n}$) is degraded as well. The "transversal damage factor" ξ, ($0 < \xi \leq 1$) illustrated in Figs. 4.8c and 4.9c was introduced to take into account the stiffness degradation in the transversal direction.

The transversal damage factor ξ has a similar effect on stiffness as the material parameter ζ in Eq. (3.77) of the MK model.

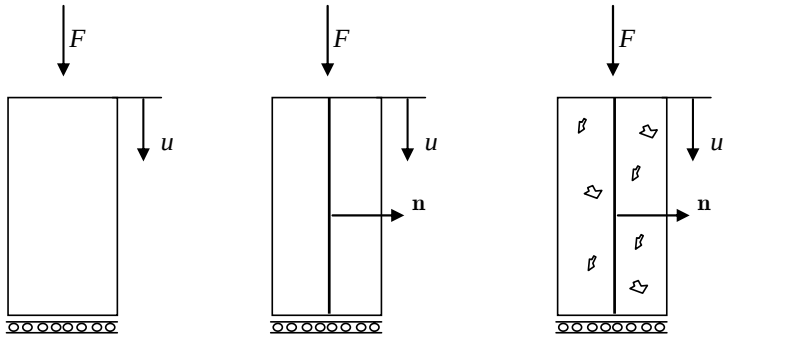

Figure 4.9. Axial stiffness of undamaged (a) and split (b) specimen is the same. Illustration of the transversal damage factor (c).

4.4.4 Anisotropic stiffness degradation of transversely isotropic materials

The conditions describing active and passive crack behaviour introduced in Section 4.4.3 are valid for transversely isotropic material as well. An additional feature was introduced to improve the numerical behaviour of the proposed model:

1. Instead of vanishing shear stresses on the crack surface, a residual shear stiffness was introduced to avoid numerical problems.
   - the residual shear stiffness for an active crack is $\mu_{R,T}$.
   - the residual shear stiffness for a passive crack is $\mu_{R,C}$.

4.4.4.1 Damage-induced anisotropy

The proposed method is based on the equations derived for materials having two 'preferred' directions. The damage vector $\mathbf{D}$ is considered as a new preferred direction besides the preferred direction $\mathbf{M}$ of the transversely isotropic material as illustrated in Fig. 4.10. Therefore the resulting material is anisotropic. The concept of the proposed method was described in Section 4.4.3.

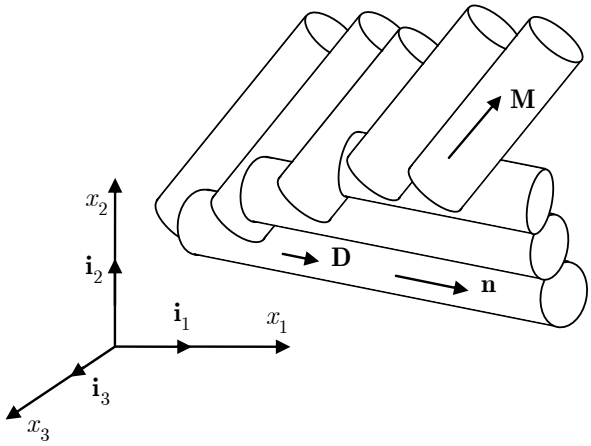

Figure 4.10. Material with two preferred directions. $\mathbf{M}$ *defines the direction of the undamaged transversely isotropic material. The unit vector* $\mathbf{n}$ *defines the second preferred direction (*$\mathbf{n} \parallel \mathbf{D}$*).*

The elastic strain energy W_D density for a material with two preferred directions is based on the equation given by Rogers (1990). He gives the stress-strain relation in the following form:

$$
\begin{aligned}
\sigma_{ij} &= 2\mu\varepsilon^e_{ij} + 2\mu_1(M_{ik}\varepsilon^e_{kj} + \varepsilon^e_{ik}M_{kj}) + 2\mu_2(B_{ik}\varepsilon^e_{kj} + \varepsilon^e_{ik}B_{kj}) \\
&\quad + 2\mu_2(A_{ik}\varepsilon^e_{kj} + \varepsilon^e_{ik}A_{kj}) \\
&\quad + (\lambda\varepsilon^e_{kk} + \alpha_1 M_{kl}\varepsilon^e_{lk} + \alpha_2 B_{kl}\varepsilon^e_{lk} + \alpha_3 A_{kl}\varepsilon^e_{lk})\delta_{ij} \\
&\quad + (\alpha_1\varepsilon^e_{kk} + \beta_1 M_{kl}\varepsilon^e_{lk} + \beta_3 B_{kl}\varepsilon^e_{lk} + \beta_4 A_{kl}\varepsilon^e_{lk})M_{ij} \\
&\quad + (\alpha_2\varepsilon^e_{kk} + \beta_3 M_{kl}\varepsilon^e_{lk} + \beta_2 B_{kl}\varepsilon^e_{lk} + \beta_5 A_{kl}\varepsilon^e_{lk})B_{ij} \\
&\quad + (\alpha_3\varepsilon^e_{kk} + \beta_4 M_{kl}\varepsilon^e_{lk} + \beta_5 B_{kl}\varepsilon^e_{lk})A_{ij}
\end{aligned}
\tag{4.33}
$$

where the 13 material parameters are: λ, μ, μ_1, μ_2, μ_3, α_1, α_2, α_3, β_1, β_2, β_3, β_4 and β_5. The tensors related to the material direction are defined by the components of the vectors M_k and D_k:

$$
\begin{aligned}
M_{ij} &= M_i M_j \\
A_{ij} &= \frac{n_k M_k}{2}(n_i M_j + n_j M_i) \\
B_{ij} &= n_i n_j \\
n_i &= D_i \,/\, \sqrt{D_k D_k}
\end{aligned}
\tag{4.34}
$$

Based on Eqs. (3.12) and (4.33) the following form of elastic strain energy density W_D was introduced:

$$
\begin{aligned}
W_D &= \frac{1}{2}\lambda\varepsilon^e_{kk}\varepsilon^e_{ll} + \mu_T\varepsilon^e_{kl}\varepsilon^e_{kl} + 2(\mu_L - \mu_T)M_{kl}\varepsilon^e_{lm}\varepsilon^e_{mk} + \beta(M_{kl}\varepsilon^e_{kl})^2 \\
&\quad + \alpha M_{kl}\varepsilon^e_{kl}\varepsilon^e_{mm} \\
&\quad + \sqrt{D_k D_k}\,[\,\lambda_D\varepsilon^e_{kk}\varepsilon^e_{ll} + \mu_{TD}\varepsilon^e_{kl}\varepsilon^e_{kl} + 2(\mu_{LD} - \mu_{TD})M_{kl}\varepsilon^e_{lm}\varepsilon^e_{mk} \\
&\quad + \beta_D(M_{kl}\varepsilon^e_{kl})^2 + \alpha_D M_{kl}\varepsilon^e_{kl}\varepsilon^e_{mm} + \beta_2(n_k n_l\varepsilon^e_{kl})^2 \\
&\quad + (\mu_2 n_k n_l + \mu_3 A_{kl})\varepsilon^e_{lm}\varepsilon^e_{mk} + (\,\alpha_2 n_k n_l + \alpha_3 A_{kl}\,)\,\varepsilon^e_{kl}\varepsilon^e_{mm} \\
&\quad + (\,\beta_3 M_{kl} n_m n_n + \beta_4 M_{kl} A_{mn} + \beta_5 A_{kl} n_m n_n\,)\,\varepsilon^e_{kl}\varepsilon^e_{mn}\,]
\end{aligned}
\tag{4.35}
$$

where the material parameters μ_T, μ_L, λ, α and β determine the elastic behaviour of a transversely isotropic material as described in Section 3.4. The remaining 13 parameters (λ_D, μ_{TD}, μ_{LD}, β_D, α_D, α_2, α_3, μ_2, μ_3, β_2, β_3, β_4, β_5) depend on the damage vector orientation and the sign of the normal traction σ^N. The parameters are determined such that the features described in Sections 4.4.3

and 4.4.4 are attained. The parameters have to be derived both for active ($\sigma^N \geq 0$) and passive ($\sigma^N < 0$) cracks.

As discussed earlier and shown in Eqs. (4.35) and (4.34), the damage vector orientation determines the second preferred direction of the material, while the damage vector length $\sqrt{D_k D_k}$ determines the "intensity" of the anisotropy. The elastic strain energy density of Eq. (4.35) reduces to the energy equation of the transversely isotropic material (Eq. (3.12)) when $\sqrt{D_k D_k} = 0$. The anisotropy of the material increases with increasing length of the damage vector.

When solving the 13 material parameters in Eq. (4.35), the strain energy is expressed in a local rectangular coordinate system, the orientation of which is defined by the damage vector D_k and the material symmetry vector M_k (see Fig. 4.3). In the local coordinate system the x_1'-axis is parallel to the damage vector. The x_2'-axis direction is chosen such that the material symmetry vector M_k is located in the plane $x_1' - x_2'$.

The strain energy of the fully damaged material in the local coordinate system is obtained by inserting $M_i = M_i'$ and $n_i = n_i'$ into Eq. (4.35), where:

$$
\begin{aligned}
& n_1' = 1 && n_2' = 0 && n_3' = 0 \\
& M_1' = M_N && M_2' = \sqrt{1 - (M_N)^2} && M_3' = 0 \\
& M_N = M_k n_k \\
& D_k D_k = 1
\end{aligned}
\tag{4.36}
$$

The use of Eq. (4.36) simplifies the strain energy equation.

The solution of the unknown material parameters is based on the use of a (undamaged) constitutive matrix and fully damaged material stiffness matrices. The constitutive tensor for undamaged transversely isotropic material C_{ijkl}' in the local coordinate system is obtained from Eq. (4.35) as follows:

$$
C_{ijkl}' = \frac{\partial^2 W_D}{\partial \varepsilon_{ij}'^e \partial \varepsilon_{kl}'^e}, \text{ where } \; D_k = 0 \;\; \forall \;\; k \tag{4.37}
$$

where $\varepsilon_{ij}^{\prime e}$ is the elastic strain tensor in the local coordinate system. The corresponding matrix form is:

$$[\mathbf{C}'] = \frac{\partial^2 W_D}{\{\partial \boldsymbol{\varepsilon}'^e\}\{\partial \boldsymbol{\varepsilon}'^e\}}, \text{ where } \{\mathbf{D}\} = \{\mathbf{0}\} \tag{4.38}$$

where $\{\boldsymbol{\varepsilon}'^e\}$ is the elastic strain vector in the local coordinate system. The secant stiffness tensor and matrix for fully damaged material obtained from Eq. (4.35) and (4.36) are

$$K'_{ijkl} = \frac{\partial^2 W_D}{\partial \varepsilon_{ij}^{\prime e} \partial \varepsilon_{kl}^{\prime e}}, \quad \text{where } D_k D_k = 1 \tag{4.39}$$

$$[\mathbf{K}'] = \frac{\partial^2 W_D}{\{\partial \boldsymbol{\varepsilon}'^e\}\{\partial \boldsymbol{\varepsilon}'^e\}}, \quad \text{where } \|\mathbf{D}\| = 1 \tag{4.40}$$

The secant stiffness and constitutive matrices in the damage coordinate system obtained from equations (4.37) and (4.39) are denoted by $[\mathbf{K}']$ and $[\mathbf{C}']$. The matrices are given in Appendix A. The shape of the constitutive matrix $[\mathbf{C}']$ is shown in Fig. 4.11a. Solution of the 13 unknown components in Eq. (4.35) is based on the components of matrices $[\mathbf{K}']$ and $[\mathbf{C}']$. The procedure is illustrated in Fig. 4.11.

$$\begin{bmatrix} C'_{11} & C'_{12} & C'_{13} & C'_{14} & 0 & 0 \\ & C'_{22} & C'_{23} & C'_{24} & 0 & 0 \\ & & C'_{33} & C'_{34} & 0 & 0 \\ & & & C'_{44} & 0 & 0 \\ & \textit{symm.} & & & C'_{55} & C'_{56} \\ & & & & & C'_{66} \end{bmatrix}$$

(a) Transversal isotropic constitutive matrix in damage coordinate system

$$\downarrow$$

$$\begin{bmatrix} 0 & 0 & 0 & 0 & 0 & 0 \\ & \xi C'^{p}_{11} & \xi C'^{p}_{12} & 0 & 0 & 0 \\ & & \xi C'^{p}_{22} & 0 & 0 & 0 \\ & & & 0 & 0 & 0 \\ & \textit{symm.} & & & 0 & 0 \\ & & & & & \xi C'^{p}_{33} \end{bmatrix}$$

(b) Plane stress part of fully damaged transversal isotropic stiffness matrix in damage coordinate system. C'^{p}_{ij} refers to the plane stress state. ξ is the transversal damage factor.

$$\downarrow$$

$$\begin{bmatrix} 0 & 0 & 0 & 0 & 0 & 0 \\ & \xi C'^{p}_{11} & \xi C'^{p}_{12} & 0 & 0 & 0 \\ & & \xi C'^{p}_{22} & 0 & 0 & 0 \\ & & & \mu_{R,T} & 0 & 0 \\ & \textit{symm.} & & & \mu_{R,T} & 0 \\ & & & & & \xi C'^{p}_{33} \end{bmatrix}$$

(c) Active crack. Stiffness matrix for fully damaged transversal isotropic material in damage coordinate system
$\mu_{R,T}$ is residual shear modulus for active crack

$$\begin{bmatrix} \xi C'^{c}_{11} & \xi C'^{c}_{12} & \xi C'^{c}_{13} & 0 & 0 & 0 \\ & \xi C'^{c}_{22} & \xi C'^{c}_{23} & 0 & 0 & 0 \\ & & \xi C'^{c}_{33} & 0 & 0 & 0 \\ & & & \mu_{R,C} & 0 & 0 \\ & \textit{symm.} & & & \mu_{R,C} & 0 \\ & & & & & \xi C'^{c}_{44} \end{bmatrix}$$

(d) Passive crack. Stiffness matrix for fully damaged transversal isotropic material in damage coordinate system
$\mu_{R,C}$ is residual shear modulus for passive crack. ξ is the transversal damage factor.

Figure 4.11. Derivation of stiffness matrix coefficients in the damage coordinate system $(x'_1,\ x'_2,\ x'_3)$ shown in Fig. 4.3.

4.4.4.2 Parameter derivation for an active crack

Consider the case in which material is fully damaged ($\|\mathbf{D}\| = 1$) and a crack is open. Therefore the stresses $\sigma'_{11}, \sigma'_{12}, \sigma'_{13}$ are assumed to vanish on the crack surface as described in Section 4.4.3. The corresponding stress-strain relation can be written in the local coordinate system as follows:

$$\begin{Bmatrix} 0 \\ \sigma'_2 \\ \sigma'_3 \\ 0 \\ 0 \\ \sigma'_6 \end{Bmatrix} = [\mathbf{C}']\{\boldsymbol{\varepsilon}'^e\} \tag{4.41}$$

where the notation described in Section 2.2 is used for the stress and strain components. $[\mathbf{C}']$ is the stiffness matrix for undamaged (virgin) material as described in Eq. (4.38) and $\{\boldsymbol{\varepsilon}'^e\}$ is the corresponding strain vector. Eq. (4.41) corresponds to the state of plane stress. Eliminating the strain components ε'^e_1, ε'^e_4 and ε'^e_5 Eq. (4.41) can be written as:

$$\begin{Bmatrix} \sigma'_2 \\ \sigma'_3 \\ \sigma'_6 \end{Bmatrix} = \left[\mathbf{C}'^p\right] \begin{Bmatrix} \varepsilon'^e_2 \\ \varepsilon'^e_3 \\ \varepsilon'^e_6 \end{Bmatrix}, \quad \text{where } \left[\mathbf{C}'^p\right] = \begin{bmatrix} C'^p_{11} & C'^p_{12} & 0 \\ \textit{symm.} & C'^p_{22} & 0 \\ & & C'^p_{33} \end{bmatrix} \tag{4.42}$$

where $[\mathbf{C}'^p]$ is the stiffness matrix for the state of plane stress, given in Eq. (A.3) of Appendix A. Since the stiffness corresponding to the stresses $\sigma'_{11}, \sigma'_{12}, \sigma'_{13}$ was assumed to be zero, the stiffness matrix $\left[\hat{\mathbf{K}}'^{act}\right]$ for fully damaged material is:

$$\left[\hat{\mathbf{K}}'^{act}\right] = \begin{bmatrix} 0 & 0 & 0 & 0 & 0 & 0 \\ & C'^p_{11} & C'^p_{12} & 0 & 0 & 0 \\ & & C'^p_{22} & 0 & 0 & 0 \\ & & & 0 & 0 & 0 \\ & \textit{symm.} & & & 0 & 0 \\ & & & & & C'^p_{33} \end{bmatrix} \tag{4.43}$$

The shear stiffness $\mu_{R,T}$ was introduced to improve numerical behaviour as follows:

$$\left[\tilde{\mathbf{K}}'^{act}\right]=\begin{bmatrix} 0 & 0 & 0 & 0 & 0 & 0 \\ & C'^{p}_{11} & C'^{p}_{12} & 0 & 0 & 0 \\ & & C'^{p}_{22} & 0 & 0 & 0 \\ & & & \mu_{R,T} & 0 & 0 \\ & \textit{symm.} & & & \mu_{R,T} & 0 \\ & & & & & C'^{p}_{33} \end{bmatrix} \tag{4.44}$$

As described in Section 4.4.3, besides anisotropic damaging the transversal damage factor $\xi \quad (0 < \xi \leq 1)$ was introduced to degrade stiffness in the transversal direction. The stiffness matrix $\left[\mathbf{K}'^{act}\right]$ for fully damaged material is:

$$\left[\mathbf{K}'^{act}\right] = \xi\left[\tilde{\mathbf{K}}'^{act}\right] \tag{4.45}$$

Using Eqs. (4.40) and (4.45) the 13 unknown parameters in Eq. (4.35) can be solved from the following equation:

$$\left[\mathbf{K}'\right] = \xi\left[\tilde{\mathbf{K}}'^{act}\right] \tag{4.46}$$

The matrices $\left[\mathbf{K}'\right]$ and $\left[\tilde{\mathbf{K}}'^{act}\right]$ are given in Appendix A. The explicit solution of the equations is not given here (see Appendix B). The solution was carried out using Mathematica (2003) software. When the material orientation is perpendicular to the damage vector orientation ($M_N = 0$ in Eq. (4.36)), the non-zero parameters are

$$
\begin{aligned}
\beta_2 &= -2\mu_{R,T} + \frac{2\,\xi\,\mu_T(\lambda+\mu_T)}{\lambda+2\mu_T} \\
\beta_3 &= 2\,\xi\left(\mu_T - \mu_L - \frac{\alpha\,\mu_T}{\lambda+2\mu_T}\right) \\
\alpha_2 &= 2\,\xi\left(\mu_L - 2\mu_T - \frac{2{\mu_T}^2}{\lambda+2\mu_T}\right) \\
\mu_2 &= \mu_{R,T} - \xi\,\mu_L \\
\beta_D &= (\xi-1)\beta - \frac{\xi\,\alpha^2}{2(\lambda+2\mu_T)} \\
\alpha_D &= \left(\frac{2\,\xi\,\mu_T}{\lambda+2\mu_T} - 1\right)\alpha + 2\xi(\mu_L - \mu_T) \\
\mu_{TD} &= \xi\,\mu_L - \mu_T \\
\lambda_D &= \xi\left(4\mu_T - 2\mu_L - \frac{4{\mu_T}^2}{\lambda+2\mu_T}\right) - \lambda
\end{aligned}
\tag{4.47}
$$

4.4.4.3 Parameter derivation for a passive crack

The derivation of the 13 unknown material parameters is similar to the approach used in the previous section. When compressive stress is closing the crack, the crack (damage) is deactivated and the stiffness in the direction of σ^N is recovered. As mentioned in Section 1.2, frictional sliding is outside the scope of this work, therefore the sliding was assumed to be frictionless. The shear strain γ shown in Fig. 4.12b represents sliding in the model. To avoid numerical problems the shear stiffness $\mu_{R,C}$ corresponding to the shear strain γ was introduced.

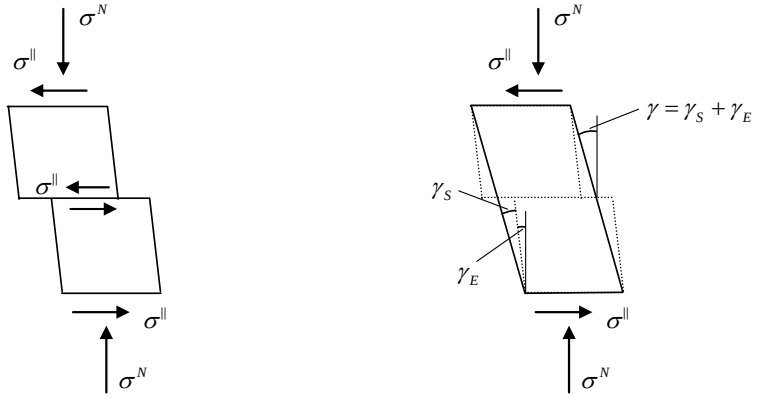

a) True cracked material behaviour
$\sigma^{\|} = \sigma^{\|}(\sigma^N, \textit{friction})$

b) Model behaviour
$\sigma^{\|} = \mu_{RC}\,\gamma$, where $\mu_{RC} = \mu_{RC}(\sigma^N)$

Figure 4.12. Modelling of passive crack behaviour. γ_S represents sliding and γ_E shear deformation.

Due to the frictionless sliding, the shear stresses (σ_4', σ_5') are assumed to vanish on the crack surface as described in Section 4.4.3. The corresponding stress-strain relation can be written in the local coordinate system as follows:

$$\begin{Bmatrix} \sigma_1' \\ \sigma_2' \\ \sigma_3' \\ 0 \\ 0 \\ \sigma_6' \end{Bmatrix} = [\mathbf{C}']\{\boldsymbol{\varepsilon}'^e\} \tag{4.48}$$

Eliminating the strain components $\varepsilon_4'^e$ and $\varepsilon_5'^e$ Eq. (4.41) can be written as:

$$\begin{Bmatrix} \sigma_1' \\ \sigma_2' \\ \sigma_3' \\ \sigma_6' \end{Bmatrix} = \left[\mathbf{C}'^c\right] \begin{Bmatrix} \varepsilon_1'^e \\ \varepsilon_2'^e \\ \varepsilon_3'^e \\ \varepsilon_6'^e \end{Bmatrix}, \quad \text{where } \left[\mathbf{C}'^c\right] = \begin{bmatrix} C_{11}'^c & C_{12}'^c & C_{13}'^c & \\ & C_{22}'^c & C_{23}'^c & 0 \\ & \textit{symm.} & C_{33}'^c & 0 \\ & & & C_{44}'^c \end{bmatrix} \tag{4.49}$$

where the stiffness matrix $[\mathbf{C}'^{c}]$ is given in Eq. (A.4) of Appendix A. Since the stiffness corresponding to the stresses σ'_{12} and σ'_{13} was assumed to be zero, the stiffness matrix $\left[\tilde{\mathbf{K}}'^{pass}\right]$ for fully damaged material is:

$$\left[\tilde{\mathbf{K}}'^{pass}\right]=\begin{bmatrix} C'^{c}_{11} & C'^{c}_{12} & C'^{c}_{13} & 0 & 0 & 0 \\ & C'^{c}_{22} & C'^{c}_{23} & 0 & 0 & 0 \\ & & C'^{c}_{33} & 0 & 0 & 0 \\ & & & \mu_{R,C} & 0 & 0 \\ & \textit{symm.} & & & \mu_{R,C} & 0 \\ & & & & & C'^{c}_{44} \end{bmatrix} \tag{4.50}$$

where $\mu_{R,C}$ is the residual shear modulus introduced for a passive crack. Similar to the active crack, the 13 unknown parameters in Eq. (4.35) can be solved from the following equation:

$$[\mathbf{K}'] = \xi\left[\tilde{\mathbf{K}}'^{pass}\right] \tag{4.51}$$

The matrices $[\mathbf{K}']$ and $\left[\tilde{\mathbf{K}}'^{pass}\right]$ are given in Appendix A. The material parameters obtained from Eq. (4.51) are given in Appendix B. When the material orientation is perpendicular to the damage vector orientation ($M_N = 0$ in Eq. (4.36)), the non-zero parameters are:

$$\begin{aligned}
\alpha_D &= (\xi-1)\alpha + 2\xi(\mu_L - \mu_T) \\
\alpha_2 &= 2\xi(\mu_L - \mu_T) \\
\beta_2 &= \xi\mu_T - 2\mu_{R,C} \\
\beta_3 &= 2\xi(\mu_T - \mu_L) \\
\beta_D &= (\xi-1)\beta \\
\mu_2 &= \mu_{R,C} - \xi\mu_L \\
\mu_D &= \xi\mu_L - \mu_T \\
\lambda_D &= (\xi-1)\lambda + 2\xi(\mu_T - \mu_L)
\end{aligned}$$

4.4.5 Damage vector evolution

A model of a growing, pre-existing crack was introduced to simulate damage evolution and failure modes of brittle materials both under compression and tension. Formation of new cracks was not considered. The damage evolution equation was motivated by the formation mechanism of wing cracks. A damage vector determines the orientation of anisotropic damage of an initially transversely isotropic material.

As briefly discussed in Section 3.2, the wing crack formation under compressive stress is considered to start with sliding along the primary crack (Nemat-Nasser and Deng, 1994; Renshaw and Schulson, 2001). The sliding generates stress concentration at the tips of the primary crack and initiates wing cracks as illustrated in Fig. 4.13. The wing cracks propagate parallel to the direction of compressive stress.

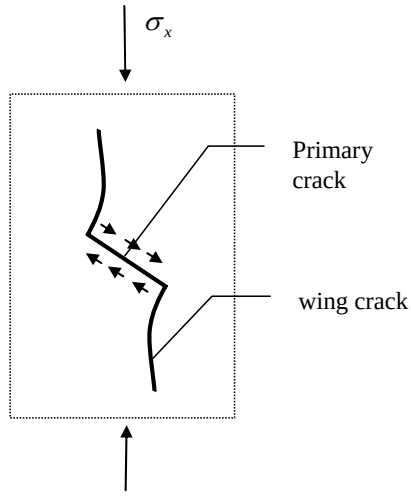

Figure 4.13. Wing crack formation under biaxial compression when the primary crack is inclined at 45° to the compressive stress σ_x.

Numerical models motivated by the wing crack growth mechanism and the splitting failure mode are of considerable current interest (Chen and Ravichandran, 2000; Huang et al., 2002; Mitaim and Detournay, 2004; Tang et al., 2005). Huang et al. (2002) introduced an isotropic damage model with a single damage parameter *D*. The model takes account of e.g. the effects of

friction and flaw distribution on failure strength. Swoboda and Yang (1999a; 1999b) introduced a model capable of simulating kinking of pre-existing cracks. The model based on three damage vectors (or a second order tensor) is capable of predicting anisotropic damaging of an isotropic material.

As stated in Section 4.4.1, the proposed model is based on the assumption of a pre-existing crack. A pre-existing damage vector D_i^0 represents the orientation and size of the pre-existing crack as described in Section 4.4.2. The damage vector evolution initiates when the damage criterion is fulfilled, i.e. $F = 0$.

In order to simulate both wing crack and tensile crack propagation mechanisms, the direction of damage vector evolution is based on the shear traction $\varepsilon_i^{\parallel}$ and normal traction ε_i^N. The tractions are determined as follows (Carol et al., 1991; Bazant and Zi, 2003):

$$\begin{aligned} \varepsilon^N &= n_k \varepsilon_{kl}^e n_l \\ \varepsilon_i^N &= \varepsilon^N n_i \\ \varepsilon_i^{\parallel} &= \varepsilon_{ik}^e n_k - \varepsilon^N n_i \end{aligned} \tag{4.52}$$

where the direction of the unit normal vector n_k is parallel to that of the damage vector as defined in Eq. (4.28).

The shear traction $\varepsilon_i^{\parallel}$ is considered the driving "force" in the wing crack initiation mechanism. The traction direction with respect to the damage vector determines the wing crack evolution direction (kinking angle) as shown in Fig. 4.14a.

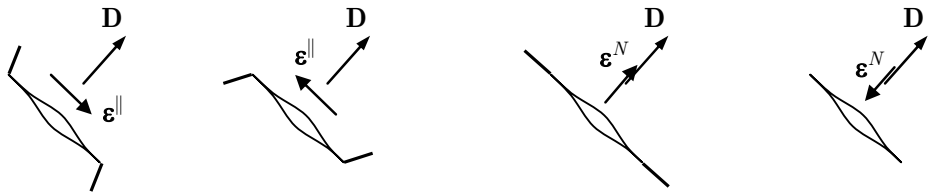

Figure 4.14. Crack propagation determined by the shear traction $\boldsymbol{\varepsilon}^{\parallel}$ *(a) and the normal traction* $\boldsymbol{\varepsilon}^N$ *(b).*

As shown in Fig. 4.14b, the normal traction ε_i^N is assumed to activate crack growth in the direction of the damage vector normal. This corresponds to the fracture mode I in Irwin's notation. When the normal traction is "compressive" the traction does not activate the "mode I evolution".

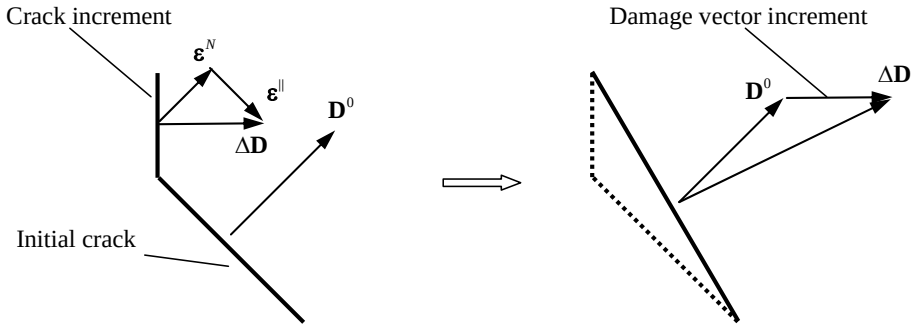

Figure 4.15. Direction of damage vector evolution determined by the shear traction $\boldsymbol{\varepsilon}^{\|}$ *and normal traction* $\boldsymbol{\varepsilon}^N$.

As discussed above, the normal traction ε_i^N and shear traction $\varepsilon_i^{\|}$ are considered driving forces in crack propagation. It is therefore logical to use tractions to construct an equation for damage vector evolution. The evolution direction depends on the traction directions as shown in Fig. 4.15. The following equation was proposed:

$$\begin{aligned} \dot{D}_i &= \dot{\lambda}\,\Omega_i \\ \Omega_i &= \eta_1 H(\varepsilon^N)\,\varepsilon^N n_i + \eta_2 \varepsilon_i^{\|} \end{aligned} \tag{4.53}$$

where the positive material parameters η_1 and η_2 determine the kinking angle. The Heaviside function $H(\varepsilon^N)$ either activates or deactivates the tensile crack growth mechanism (fracture mode I) as follows:

$$\begin{aligned} H(\varepsilon^N) &= 1, \qquad \text{when} \quad \varepsilon^N > 0 \\ H(\varepsilon^N) &= 0, \qquad \text{when} \quad \varepsilon^N \leq 0 \end{aligned} \tag{4.54}$$

As shown in Eq. (4.53), tensile crack growth is activated when the tensile strain is positive with respect to the damage vector orientation despite the stress state. As shown in Section 4.2, the strain ε^N does not give information about the

corresponding normal stress σ^N. Therefore the normal stress may be either positive or negative.

As proposed by Van (2001), it was assumed that damage can only grow, therefore Van introduced the following essential condition for damage vector evolution:

$$D_k \dot{D}_k \geq 0 \tag{4.55}$$

Evolution equation (4.53) fulfils the condition of Eq. (4.55). In numerical computation it was found that the condition given in Eq. (4.55) enables limitless crack rotation. The condition does not guarantee that the Clausius-Duhem inequality equation is fulfilled. The rotation may induce stiffness recovery of already degraded stiffness as illustrated in numerical verification tests (Section 5.2). Therefore a new condition based on the Clausius-Duhem inequality equation Eq. $(3.21)_2$ was introduced. The inequality equation is:

$$\gamma^d = Y_k \dot{D}_k - B\dot{\kappa} \geq 0 \tag{3.21}_2$$

Inserting Eqs. (4.53) and (3.71) into Eq. $(3.21)_2$ the following expression is obtained:

$$\gamma^d = \dot{\lambda}\,(Y_k \Omega_k - B) \geq 0 \tag{4.56}$$

From which the following condition is obtained:

$$Y_k \Omega_k \geq B \tag{4.57}$$

A conservative solution is obtained if B is replaced by $B^{\max}$, which is the maximum value that B can have. The value of $B^{\max}$ depends on the material parameters. In the upcoming numerical examples $B^{\max} < 1.0 \cdot 10^{-3}$, but the conservative value of 0.01 was used. In the numerical examples the condition of (4.57) was applied as follows:

1) Damage increment direction Ω_i is calculated from Eq. (4.53).

2) The condition of Eq. (4.57) is checked. If the condition is not fulfilled the damage increment vector is modified such that the condition will be fulfilled as illustrated in Fig. 4.16.

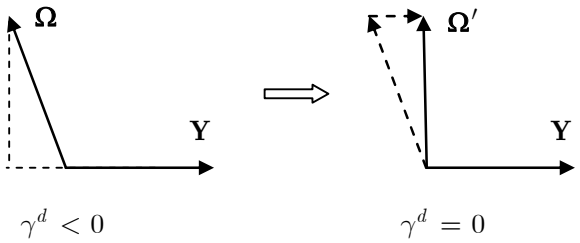

Figure 4.16. Illustration of calculation of the allowable direction of the damage increment Ω_i' *according to Eq. (4.57) when* $B = 0$.

The evolution according to Eq. (4.53) is illustrated in Fig. 4.17. The evolution equation is cost-effective in numerical applications. The evolution direction takes into account the two axial failure modes such that both the axial splitting failure mode (Fig 3.2c) and the tensile failure mode (Fig 3.2e) can be simulated.

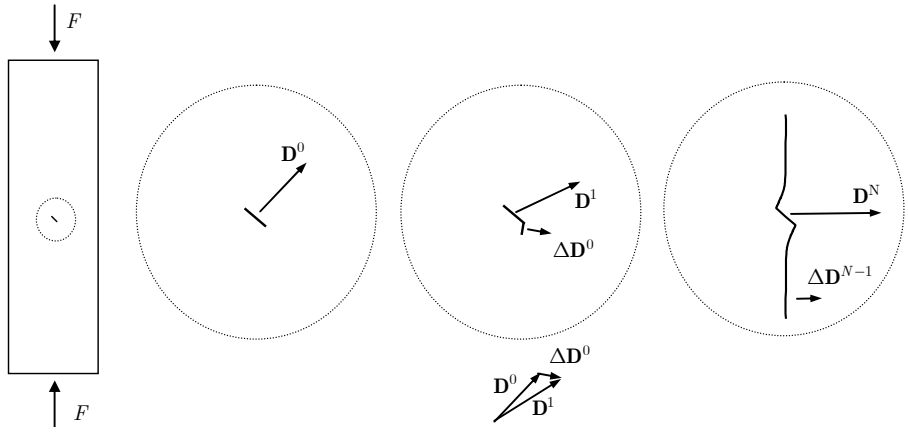

Figure 4.17. Illustration of damage vector evolution under uniaxial compression when the primary (initial) crack is inclined at 45° to the compressive force F. $\mathbf{D}^0$ *is the initial damage vector,* $\Delta\mathbf{D}^k$ *is the damage increment obtained from Eq. (4.53) and* $\mathbf{D}^N$ *is the damage at the end of analysis.*

Because this approach is not based on the use of the normality rule described in Section 3.6.1, the dissipation inequality of Eq. (3.21) must be verified either

analytically or numerically. The inequality has been studied numerically in FE implementation (see Section 5.2).

4.4.6 Evolution of anisotropic damage

It is known that the material orientation (M_i) affects the kinking angle of a pre-existing crack. The maximum energy-release-rate criterion of the theory of fracture mechanics can be employed in predicting the kink angle of anisotropic materials (Obata et al., 1989; Azhdari and Nemat-Nasser, 1996).

The damage evolution Eq. (4.53) introduced in Section 4.4.5 is based on the strain state and the damage vector orientation and is independent of material orientation information. The material orientation effect is taken into account indirectly through strains, because strains depend on the material orientation.

In CDM models the damage growth direction of anisotropic materials is often based on the use of the damage characteristic tensor L_{ijkl} as described in Eq. (3.91). A brief review of various damage characteristic tensors has been introduced by Zhu and Cescotto (1995). In the associative approach of the MK model the evolution equation has the following form when L_{ijkl} is used (see Section 3.8.2.2):

$$\begin{aligned} \dot{D}_{ij} &= \dot{\lambda}\frac{L_{ijkl}}{Y^{eq}}Y_{kl} \\ Y^{eq} &= \sqrt{\frac{1}{2}Y_{ij}L_{ijkl}Y_{kl}} \end{aligned} \tag{4.58}$$

As discussed in Section 3.8.2.2, the damage characteristic tensor L_{ijkl} can be a function of internal state variables and material orientation. The evolution Eq. (4.53) can be modified in anisotropic form similar to Eq. (4.58) as follows:

$$\dot{D}_i^* = L_{ik}\dot{D}_k \tag{4.59}$$

where $\dot{D}_i^*$ is the damage rate for anisotropic material, L_{ik} is the second order damage characteristic tensor and $\dot{D}_k$ is the damage rate given in Eq. (4.53). The damage characteristic tensor can be defined experimentally as described by

Chow and Lu (1989). The tensor was assumed to equal the unit tensor in the upcoming numerical examples as follows:

$$L_{ik} = \delta_{ik} \tag{4.60}$$

4.5 Application of the wing crack approach

The equations needed in the FE implementation of the proposed wing crack model were introduced in Sections (4.5.3–4.5.2). Most of the derivatives were solved using Mathematica (2003) software. The explicit expressions of derivatives were not given.

The introduced wing crack model is based on the assumption of vanishing shear and normal tractions on the crack surface (see Section 4.4). The surface orientation and size are determined by the damage vector D_k normal to the crack surface. Damaging introduces anisotropy in the initially transversely isotropic material. Eq. (4.35) determining the elastic strain energy of the damaged material consists of 13 unknown parameters, which can be solved from the conditions given in sections 4.4.4.2 and 4.4.4.3. Only three parameters must be defined by the user: residual shear moduli for the active and passive crack $\mu_{R,T}$, $\mu_{R,C}$ and the transversal damage factor ξ. In addition, parameters defining the initial damage surface and softening as well as the pre-existing damage vector size and orientation are also needed. The determination of material parameters is considered in Section 4.5.5.

4.5.1 Helmholtz free energy

The Helmholtz free energy per unit mass ψ for a damaged transversely isotropic material is:

$$\begin{aligned}\rho\psi = &\frac{1}{2}\lambda\varepsilon^e_{kk}\varepsilon^e_{ll} + \mu_T\varepsilon^e_{kl}\varepsilon^e_{kl} + 2(\mu_L - \mu_T)M_{kl}\varepsilon^e_{lm}\varepsilon^e_{mk} + \beta(M_{kl}\varepsilon^e_{kl})^2 \\ &+\alpha M_{kl}\varepsilon^e_{kl}\varepsilon^e_{mm} \\ &+\sqrt{D_k D_k}\,[\,\lambda_D\varepsilon^e_{kk}\varepsilon^e_{ll} + \mu_{TD}\varepsilon^e_{kl}\varepsilon^e_{kl} + 2(\mu_{LD} - \mu_{TD})M_{kl}\varepsilon^e_{lm}\varepsilon^e_{mk} \\ &+\beta_D(M_{kl}\varepsilon^e_{kl})^2 + \alpha_D M_{kl}\varepsilon^e_{kl}\varepsilon^e_{mm} + \beta_2(n_k n_l\varepsilon^e_{kl})^2 \\ &+(\mu_2 n_k n_l + \mu_3 A_{kl})\varepsilon^e_{lm}\varepsilon^e_{mk} + (\,\alpha_2 n_k n_l + \alpha_3 A_{kl}\,)\,\varepsilon^e_{kl}\varepsilon^e_{mm} \\ &+(\,\beta_3 M_{kl} n_m n_n + \beta_4 M_{kl} A_{mn} + \beta_5 A_{kl} n_m n_n\,)\,\varepsilon^e_{kl}\varepsilon^e_{mn}\,] \\ &+\frac{h}{n_h + 1}(\kappa\,)^{(n_h+1)}\end{aligned} \tag{4.61}$$

where the damaged and elastic part are obtained from Eq. (4.35). h and n_h are material parameters to be defined by the user. κ is an internal variable related to the material softening. Although the 13 parameters (λ_D, μ_{TD}, μ_{LD}, β_D, α_D, α_2, α_3, μ_2, μ_3, β_2, β_3, β_4, β_5) are functions of the damage vector D_k and traction σ^N the parameters were assumed to be constants in the derivation of the material Jacobian of Eq. (4.64). The last term represents the free energy induced due to the damage development. The term corresponds to $\rho\psi^d$ in the MK model (see Eq. (3.75)).

It can be assumed that the material softening parameters in the direction of the material orientation axis M_k are not the same as in the transversal direction. The anisotropic softening parameters were not available for the materials in the numerical examples (Chapter 5). Therefore in subsequent applications it was assumed that softening is isotropic.

The thermodynamic conjugate forces are obtained substituting Eq. (4.61) into Eqs. $(3.18)_{1\text{–}3}$ as described in Section 3.6.1:

$$\begin{aligned}\sigma_{ij} &= \rho \frac{\partial \psi}{\partial \varepsilon^e_{ij}} \\ B &= \rho \frac{\partial \psi}{\partial \kappa} \\ Y_i &= -\rho \frac{\partial \psi}{\partial D_i}\end{aligned} \tag{4.62}$$

The secant stiffness is obtained from Eq. (4.62) as follows:

$$K_{ijkl} = \frac{\partial \sigma_{ij}}{\partial \varepsilon^e_{kl}} \tag{4.63}$$

The material Jacobian derivation was prescribed in Section 3.7.2.1. Noting that $\dot{\kappa} = \dot{\lambda}$ (see Eq. (4.67)), the Jacobian obtained from Eq. (3.74) is written as:

$$K^t_{ijkl} = \frac{\partial \sigma_{ij}}{\partial \varepsilon^e_{kl}} - \frac{1}{\dfrac{\partial F}{\partial \lambda} + \dfrac{\partial F}{\partial \dot{\lambda}} \dfrac{1}{\Delta t}} \frac{\partial \sigma_{ij}}{\partial D_m} \frac{\partial G}{\partial Y_m} \frac{\partial F}{\partial \varepsilon^e_{kl}} \tag{4.64}$$

where the damage surface F is given in Eq. (4.69) and the damage potential G in Eq. (4.65).

4.5.2 Evolution equation

To follow the procedure and formalism of continuum thermodynamics (Section 3.6.1), the evolution equation was reformulated in potential form although it was not compulsory. The following damage potential function was introduced:

$$G = \Omega_k Y_k - B \tag{4.65}$$

where Y_k is obtained from Eq. (4.62) and Ω_k is based on the evolution Eq. (4.53):

$$\Omega_i = \eta_1 H(\varepsilon^N)\, \varepsilon^N n_i + \eta_2 \varepsilon^{\|}_i \tag{4.66}$$

The normal strain ε^N and the tractions $(\varepsilon^N_i,\, \varepsilon^{\|}_i)$ are obtained from (4.52). Substituting Eq. (4.65) into Eq. $(3.29)_2$ the following relation is obtained:

$$\dot{\kappa} = \dot{\lambda} \tag{4.67}$$

The damage vector evolution equation is obtained from Eq. (3.29):

$$\dot{D}_i = \dot{\lambda} \frac{\partial G}{\partial Y_i} \tag{4.68}$$

Substituting Eq. (4.65) into Eq. (4.68) gives the evolution equation derived in Section 4.4.5.

4.5.3 Damage surface for transversal isotropy

Consistent viscoplasticity formulation as described in Section 3.7.2 was applied. The following strain-based dynamic damage surface was applied:

$$\begin{aligned} F &= F_0(\varepsilon_{ij}^e) - c\Big[1 - e^{-m_c \dot{D}^{ekv}}\Big] - B \\ B &= h\,\kappa^{n_h} \end{aligned} \tag{4.69}$$

where c is the material parameter for damage rate dependency and h is a hardening parameter. Parameters n_h and m_c are related to the shape of the rate-dependent hardening diagram. $F_0(\varepsilon_{ij}^e)$ is the initial damage surface defined in Eq. (4.71). With the evolution law of Eq. (3.29) the equivalent damage rate is defined as

$$\begin{aligned} \dot{D}^{ekv} &= \sqrt{\dot{D}_k \dot{D}_k} \\ &= \dot{\lambda} \sqrt{\frac{\partial G}{\partial Y_k} \frac{\partial G}{\partial Y_k}} \end{aligned} \tag{4.70}$$

As described earlier, in damage models the damage surface is often written as a function of the conjugate force Y_{ij} corresponding to the damage tensor D_{ij}. In this study, a strain-based damage surface was proposed. A four-parameter damage surface used in the upcoming examples is written as follows:

$$\begin{aligned} F_0(\varepsilon_{ij}^e) = {} & 2x_0(I_1 - I_{12} + x_0) + I_2 + (a^2 - 1)I_{22} \\ & + z_0(z_0 + 2\,a\,I_{12}) - R^2 \end{aligned} \tag{4.71}$$

where

$$
\begin{aligned}
I_1 &= \varepsilon^e_{kk} \\
I_{12} &= M_{kl}\varepsilon^e_{kl} \\
I_2 &= \varepsilon^e_{kl}\varepsilon^e_{kl} \\
I_{22} &= M_{kl}\varepsilon^e_{lm}\varepsilon^e_{mk}
\end{aligned}
\tag{4.72}
$$

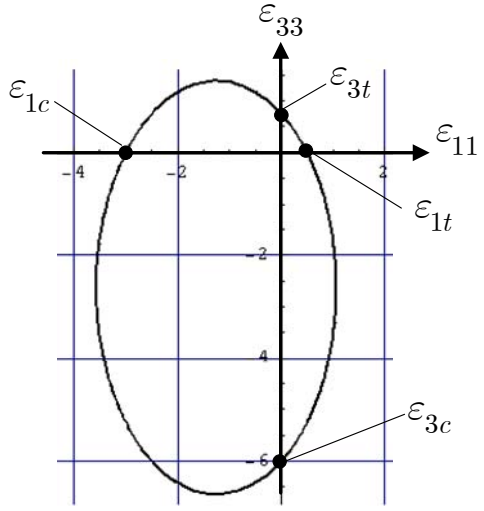

Figure 4.18. Four-parameter transverse isotropic damage surface in the plane strain space when $\mathbf{M} \parallel \mathbf{i}_3$.

The damage surface is illustrated in Fig. 4.18. The material parameters (x_0, z_0, a, R) in Eq. (4.71) can be given as a function of failure strains shown in Fig. 4.18. The failure strains $(\varepsilon_{1c}, \varepsilon_{1t}, \varepsilon_{3c}, \varepsilon_{3t})$ are considered as positive quantities. The coefficients are defined in the strain space when $\mathbf{M} \parallel \mathbf{i}_3$ as follows:

$$
t_R = \frac{\varepsilon_{3t}}{\varepsilon_{1t}} \qquad c_R = \frac{\varepsilon_{3c}}{\varepsilon_{1c}} \tag{4.73}
$$

$$
R^2 = \frac{1}{4}\left[\left(\frac{c_R}{t_R} + 2\right)(\varepsilon_{1c})^2 - 2\varepsilon_{1c}\varepsilon_{1t} + \left(2 + \frac{t_R}{c_R}\right)(\varepsilon_{1t})^2\right] \tag{4.74}
$$

$$
a = \frac{1}{\sqrt{c_R\, t_R}} \tag{4.75}
$$

$$z_0 = \frac{c_R \varepsilon_{1c} - t_R \varepsilon_{1t}}{2\sqrt{c_R t_R}} = \frac{(c_R \varepsilon_{1c} - t_R \varepsilon_{1t})a}{2} \tag{4.76}$$

$$x_0 = \frac{\varepsilon_{1c} - \varepsilon_{1t}}{2} \tag{4.77}$$

4.5.4 Pre-existing damage distribution

As discussed in Section 1.2, crack distribution studies are outside the scope of this work. To illustrate the usefulness of the proposed method, pre-existing damage size and orientation were assumed to be normally distributed. The Pre-existing damage vector components are defined as follows:

1. To define the orientation of pre-existing cracks, each component *k* ($k = 1, 2, 3$) of damage vector $\mathbf{D}$ is obtained from the normal distribution based on the given mean value m_{Dk} and standard deviation s_{Dk}.

2. After determining the components, the damage vector length $\|\mathbf{D}_0\|$ is set based on the lognormal distribution with the given mean value $m_{\|D0\|}$ and the standard deviation $s_{\|D0\|}$. Therefore the distribution parameters m_{Dk} and s_{Dk} do not represent the real distribution of the components of pre-existing damage. The parameters s_{Dk} and m_{Dk} are relative; they determine the orientation but not the size.

The orientation and size distribution of the pre-existing cracks was not known. In the upcoming examples the orientation of pre-existing damage was assumed to depend on the orientation of the material symmetry axis $\mathbf{M}$ when a transversely isotropic material was considered. Otherwise pre-existing cracks were assumed to be randomly oriented.

4.5.5 Determination of material parameters

4.5.5.1 Elastic properties

A total of five material parameters given in Eqs. (3.12) and (3.13) are needed to define the elastic behaviour of a transversely isotropic material. In addition to the material properties, the material orientation axis **M** shown in Fig. 3.12 has to be defined. Usually the above-mentioned material parameters are available for common transversely isotropic materials.

4.5.5.2 Damaged material parameters

To define the damaged material stiffness, four material parameters given in Eqs. (4.35) and (4.44) must be defined:

- Shear modules for active and passive crack: $\mu_{R,C},\ \mu_{R,T}$
- Threshold stress σ^{TR} for damage deactivation
- Transversal damage factor ξ
- Upper limit of damage to retain positive definiteness of the stiffness matrix.

In this work, the residual shear modulus μ_R was assumed to be a function of the normal compressive traction σ^N obtained from Eq. (4.27) as illustrated in Figs. 4.19 and 4.20:

$$\begin{aligned} \mu_R &= \mu_{R,T} + \frac{\sigma^N}{\sigma^{TR}}(\mu_{R,C} - \mu_{R,T}), && \sigma^{TR} \leq \sigma^N \leq 0 \\ \mu_R &= \mu_{R,C}, && \sigma^N < \sigma^{TR} \\ \mu_R &= \mu_{R,T}, && \sigma^N > 0 \end{aligned} \tag{4.78}$$

where σ^{TR} is the threshold compressive stress value. There are two reasons for using the approach described in Eq. (4.78): firstly, numerical difficulties occur if there is a jump in material parameters when an open crack is closed; secondly, the approach simulates both degradation of shear stiffness due to damage and apparent dependence of shear stiffness on compressive stress. Therefore in the numerical implementation of the WCD model both $\mu_{R,T}$ in Eq. (4.44) and $\mu_{R,C}$ in Eq. (4.50)were replaced by μ_R given in Eq. (4.78).

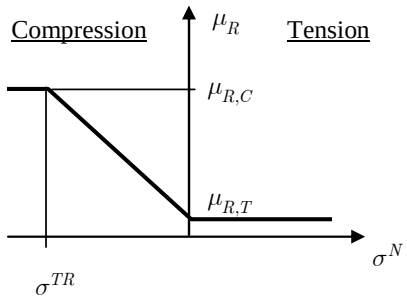

Figure 4.19. Residual shear modulus as a function of normal traction σ^N.

Residual shear modulus for active crack $\mu_{R,T}$

The residual shear modulus $\mu_{R,T}$ for an active crack was introduced to retain positive definiteness of the secant stiffness matrix. Therefore $\mu_{R,T}$ is not considered a physical material parameter but numerical. In the following numerical examples, the value of $\mu_{R,T}$ was set to about 2% of the undamaged shear modulus. To avoid numerical difficulties the residual shear modulus μ_R was given as a function of compressive traction as described in Eq. (4.78).

Residual shear modulus for passive crack and threshold stress $\mu_{R,C}$, σ^{TR}

The shear stress of damaged material in the direction of the crack surface is often assumed to be a function of the compressive stress that is closing the crack (Fig. 4.20). The relation between shear and normal stresses could be modelled using e.g. the classical Coulomb friction law or the thermodynamic approach of Halm and Dragon (Halm and Dragon, 1998). However, as mentioned in Section 1.2, modelling of frictional sliding was outside the scope of this work.

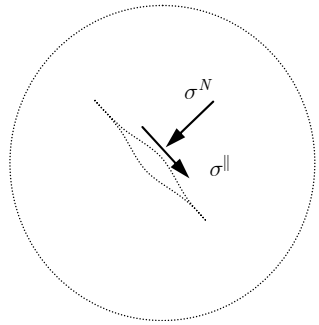

Figure 4.20. Normal and shear tractions.

Neither the residual shear modulus under compression $\mu_{R,C}$ nor the threshold stress σ^{TR} is a known material parameter, but they could be defined experimentally. In the numerical examples the threshold stress σ^{TR} was 30% of the tensile strength. The residual shear modulus under compression $\mu_{R,C}$ was assumed to be about 40% of the undamaged shear modulus.

Parameters $\mu_{R,C}$ and σ^{TR} do not significantly affect the results of the numerical examples (see Chapter 5) because crack deactivation does not take place in the examples, except for Example 5.2.1, which illustrates the efficiency of the method in crack activation-deactivation cycles.

If the proposed method is applied in cyclic loading cases, the parameters $\mu_{R,C}$ and σ^{TR} must be experimentally verified.

Transversal damage factor ξ

The transversal damage factor ξ enables modelling of "transversal" stiffness degradation as described in Section 4.4.3 and in the numerical examples (see Fig. 5.9). Factor ξ reduces stiffness in the direction perpendicular to the damage vector. Without factor ξ the stiffness is not degraded in pure uniaxial compression where the failure mode is splitting, because the splitting crack does not affect the stiffness in the load direction. The effect is illustrated in Fig. 4.21. Factor ξ can be considered to take account of the effects of other failure modes besides the splitting mode. Before using the transversal damage factor ξ it should be experimentally verified. The use of the factor is illustrated in the numerical example of Section 5.2.1. In the other numerical examples the effect of the factor has been neglected: $\xi = 1$.

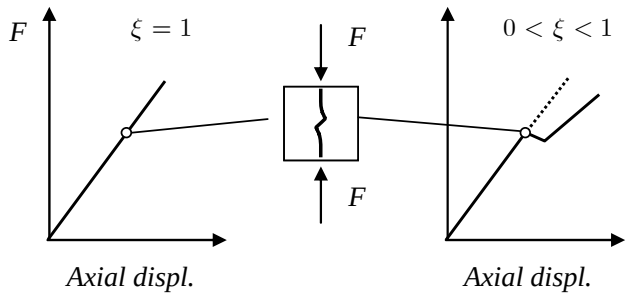

Figure 4.21. Effect of the reduction factor ξ on axial stiffness degradation under uniaxial compression.

Parameter treatment for active and passive cracks

As described in Sections 4.4.4.2 and 4.4.4.3, the material parameters which need not be explicitly defined (λ_D, μ_{TD}, μ_{LD}, β_D, α_D, α_2, α_3, μ_2, μ_3, β_2, β_3, β_4, β_5) are different for active and passive cracks. When an open crack is closed, there is an abrupt change in stiffness, i.e. an abrupt change in material parameters. To avoid numerical difficulties the material parameters were assumed to be a function of the normal compressive traction σ^N and the threshold stress σ^{TR} similar to the residual shear modulus described in Eq. (4.78).

Upper limit of damage

Although material rupture has taken place when the damage vector length equals one as described earlier, the damage vector upper limit was set at 0.9999995 in numerical examples to retain positive definiteness of the stiffness matrix.

4.5.5.3 Damage evolution parameters

The ratio of the parameters η_1 and η_2 in the damage evolution Eq. (4.66) defines the wing crack "kinking angle" α shown in Fig. 4.22b. The angle depends both on the stress state and on the material considered. The parameter ratios $\eta_1 / \eta_2 = 1$ and $\eta_1 / \eta_2 = 1/2$ were studied numerically under uniaxial compression when the angle of the inclined pre-existing damage was 45°. The numerical studies showed that when the pre-existing damage is small the difference is negligible. In practice the ratio η_1 / η_2 has an effect on the time needed to form a splitting crack as illustrated in Fig. 4.22a.

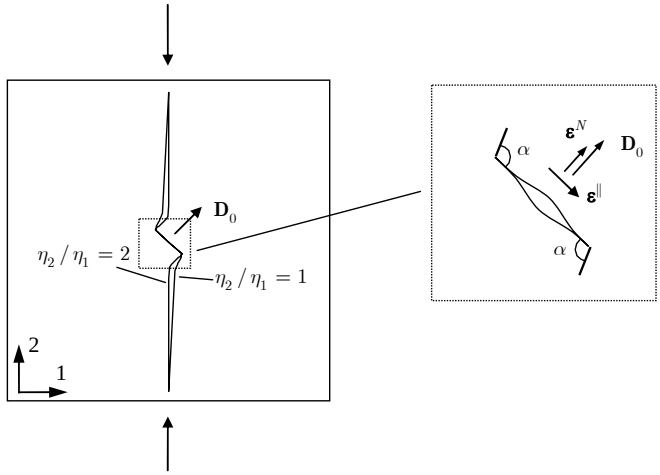

a) b)

Figure 4.22. a) Effect of the ratio η_1 / η_2 on splitting crack evolution under uniaxial compression (material parameters are the same as in the numerical example of Section 5.2.1: $\eta_1 = 1.0 \cdot 10^4$). b) Wing crack kinking angle α.

4.5.5.4 Damage surface and softening parameters

The following parameters must be defined:

- The initial damage surface is based on compressive end tensile strengths in the two directions as described in Eq. (4.73). Parameters R, x_0, z_0 and a must be defined.
- Softening parameters h and n_h as described in Eq. (4.69) must be defined.
- Damage rate-dependent parameters c and m_c (see Eq. (4.69)) must be defined.

The above-mentioned parameters could be determined from tensile and compression tests as a function of the strain rate. Because the material parameters were not available, the procedure described below was applied in this work.

Although tensile and compressive strengths for various materials are available, the complete stress-strain curve which defines the damage initiation stress and the shape of the curve are not generally available. Quasi-brittle material

damaging initiates at stress level σ_0 which is lower than the ultimate stress σ_u as illustrated in Fig. 4.23.

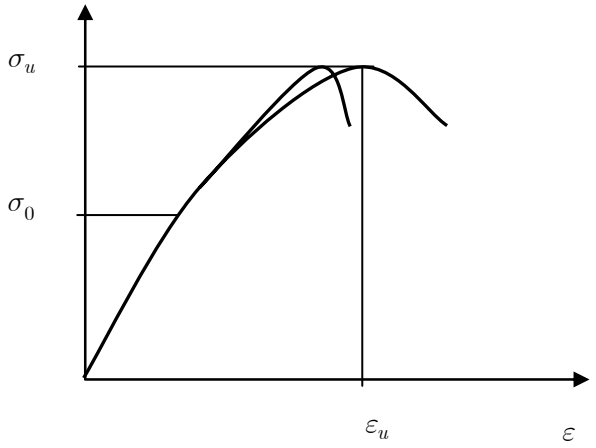

Figure 4.23. Stress-strain diagram for materials having the same σ_u and σ_0 but a different shape of the softening diagram.

Because the ratio of the damage initiation stress and ultimate stress (σ_0 / σ_u) is not known, damage was assumed to initiate at a stress level 20% lower than the tensile strength. Based on this assumption the initial damage surface parameters can be defined (R, x_0, z_0 and a) when uniaxial compressive and tensile strengths are known.

Although the proposed approach resembles modelling of creep brittle materials, the damage rate-dependent approach was introduced into the proposed model to avoid localisation of deformations. With the damage rate-dependent approach, material strength is a function of strain rate. Therefore all the material parameters affecting material strength must be defined at a known strain rate. Because the strain rate was not known, it was assumed in the numerical examples that tensile and compressive strength are obtained when the strain rate is 10^{-3} 1/s.

Softening parameters (h and n_h) were adjusted assuming that the uniaxial tensile strength at $\dot{\varepsilon} = 0$ is 5% lower than the ultimate tensile strength at $\dot{\varepsilon} = 10^{-3} s^{-1}$. If the fracture energy G_F is known, softening parameters could be adjusted such that the absorbed energy is the same as the fracture energy G_F as described in the

upcoming example in Section 5.1. Because the softening diagram shape is unknown, it is assumed that the softening is linear, i.e. $n_h = 1$.

Damage rate-dependent parameters (c and m_c) were determined such that the known uniaxial tensile strength was attained with a strain rate of 10^{-3} 1/s. The procedure is illustrated in Figs. 4.24 and 4.25. In the determination it was assumed that $c = 0.05\,R$, where R is the radius of the initial damage surface as described in Eq. (4.73).

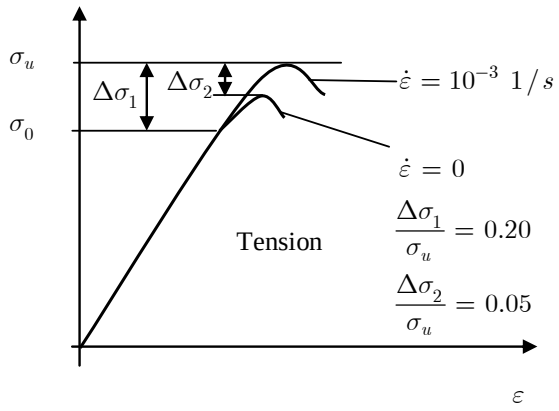

Figure 4.24. Determination of material parameters $\sigma_0 / \sigma_u = 0.8$.

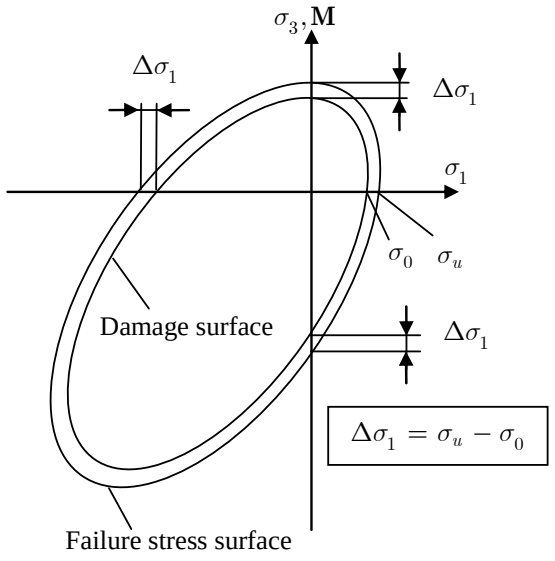

Figure 4.25. Determination damage surface in the stress space.

4.6 Conclusions of the model formulation

As described in section 1.1, the objective was to introduce a continuum damage model capable of simulating compressive and tensile failure modes in brittle failure of transversely isotropic materials.

Unilateral condition

It was shown in Section 4.2 that the strain-based crack opening/closure criteria cannot be reliably applied when the stress state is two- or three-dimensional, but a stress based criterion should be used instead.

The main reasons for finding another solution method instead of developing the MK model were: a) The invalid opening/closure criterion of the MK model and b) the need to calculate an eigensystem at each increment.

Upper limit of damage

A method based on the positive definiteness of the secant stiffness matrix for determining the upper limit of the damage tensor was introduced in Section 4.3.2. As discussed in the previous sections, the upper limit of damage tensor D_{ij} is generally undefined in the phenomenological damage models described in Section 3.6.2.4.

Wing crack damage (WCD) model

A new *wing crack damage model* was introduced for modelling of transversely isotropic materials. The method is capable of simulating both the axial splitting failure mode due to the wing crack growth mechanism under compression, and the tensile cracking failure mode under tension.

In the proposed model, damage vector D_k is used to represent the size and orientation of the plane crack. The derived strain energy equations are based on the equations derived for materials having two preferred directions. The damage vector and the axis of the material symmetry of virgin transversely isotropic material define the two directions.

The evolution equation of damage vector D_k is based on the wing crack growth mechanism. The evolution direction is determined by the normal and shear strain tractions on the crack surface. The approach is non-associative; therefore it must be verified either analytically or numerically whether the Clausius-Duhem inequality equation is fulfilled. In this work it is verified numerically.

The rupture criterion of the material is the same as the upper limit of the damage. The limit is reached when the length of the damage vector equals unity.

Damage surface of the WCD model

Damage initiation in the WCD model is based on the damage surface given in the strain space. A four-parameter surface was introduced. It enables definition of the damage surface when tensile and compressive strengths are known both in the direction of the material symmetry axis and the transverse direction. A more detailed surface can be easily applied if necessary.

Stiffness degradation in the WCD model due to damaging is based on the strain softening approach. The softening function was assumed to be linear and isotropic, although more precise anisotropic functions can be applied if material parameters are known. Softening was assumed to be a function of the damage rate. The rate dependency was applied only to avoid mesh sensitivity and localisation problems.

Pre-existing cracks

The proposed method is based on the assumption of pre-existing cracks. A pre-existing damage vector represents a crack. If the pre-existing damage vectors are small enough they do not affect damage initiations stress. Increasing the length of pre-existing damage vectors makes it possible to study the effect of size and orientation distribution of pre-existing cracks on strength and failure modes.

5. Numerical results and verification of wing crack and MK damage models

The damage model described in the previous Sections has been implemented in ABAQUS/Standard FE software as a user material subroutine (UMAT).

As described in Section 3.9, the model of Murakami and Kamiya (1997) (MK model), was not further enhanced. Therefore this work concentrated on the development of the proposed wing crack damage model only.

In the upcoming paragraphs the validity of the wing crack damage model was verified by testing it against five basic structures composed of known natural materials (ice, marble and concrete). Only one verification test, using concrete as the test material, was executed using the modified MK model.

Not all the material parameters were available for verification. Therefore, the missing parameters were defined following the procedure described in Section 4.5.5. The parameters were not fitted to obtain equivalent results with experiments, although a better correspondence would have been achieved.

All of the following examples were analysed with ABAQUS/Standard software using a dynamic analysis method with implicit time integration, except in Section 5.2 where static loading was applied.

5.1 Model verification test 1

5.1.1 Mesh sensitivity analysis

The objective of this example was to show that the proposed model is not mesh sensitive. As shown in the following pages, the damage rate-dependent failure surface proved to be an efficient tool for avoiding mesh-dependent solutions. To illustrate the effectiveness of the proposed method, models without the damage rate-dependent failure surface were studied as well.

In addition to the load-displacement diagram, the energy dissipated in each of the models was studied. If due to softening the deformations localise into a single element, the dissipated energy within the loading-unloading cycle decreases with decreasing element size.

In the mesh sensitivity study, the tensile test of the tapered bar shown in Fig. 5.1 was simulated. The specimen end velocity was 0.1 mm/s, which would correspond to the average strain rate of 0.001/s if the bar were not tapered. After tension of 20 μm the bar end was returned to the original position. The tensile phase time was 0.2s.

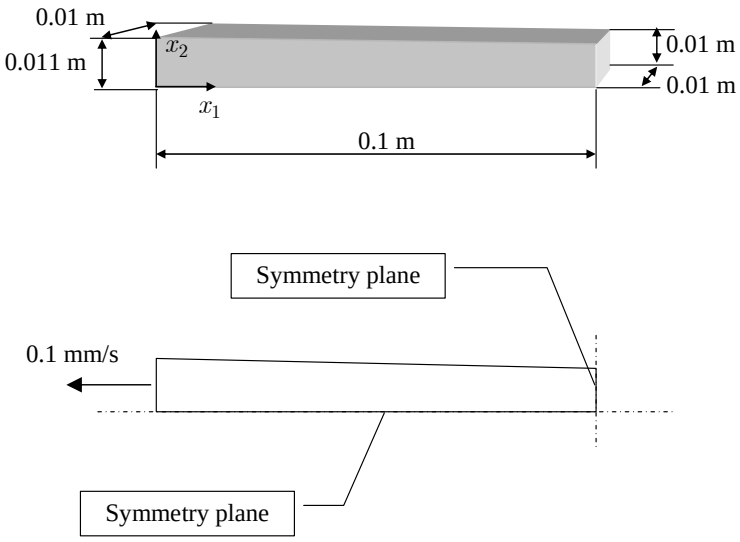

Figure 5.1. Tapered bar geometry and boundary conditions.

Because of the brittle-like softening, the specimen response is dynamic after material failure at the narrow end. An implicit time integration method was used. The sample was modelled with linear brick elements (C3D8) with various mesh densities. The mesh densities studied were 10, 100 and 200. The element mesh was denser at the narrow end such that the ratio of the smallest and the largest element length (l_N / l_1 in Fig. 5.2) was 100 for the 10-element model and 1000 for the 100 and 200-element models respectively.

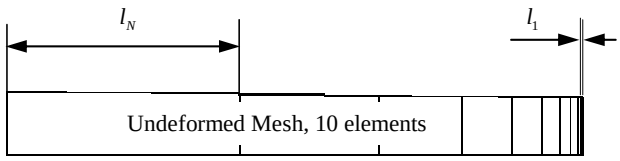

Figure 5.2. Finite element mesh of 10 elements, $l_N / l_1 = 100$.

The material properties are shown in Tables 5.1, 5.2 and 5.3. The properties are the same as used for columnar ice in the upcoming example in Section 5.3.1. The damage surface parameters (a, R^2, x_0 and z_0) shown in Table 5.3 were obtained based on the following assumption (see Section 4.5.5.4):

- Damage initiation was assumed to start at the stress level $0.8\ \sigma_t = 0.28$ MPa, where σ_t is the tensile strength in the transverse direction. Therefore the damage initiation stress is 0.07 MPa less than the ultimate stresses given in Table 5.1.

The hardening parameter h shown in Table 5.3 was determined such that the tensile strength in the transverse direction is $0.95\ \sigma_t = 0.333$ MPa when strain rate equals zero: $\dot{\varepsilon} = 0$. The hardening rate-dependent parameter m_c was determined such that the tensile strength equals the ultimate strength given in Table 5.1 when $\dot{\varepsilon} = 10^{-3}\ 1/\mathrm{s}$ ($\sigma_t = 0.35$ MPa).

After failure at the narrow end the elastic strain energy stored in the bar induces a dynamic response in the bar. The solution was found to be sensitive to the increment length such that the angle of the unloading path varied when the increment length was large. In the automatic time incrementation procedure the maximum time increment was set to 0.001s and the half step force residual tolerance (HAFTOL) to 50N. The mass proportional damping coefficient was set to α = 200E3. Artificial (numerical) damping of α = -0.1 was used.

Pre-existing small cracks were assumed to be perpendicular to the tension direction. Therefore the damage vectors were set parallel to the tension direction. The length of the damage vector was set to 1.0E-5.

*Table 5.1. Tensile (σ_t) and compressive (σ_c) stresses along and transverse to the direction **M**.*

Ultimate stress			
Direction **M**		Transverse direction	
σ_t (MPa)	σ_c (MPa)	σ_t (MPa)	σ_c (MPa)
1.1	6.0	0.35	3.0
Damage initiation stress			
Direction **M**		Transverse direction	
σ_t (MPa)	σ_c (MPa)	σ_t (MPa)	σ_c (MPa)
1.03	5.93	0.28	2.93

Table 5.2. Wing crack model: elastic material properties and material orientation. Subscripts refer to the direction of material orientation axis M as shown in Fig. 3.12 and Eq. (3.13).

Elastic material properties						Material orientation		
E_{11} (GPa)	E_{33} (GPa)	G_{13} (GPa)	ν_{21}	ν_{31}	ρ (kg)	M_1	M_2	M_3
6.0	8.5	3.2	0.313	0.301	1000	0	1	0
Residual Shear						Damage evolution		
$\mu_{R,C}$ (GPa)		$\mu_{R,T}$ (GPa)	ξ	σ^{TR} (MPa)		η_1	η_2	
$0.4 \cdot (G_{13} + G_{21})$		$0.02 \cdot (G_{13} + G_{21})$	1.0	0.1		1.0E+4	1.0E+4	

Table 5.3. Wing crack model: material properties; m is the mean and s is the standard deviation.

Damage surface **F**							
R^2	a	x_0	z_0	h	n_h	c	m_c (s)
1.627E-6	0.3409	4.683E-4	1.0786E-3	1.9E-5	1	$0.05\,R$	6.0E-4

Distribution of orientation and size of pre-existing damage							
$\|\mathbf{D}^0\|$		D_1^0		D_2^0		D_3^0	
$m_{\|D0\|}$	$s_{\|D0\|}$	m_{D1}	s_{D1}	m_{D2}	s_{D2}	m_{D3}	s_{D3}
1.0E-5	0.00	1.00	0.00	0.00	0.00	0.00	0.00

5.1.2 Results of verification

The displaced shapes in Fig. 5.3a and the distribution of the damage in Fig. 5.4a show that instead of localising in a single element, the damage is distributed into several. Also the force-displacement diagrams of Fig. 5.5 show that with mesh densities of 10, 100 and 200 elements, the force displacement paths practically coincide.

When the damage rate effect was neglected, the response was dependent on the mesh density as shown in Figs. 5.3b, 5.4b and 5.7. As shown in Fig. 5.3b, damaging and deformations localise in one element only, compared with several when the rate effect is taken into account (Fig. 5.3a).

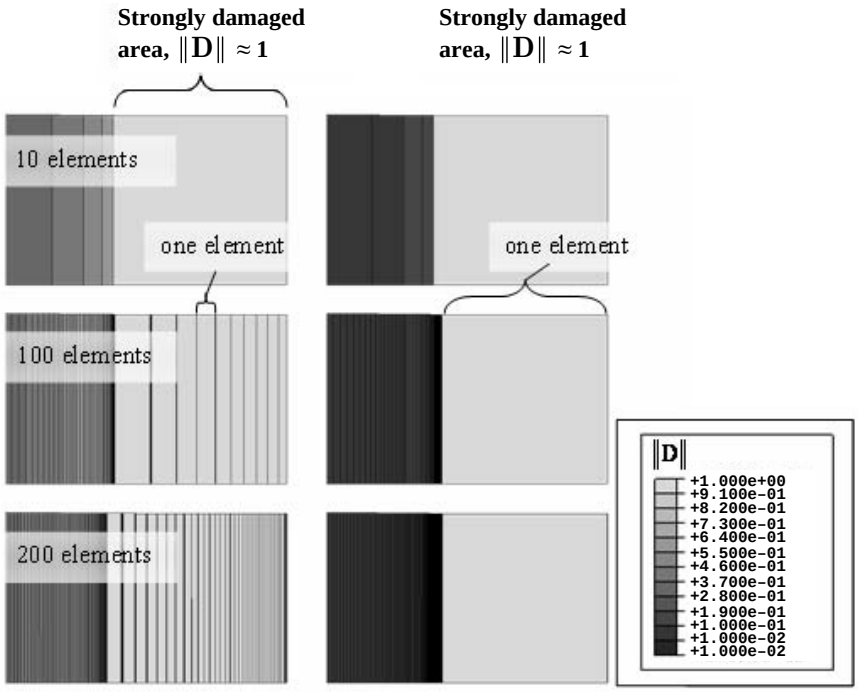

Figure 5.3. Displacement shape and damage contour plot of the damage vector length at the beam end. Displacement magnification factor = 400. Deformations localise in one element only (b) if the damage rate effect is neglected.

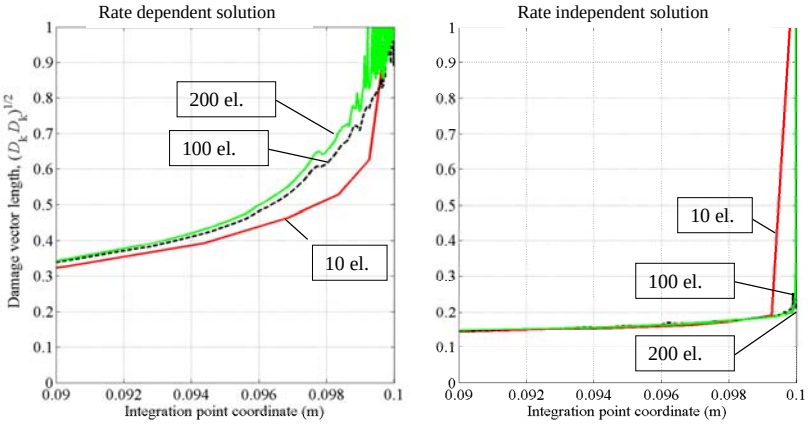

Figure 5.4. Distribution of damage $\sqrt{D_k D_k}$ along the x_1-coordinate of the bar. In the rate-independent solution (right) damage is localised in a single element only.

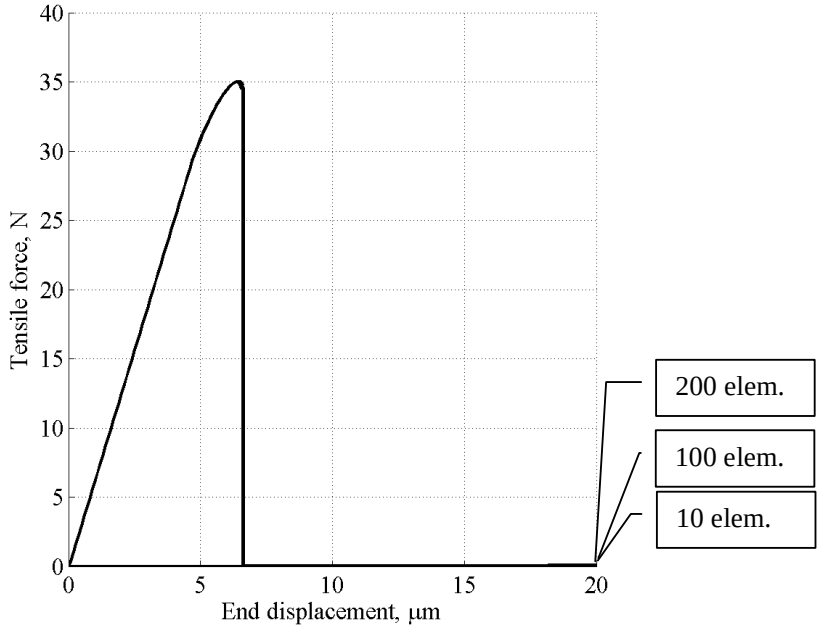

Figure 5.5. Force-displacement diagrams for loading-unloading cycle.

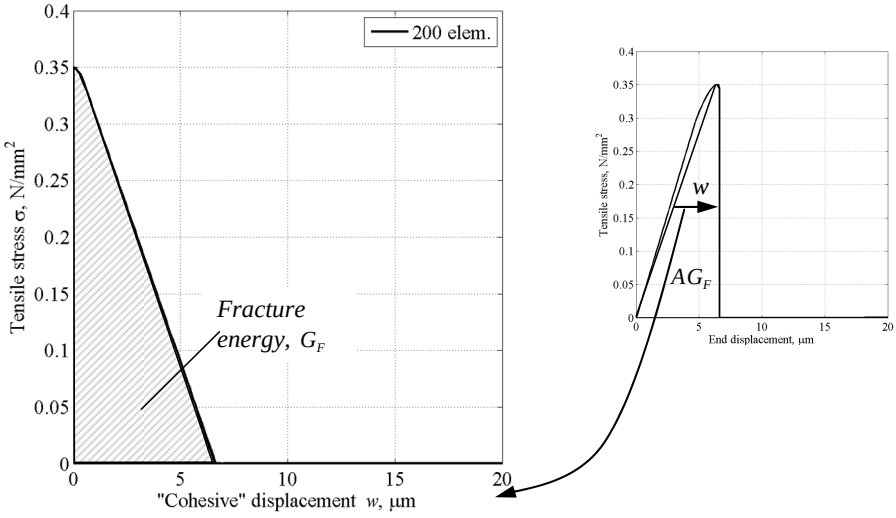

Figure 5.6. Softening curve according to the fictitious crack approach.

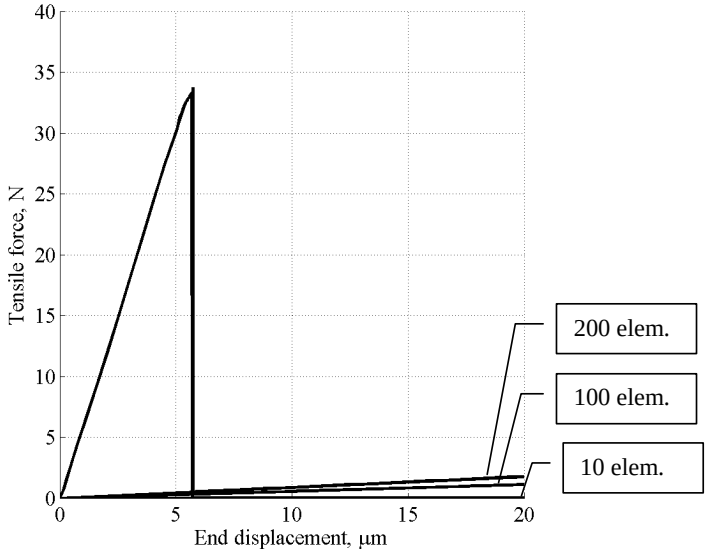

Figure 5.7. Force-displacement diagrams when the damage rate effect is neglected.

To compare the displacement response with softening diagrams of the fictitious crack approach, the softening curve was drawn as shown in Fig. 5.6 following the procedure given by Hillerborg (1983). In Hillerborg's notation the displacement *w* (Fig. 5.6) is considered as an "additional deformation due to the fracture zone." The area inside the $\sigma - w$ curve shown in Fig. 5.6 represents the energy absorbed by the fictitious crack, which is considered to equal the fracture energy G_F as briefly described in Section 3.3.1.

The absorbed energies per unit area shown in Table 5.4 were obtained as follows:

$$W_D = \frac{1}{A}\int F\,du \tag{5.1}$$

where *A* is the area of the narrow end of the bar, *F* is the tensile force and *u* is the bar end displacement. The corresponding energy in the fictitious crack approach is

$$G_F = \frac{1}{A}\int F\,dw \tag{5.2}$$

where the "additional displacement" *w* is illustrated in Figure 5.6.

Table 5.4. Energy absorbed per unit area during the loading-unloading cycle.

	Energy absorbed per area, J / m^2		
	10 elem.	100 elem.	200 elem.
With D-rate effect*, W_D	1.3174	1.3205	1.3223
With D-rate effect$^+$, G_F	1.2082	1.2312	1.2330
No D-rate effect*, W_D	0.9690	0.9656	0.9630
No D-rate effect$^+$, G_F	0.9511	0.9450	0.9391

\+ According to the fictitious crack approach (see Eq. (5.2) and Fig. 5.6)
* see Eq. (5.1)

5.2 Model verification test 2

5.2.1 Wing crack damage evolution – Clausius-Duhem inequality

In order to illustrate the behaviour of the proposed model under uniaxial compression and tension, as well as the tension-compression cycle, the cube shown in Fig. 5.8 was analysed. The example demonstrates both the response in cyclic loading and evolution of the damage, and tests the fulfilment of the Clausius-Duhem inequality when the evolution constraints of Eq. (4.55) are applied instead of Eq. (4.57). The constraints were the following:

$$D_k \dot{D}_k \geq 0 \tag{4.55}$$

$$Y_k \Omega_k \geq B \tag{4.56}$$

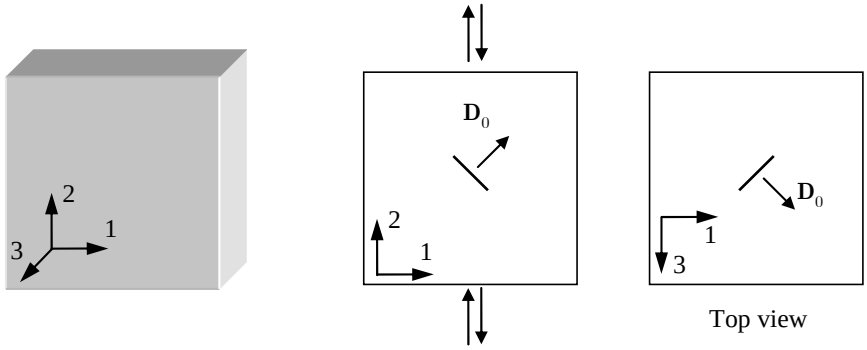

Figure 5.8. Analysed cube of 0.1x0.1x0.1 m^3 and initial damage orientation.

The cube was modelled with a single C3D8R element which has only one integration point. The hourglass stiffness was set to 90 MPa. The load was displacement controlled such that in cyclic loading the tensile displacement was 13.2 μm. After tension the cube was compressed to 75 μm (from its initial position).

The initial damage vector was inclined at 45° to the axial loading as shown in Fig. 5.8. The length of the initial damage vector was set to 0.1. The material parameters are given in Tables 5.5 and 5.6. The material is isotropic. Damage is initiated with a uniaxial tensile stress of 2.33 MPa and compressive stress of 12.12 MPa.

The value of the parameter ξ describing "transversal" damaging was set to 0.85 (see Fig. 4.11 and Sections 4.4.4.2 and 4.4.4.3). Therefore material softening takes place also in the direction transverse to the damage vector orientation.

Table 5.5. Wing crack model: elastic material properties and material orientation. Subscripts refer to the direction of material orientation axis M as shown in Fig. 3.12 and Eq. (3.13).

Material properties						Material orientation		
E_{11} (GPa)	E_{33} (GPa)	G_{13} (GPa)	ν_{21}	ν_{31}	ρ (kg)	M_1	M_2	M_3
20	20	7.69	0.20	0.20	2.5E3	1	0	0

Residual Shear				Damage evolution	
$\mu_{R,C}$ (GPa)	$\mu_{R,T}$ (GPa)	ξ	σ^{TR} (MPa)	η_1	η_2
$0.4 \cdot G_{13}$	$0.02 \cdot G_{13}$	0.85	0.1	1.0E+4	1.0E+4

Table 5.6. Wing crack model: material properties; m is the mean and s is the standard deviation.

Damage surface **F**							
R^2	a	x_0	z_0	h	n_h	c	m_c (s)
1.210E-6	1.00	7.413E-4	7.413E-4	5.0E-6	1	0.1E-6	3.5E-4

Distribution of orientation and size of pre-existing damage							
$\|\mathbf{D}^0\|$		D_1^0		D_2^0		D_3^0	
$m_{\|D0\|}$	$s_{\|D0\|}$	m_{D1}	s_{D1}	m_{D2}	s_{D2}	m_{D3}	s_{D3}
0.1	0.00	1.00	0.00	1.00	0.00	1.00	0.00

5.2.2 Results of verification

The diagrams for the compression, tension and tension-compression cycles are shown in Figs. 5.9–5.12, 5.16 and 5.17.

The Clausius-Duhem inequality (Eq. $(3.21)_2$) has the following form in the WCD approach:

$$\gamma^d = Y_k \dot{D}_k - B\dot{\kappa} \geq 0 \tag{5.3}$$

In order to test the fulfilment of the Clausius-Duhem inequality, the power of dissipation γ^d was evaluated at the integration point of the element as shown in Figs. 5.9–5.11.

Failure modes

Figs. 5.9 and 5.10 illustrate the damage evolution under pure compression and tension. The failure modes were axial splitting under compression and transverse cracking under tension.

Evolution of the splitting crack under compression is illustrated in Fig. 5.9. The stiffness is degraded during splitting crack development due to the transversal damage factor ξ.

The tension test simulation shown in Fig. 5.10 illustrates the stiffness recovery when the crack is closed after tensile damage.

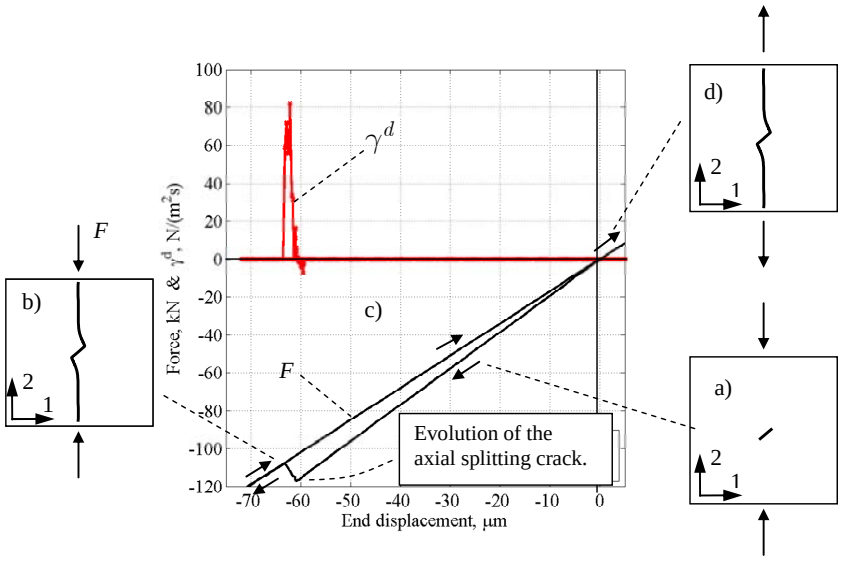

Figure 5.9. Force-displacement diagram and power of dissipation γ^d in the compression tension cycle. The letters a, b,..., d show the time sequence. The damage evolution constraint of Eq. (4.55) was applied. The Clausius-Duhem inequality equation was not fulfilled.

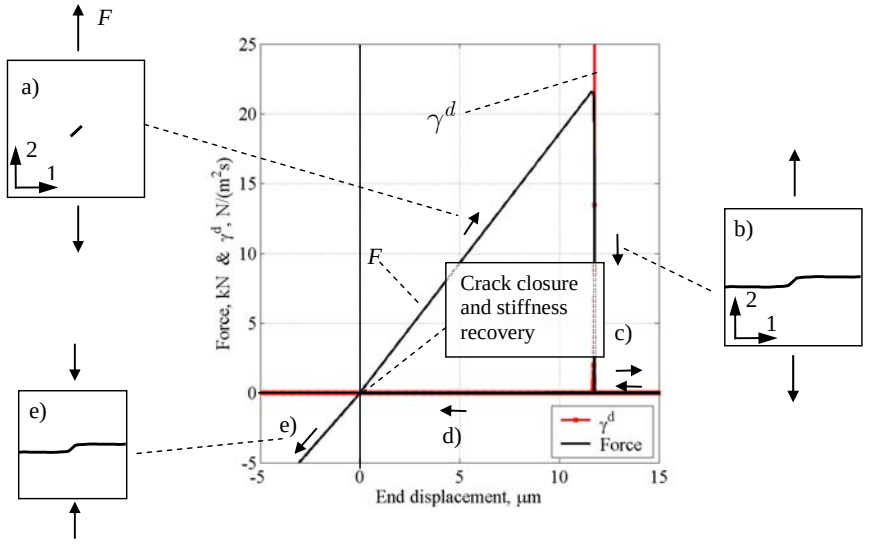

Figure 5.10. Force-displacement diagram and power of dissipation γ^d in the tension compression cycle. The damage evolution constraint of Eq. (4.55) was applied. The Clausius-Duhem inequality equation was not fulfilled.

In the cyclic loading case the tension phase was carried out such that the material was only partly damaged under tension (see Fig. 5.11b). As shown in Fig. 5.11, stiffness was recovered after the tension phase when the crack was closed due to compression. Damage also occurred during the compression phase. Although the material was being damaged during compression, there was no significant stiffness degradation in the loading direction because the developed crack was parallel to the loading direction. During damage evolution in the compression phase, the crack rotated from the transverse to the axial orientation. During rotation the stiffness was temporarily degraded (Fig. 5.11c) and then recovered (Fig. 5.11d). When the orientation approached axial orientation, the stiffness was degraded due to the transversal damage factor ξ (Fig. 5.11e).

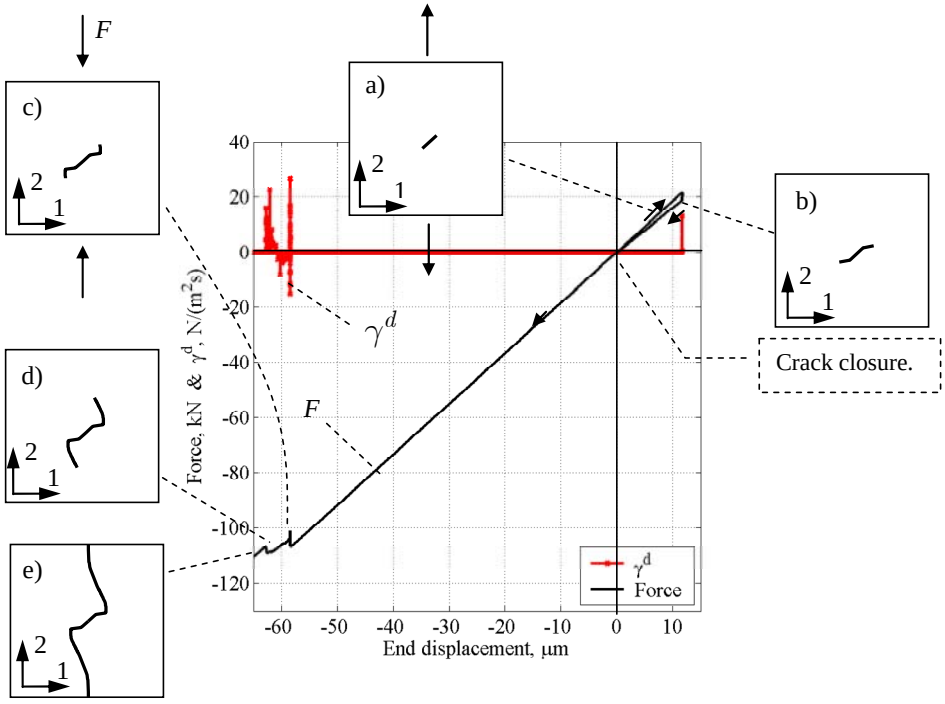

Figure 5.11. Force-displacement diagram and power of dissipation γ^d in the tension compression cycle. The letters a, b,..., e show the time sequence. The damage evolution constraint of Eq. (4.55) was applied. The Clausius-Duhem inequality equation was not fulfilled.

Clausius-Duhem inequality

In order to fulfil the Clausius-Duhem inequality of Eq. (5.3), γ^d must be positive. As shown in Figs. 5.9, 5.10 and 5.11, the inequality was not fulfilled throughout the analysis when the constraint of Eq. (4.55) was applied.

The inequality was fulfilled when the constraint of Eq. (4.57) was applied. The force displacement diagram obtained when Eq. (4.57) was applied is shown in Figs. 5.12 and 5.17.

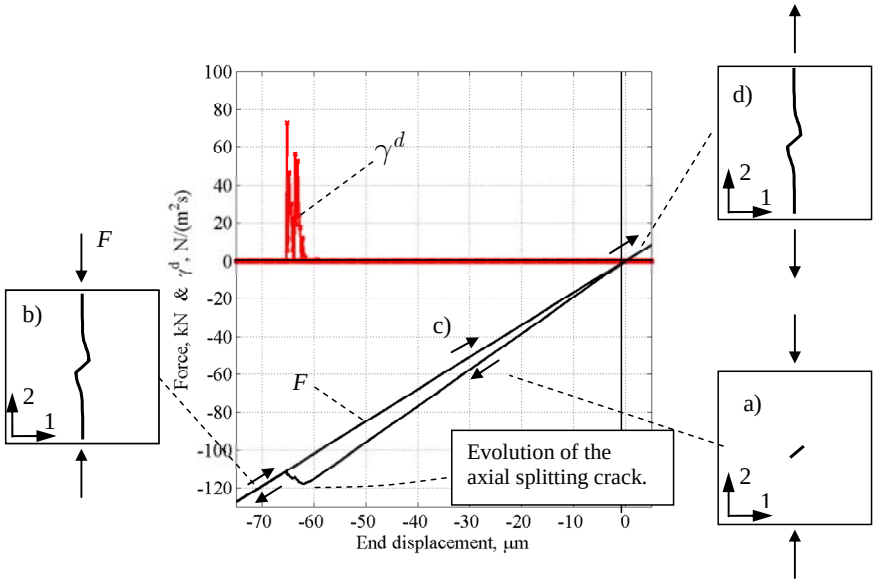

Figure 5.12. Force-displacement diagram and power of dissipation γ^d in the compression tension cycle. The letters a, b,..., d show the time sequence. The damage evolution constraint of Eq. (4.57) was applied. The Clausius-Duhem inequality equation was fulfilled.

When the damage evolution is limited by the constraint of Eq. (4.55), material stiffening due to the crack rotation may occur. The phenomenon is illustrated in Figs. 5.13 and 5.16. Assuming that the virgin material stiffness in the loading direction is E_{22}^v, the damage evolution acts as follows:

a) The pre-existing crack degrades the stiffness in the loading direction; $E_{22}^0 < E_{22}^v$

b) Due to damage development an axial splitting crack develops; therefore the representative crack rotates such that the orientation of the representative crack is parallel to the loading. Therefore the stiffness in the loading direction equals the stiffness of the virgin material, i.e. stiffness in the loading direction is recovered.

If the transversal damage is neglected ($\xi = 1$) and displacement-controlled loading is applied in the above-mentioned case, the reaction force is increased during damage development due to the stiffness recovery as shown in Figs. 5.13 and 5.16. It also means that the strain energy density is increased due to the damage evolution. Clearly the stiffness must not be recovered due to damage evolution. When stiffness recovery takes place the Clausius-Duhem inequality equation is not fulfilled, $\gamma^d < 0$.

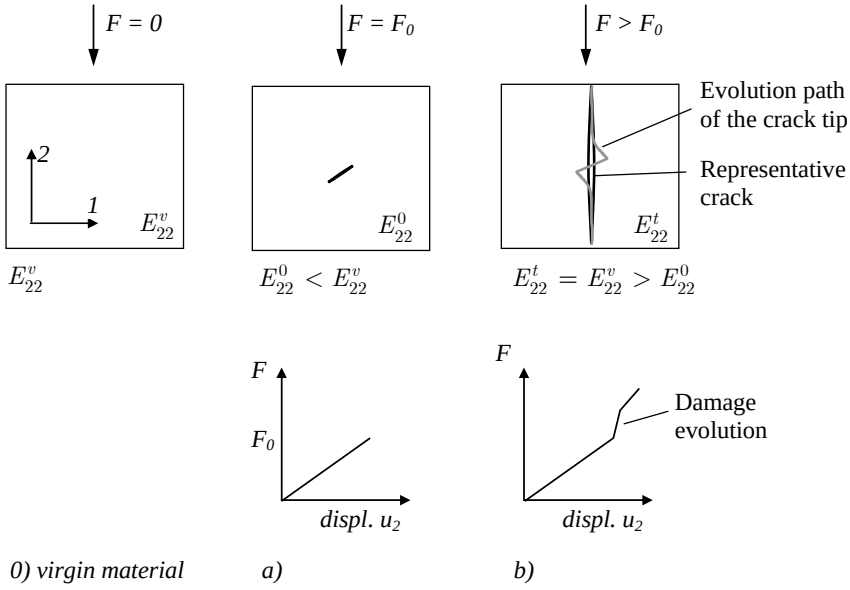

Figure 5.13. Stiffness recovery due to damage development when the damage evolution constraint of Eq. (4.55) is applied. The transversal damage effect is neglected ($\xi = 1$).

Damage evolution and rotation of the representative crack under the constraint of Eq. (4.57) is illustrated in Figs. 5.14 and 5.17. When the constraint of Eq. (4.57) is used, the stiffness recovery does not take place and the Clausius-Duhem inequality is fulfilled $\gamma^d \geq 0$.

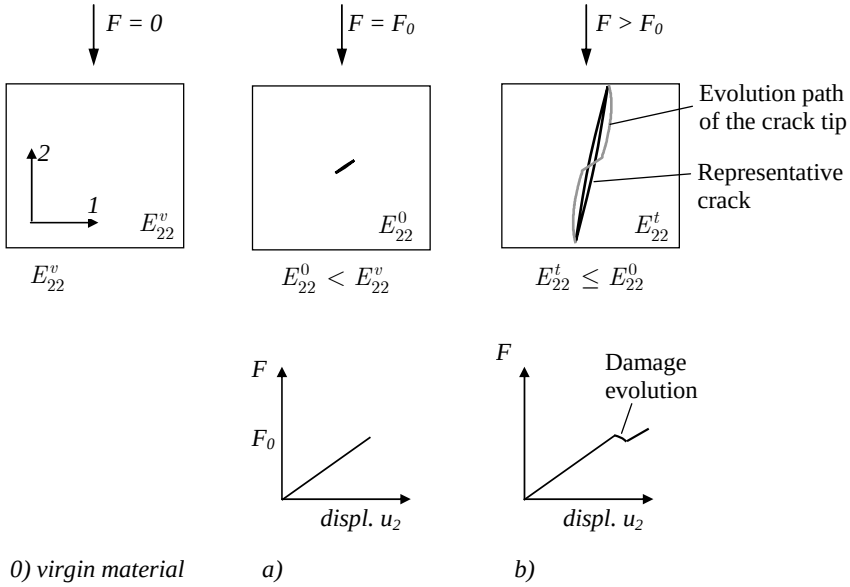

Figure 5.14. Damage development when the damage evolution constraint of Eq. (4.57) is applied. The transversal damage effect is neglected ($\xi = 1$).

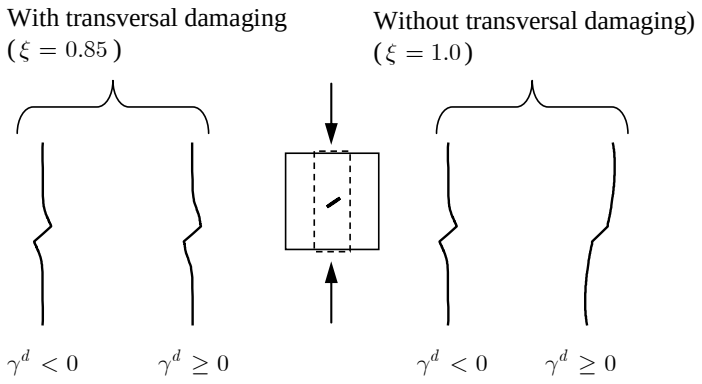

Figure 5.15. Damage evolution paths under uniaxial compression; $\gamma^d \geq 0$ when constraint of Eq. (4.57) is applied. $\gamma^d < 0$ when the constraint of Eq. (4.55) is applied.

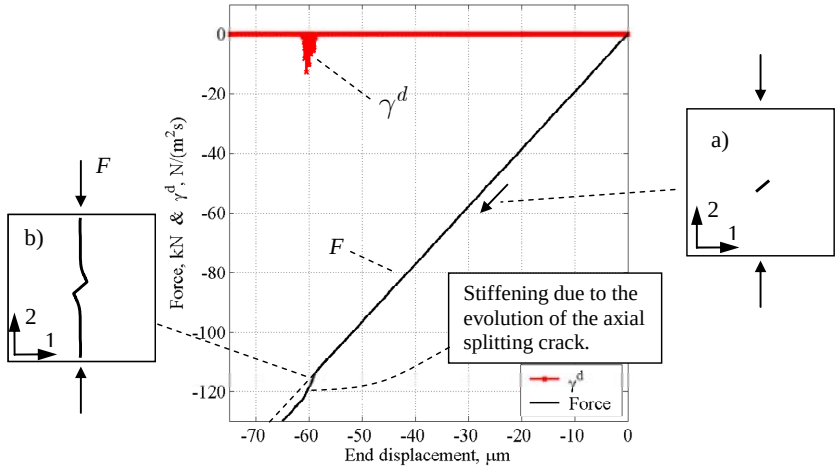

Figure 5.16. Force-displacement diagram and power of dissipation γ^d under uniaxial compression when the transversal damage effect is neglected ($\xi = 1$). The damage evolution constraint of Eq. (4.55) was applied. The Clausius-Duhem inequality equation was not fulfilled.

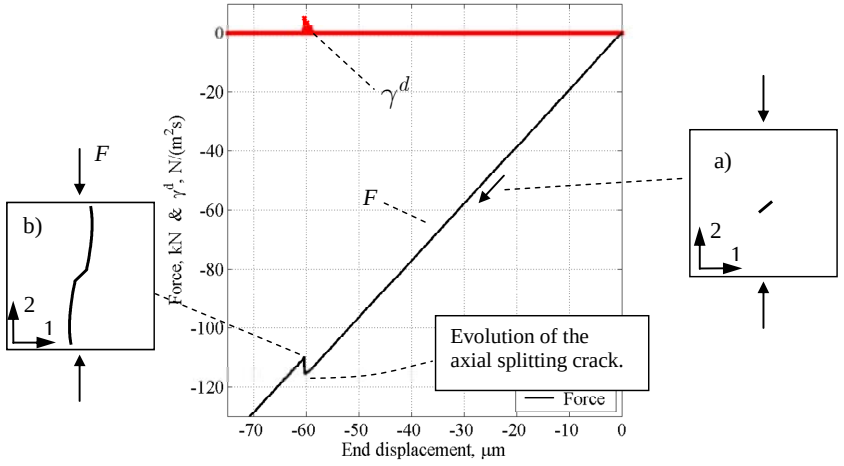

Figure 5.17. Force-displacement diagram and power of dissipation γ^d under uniaxial compression when the transversal damage effect is neglected ($\xi = 1$). The damage evolution constraint of Eq. (4.57) was applied. The Clausius-Duhem inequality equation was fulfilled.

5.3 Model verification test 3

5.3.1 Saline columnar ice

5.3.1.1 Ice material properties

Because of its anisotropic nature, columnar ice properties are different in the horizontal and vertical directions. If the c-axes are randomly oriented in the horizontal direction, the ice can be considered transversely isotropic. Therefore five independent parameters are needed to model its elastic response. Although ice strength has been measured and studied quite extensively, the elastic material properties of columnar ice have not been widely examined. Numerical values of Young's modules in both the vertical (E_v) and horizontal (E_h) direction are available in the literature, but Poisson's ratios and shear modulus (*G*) have not received much attention in ice studies.

When the c-axes are oriented, the ratio E_v / E_h is 1.23 (Michel, 1978; Sinha, 1989). Theoretical elastic properties based on single crystal characteristics deviate from the properties of polycrystalline columnar ice (S2) based on laboratory tests. Theoretically, Young modulus for S2 ice in the vertical direction is only a few percent higher than in the horizontal plane (Michel, 1978; Sinha, 1989). The value of *E* has been found to vary significantly with porosity (Cox and Weeks, 1983; Mellor, 1983; Takekuma et al., 1983; Cole, 1998). Andersson (1958) demonstrated experimentally a decrease in *E* with increasing porosity (Cox and Weeks, 1983).

Measured values of *E* depend on the test method used. Because of the viscoelastic behaviour of ice, there is more variation in static measurements than in high frequency vibrational methods (Cox and Weeks, 1983; Mellor, 1983).

Häusler (1981) obtained a value of 15.1 ±2.9 GPa in the vertical direction, which is significantly higher than the theoretical value for E_v reported by Michel (1978). The experimental and theoretical results shown in Table 5.7 indicate that in nature the ratio between the vertical and horizontal Young's modulus is higher than the theoretical value proposed by Michel (1978).

Table 5.7. Elastic properties of columnar polycrystalline ice.

Author	**Eh, GPa**	**Ev, GPa**	**Strain rate 1/s**	**T, °C**	**Type, (salinity, ‰)**	**Notes**
(Michel, 1978)	9.40	9.72		-10	S2, Theoretical, based on single crystal	
(Häusler, 1981)	4.56 ±1.94	15.1 ±2.9	0.2	-10	Saline, (10.6), columnar	Lab ice
(Takekuma et al., 1983)	~0.9	~2.5	0.036...90	-4..-20	Saline, columnar	Sea ice
(Varsta, 1983)	7.28	10.16	0.25	-6	Saline, columnar	Sea ice
(Kuehn et al., 1988)	6.0	8.5	1.0	-10	Saline, columnar (4.3)	Lab ice, Tension
(Kuehn et al., 1988)	-	8.0	1.0	-10	Saline, columnar (4.3)	Sea ice, Tension
(Sinha, 1988)	4.0	-	0.0001	-20	Fresh water	Lab ice
(Sinha, 1988)	9.5	-	10.0	-20	Fresh water	Lab ice

5.3.1.2 Ice failure mechanisms

The brittle failure of columnar ice cubes was studied under uni- and biaxial compression. As described in the previous section, columnar ice is transversely isotropic. Its behaviour depends on the temperature, orientation and strain rate.

Although all material parameters were not available, this example illustrates the wing crack model capability to capture the brittle failure modes under compression and tension.

According to Schulson (2001), the dominant brittle failure mechanism under axial compression is axial splitting. The split angle depends on the orientation of the sample and the stress state. The mechanisms are illustrated in Fig 5.18. The tensile failure mechanism is tensile cracking perpendicular to the loading direction (Schulson, 1987; Kuehn et al., 1988).

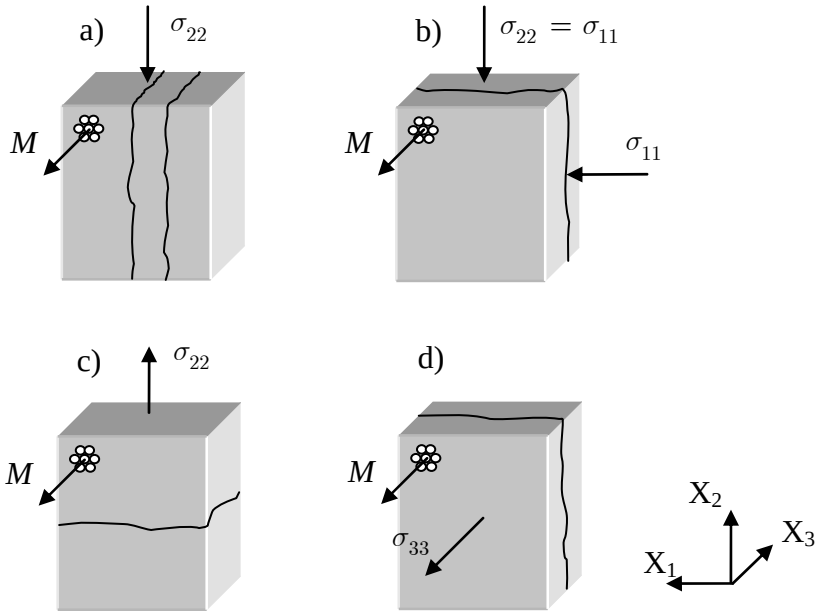

Figure 5.18. Compressive and tensile failure mechanisms (a–c redrawn from Schulson (2001)).

Based on the tests of Gratz and Schulson (1997) the uniaxial compressive strength along the columns was assumed to be 6.0 MPa, and 3.0 MPa across the columns.

Kuehn et al. (1988) obtained a tensile strength of 1.1 MPa along the column direction and 0.35 MPa in the direction perpendicular the columns. The Young modulus along the columns was 8.5 GPa and 6.0 GPa across the column direction (Kuehn et al., 1988). The shear modulus G_{23} and the Poisson ratios ν_{12}, ν_{31} were obtained from the equations given by Derradji-Aouat et al. (2000). Thus the material properties in the coordinate system shown in Fig. 5.18 are:

$$
\begin{aligned}
E_{11} &= 6.0 \text{ GPa} & \sigma_{33c} &= 6.0 \text{ MPa} \\
E_{33} &= 8.5 \text{ GPa} & \sigma_{33t} &= 1.1 \text{ MPa} \\
G_{23} &= 3.2 \text{ GPa} & \sigma_{11c} &= 3.0 \text{ MPa} \\
\nu_{12} &= 0.313 & \sigma_{11t} &= 0.35 \text{ MPa} \\
\nu_{31} &= 0.301 & \rho_{ice} &= 915 \text{ kg/m}^3
\end{aligned}
\tag{5.4}
$$

where σ_{11c} and σ_{33c} are compressive strengths in direction 1 and 3 respectively, and σ_{11t} and σ_{33t} are the tensile strengths.

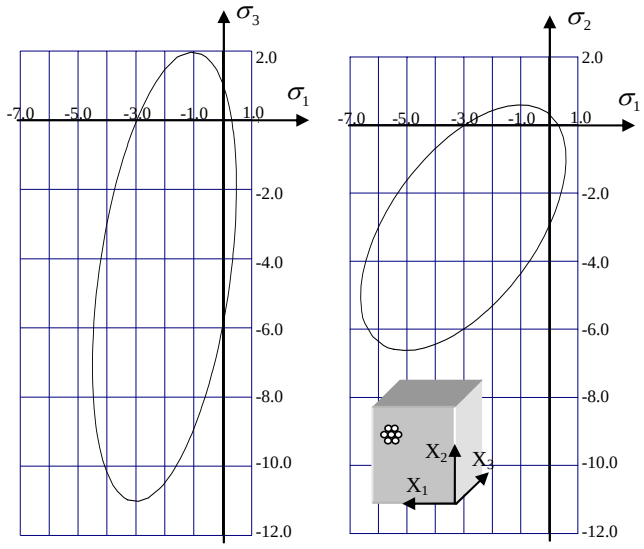

Figure 5.19. Damage surface in plane stress space; units: MPa.

The material parameters were defined as described in Section 4.5.5. The parameters are the same as in example 5.1, except for the size and orientation of initial damage which are as shown in Table 5.8. The damage surface is shown in Fig. 5.19. To study the effect of initial damage size on the ultimate stress, analysis was carried out also using smaller damage, as shown in Table 5.9.

Brine pockets are formed during freezing when salt water is trapped in sea ice. “The entrapped brine occurs in the form of fine pockets of fluid between platelets of pure ice...” (Sanderson, 1988, p. 13). Although the real shape of brine pockets is not known, the pockets were considered to be oriented microcracks, as done by (Zhan et al., 1996).

The shape and orientation of brine pockets was assumed to be such that the normal of the crack surface is perpendicular to the columns. Therefore the initial damage vector components were assumed to be distributed such that major components were in the transversal plane ($X_1 - X_2$) and minor components were parallel to the columns. The average length of the initial damage vector

was set to 0.05 and the standard deviation to 0.01. The vector length is not based on measured values.

Table 5.8. Orientation of initial damage; m is the mean and s is the standard deviation.

Distribution of orientation and size of pre-existing damage							
$\|\mathbf{D}^0\|$		D_1^0		D_2^0		D_3^0	
$m_{\|D0\|}$	$s_{\|D0\|}$	m_{D1}	s_{D1}	m_{D2}	s_{D2}	m_{D3}	s_{D3}
0.05	0.01	0.0	1.0	0.00	1.0	0.00	0.1

Table 5.9. Orientation of initial (small) damage; m is the mean and s is the standard deviation.

Distribution of orientation and size of pre-existing damage							
$\|\mathbf{D}^0\|$		D_1^0		D_2^0		D_3^0	
$m_{\|D0\|}$	$s_{\|D0\|}$	m_{D1}	s_{D1}	m_{D2}	s_{D2}	m_{D3}	s_{D3}
1.0E-5	1.0E-5	0.0	1.0	0.00	1.0	0.00	0.1

5.3.1.3 Model of an ice cube

The side length of the cubic sample was the same as used by Gratz and Schulson (1994): 159 mm. The number of linear brick elements (C3D8R) in the model was 1872. The cube was loaded through perfectly stiff frictionless plates using the contact feature of ABAQUS/Standard FE software. In the biaxial loading case the load was pressure-controlled. The stress ratio $\sigma_{22} / \sigma_{11} = 1$ was kept constant during loading. The stress rate of σ_{22} was set to 2.0 MPa/s.

Under tension, the displacements of the bottom face nodes in direction 2 were restrained, while the topmost nodes were displacement rate-controlled. The

loading rate with displacement-controlled loading was set to 10^{-3} m/s in both compression and tension loading cases.

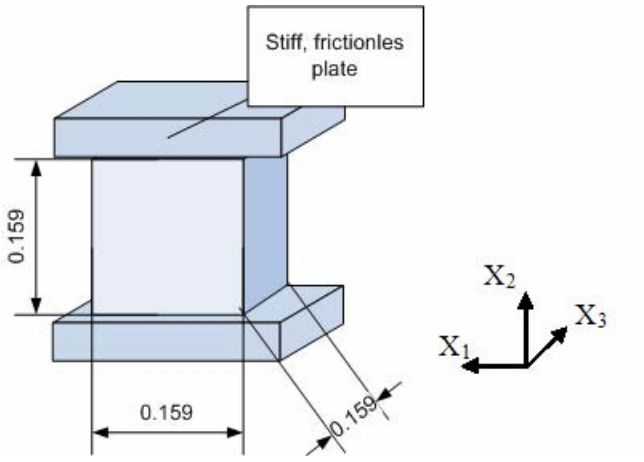

Figure 5.20. FE model dimensions under axial compression.

5.3.2 Results of verification

The ultimate stresses obtained from numerical simulations are given in Table 5.10. As described in the upcoming sections, the failure modes were the same as illustrated in Fig. 5.18.

The definition of failure stress is not clear when the failure mode is splitting, because splitting does not reduce stiffness in the loading direction. Therefore, the value of ultimate compressive stress is the stress value (see Fig. 5.24) obtained when the average length of the damage vector equals ~1.0.

Table 5.10. Ultimate stresses obtained in numerical simulation, MPa.

	σ_{11c}	σ_{11t}	σ_{33t}	$\sigma_{11} = \sigma_{22}$
Test	3.0	0.35	1.1	-
FEM, ($\|\mathbf{D}^0\|$, Table 5.8)	3.25*	0.30	1.03	6.16*
FEM, (small $\|\mathbf{D}^0\|$, Table 5.9)	3.29*	0.35	1.05	6.20*

* Obtained when average length of the damage vector = 1.0

As described in Section 5.1 (see also Section 4.5.5.4), material parameters were adjusted such that the tensile strength σ_{11t} equals 0.35 MPa during tension of the tapered bar shown in Fig. 5.1 when the strain rate $\dot{\varepsilon} = 10^{-3} / s$. The strength in the column direction (σ_{33}) is therefore affected by parameters based on σ_{11t}. This explains the lower value of σ_{33t} shown in Table 5.10. The ultimate tensile stress for σ_{11t} equals 0.35 MPa when the initial damage is small.

The results shown in Table 5.10 illustrate the effect of initial damage size on ultimate stress.

5.3.2.1 Tensile test simulations

The tensile failure modes obtained in numerical simulations were similar to the modes obtained in tests as illustrated in Figs. 5.18. As shown in Figs. 5.21–5.23, the failure mode was cracking perpendicular to loading.

Damage vector evolution as a function of displacement is illustrated in Figs. 5.22 and 5.23. As shown in Fig. 5.22, the direction of damage vector evolution is correct despite the unfavourable initial direction.

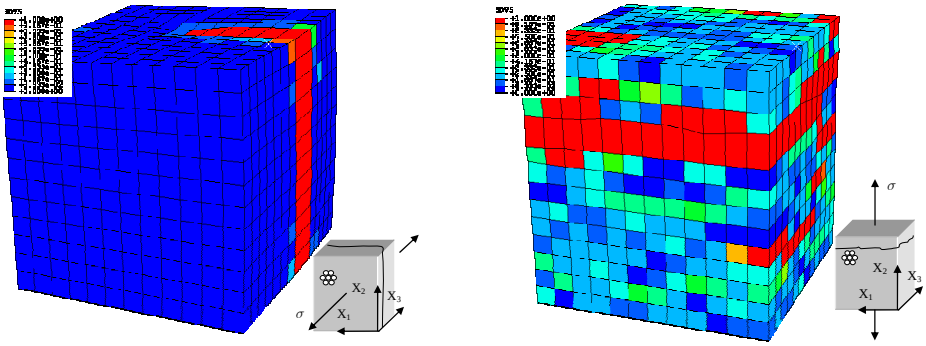

Figure 5.21. Contour plot of the length of the damage vector under tension along (left) and across (right) the columns.

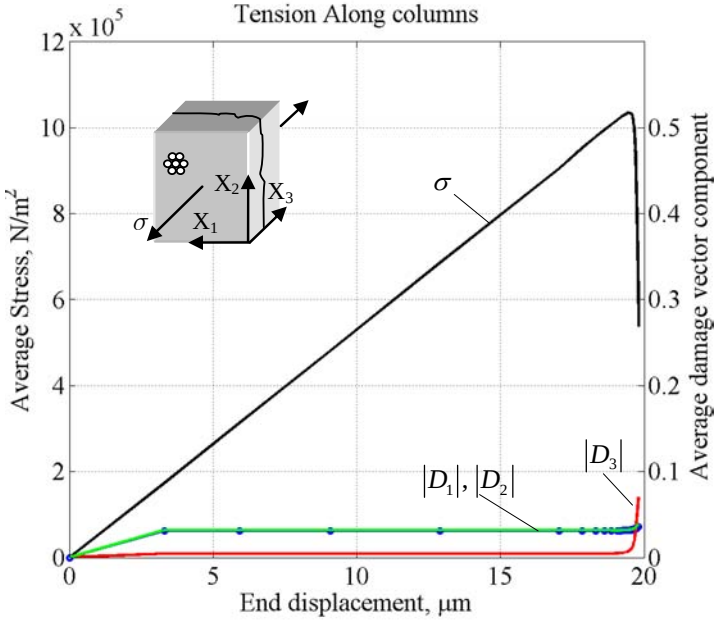

Figure 5.22. Evolution of damage vector components and average stress.

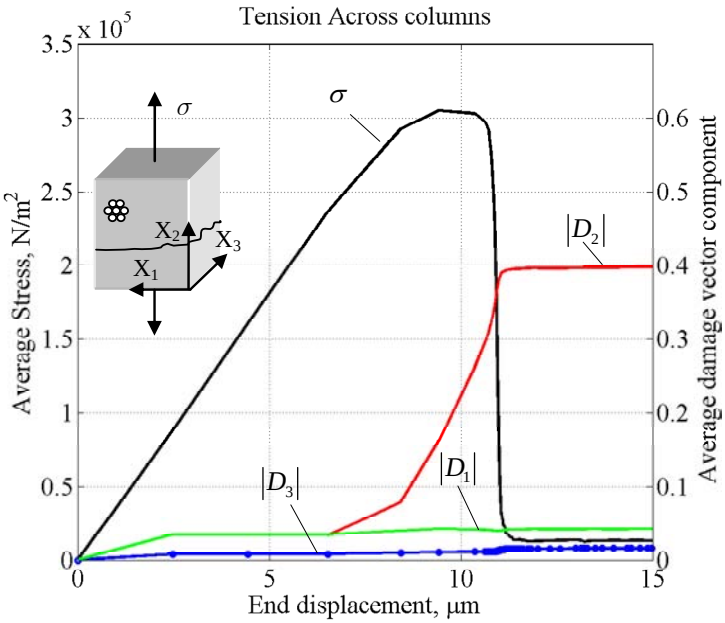

Figure 5.23. Evolution of damage vector components and average stress.

5.3.2.2 Compression test simulations

Although the direction of damage evolution is correct in compression test simulations as shown in Figs. 5.24 and 5.25, the failure mode is not as visual as in the tensile test simulations (see Fig. 5.26). Damage vector orientations at the end of the analyses correspond to the splitting failure mode.

As shown in Figs. 5.24 and 5.25, there is no drop in the average stress curve although the damage is fully developed. The drop does not take place because the splitting crack (parallel to the loading) does not reduce the stiffness in the loading direction. Therefore the load can be increased beyond the point where the damage is fully developed.

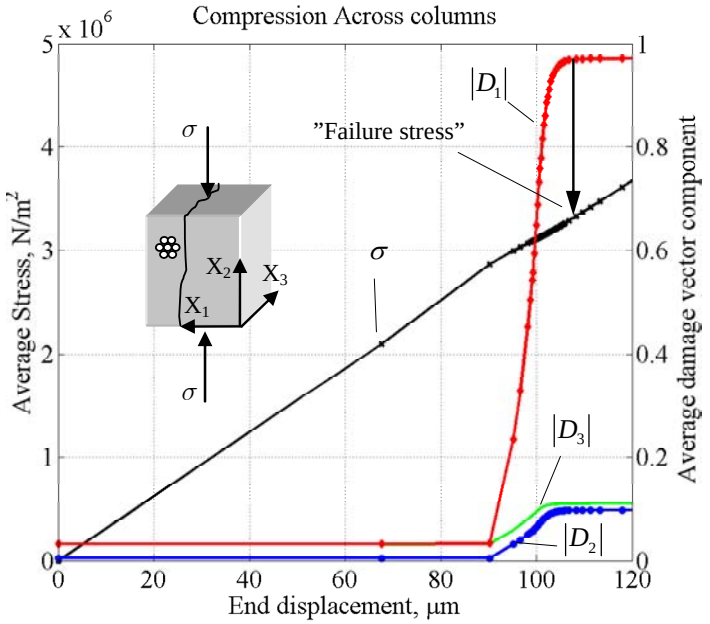

Figure 5.24. Evolution of damage vector components and average stress under compression across columns.

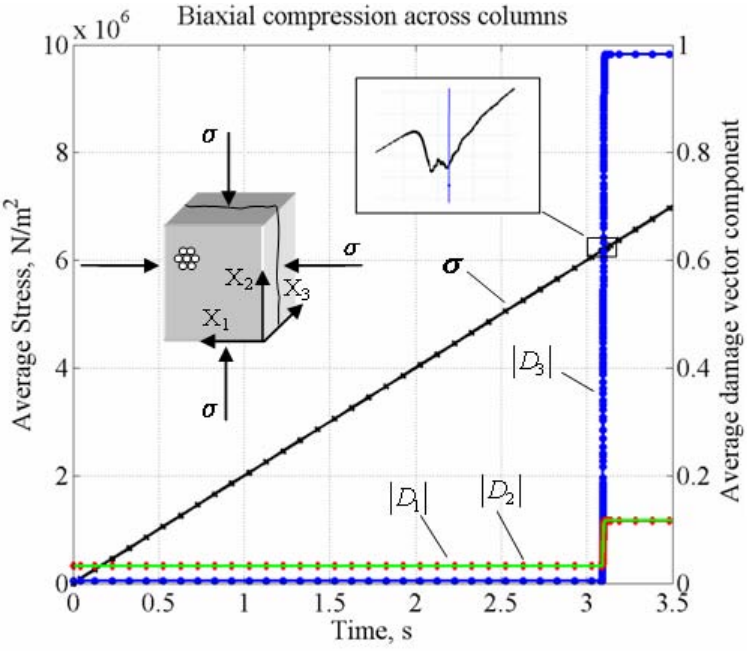

Figure 5.25. Evolution of damage vector components and average stress.

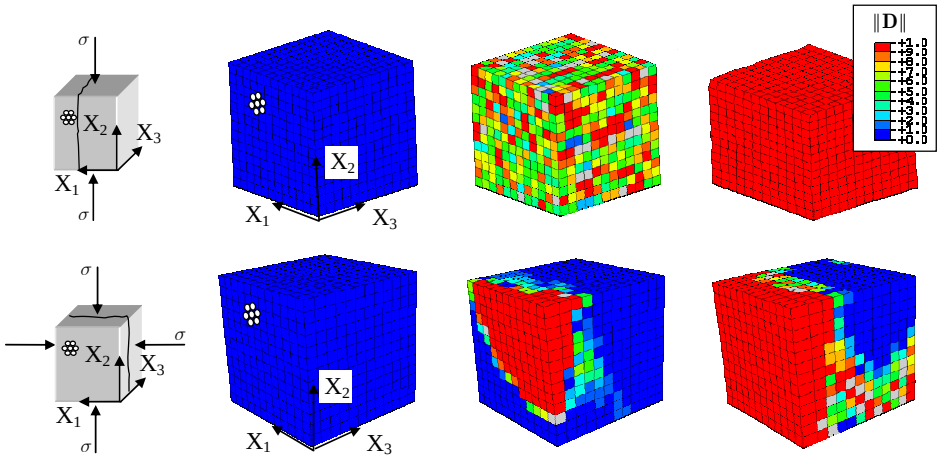

Figure 5.26. Contour plot of evolution of length of damage vector under compression across the columns (above) and under confined compression (below).

5.4 Model verification test 4

5.4.1 Hualien marble – the ring test simulation

Many rocks are anisotropic and brittle. This example illustrates the usefulness of the proposed wing crack method in the analysis of transversely isotropic marble. Numerical results are compared with the experimental results obtained from Chen and Hsu (2001).

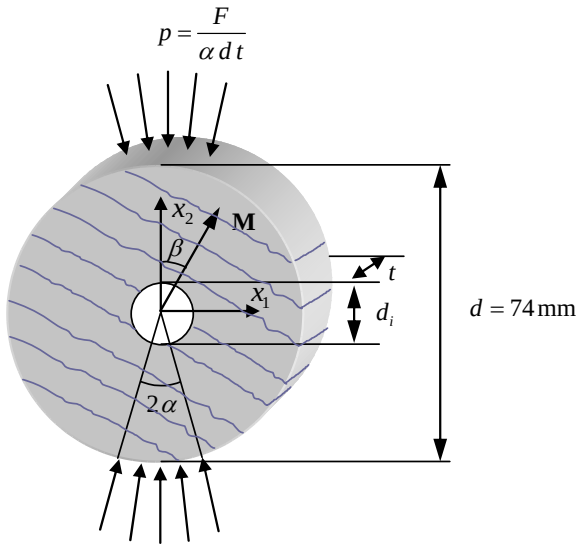

Figure 5.27. Geometry of the ring split test by Chen and Hsu (2001). The vector **M** *represents the material symmetry axis orientation. Disk thickness t = 11.55 mm.*

The objective of the numerical examples was to:

1. Compare failure modes based on FE analysis with the experimental modes given by Chen and Hsu (2001).
2. Compare the numerical and experimental failure loads as a function of material symmetry axis orientation.

5.4.1.1 Experimental tests and results

The objective of the ring tests of Chen and Hsu (2001) was to obtain the tensile strength as a function of the material symmetry axis angle with respect to the loading direction. Although the external load is compression, the ring test itself can be considered an indirect tensile test.

The dimensions and elastic material properties of the disk shown in Fig. 5.27 are given in Table 5.11. The material properties are expressed in the material coordinate system shown in Fig. 5.28. The thickness t in Table 5.11 is the average thickness of all ring tests.

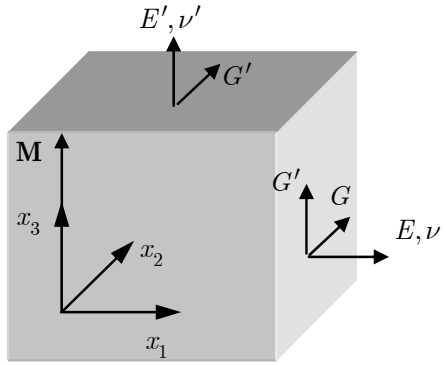

Figure 5.28. Coordinate system used in material property definition. Vector $\mathbf{M}$ *represents the material symmetry axis orientation. (*$E_{11} = E,\ \ E_{33} = E',\ G_{23} = G',\ \nu_{12} = \nu,\ \nu_{31} = \nu'$*, see Eq. (3.14)). The prime refers to the notation of Chen and Hsu (2001).*

Table 5.11. Geometrical and elastic material properties in the ring tests (Chen and Hsu, 2001).

d (mm)	d_i (mm)	t * (mm)	E_{11} (GPa)	E_{33} (GPa)	G_{23} (GPa)	ν_{12}	ν_{31}	ρ (kg)
74.0	16.4 12.8 4.8	11.55	78.3	67.68	25.34	0.267	0.185	1691

* Average thickness of test specimens

Chen and Hsu (2001) studied the behaviour of Hualien marble both experimentally and using the Boundary Element Method (BEM). The marble has a visible black-and-white foliated structure, based on which Chen and Hsu assumed it to be transversely isotropic. They carried out a total of 42 tests with three hole diameters and seven material inclination angles. The failure mode was splitting along the loading line.

Chen and Hsu (2001) used BEM to determine the relation between the compressive force *F* and tensile strength σ_t. They also used it to determine the stress distribution around the central hole. Then they assumed that disk rupture takes place when the maximum tensile stress is attained at the intersection of the

loading line and the hole as shown in Fig. 5.35. Based on these assumptions and the test results shown in Table 5.12 and Fig. 5.29, they obtained the tensile strength values given in Fig. 5.30. From their analysis they concluded that "*...the tensile strength of Hualien marble decreases with the increase in the hole diameter...*"(ibid).

Table 5.12. Average ultimate compressive force F obtained experimentally by Chen and Hsu (2001).

β (degree)	F (kN) (d_i = 4.8)	F (kN) (d_i = 12.8)	F (kN) (d_i = 16.4)
0	11.00	6.79	6.13
15	10.33	6.65	5.90
30	8.49	6.59	5.21
45	7.28	5.04	4.20
60	5.19	3.60	3.14
75	4.28	3.36	2.88
90	3.88	2.67	2.73

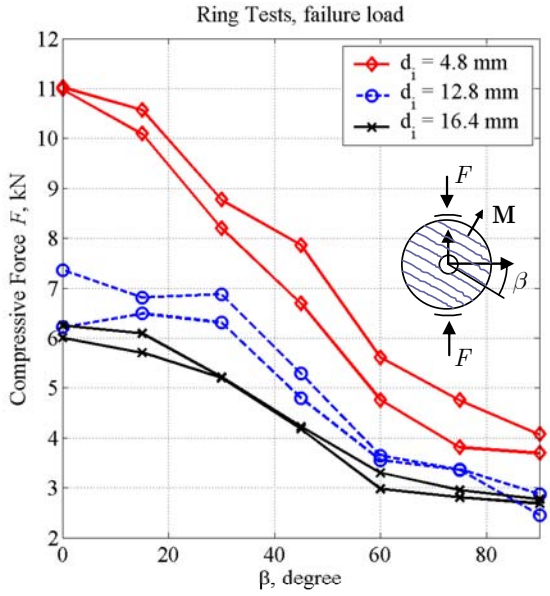

Figure 5.29. Experimental compressive force F by Chen and Hsu (2001).

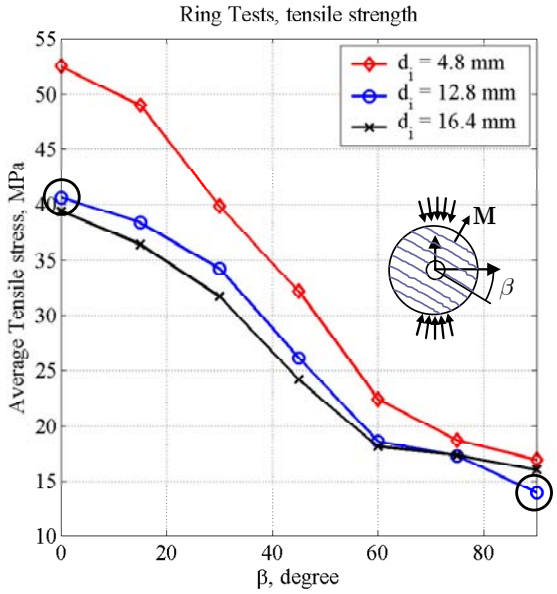

Figure 5.30. Tensile strength obtained from tests with BEM by Chen and Hsu (2001). The circled tensile strength values were used to determine the damage surface for FE analysis.

5.4.1.2 FE simulation of Hualien marble and its tests

Although Chen and Hsu (2001) concluded that tensile strength is a function of the hole diameter, in this study the tensile strength was assumed to be independent of the specimen geometry. The damage surface was determined based on the tensile strengths obtained from tests with a hole diameter of 12.8mm (see Fig. 5.30), when the material inclination angle is 0º and 90º. The compressive ($\sigma_{c,ij}$) and tensile ($\sigma_{t,ij}$) strengths used in damage surface determination are given in Table 5.13. The subscripts *i* and *j* refer to the coordinates of the material orientation axis shown in Fig. 5.28.

Table 5.13. Compressive and tensile strength based on marble tests (Chen and Hsu, 2001).

$\sigma_{c,11}$ [¶] (MPa)	$\sigma_{c,33}$ [¶] (MPa)	$\sigma_{t,11}$ [†] (MPa)	$\sigma_{t,33}$ [‡] (MPa)
22.93	76.43	40.61	13.94

[¶] Given by Chen and Hsu (2001)
[†] Average of ring tests when β = 0° and d_i = 12.8mm (see Fig 5.31)
[‡] Average of ring tests when β = 90° and d_i = 12.8mm (see Fig 5.31)

Because the damage evolution parameters were not known, the material parameters were obtained following the procedure described in Section 4.5.5:

- Damage initiation stress $0.8 \cdot \sigma_{t,33} = 11.2$ MPa
- Static tensile strength $0.95 \cdot \sigma_{t,33} = 13.2$ MPa
- Tensile strength $\sigma_{t,33} = 13.9$ MPa when strain rate $\dot{\varepsilon} = 10^{-3} / s$

The material parameters are shown in Table 5.16 and the damage initiation stresses in Table 5.15.

Due to the foliated structure of the material, flaws were assumed to be parallel to the layers, i.e. the pre-existing damage vector $\mathbf{D}_0$ was assumed to be nearly parallel to the material orientation vector $\mathbf{M}$ as illustrated in Fig. 5.31. A small deviation in the orientation of the pre-existing damage vector was assumed as follows:

$$\frac{s_{D\perp M}}{m_{D\parallel M}} = 0.1 \tag{5.5}$$

where $s_{D\perp M}$ is the standard deviation of the damage vector component that is perpendicular to vector $\mathbf{M}$ ($\mathbf{D}_{0\perp\mathbf{M}}$ in Fig. 5.31); $m_{D\parallel M}$ is the mean of the damage vector component that is parallel to $\mathbf{M}$ ($\mathbf{D}_{0\parallel\mathbf{M}}$ in Fig. 5.31). $\mathbf{D}_{0\perp\mathbf{M}}$ was assumed to be normally distributed with a mean of 0. The effect of two different pre-existing damage sizes shown in Table 5.14 was studied.

Table 5.14. Mean $m_{\|D0\|}$ and standard deviation $s_{\|D0\|}$ for the pre-existing damage vector length ($\|\mathbf{D}_0\|$) distribution.

Case	$m_{\|D0\|}$	$s_{\|D0\|}$
a	0.01	0.001
b	0.075	0.005

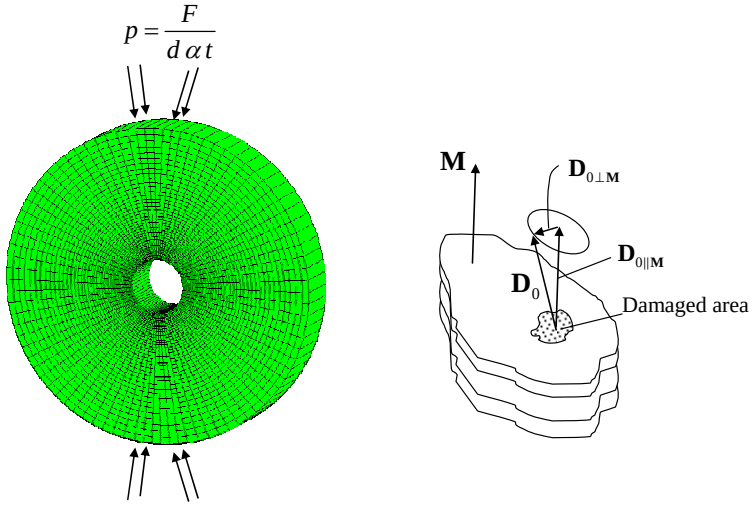

Figure 5.31. a) FE model of marble ring, b) foliated structure and orientation of pre-existing damage.

The samples were modelled using linear brick elements (C3D8). The FE model is shown in Fig. 5.31. According to Chen et al. (1998), the contact angle α in the tests (see Fig. 5.27) was always less than 15°. The value of 10° was used for α in the FE simulation. The pressure loading rate was set to 1 MPa/150 s.

*Table 5.15. Tensile (σ_t) and compressive (σ_c) stresses along and transverse to the direction **M**.*

Ultimate stress			
Direction **M**		Transverse direction	
σ_t (MPa)	σ_c (MPa)	σ_t (MPa)	σ_c (MPa)
13.94	76.43	40.61	22.93
Damage initiation stress			
Direction **M**		Transverse direction	
σ_t (MPa)	σ_c (MPa)	σ_t (MPa)	σ_c (MPa)
11.2	73.6	37.8	20.1

Table 5.16. Material properties of Hualien marble; m is the mean and s is the standard deviation.

Damage surface **F**							
R^2	a	x_0	z_0	h	n_h	c	m_c (s)
3.00E-7	0.834	7.495E-5	3.898E-4	6.5E-4	1	$0.05\,R$	6.5E-2

Table 5.17. Elastic material properties of Hualien marble. Subscripts refer to the direction of the material orientation axis M (see Fig. 5.28 and Eq. (3.13)).

Elastic material properties						Material orientation		
E_{11} (GPa)	E_{33} (GPa)	G_{13} (GPa)	ν_{21}	ν_{31}	ρ (kg)	M_1	M_2	M_3
78.3	67.68	25.34	0.267	0.185	1691	$\mathrm{Cos}\,\beta$	$\mathrm{Sin}\,\beta$	0
Residual Shear						Damage evolution		
$\mu_{R,C}$ (GPa)		$\mu_{R,T}$ (GPa)	ξ	σ^{TR} (MPa)		η_1	η_2	
$0.4\cdot(G_{13}+G_{21})$		$0.02\cdot(G_{13}+G_{21})$	1.0	0.1		1.0E+4	1.0E+4	

5.4.2 Results of verification

A total of 42 FE analyses were done. Each of the three rings was analysed with seven material orientation angles using two different pre-existing damage distributions (see Table 5.14). In addition, the effect of the sampling variation on the failure load was studied when the hole diameter d_i was 12.8mm.

As shown in Figs. 5.32 and 5.33, failure loads obtained by numerical simulation coincide well with the experimental results. The correspondence between numerical and experimental results is best when the material orientation angle β is 90º. The failure mode was splitting in all analysed specimens.

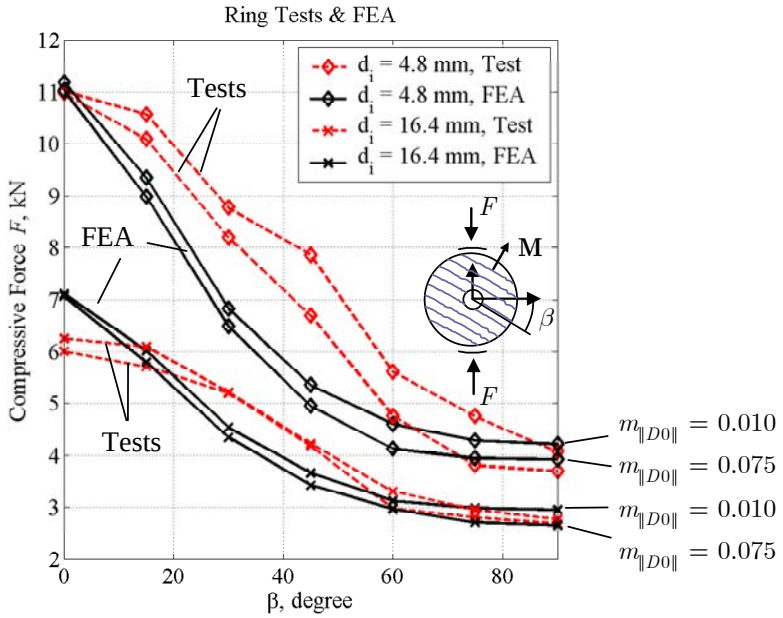

Figure 5.32. Comparison of test and FE analysis results with different mean lengths of the pre-existing crack.

As discussed in the previous section, Chen and Hsu (2001) concluded that tensile strength is a function of the hole diameter. Although numerical simulation was based on strength values obtained from ring tests with an inner diameter of 12.8mm, the proposed *wing crack* approach was able to predict quite accurate failure loads for rings with hole diameters of 4.8mm and 16.4mm also.

The difference between numerical simulation and test results was greatest when material orientation axis $\mathbf{M}$ was inclined at 45º to the loading direction.

The damage surface used in this work (see Section 4.5.3) is based on uniaxial tensile and compressive strengths obtained when the load is parallel ($\beta = 0$) and perpendicular ($\beta = 90°$) to the material orientation axis $\mathbf{M}$. Therefore, it is obvious that the proposed method cannot predict the correct failure load when the material orientation axis is inclined to the loading. A more detailed failure surface can be derived to obtain more accurate results when $0 < \beta < 90°$.

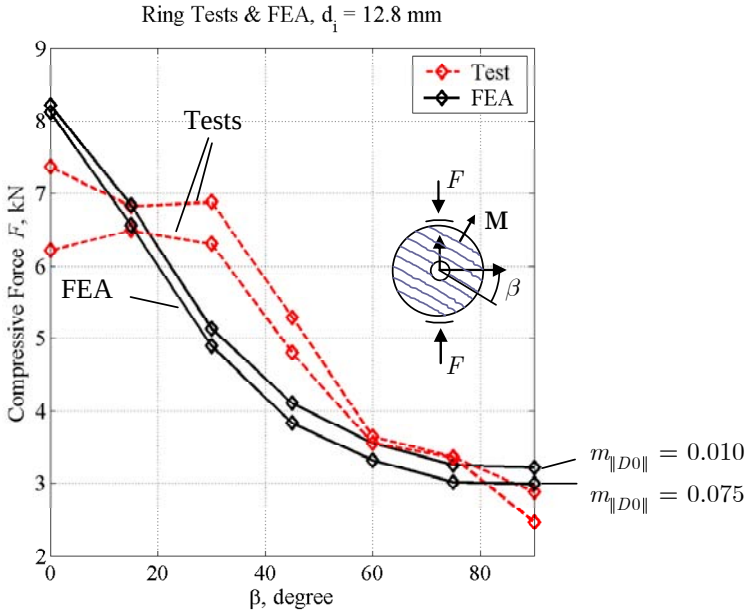

Figure 5.33. Comparison of test and FE analysis results.

The effect of pre-existing damage size was studied by analysing rings using two different sizes and distributions as shown in Table 5.14. An increase of the pre-existing damage size decreases the failure load as shown in Figs. 5.32 and 5.33.

Although the statistical parameters were the same, there is always a variation between samples. To study the effect of sampling variation, five samples with seven orientation directions were analysed. Although the number of analyses was small, it appeared that the structure is sensitive to sampling variations when the material orientation angle β > 60º as shown in Fig. 5.34.

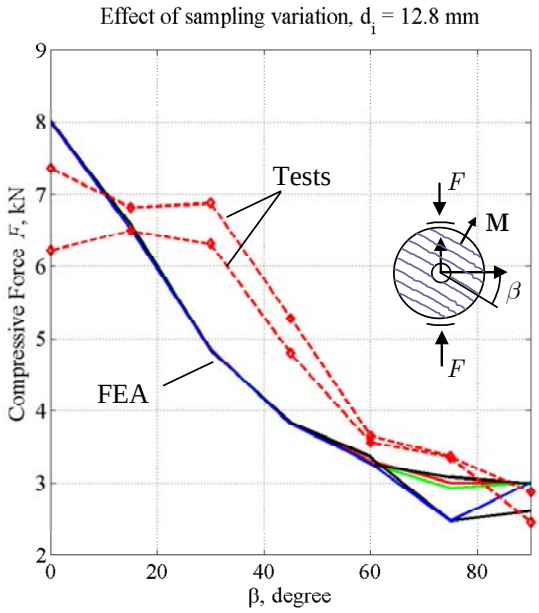

Figure 5.34. Effect of sampling variation on the failure load, when the hole diameter is 12.8 mm and $m_{\|D0\|} = 0.075$ *(case b in Table 5.14).*

As discussed in the previous section, Chen and Hsu (2001) assumed in the determination of tensile strength that failure initiates at the intersection of the load line and hole as shown in Fig. 5.35. The numerical results based on the proposed *wing crack* method showed that damage initiation takes place at the intersection only when $\beta = 0$ or $\beta = 90°$. Otherwise damage initiation occurs on the weaker side w as illustrated in Fig. 5.35.

Due to the foliated structure, the tensile strength in the circumferential direction is higher on the right side than on the left of the upper part of the hole, as shown in Fig. 5.35b, when $\beta = 45°$. Also the circumferential stress is higher on the right side as illustrated in Fig. 5.36. Therefore damage initiates on the left side as shown in Fig. 5.37.

The damaged area is illustrated in Figs. 5.37 and 5.38. The damage evolution path consists of several branches, which is common in brittle failure of materials.

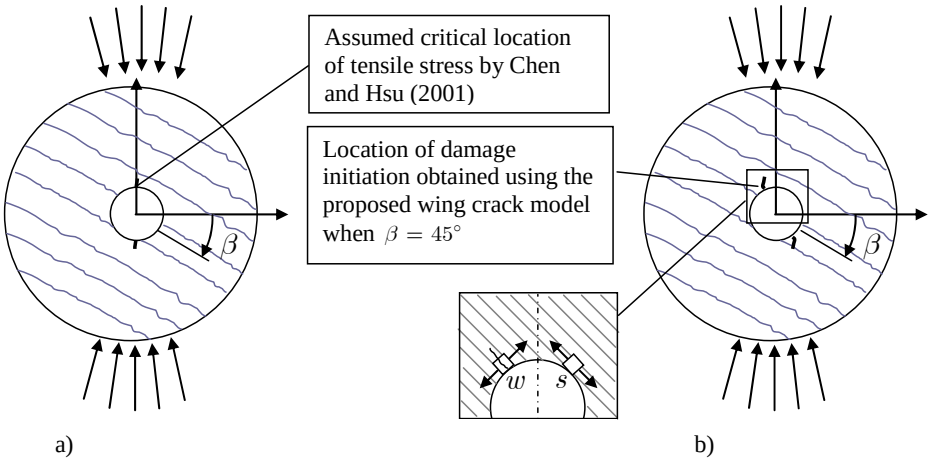

Figure 5.35. a) Assumed location of critical tensile stress by Chen and Hsu (2001), b) location of damage initiation according to numerical analysis using the proposed wing crack model. w *is the weaker side of the upper part of the hole.*

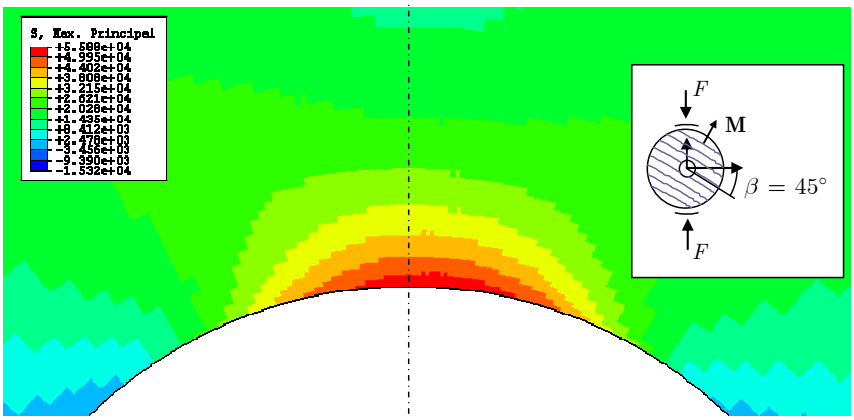

Figure 5.36. Maximum principal stress contour when d_i *=12.8mm,* $\beta = 45^\circ$ *and* $m_{\|D0\|} = 0.075$ *(case b in Table 5.14).*

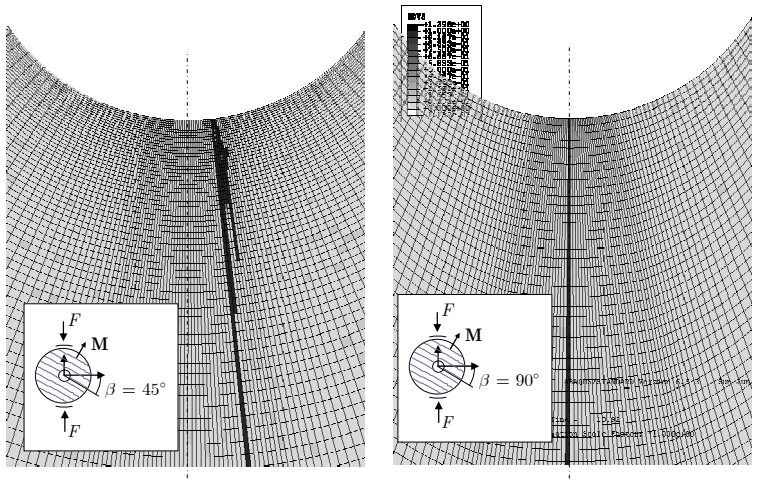

Figure 5.37. Damaged area (dark) obtained in numerical simulation of ring tests; d_i =12.8mm and $m_{\|D0\|} = 0.075$ (case b in Table 5.14); $\beta = 45°$ (left) and $\beta = 90°$ (right).

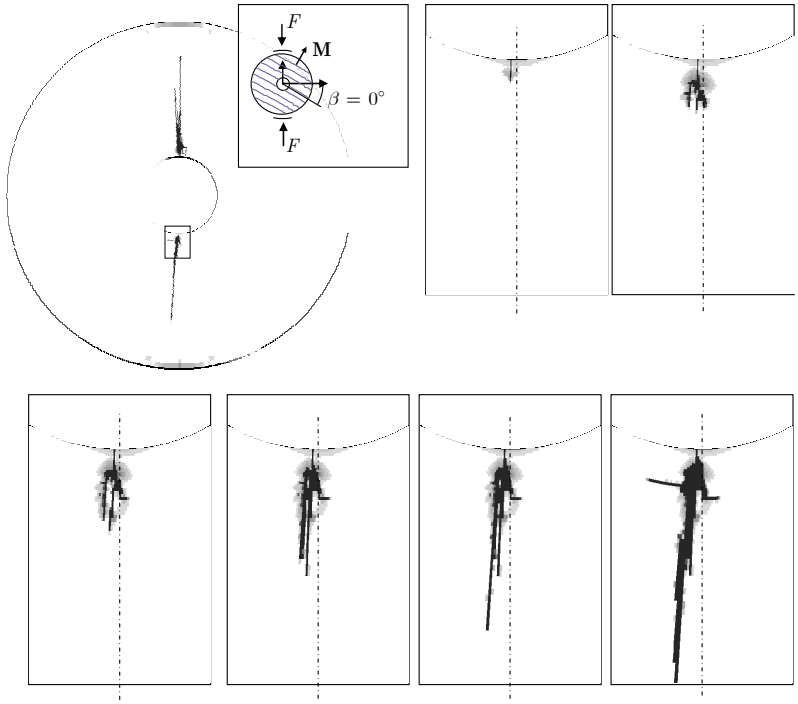

Figure 5.38. Evolution of damage pattern obtained in numerical simulation of ring tests when d_i =12.8mm, $\beta = 0°$ and $m_{\|D0\|} = 0.075$ (case b in Table 5.14).

5.5 Model verification test 5

5.5.1 Plate with 3-D defect

A plate with an inclined three-dimensional defect as shown in Fig. 5.39 was analysed under compression and tension using both the modified Murakami-Kamiya (MK) and the proposed wing crack models.

The objective of this example was to demonstrate splitting crack evolution under compression, and kinking of the crack under tension when the stress state is three-dimensional.

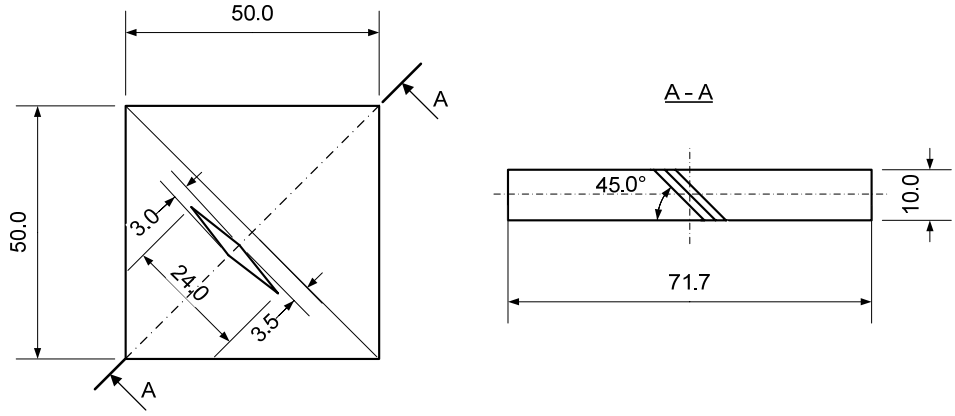

Figure 5.39. Dimensions of the cracked plate (mm).

The damage surface, damage evolution and the elastic material properties were the same as used in the example in Section 5.2.1. The hardening parameters were different. The material parameters are shown in Tables 5.18 and 5.19. The elastic material properties and the damage surface resemble concrete material with a tensile strength of 4.4 MPa and compressive strength of 18.5 MPa.

In the wing crack model the pre-existing damage was assumed to be small and randomly oriented. The rate-independent damage surface shown in Fig. 5.41 was applied.

The material parameters η_1, η_2, η_3 and η_4 used in the MK model were the same as used by Murakami and Kamiya (1997) in their example for concrete.

The hardening parameter was adjusted such that the tensile failure stress is the same as in the wing crack model. The MK model is more ductile than the wing crack model as shown in Fig. 5.40.

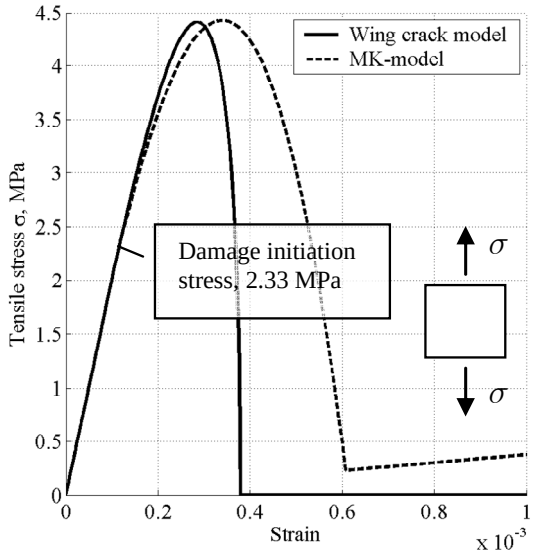

Figure 5.40. Stress-strain curves under uniaxial tension for the damage models. Tensile strength 4.4 MPa.

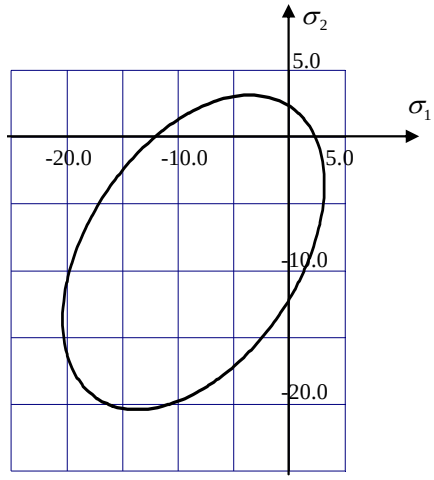

Figure 5.41. Damage surface in plane stress space for both models. Units are in MPa.

Table 5.18. Material parameters for the modified MK model.

η_1	η_2	η_3	η_4	ζ	h
-400E6 MPa	-900e6 MPa	100E6 MPa	-23.5E6 GPa	0.2	1.24E-6

Table 5.19. Material parameters for the wing crack damage model.

Distribution of orientation and size of pre-existing damage								
$\|\mathbf{D}^0\|$		D_1^0		D_2^0		D_3^0		Hardening
$m_{\|D0\|}$	$s_{\|D0\|}$	m_{D1}	s_{D1}	m_{D2}	s_{D2}	m_{D3}	s_{D3}	h
0.0001	0.0	0.0	0.1	0.0	0.1	0.0	0.1	6.5E-4

The plate was modelled using first-order tetrahedral elements (C3D4). Although the first-order tetrahedral element is not the best choice for accurate stress analysis, elements can be used to illustrate the failure modes of the structure shown in Fig. 5.42. The loading was displacement-rate controlled with a rate of 0.01 mm/s. The top and bottom surfaces of the sample were assumed to remain planar during loading.

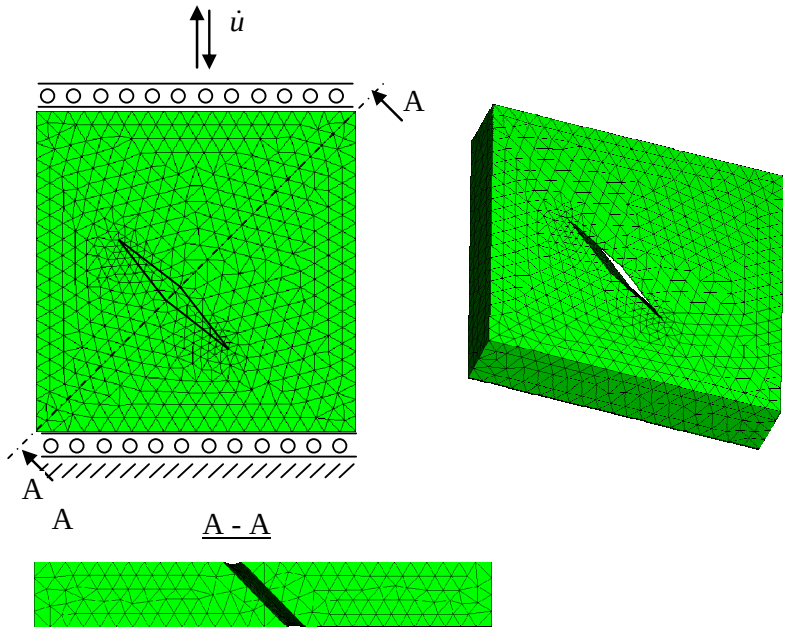

Figure 5.42. FE model of the plate.

5.5.2 Results of verification

The failure patterns under tension are similar, as shown in Fig. 5.44, although the load displacement curves shown in Fig 5.43 are dissimilar. Due to the more ductile-like stress-strain curve, the failure load of the MK model is higher under tension than that of the wing crack model. The behaviour of the wing crack model is clearly brittle-like.

Splitting is the compressive failure mode for both models as shown in Fig. 5.46. As shown in Fig. 5.45 the force displacement curves are almost linear up to the failure load, as is the case in uniaxial compression of brittle materials. The material parameter ζ of the MK model enables stiffness degradation in the loading direction also. Therefore the failure load is lower for the MK model.

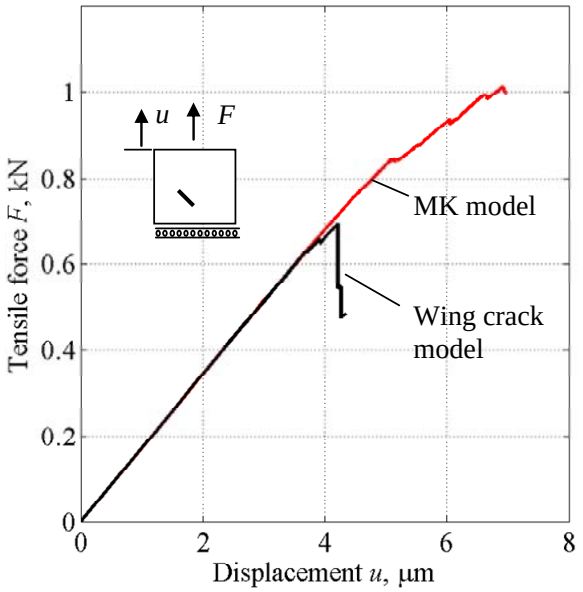

Figure 5.43. Tensile force curve as a function of displacement.

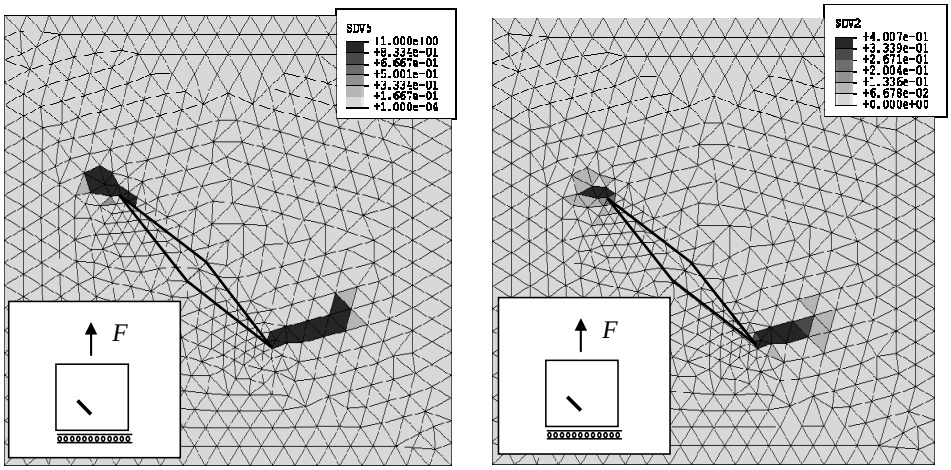

a) Wing crack model b) MK model

Figure 5.44. Failure modes under tension. The dark colour is the damaged area.

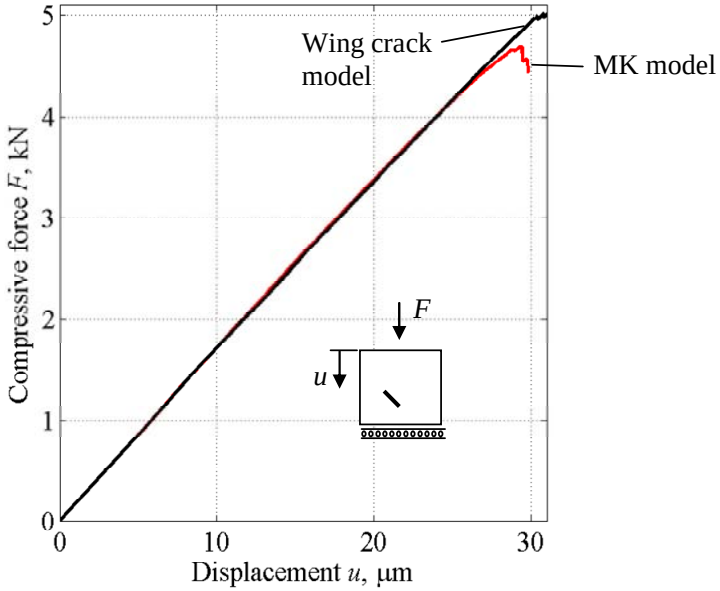

Figure 5.45. Compressive force curve as a function of displacement.

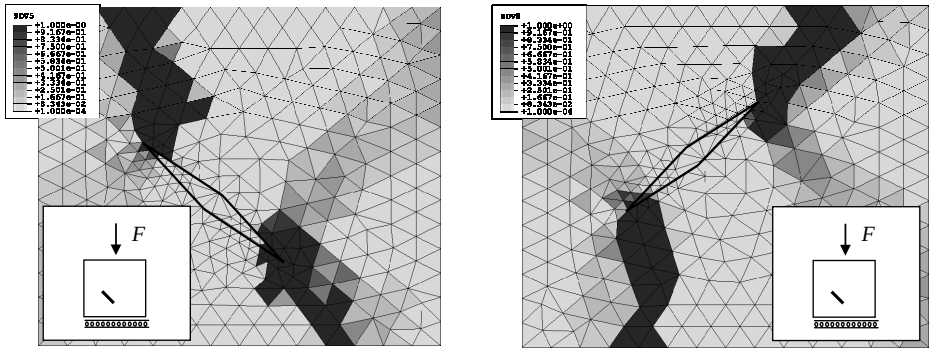

a) Wing crack model

b) MK model (backside view)

Figure 5.46. Failure modes under compression. The dark colour represents the damaged area.

5.6 Conclusions from the test results

The proposed WCD model proved to be efficient in modelling the behaviour of isotropic and transversely isotropic materials. The correct brittle failure modes were captured.

The validity of the proposed wing crack damage (WCD) model was verified by numerical simulation of five specimens in various loading conditions. The specimens were composed of known transversely isotropic materials like ice and marble, as well as concrete that was considered an isotropic material.

The material parameters needed in the model were not all known. Where they were not, they were determined following the procedure described in Section 4.5.5. The parameters were not fitted to obtain identical results with the experiments.

Model verification test 1 – mesh sensitivity analysis

The verification analysis with a tapered bar under uniaxial tension showed that due to the applied rate-dependent damaging feature, the proposed model is not imposed on localisation of deformations in a single element layer, although the strain softening approach was applied.

The analysis without rate dependency showed that deformations localise in one element independently of element size.

Model verification test 2 – Clausius-Duhem inequality

It was numerically established that the condition of Eq. (4.55) alone does not guarantee the fulfilment of the Clausius-Duhem inequality.

When the proposed condition of Eq. (4.57) was applied the Clausius-Duhem inequality equation was fulfilled, as shown in the verification test.

Model verification test 3 – Columnar ice

The behaviour of columnar ice cubes both under compression and under tension were verified numerically using the WCD model. Columnar ice is known to be a transversely isotropic material with different strength in the material symmetry axis direction and transversal directions.

The capability of modelling oriented pre-existing cracks was applied in the verification case. The normal of the crack surface was assumed to be normal to the columns as in nature.

Under tension, both the failure modes and the failure loads were in line with the test results. Although the damage vector evolution indicated correct failure modes under uniaxial compression and confined compression simulations, the failure modes were not as visual as under tension test simulations.

Model verification test 4 – marble ring test simulation

The numerical simulation of ring tests with Hualien marble revealed the capability of the WCD model in modelling transversely isotropic materials. In ring tests, the tensile strength of a specimen is determined indirectly from the known compressive ultimate load. Because of the foliated structure of Hualien marble, the tensile strength is a function of the material orientation angle with respect to the loading direction. The strength was experimentally verified by Chen and Hsu (2001).

The capability of modelling-oriented, pre-existing cracks was exploited also in this verification test. Due to the foliated structure of the marble, pre-existing cracks were assumed to be parallel to the foils. The effect of length of pre-existing cracks on the failure load was studied based on two different means and standard deviations. The effect of sampling variation was also studied.

The resemblance between the test results and the numerically obtained results was good. The deviation was greatest when the angle between the material orientation axis and the loading axis was about 45º. The deviation can be explained by a fairly simple damage surface used in the WCD model. The surface is based on the strength obtained with orientation angles of 0º and 90º. A

more precise damage surface would give more accurate results when the angle is between 0^o and 90^o.

Not only the pre-existing damage size but also sampling variation was found to affect the failure load. Damage size, location and orientation have a significant effect on failure load because damage initiation tends to start from the weakest point, therefore sampling variation also affects the failure load.

Based on numerical simulation, it appeared that the location of crack initiation is a function of the material orientation angle. When the angle was 0^o the damage evolution path was strongly branched.

Model verification test 4 – Plate with 3-D defect

The plate with an inclined three-dimensional defect was analysed to illustrate both the MK and WCD models' ability to predict the direction of crack evolution also when the stress state is three-dimensional. The material parameters were similar to those of concrete. Both models were able to predict the formation of splitting and tensile cracks.

6. Discussion of results and further developments

As described in Section 1.1 the fundamental objectives of this work were:

a) To enhance the Murakami Kamiya (MK) model,

b) To introduce a new model, the wing crack damage (WCD) model, for analysis of brittle transversely isotropic materials, and

c) To implement both models in ABAQUS/Standard FE software.

In this work the hypothesis that the brittle failure phenomenon can be estimated by a model, namely the wing crack damage model (WCD model), was tested. It was shown that the proposed WCD model can be successfully applied in the numerical analysis of brittle, transversely isotropic materials.

In order to verify the efficiency of the WCD model it was implemented in ABAQUS/Standard FE software as a user material subroutine.

Murakami Kamiya (MK) model

Continuum damage models motivated by the axial splitting mechanism are of considerable current interest. Most of the models are phenomenological, based on neither the effective stress nor the effective strain concept. The Helmholtz free energy equation is often formulated by the use of projection tensor. The projection tensor is used to dismantle negative strains from the strain tensor. Formulation of the projection tensor requires determination of principle strains. The drawback is that the derivatives of the projection tensor needed in numerical applications cannot be explicitly formulated. In this work the MK model was enhanced by obtaining the derivatives numerically.

In the continuum damage models the associative approach is often used; the damage surface (damage potential) is a function of the thermodynamic conjugate force for damage. Although the Clausius-Duhem inequality equation is fulfilled in the associative, convex approaches, the use of the conjugate force makes the determination of general damage surface quite complicated. A strain-based

damage surface was applied both for the MK and WCD models. Therefore determination of the damage surface is straightforward for various materials.

The upper limit of damage is not well defined in the phenomenological models; therefore further conditions are required to retain positive definiteness of the strain energy density. In this work the MK model was enhanced by introducing a condition based on the eigenvalues of the secant stiffness matrix, to define the upper limit for MK model.

Unilateral behaviour

The unsymmetrical behaviour due to the opening and closure of cracks is called *unilateral behaviour*. The unilateral feature is important in the analysis of brittle failure, even though cyclic loading cases were not considered. In dynamic analysis, the stress relief due to fast crack formation induces stress wave propagation. Due to the stress wave propagation, reflection and interaction of the waves, cracks already formed may close.

Studies on strain- and stress-based criteria described in Section 4.2 showed that strain-based crack opening/closure criteria cannot be reliably applied when the stress state is two- or three-dimensional. It was further shown that a stress-based criterion should be used instead.

The invalid opening/closure criterion of the MK model and the need to calculate the eigensystem at each increment were the main reasons to find another solution method instead of further developing the MK model.

Wing crack damage model

The proposed method was introduced to overcome the difficulties discussed above. Formulation of the Helmholtz free energy equation is based on the concept where it is assumed that the surface of an open crack is free of stresses and that the virgin material is transversely isotropic. The damage vector was used to determine the orientation of the surface. The sign of normal traction (based on the damage vector and stress tensor) was used to obtain information about the crack state, whether it is open or closed. Material rupture takes place when the damage vector length reaches unity.

In the proposed WCD model the upper limit of the damage is well defined, therefore the positive definiteness of the strain energy is retained.

The direction of the damage also represents the preferred material direction. A transversely isotropic material has one preferred material direction; therefore the second preferred direction due to damage introduces anisotropy. This fact was taken into account in the proposed method because it is based on the equations derived for materials having two preferred directions. All the material parameters used to define the strain energy density of damaged material have a clear physical background.

The proposed new method is well defined because it is motivated by an experimentally and theoretically verified mechanism, namely the wing crack formation mechanism. In this approach the direction of shear traction on the crack surface determines the kinking direction of the developing wing crack. Numerical studies showed that the method is capable of simulating wing crack growth, the axial splitting failure mode, and tensile cracking. The approach was based on the assumption of pre-existing cracks.

It is well known that all materials are prone to various defects like cracks. Orientation, size and distribution of the defects affect the material response and strength. The proposed new method based on the pre-existing damage makes it possible to study the effect of size and orientation of these pre-existing defects on the behaviour of materials.

Rate-dependent damaging

Stiffness degradation due to the damage evolution was modelled applying the strain softening approach combined with the damage rate-dependent damage surface. Therefore problems arising from the localisation of deformations were avoided as shown in the numerical examples.

Verification of the WCD model by numerical simulation

Both the proposed WCD and MK models were implemented in ABAQUS/ Standard FE software as a user subroutine. The validity of the wing crack damage model was verified by testing it against five basic structures composed

of known natural materials (ice, marble and concrete). One of the tests was executed using the modified MK model.

The verification tests revealed the capability of the proposed WCD model in the analysis of brittle materials. The model can be used in the analysis of brittle failure of materials; both axial splitting and tensile failure modes were captured. Both the failure modes and failure loads obtained in the simulation corresponded well with the reference results.

6.1 Need for further development

Although the proposed wing crack damage (WCD) model was found to be efficient in analysing brittle materials, some further developments can be suggested. The main needs are listed below.

1. Frictional sliding of crack surfaces and the effect of compressive force on sliding could be taken into account.
2. The apparent Poisson ratio is known to change when a material is undergoing damage. The effect could be included in the WCD model.
3. Structural failure is often associated with some amount of plastic flow besides the damaging process. Therefore the combined damage and plasticity model could be considered.
4. Nucleation of cracks could be included in the model.

7. Conclusions

In this work a new continuum damage model, the wing crack damage (WCD) model was introduced. The proposed method was found to be efficient in analysing the brittle failure of transversely isotropic solids. The method can be applied in the analysis of axial splitting and tensile cracking failure modes. The model was implemented in ABAQUS/Standard FE software as a user material subroutine.

In addition the model proposed by Murakami and Kamiya (1997) was enhanced and implemented in ABAQUS/Standard FE software.

Wing crack damage model (WCD model)

A new *wing crack damage model* was introduced for modelling of transversely isotropic materials. The method is capable of simulating the axial splitting failure mode due to the wing crack growth mechanism under compression, as well as the tensile cracking failure mode under tension.

The derived strain energy equations are based on the equations derived for materials having two preferred directions.

The evolution equation of damage vector D_k is based on the wing crack growth mechanism. Because of the non-associative approach the Clausius-Duhem inequality equation was verified numerically.

Unilateral condition

It was shown in Section 4.2 that the strain-based crack opening/closure criteria cannot be reliably applied when the stress state is two- or three-dimensional, but a stress-based criterion should be used instead.

The main reasons for finding another solution method instead of developing the MK model were the invalid opening/closure condition and the need to calculate the eigensystem at each increment.

Upper limit of damage

A method based on the positive definiteness of a secant stiffness matrix for determining the upper limit of the damage tensor was introduced in Section 4.3.2.

Rate-dependent damaging

Due to damaging, the stiffness of the material is degraded. In continuum damage models the degradation is described by the strain softening approach. The strain softening applications are subject to mesh sensitivity and localisation problems. Rate-dependent solution methods can be applied to avoid mesh sensitivity problems; therefore the rate-dependent “consistency model” was utilised in the proposed WCD model. Problems arising from the localisation of deformations were thus avoided, as shown in the numerical examples.

Damage surface

Damage initiation in the WCD model is based on the damage surface given in the strain space. A four-parameter surface was introduced. It enables definition of the damage surface when tensile and compressive strengths are known both in the direction of the material symmetry axis and in the transverse direction. A more detailed surface can be easily applied if material parameters were available.

Pre-existing cracks

The proposed method is based on the assumption of pre-existing cracks. The method makes it possible to study the effect of the size and orientation distribution of pre-existing cracks on the strength and failure modes.

Numerical verification

The validity of the proposed wing crack damage (WCD) model was verified by numerical simulation of five specimens in various loading conditions. The specimens were composed of known transversely isotropic materials like ice and marble, and concrete that was considered an isotropic material.

The proposed WCD model proved to be efficient in modelling the behaviour of isotropic and transversely isotropic materials. The correct brittle failure modes were captured.

References

ABAQUS. 2003. ABAQUS Online Documentation: Version 6.4-1, Theory Manual [CD-ROM]. ABAQUS Inc., USA: Generated: Wed September 17, 2003 at 13:34:58; Build ID: 2003_09_17-10.01.59 15383.

Alliche, A. 2004. Damage model for fatigue loading of concrete. International Journal of Fatigue, Vol. 26, No. 9, pp. 915–921.

Ashby, M. F. & Hallam, N. C. 1986. The failure of brittle solids containing small cracks under compressive stress states. Acta Metallurgica, Vol. 34, No. 3, pp. 497–510.

Azhdari, A. & Nemat-Nasser, S. 1996. Energy-release rate and crack kinking in anisotropic brittle solids. Journal of the Mechanics and Physics of Solids, Vol. 44, No. 6, pp. 929–951.

Basista, M. & Gross, D. 1989. A note on brittle damage description. Mechanics Research Communications, Vol. 16, No. 3, pp. 147–154.

Bazant, Z. P. 2002. Concrete fracture models: testing and practice. Engineering Fracture Mechanics, Vol. 69, No. 2, pp. 165–205.

Bazant, Z. P. & Planas, J. 1998. Fracture and Size Effect in Concrete and Other Quasibrittle Materials. Boca Raton (FL): CRC Press LLC. 616 p. ISBN 0-8493-8284-X.

Bazant, Z. P. & Zi, G. 2003. Microplane constitutive model for porous isotropic rocks. International Journal for Numerical and Analytical Methods in Geomechanics, Vol. 27, No. 1, pp. 25–47.

Bazant, Z. P., Gettu, R., Jirasek, M., Barr, B. I. G., Carol, I., Carpinteri, A., Elices, M., Huet, C., Mihashi, H., Nemati, K. M., Planas, J., Ulm, F. J., Van Mier, J. G. M., Van Vliet, M. R. A., Burtscher, S., Chiaia, B., Dempsey, J. P., Ferro, G., Gopalaratnam, V. S., Prat, P., Rokugo, K., Saouma, V. E., Slowik, V., Vitek, L. & Willam, K. 2004. RILEM TC QFS Quasibrittle fracture scaling and

size effect – Final report. Materials and Structures/Materiaux et Constructions, Vol. 37, No. 272, pp. 547–568.

Belytschko, T. & Black, T. 1999. Elastic crack growth in finite elements with minimal remeshing. International Journal for Numerical Methods in Engineering, Vol. 45, No. 5, pp. 601–620.

Betten, J. 1983. Damage Tensors in Continuum Mechanics. Journal de Mecanique Theorique et Appliquee, Vol. 2, No. 1, pp. 13–32.

Betten, J. 1986. Applications of tensor functions to the formulation of constitutive equations involving damage and initial anisotropy. Engineering Fracture Mechanics, Vol. 25, No. 5–6, pp. 573–584.

Bhattacharya, K., Ortiz, M. & Ravichandran, G. 1998. Energy-based model of compressive splitting in heterogeneous brittle solids. Journal of the Mechanics and Physics of Solids, Vol. 46, No. 10, pp. 2171–2181.

Cannon, N. P., Schulson, E. M., Smith, T. R. & Frost, H. J. 1990. Wing cracks and brittle compressive fracture. Acta Metallurgica et Materialia, Vol. 38, No. 10, pp. 1955–1962.

Carol, I., Bazant, Z. P. & Prat, P. C. 1991. Geometric damage tensor based on microplane model. Journal of Engineering Mechanics, Vol. 117, No. 10, pp. 2429–2448.

Carol, I., Rizzi, E. & Willam, K. 2001. On the formulation of anisotropic elastic degradation. I. Theory based on a pseudo-logarithmic damage tensor rate. International Journal of Solids and Structures, Vol. 38, No. 4, pp. 491–518.

Carosio, A., Willam, K. & Etse, G. 2000. On the consistency of viscoplastic formulations. International Journal of Solids and Structures, Vol. 37, No. 48–50, pp. 7349–7369.

Cazacu, O., Cristescu, N. D., Shao, J. F. & Henry, J. P. 1998. New anisotropic failure criterion for transversely isotropic solids. Mechanics of Cohesive-frictional Materials, Vol. 3, No. 1, pp. 89–103.

Chaboche, J. L. 1993. Development of continuum damage mechanics for elastic solids sustaining anisotropic and unilateral damage. International Journal of Damage Mechanics, Vol. 2, No. 4, pp. 311–329.

Challamel, N., Lanos, C. & Casandjian, C. 2005. Strain-based anisotropic damage modelling and unilateral effects. International Journal of Mechanical Sciences, Vol. 47, No. 3, pp. 459–473.

Chaves, E. W. V. 2003. A Three Dimensional Setting for Strong Discontinuities Modelling in Failure Mechanics. Ph.D.-thesis, Technical University of Catalonia (UPC). Barcelona, Spain.

Chen, C. S. & Hsu, S. C. 2001. Measurement of indirect tensile strength of anisotropic rocks by the ring test. Rock Mechanics and Rock Engineering, Vol. 34, No. 4, pp. 293–321.

Chen, C. S., Pan, E. & Amadei, B. 1998. Determination of deformability and tensile strength of anisotropic rock using Brazilian tests. International Journal of Rock Mechanics and Mining Sciences, Vol. 35, No. 1, pp. 43–61.

Chen, W. & Ravichandran, G. 2000. Failure mode transition in ceramics under dynamic multiaxial compression. International Journal of Fracture, Vol. 101, No. 1–2, pp. 141–159.

Chow, C. L. & Lu, T. J. 1989. On evolution laws of anisotropic damage. Engineering Fracture Mechanics, Vol. 34, No. 3, pp. 679–701.

Cole, D. M. 1998. Modeling the cyclic loading response of sea ice. International Journal of Solids and Structures, Vol. 35, No. 31–32, pp. 4067–4075.

Comi, C. & Perego, U. 2001. Fracture energy based bi-dissipative damage model for concrete. International Journal of Solids and Structures, Vol. 38, No. 36–37, pp. 6427–6454.

Cormery, F. & Welemane, H. 2002. A critical review of some damage models with unilateral effect. Mechanics Research Communications, Vol. 29, No. 5, pp. 391–395.

Cotterell, B. 2002. The past, present, and future of fracture mechanics. Engineering Fracture Mechanics, Vol. 69, No. 5, pp. 533–553.

Cotterell, B. & Rice, J. R. 1980. Slightly curved or kinked cracks. International Journal of Fracture, Vol. 16, No. 2, pp. 155–169.

Cox, G. F. N. & Weeks, F. 1983. Profile properties of undeformed first year sea ice. Hanover, New Hampshire, USA: U.S. Army Cold Regions Research and Engineering Laboratory (CRREL). CRREL Report 88-13. 63 p.

Davison, L. & Stevens, A. L. 1973. Thermomechanical Constitution of Spalling Elastic Bodies. Journal of Applied Physics, Vol. 44, No. 2, pp. 668–674.

Derradji-Aouat, A., Sinha, N. K. & Evgin, E. 2000. Mathematical modelling of monotonic and cyclic behaviour of fresh water columnar grained S-2 ice. Cold Regions Science and Technology, Vol. 31, No. 1, pp. 59–81.

Dragon, A., Halm, D. & Desoyer, T. 2000. Anisotropic damage in quasi-brittle solids: modelling, computational issues and applications. Computer Methods in Applied Mechanics and Engineering, Vol. 183, No. 3–4, pp. 331–352.

Dube, J.-F., Pijaudier-Cabot, G. & Laborderie, C. 1996. Rate Dependent Damage Model for Concrete in Dynamics. Journal of Engineering Mechanics, Vol. 122, No. 10, pp. 939–947.

Edelen, D. 1972. A Nonlinear Onsager Theory of Irreversibility. International Journal of Engineering Science, Vol. 10, pp. 481–490.

Elices, M., Guinea, G. V., Gomez, J. & Planas, J. 2002. The cohesive zone model: advantages, limitations and challenges. Engineering Fracture Mechanics, Vol. 69, No. 2, pp. 137–163.

Elices, M. & Planas, J. 1996. Fracture mechanics parameters of concrete : An overview. Advanced Cement Based Materials, Vol. 4, No. 3–4, pp. 116–127.

Espinosa, H. D. & Brar, N. S. 1995. Dynamic failure mechanisms of ceramic bars: Experiments and numerical simulations. Journal of the Mechanics and Physics of Solids, Vol. 43, No. 10, pp. 1615–1619.

Florez-Lopez, J. 1995. Simplified model of unilateral damage for RC frames. Journal of Structural Engineering, Vol. 121, No. 12, pp. 1765–1772.

Fonseka, G. U. & Krajcinovic, D. 1981. Continuous Damage Theory of Brittle Materials – 2. Uniaxial ond Plane Response Modes. Journal of Applied Mechanics, Transactions ASME, Vol. 48, No. 4, pp. 816–824.

Fremond, M. & Nedjar, B. 1995. Damage in concrete: the unilateral phenomenon. Nuclear Engineering and Design, Vol. 156, No. 1–2, pp. 323–335.

Gambarotta, L. 2004. Friction-damage coupled model for brittle materials. Engineering Fracture Mechanics, Vol. 71, No. 4–6, pp. 829–836.

Georgin, J. F. & Reynouard, J. M. 2003. Modeling of structures subjected to impact: Concrete behaviour under high strain rate. Cement and Concrete Composites, Vol. 25, No. 1, pp. 131–143.

Gratz, E. T. & Schulson, E. M. 1994. Preliminary observations of brittle compressive failure of columnar saline ise under triaxial loading. Annals of Glaciology, Vol. 19, pp. 33–38.

Gratz, E. T. & Schulson, E. M. 1997. Brittle failure of columnar saline ice under triaxial compression. Journal of Geophysical Research, Vol. 102, No. B3, pp. 5091–5107.

Gupta, V. & Bergstrom, J. S. 2002. A progressive damage model for failure by shear faulting in polycrystalline ice under biaxial compression. International Journal of Plasticity, Vol. 18, No. 4, pp. 507–530.

Guzina, B. B., Rizzi, E., Willam, K. & Pak, R. Y. S. 1995. Failure predictions of smeared-crack formulations. Journal of Engineering Mechanics, Vol. 121, No. 1, pp. 150–161.

Halm, D. & Dragon, A. 1998. An anisotropic model of damage and frictional sliding for brittle materials. European Journal of Mechanics – A/Solids, Vol. 17, No. 3, pp. 439–460.

Halm, D., Dragon, A. & Charles, Y. 2002. A modular damage model for quasi-brittle solids – interaction between initial and induced anisotropy. Archive of Applied Mechanics, Vol. 72, No. 6–7, pp. 498–510.

Häusler, F. U. 1981. Multi-axial compressive strength tests on saline ice with brush-type loading. In: Michel, B., Davar, K., Frederking, R., Gerard, R., Hausser, R., Kry, R. & Michel, J. (eds.). International Symposium on Ice (IAHR). July 27–31, 1981. Quebec, Canada: Universite Laval, Quebec, Canada. Vol. 2. Pp. 526–536.

Hayakawa, K., Murakami, S. & Liu, Y. 1998. An irreversible thermodynamics theory for elastic-plastic-damage materials. European Journal of Mechanics – A/Solids, Vol. 17, No. 1, pp. 13–32.

Heeres, O. M., Suiker A. S. J. & de Borst, R. 2002. A comparison between the Perzyna viscoplastic model and the Consistency viscoplastic model. European Journal of Mechanics – A/Solids, Vol. 21, pp. 1–12.

Hellan, K. 1984. Introduction to fracture mechanics. McGraw-Hill. Inc. 302 p. ISBN 0-07-028048-7.

Hillerborg, A. 1983. Analysis of one single crack. In: Wittmann, F. H. (ed.). Fracture Mechanics of Concrete. Elsevier, Amsterdam, Netherlands. Pp. 223–249. ISBN 0-444-42199-8.

Hillerborg, A., Modeer, M. & Petersson, P.-E. 1976. Analysis of crack formation and crack growth in concrete by means of fracture mechanics and finite elements. Cement and Concrete Research, Vol. 6, No. 6, pp. 773–781.

Horii, H. & Nemat-Nasser, S. 1986. Brittle failure in compression: splitting, faulting and brittle-ductile transition. Philosophical Transactions of the Royal Society of London A: Mathematical and Physical Sciences, Vol. 319, pp. 337–374.

Huang, C., Subhash, G. & Vitton, S. J. 2002. A dynamic damage growth model for uniaxial compressive response of rock aggregates. Mechanics of Materials, Vol. 34, No. 5, pp. 267–277.

Kachanov, M. L. 1982. A microcrack model of rock inelasticity part I: Frictional sliding on microcracks. Mechanics of Materials, Vol. 1, No. 1, pp. 19–27.

Kang, H. D. & Willam, K. J. 2000. Performance evaluation of elastoviscoplastic concrete model. Journal of Engineering Mechanics, Vol. 126, No. 9, pp. 995–1000.

Kendall, K. 1978. Complexities of compression failure. Proceedings of the Royal Society of London A: Mathematical and Physical Sciences, Vol. 361, pp. 245–263.

Koh, C. G., Liu, Z. J. & Quek, S. T. 2001. Numerical and experimental studies of concrete damage under impact. Magazine of Concrete Research, Vol. 53, No. 6, pp. 417–427.

Kolari, K., Kouhia, R, & Kärnä, T. 2002. Ice Failure Simulation – Softening Material Model. In: Squire, V. & Langhorne, P. (eds.). Proceedings of the 16th International Symposium on Ice.Dunedin, New Zealand, 2nd–6th December, 2002. Ice in the Environment, Volume one. Dunedin, New Zealand: International Association of Hydraulic Engineering and Research. Pp. 489–494. ISBN 1-877139-52-1.

Kolari, K., Kouhia, R, & Kärnä, T. 2003. On viscoplastic regularization of strain softening solids. In: Råback, P., Santaoja, K. & Stenberg, R. (eds.). Proceedings of the VIII Finnish Mechanics Days 12.6.–13.6.2003. Espoo, Finland. Pp. 489–496.

Kolari, K., Kouhia, R., & Kärnä, T. 2004. Ice Failure Analysis using Strain-softening Viscoplastic Material Model. In: Neittaanmäki, P., Rossi, T., Majava, K. & Pironneau, O. (eds.). Proceedings of European Congress on Computational Methods in Applied Sciences and Engineering [CD-ROM]. European Congress on Computational Methods in Applied Sciences and Engineering. Jyväskylä, Finland, 24-7-2004. Jyväskylä, Finland: University of Jyväskylä, Department of Mathematical Information Technology. Vol. 1. Pp. 1–7. ISBN 951-39-1868-8.

Krajcinovic, D. 1989. Damage mechanics. Mechanics of Materials, Vol. 8, No. 2–3, pp. 117–197.

Krajcinovic, D. & Fonseka, G. U. 1981. Continuous Damage Theory of Brittle Materials – 1. General Theory. Journal of Applied Mechanics, Transactions ASME, Vol. 48, No. 4, pp. 809–815.

Kuehn, G. A., Lee, R. W., Nixon, W. A., & Schulson, E. M. 1988. The Structure and Tensile Behavior of First Year Sea Ice And Laboratory-Grown Saline Ice. In: Sodhi, D. S., Luk, C. H. & Sinha, N. K. (eds.). OMAE 1988 Houston, Proceedings of the Seventh International Conference on Offshore Mechanics and Arctic Engineering. Volume IV: Arctic Engineering and Technology. Houston, Texas, USA. Feb 7–12, 1988. Houston, TX, USA: ASME, New York, NY, USA. Vol. 4. Pp. 11–17.

Kuehn, G. A., Schulson, E. M., Jones, D. E., & Zhang, J. 1992. Compressive strength of ice cubes of different sizes. Proceedings of the 11th International Conference on Offshore Mechanics and Arctic Engineering – OMAE 92, Jun 7–12, 1992. Calgary, Alberta, Can: Publ by ASME, New York, NY, USA. Vol. 4. Pp. 349–356.

Kuna-Ciskal, H. & Skrzypek, J. J. 2004. CDM based modelling of damage and fracture mechanisms in concrete under tension and compression. Engineering Fracture Mechanics, Vol. 71, No. 4–6, pp. 681–698.

Lambert, D. E. & Ross, A. C. 2000. Strain rate effects on dynamic fracture and strength. International Journal of Impact Engineering, Vol. 24, No. 10, pp. 985–998.

Leckie, F. A. & Onat, E. T. 1981. Tensorial nature of damage measuring internal variables. In: Hult, J. & Lemaitre, J. L. (eds.). Proceedings of IUTAM Symposium on Physical Nonlinearities in Structural Analysis, Springer, Senlis, France. Pp. 140–155.

Lehner, F. & Kachanov, M. 1996. On modelling of “winged” cracks forming under compression. International Journal of Fracture, Vol. 77, No. 4, pp. R69–R75.

Lemaitre, J. 1992. A Course on Damage Mechanics. Springer-Verlag. 210 p. ISBN 0387536094.

Lemaitre, J. & Chaboche, J.-L. 1990. Mechanics of solid materials. Cambridge University Press. 556 p. ISBN 0 521 32853 5.

Li, W. & Siegmund, T. 2002. An analysis of crack growth in thin-sheet metal via a cohesive zone model. Engineering Fracture Mechanics, Vol. 69, No. 18, pp. 2073–2093.

Litewka, A. & Debinski, J. 2003. Load-induced oriented damage and anisotropy of rock-like materials. International Journal of Plasticity, Vol. 19, No. 12, pp. 2171–2191.

Lu, Y. F. & Shao, J. F. 2002. Modelling of anisotropic damage in brittle rocks under compression dominated stresses. International Journal for Numerical and Analytical Methods in Geomechanics, Vol. 26, No. 10, pp. 945–961.

Luo, D., Takezono, S., Tao, K. & Minamoto, H. 2003. The Mechanical Behavior Analysis of CFCC with Overall Anisotropic Damage by the Micro-Macro Scale Method. International Journal of Damage Mechanics, Vol. 12, No. 2, pp. 141–162.

Malvern, L. E. 1969. Introduction to the Mechanics of a Continuous Medium. Prentice Hall. 713 p. ISBN 0-13-487603-2.

Mathematica [version 5.1.0.0]. 2003. Wolfram Research, Inc., 100 Trade Center Drive, Champaign, IL, 61820-7237, USA.

Mellor, M. 1983. Mechanical Behavior of Sea Ice. Hanover, New Hampshire, USA: U.S. Army Cold Regions Research and Engineering Laboratory (CRREL). Monograph 83-1. 102 p.

Michel, B. 1978. Ice mechanics. Québec: Université Laval. 499 p. ISBN 0-7746-6876-8.

Mikkola, M. J. & Piila, P. 1984. Nonlinear Response of Concrete by Use of the Continuous Damage Theory. Proceedings of the International Conference on Computer-Aided Analysis and Design of Concrete Structures. Split, Yugoslavia: Pineridge Press, Swansea, Wa. Pp. 179–189. ISBN 0-906674-33-6.

Mitaim, S. & Detournay, E. 2004. Damage around a cylindrical opening in a brittle rock mass. International Journal of Rock Mechanics and Mining Sciences, Vol. 41, No. 8, pp. 1447–1457.

Murakami, S. 1990. A Continumm Mechanics Theory of Anisotropic Damage. In: Boehler, J. P. (ed.). Proceedings of the IUTAM/ICM Symposium on Yielding, Damage, and Failure of Anisotropic Solids, Aug 24–28 1987. Villard-de-Lans, Fr: MEP, Bury St. Edmunds, Engl. Pp. 465–482. ISBN 0-85298-735-8.

Murakami, S. & Kamiya, K. 1997. Constitutive and damage evolution equations of elastic-brittle materials based on irreversible thermodynamics. International Journal of Mechanical Sciences, Vol. 39, No. 4, pp. 473–486.

Nard, H. L. & Bailly, P. 2000. Dynamic behaviour of concrete: the structural effects on compressive strength increase. Mechanics of Cohesive-frictional Materials, Vol. 5, No. 6, pp. 491–510.

Nemat-Nasser, S. & Deng, H. 1994. Strain-rate effect on brittle failure in compression. Acta Metallurgica et Materialia, Vol. 42, No. 3, pp. 1013–1024.

Nemat-Nasser, S. & Horii, H. 1982. Compression-induced nonplanar crack extension with application to splitting, exfliation, and rockburst. Journal of Geophysical Research, Vol. 87, No. B8, pp. 6805–6821.

Nemat-Nasser, S. & Horii, H. 1984. Rock Failure in Compression. International Journal of Engineering Science, Vol. 22, No. 8–10, pp. 999–1011.

Obata, M., Nemat-Nasser, S. & Goto, Y. 1989. Branched cracks in anistropic elastic solids. Journal of Applied Mechanics, Transactions ASME, Vol. 56, No. 4, pp. 858–864.

Ohmenhauser, F., Weihe, S. & Kroplin, B. 1999. Algorithmic implementation of a generalized cohesive crack model. Computational Materials Science, Vol. 16, No. 1–4, pp. 294–306.

Oliver, J. & Huespe, A. E. 2004. Continuum approach to material failure in strong discontinuity settings. Computer Methods in Applied Mechanics and Engineering, Vol. 193, No. 30–32, pp. 3195–3220.

Oliver, J., Huespe, A., Pulido, M. D. G. & Blanco, S. 2003. Computational modeling of cracking of concrete in strong discontinuity settings. Computers and Concrete, Vol. 1, No. 1, pp. 61–76.

Oliver, J., Huespe, A. E., Pulido, M. D. G. & Chaves, E. 2002. From continuum mechanics to fracture mechanics: the strong discontinuity approach. Engineering Fracture Mechanics, Vol. 69, No. 2, pp. 113–136.

Olsson, M. & Ristinmaa, M. 2003. Damage Evolution in Elasto-Plastic Materials – Material Response Due to Different Concepts. International Journal of Damage Mechanics, Vol. 12, No. 2, pp. 115–139.

Papa, E. 1996. Unilateral damage model for masonry based on a homogenisation procedure. Mechanics of Cohesive-frictional Materials, Vol. 1, No. 4, pp. 349–366.

Pensee, V., Kondo, D. & Dormieux, L. 2002. Micromechanical analysis of anisotropic damage in brittle materials. Journal of Engineering Mechanics, Vol. 128, No. 8, pp. 889–897.

Perzyna, P. 1966. Fundamental problems in viscoplasticity. Advances in applied mechanics, Vol. 9, pp. 243–377.

Planas, J., Elices, M., Guinea, G. V., Gomez, F. J., Cendon, D. A. & Arbilla, I. 2003. Generalizations and specializations of cohesive crack models. Engineering Fracture Mechanics, Vol. 70, No. 14, pp. 1759–1776.

Renshaw, C. E. & Schulson, E. M. 2001. Universal behaviour in compressive failure of brittle materials [5]. Nature, Vol. 412, No. 6850, pp. 897–900.

Ristinmaa, M. & Ottosen, N. S. 1998. Viscoplasticity based on an additive split of the conjugated forces. European Journal of Mechanics – A/Solids, Vol. 17, No. 2, pp. 207–235.

Ristinmaa, M. & Ottosen, N. S. 2000. Consequences of dynamic yield surface in viscoplasticity. International Journal of Solids and Structures, Vol. 37, No. 33, pp. 4601–4622.

Rogers, T. G. 1990. Yield criteria, flow rules, and hardening in anisotropic plasticity. In: Boehler, J. P. (ed.). Proceedings of the IUTAM/ICM Symposium on Yielding, Damage, and Failure of Anisotropic Solids, Aug 24–28 1987. Villard-de-Lans, Fr: MEP, Bury St. Edmunds, Engl. Pp. 53–79. ISBN 0-85298-735-8.

Rots, J. G. & Blaauwendraad, J. 1989. Crack models for concrete: discrete or smeared? Fixed multi-directional or rotating? Heron, Vol. 34, No. 1, pp. 3–59.

Ruiz, G., Pandolfi, A. & Ortiz, M. 2001. Three-dimensional cohesive modeling of dynamic mixed-mode fracture. International Journal for Numerical Methods in Engineering, Vol. 52, No. 1–2, pp. 97–120.

Sanderson, T. J. O. 1988. Ice Mechanics: Risks to Offshore Structures. London: Graham and Trotman. 253 p. ISBN 0-86010-785-X.

Santaoja, K. 2001. Lecture notes on thermomechanics. Espoo, Finland: Helsinki University of Technology. 189 p. (Helsinki University of Technology, Laboratory for Mechanics of Materials ; 32. ISBN 951-22-5737-8.

Sarva, S. & Nemat-Nasser, S. 2001. Dynamic compressive strength of silicon carbide under uniaxial compression. Materials Science and Engineering A, Vol. 317, No. 1–2, pp. 140–144.

Schulson, E. M. 1987. The Fracture of Ice Ih. In: Anon (ed.). VII Symposium on the Physics and Chemistry of Ice. Grenoble, France. Vol. 48. Pp. 207–220. ISBN 2-86883-051-X.

Schulson, E. M. 2001. Brittle failure of ice. Engineering Fracture Mechanics, Vol. 68, No. 17–18, pp. 1839–1887.

Shi, Z. 2004. Numerical analysis of mixed-mode fracture in concrete using extended fictitious crack model. Journal of Structural Engineering, Vol. 130, No. 11, pp. 1738–1747.

Simo, J. C. & Ju, J. W. 1987. Strain- and stress-based continuum damage models – I. Formulation. International Journal of Solids and Structures, Vol. 23, No. 7, pp. 821–840.

Sinha, N. K. 1988. Experiments on Anisotropic and Rate Sensitive Strain Ratio and Modulus of Columnar-Grained Ice. In: Sodhi, D. S., Luk, C. H. & Sinha, N. K. (eds.). OMAE 1988 Houston, Proceedings of the Seventh International Conference on Offshore Mechanics and Arctic Engineering. Volume IV: Arctic Engineering and Technology. Houston, Texas, USA. Feb 7–12, 1988. Houston, TX, USA: ASME, New York, NY, USA. Vol. 4. Pp. 55–62.

Sinha, N. K. 1989. Kinetics of microcracking and dilatation in polycrystalline ice. IUTAM / IAHR Symposium on Ice-Structure Interaction. St. John's, Newfoundland, Canada, 14–17 August 1989. Berlin: Springer-Verlag. Pp. 69–87. ISBN 3-540-52192-5.

Skrzypek, J. J. & Kuna-Ciskal, H. 2003. Anisotropic Elastic-Brittle-Damage and Fracture Models Based on Irreversible Thermodynamics. In: Skrzypek, J. J. & Ganczarski, A. (eds.). Anisotropic Behaviour of Damaged Materials (Lecture Notes in Applied and Computational Mechanics, V. 9). Springer-Verlag, pp. 143–184. ISBN 3-540-00437-8.

Steif, P. S. 1984. Crack Extension under Compressive Loading. Engineering Fracture Mechanics, Vol. 20, No. 3, pp. 463–473.

Sukumar, N., Moes, N., Moran, B. & Belytschko, T. 2000. Extended finite element method for three-dimensional crack modelling. International Journal for Numerical Methods in Engineering, Vol. 48, No. 11, pp. 1549–1570.

Swoboda, G. & Yang, Q. 1999a. An energy-based damage model of geomaterials – II. Deductionof damage evolution laws. International Journal of Solids and Structures, Vol. 36, No. 12, pp. 1735–1755.

Swoboda, G. & Yang, Q. 1999b. Energy-based damage model of geomaterials – I. Formulation and numerical results. International Journal of Solids and Structures, Vol. 36, No. 12, pp. 1719–1734.

Takekuma, K., Tozawa, S., Yamashita, M., Tanaka, A., Sasajima, T., Kayo, Y., Kawasaki, T. & Minami, T. 1983. Field Study on Mechanical Strength of Sea Ice at East Coast of Hokkaido. Technical Review – Mitsubishi Heavy Industries, Vol. 20, No. 2, pp. 144–151.

Tang, C. A., Wong, R. H. C., Chau, K. T. & Lin, P. 2005. Modeling of compression-induced splitting failure in heterogeneous brittle porous solids. Engineering Fracture Mechanics, Vol. 72, No. 4, pp. 597–615.

Valanis, K. C. 1990. A theory of damage in brittle materials. Engineering Fracture Mechanics, Vol. 36, No. 3, pp. 403–416.

Van, P. 2001. Internal thermodynamic variables and failure of microcracked materials. Journal of Non-Equilibrium Thermodynamics, Vol. 26, No. 2, pp. 167–189.

Van, P. & Vasarhelyi, B. 2001. Second Law of thermodynamics and the failure of rock materials. In: Elsworth, D. & Heasley, K. A. (eds.). Rock Mechanics in the National Interest Proceedings of the 38th Us Rock Mechanics Symposium, Washington D.C., 7–10: July 2001. Balkema Publishers. Pp. 767–773. ISBN 9026518277.

Varsta, P. 1983. On the mechanics of ice load on ships in level ice in the Baltic Sea. Espoo: Technical Research Centre of Finland. 91 p. (VTT Publications 11.) ISBN 951-38-1843-8.

Vinet, C. & Priou, P. 1997. Micromechanical damage model taking loading-induced anisotropy into account. Aerospace Science and Technology, Vol. 1, No. 1, pp. 65–76.

Voyiadjis, G. Z. & Park, T. 1997. Anisotropic damage effect tensors for the symmetrization of the effective stress tensor. Journal of Applied Mechanics, Transactions ASME, Vol. 64, No. 1, pp. 106–110.

Voyiadjis, G. Z. & Zolochevsky, A. 1998. Creep theory for transversely isotropic solids sustaining unilateral damage. Mechanics Research Communications, Vol. 25, No. 3, pp. 299–304.

Voyiadjis, G. Z. & Deliktas, B. 2000. A coupled anisotropic damage model for the inelastic response of composite materials. Computer Methods in Applied Mechanics and Engineering, Vol. 183, No. 3–4, pp. 159–199.

Wang, W. 1997. Stationary and Propagative Instabilities in Metals – A Computational Point of View. Delft University Press. 192 p. ISBN 90-407-1449-5.

Wang, W. M., Sluys, L. J. & de Borst, R. 1997. Viscoplasticity for instabilities due to strain softening and strain-rate softening. International Journal for Numerical Methods in Engineering, Vol. 40, No. 20, pp. 3839–3864.

Weiss, J. & Schulson, E. M. 1995. The failure of fresh-water granular ice under multiaxial compressive loading. Acta Metallurgica et Materialia, Vol. 43, No. 6, pp. 2303–2315.

Zhan, C., Sinha, N. K. & Evgin, E. 1996. A three dimensional anisotropic constitutive model for ductile behaviour of columnar grained sea ice. Acta Materialia, Vol. 44, No. 5, pp. 1839–1847.

Zhu, Y. Y. & Cescotto, S. 1995. Fully coupled elasto-visco-plastic damage theory for anisotropic materials. International Journal of Solids and Structures, Vol. 32, No. 11, pp. 1607–1641.

Zolochevsky, A., Yeseleva, E. & Ehlers, W. 2005. An anisotropic model of damage for brittle materials with different behavior in tension and compression. Forschung im Ingenieurwesen/Engineering Research, Vol. 69, No. 3, pp. 170–180.

Appendix A: Stiffness matrices in damage coordinate system

In the derivation of material parameters stiffness matrices are needed in the local "damage coordinate" system shown in Fig. 4.3. The matrices are given in this appendix.

From (Eq. (4.38))

$$[\mathbf{C}'] = \frac{\partial^2 W_D}{\{\partial \boldsymbol{\varepsilon}'^e\}\{\partial \boldsymbol{\varepsilon}'^e\}}, \text{ where } \{\mathbf{D}\} = \{\mathbf{0}\}$$

the following stiffness matrix for undamaged material is obtained (upper triangle, nonzero terms):

$$\begin{aligned}
C'_{11} &= \lambda + 2M_N(\alpha + M_N\beta + 2\mu_L - 2\mu_T) + 2\mu_T \\
C'_{12} &= \alpha - 2(-1 + M_N)M_N\beta + \lambda \\
C'_{13} &= M_N\alpha + \lambda \\
C'_{14} &= \sqrt{M_N(1 - M_N)}(\alpha + 2(M_N\beta + \mu_L - \mu_T)) \\
C'_{22} &= -2\ (-1 + M_N)\alpha + 2(M_N - 1)^2\beta + \lambda \\
&\quad +4\mu_L - 4M_N\mu_L - 2\mu_T + 4M_N\mu_T \\
C'_{23} &= (1 - \mathrm{M_N})\alpha + \lambda \\
C'_{24} &= \sqrt{M_N(1 - M_N)}(\alpha + 2(\beta - \mathrm{M_N}\beta + \mu_\mathrm{L} - \mu_\mathrm{T})) \\
C'_{33} &= \lambda + 2\mu_\mathrm{T} \\
C'_{34} &= \sqrt{M_N(1 - M_N)}\,\alpha \\
C'_{44} &= -2(M_N - 1)M_N\beta + \mu_L \\
C'_{55} &= M_N(\mu_L - \mu_T) + \mu_T \\
C'_{56} &= \sqrt{M_N(1 - M_N)}\,(\mu_L - \mu_T) \\
C'_{66} &= \mu_L + M_N(\mu_T - \mu_L)
\end{aligned} \tag{A.1}$$

From (Eq. (4.40)

$$[\mathbf{K}'] = \frac{\partial^2 W_D}{\{\partial \boldsymbol{\varepsilon}'^e\}\{\partial \boldsymbol{\varepsilon}'^e\}}, \quad \text{where } \|\mathbf{D}\| = 1$$

the following stiffness matrix for fully damaged material is obtained (upper triangle, nonzero terms):

$$\begin{aligned}
K'_{11} &= 2\alpha_2 + 2\beta_2 + \lambda + \lambda_D + 2(2\mu_2 + \mu_T + \mu_{TD}) \\
&\quad +2M_N\left[\alpha + \alpha_3 + \alpha_D + \beta_3 + \beta_5 + M_N(\beta + \beta_4 + \beta_D)\right. \\
&\quad \left.+2(\mu_3 + \mu_L + \mu_{LD} - \mu_T - \mu_{TD})\right] \\
K'_{12} &= \alpha + \alpha_2 + \alpha_D + \beta_3 + \lambda + \lambda_D \\
&\quad +M_N(\alpha_3 - 2(M_N - 1)\beta - \beta_3 - (M_N - 1)(\beta_4 + 2\beta_D)) \\
K'_{13} &= \alpha_2 + M_N(\alpha + \alpha_3 + \alpha_D) + \lambda + \lambda_D \\
K'_{14} &= \frac{1}{2}\sqrt{M_N(1 - M_N)}(2\alpha + \alpha_3 + 2\alpha_D + 4M_N\beta + 2\beta_3 + 3M_N\beta_4 \\
&\quad +\beta_5 + 4M_N\beta_D + 2\mu_3 + 4(\mu_L + \mu_{LD} - \mu_T - \mu_{TD})) \\
K'_{22} &= 2\alpha_D + 2\beta + 2\beta_D + \lambda + \lambda_D + 4\mu_L + 4\mu_{LD} \\
&\quad +2(\alpha - M_N\alpha + M_N((M_N - 2)\beta - \alpha_D + M_N\beta_D \qquad \text{(A.2)} \\
&\quad -2(\beta_D + \mu_L + \mu_{LD} - \mu_T - \mu_{TD}))) - 2(\mu_T + \mu_{TD}) \\
K'_{23} &= \alpha - M_N\alpha + \alpha_D - M_N\alpha_D + \lambda + \lambda_D \\
K'_{24} &= \frac{1}{2}\sqrt{M_N(1 - M_N)}(2\alpha + \alpha_3 + 2\alpha_D - 4(-1 + M_N)\beta + \beta_4 \\
&\quad -M_N(\beta_4 + 4\beta_D) + 2(2\beta_D + \mu_3 + 2(\mu_L + \mu_{LD} - \mu_T - \mu_{TD}))) \\
K'_{33} &= \lambda + \lambda_{\mathrm{D}} + 2(\mu_{\mathrm{T}} + \mu_{\mathrm{TD}}) \\
K'_{34} &= \frac{1}{2}\sqrt{M_N(1 - M_N)}(2\alpha + \alpha_3 + 2\alpha_{\mathrm{D}}) \\
K'_{44} &= \mu_2 + M_N(-(-1 + M_N)(2\beta + \beta_4 + 2\beta_D) + \mu_3) + \mu_L + \mu_{LD} \\
K'_{55} &= \mu_2 + \mu_T + M_N(\mu_3 + \mu_L + \mu_{LD} - \mu_T - \mu_{TD}) + \mu_{TD} \\
K'_{56} &= \frac{1}{2}\sqrt{M_N(1 - M_N)}(\mu_3 + 2(\mu_L + \mu_{LD} - \mu_T - \mu_{TD})) \\
K'_{66} &= \mu_L - M_N\mu_L + \mu_{LD} + M_N(-\mu_{LD} + \mu_T + \mu_{TD})
\end{aligned}$$

The stiffness matrix $[\tilde{\mathbf{K}}'^{act}]$ corresponding open crack is the following (see Eqs. (4.42) and (4.44), upper triangle, nonzero terms)

$$\begin{aligned}
\tilde{K}'^{act}_{22} &= C'^{p}_{11} = (C'_{14}{}^{2}C'_{22} - 2C'_{12}C'_{14}C'_{24} + C'_{12}{}^{2}C'_{44} \\
&\quad + C'_{11}((C'_{24}{}^{2} - C'_{22}C'_{44})))/(\mathrm{C}'_{14}{}^{2} - \mathrm{C}'_{11}\mathrm{C}'_{44}) \\
\tilde{K}'^{act}_{23} &= C'^{p}_{12} = ((C'_{14}{}^{2}C'_{23} - C'_{14}((C'_{13}C'_{24} + C'_{12}C'_{34})) + C'_{12}C'_{13}C'_{44} \\
&\quad + C'_{11}((C'_{24}C'_{34} - C'_{23}C'_{44}))))/(C'_{14}{}^{2} - C'_{11}C'_{44}) \\
\tilde{K}'^{act}_{33} &= C'^{p}_{22} = (C'_{14}{}^{2}C'_{33} - 2C'_{13}C'_{14}C'_{34} + C'_{13}{}^{2}C'_{44} \\
&\quad + C'_{11}((C'_{34}{}^{2} - C'_{33}C'_{44})))/(C'_{14}{}^{2} - C'_{11}C'_{44}) \\
\tilde{K}'^{act}_{44} &= \tilde{K}'^{act}_{55} = \mu_{R,T} \\
\tilde{K}'^{act}_{66} &= C'^{p}_{33} = C'_{66} - C'_{56}{}^{2}/C'_{55}
\end{aligned} \tag{A.3}$$

where terms C'_{ij} are given in Eq. (A.3).

The stiffness matrix $[\tilde{\mathbf{K}}'^{pass}]$ corresponding closed crack is the following (see Eqs. (4.49) and (4.50), upper triangle, nonzero terms)

$$\begin{aligned}
\tilde{K}'^{pass}_{11} &= C'^{c}_{11} = C'_{11} - C'_{14}{}^{2}/C'_{44} \\
\tilde{K}'^{pass}_{12} &= C'^{c}_{12} = C'_{12} - C'_{14}C'_{24}/C'_{44} \\
\tilde{K}'^{pass}_{13} &= C'^{c}_{13} = C'_{13} - C'_{14}C'_{34}/C'_{44} \\
\tilde{K}'^{pass}_{22} &= C'^{c}_{22} = C'_{22} - C'_{24}{}^{2}/C'_{44} \\
\tilde{K}'^{pass}_{23} &= C'^{c}_{23} = C'_{23} - C'_{24}C'_{34}/C'_{44} \\
\tilde{K}'^{pass}_{33} &= C'^{c}_{33} = C'_{33} - C'_{34}{}^{2}/C'_{44} \\
\tilde{K}'^{pass}_{44} &= \tilde{K}'^{pass}_{55} = \mu_{R,C} \\
\tilde{K}'^{pass}_{66} &= C'^{c}_{44} = C'_{66} - C'_{56}{}^{2}/C'_{55}
\end{aligned} \tag{A.4}$$

Appendix B: Material parameters in Fortran form

The material parameters obtained from Eq. (4.46) for active damage / open crack are the following:

```
muR = muRT
 If(MN > 1.0E-3) Then
  mu3 = (-2*xi*MN*(muT*muL*(alpha**2 - 2*beta*(2*muT + lambda)) +  (muT - muL)*(
& -8*alpha*muT*(muT - muL) + alpha**2*(4*muT - muL) +  4*(muT
& - muL)**2*(2*muT + lambda) +  beta*(-8*muT**2 + 4*muT*muL - 8*muT*lambda
& + 2*muL*lambda))*MN))/ ((muT*(-1 + MN) - muL*MN)*(muL*(2*muT + lambda) +
& (-alpha**2 + alpha*(4*muT - 2*muL) + 4*muT*(-muT + muL) +  2*beta*(2*muT
& + lambda))*MN +  (alpha**2 - 4*alpha*(muT - muL) + 4*(muT - muL)**2 -
& 2*beta*(2*muT - muL + lambda))*MN**2))
 mu2 = (muR*(muT*(-1 + MN) - muL*MN)* (muL*(2*muT + lambda) + (-alpha**2
& + alpha*(4*muT - 2*muL) +  4*muT*(-muT + muL) + 2*beta*(2*muT
& + lambda))*MN +  (alpha**2 - 4*alpha*(muT - muL) + 4*(muT - muL)**2 -
& 2*beta*(2*muT - muL + lambda))*MN**2) +  xi*(muT*muL**2*(2*muT + lambda)
& -  2*muT*muL*(2*muT*(muT - muL) + alpha*(-2*muT + muL))*MN +  (alpha**2*(
& -2*muT + muL)**2 -  4*alpha*muT*(2*muT**2 - 3*muT*muL + muL**2) -
& 2*(beta*(-2*muT + muL)**2*(muT + lambda) -  2*(muT - muL)**2*(muT*(2*muT
& - muL) + (muT - muL)*lambda)))* MN**2))/ ((muT*(-1 + MN)
& - muL*MN)*(muL*(2*muT + lambda) +  (-alpha**2 + alpha*(4*muT - 2*muL)
& + 4*muT*(-muT + muL) +  2*beta*(2*muT + lambda))*MN +  (alpha**2
& - 4*alpha*(muT - muL) + 4*(muT - muL)**2 -  2*beta*(2*muT - muL
& + lambda))*MN**2))
 alpha2 = (-2*xi*(muT*muL*(2*muT*(-muT + muL) + (-2*muT + muL)*lambda) +
& muT*(2*alpha**2*muT + alpha*(-4*muT**2 + 7*muT*muL - 2*muL**2) -
& 4*beta*muT*(muT + lambda) +  (muT - muL)*(4*muT*(muT - muL) + (2*muT
& + muL)*lambda))*MN +  (muT - muL)*(alpha**2*(2*muT - muL) + alpha*muT*(
& -4*muT + 3*muL) +  2*(-(beta*(2*muT - muL)*(muT + lambda)) +  (muT
& - muL)*(2*muT*(muT - muL) + (muT - 2*muL)*lambda)))*MN**2))/ ((muT*(-1
& + MN) - muL*MN)*(muL*(2*muT + lambda) +  (-alpha**2 + alpha*(4*muT
& - 2*muL) + 4*muT*(-muT + muL) +  2*beta*(2*muT + lambda))*MN +  (alpha**2
& - 4*alpha*(muT - muL) + 4*(muT - muL)**2 -  2*beta*(2*muT - muL
& + lambda))*MN**2))
 alpha3 = (2*xi*(2*muT*muL*(alpha*muT - (muT - muL)*(2*muT + lambda)) +
& muT*(alpha**2*(4*muT - muL) -  2*alpha*(4*muT**2 - 5*muT*muL + muL**2) +
& 4*(muT - muL)**2*(2*muT + lambda) +  beta*(-8*muT**2 - 8*muT*lambda
& + 2*muL*lambda))*MN +  (muT - muL)*(-8*alpha*muT*(muT - muL)
& + alpha**2*(4*muT - muL) +  4*(muT - muL)**2*(2*muT + lambda) +  beta*(
& -8*muT**2 + 4*muT*muL - 8*muT*lambda + 2*muL*lambda))*MN**2))/ ((muT*(-1
& + MN) - muL*MN)*(muL*(2*muT + lambda) +  (-alpha**2 + alpha*(4*muT
& - 2*muL) + 4*muT*(-muT + muL) +  2*beta*(2*muT + lambda))*MN +  (alpha**2
& - 4*alpha*(muT - muL) + 4*(muT - muL)**2 -  2*beta*(2*muT - muL
& + lambda))*MN**2))
 beta5 = (-4*muT*xi*(muL*(alpha*muT - (muT - muL)*(2*muT + lambda)) +
& (alpha**2*(2*muT - muL) - alpha*(4*muT**2 - 5*muT*muL + muL**2) +  2*(
& -(beta*(2*muT - muL)*(muT + lambda)) +  (muT - muL)**2*(2*muT
& + lambda)))*MN))/ ((muT*(-1 + MN) - muL*MN)*(muL*(2*muT + lambda) +  (
& -alpha**2 + alpha*(4*muT - 2*muL) + 4*muT*(-muT + muL) +  2*beta*(2*muT
& + lambda))*MN +  (alpha**2 - 4*alpha*(muT - muL) + 4*(muT - muL)**2 -
& 2*beta*(2*muT - muL + lambda))*MN**2))
 beta4 = (-2*xi*(muT*muL*(alpha**2 - 2*beta*(2*muT + lambda)) +  (muT - muL)*(
& -8*alpha*muT*(muT - muL) + alpha**2*(4*muT - muL) +  4*(muT
```

```
& - muL)**2*(2*muT + lambda) +  beta*(-8*muT**2 + 4*muT*muL - 8*muT*lambda
& + 2*muL*lambda))*MN))/ ((muT*(-1 + MN) - muL*MN)*(muL*(2*muT + lambda) +
& (-alpha**2 + alpha*(4*muT - 2*muL) + 4*muT*(-muT + muL) +  2*beta*(2*muT
& + lambda))*MN +  (alpha**2 - 4*alpha*(muT - muL) + 4*(muT - muL)**2 -
& 2*beta*(2*muT - muL + lambda))*MN**2))
 beta3 = (2*xi*(muT*muL*(alpha*muT - (muT - muL)*(2*muT + lambda)) +
& muT*(2*alpha**2*muT - alpha*(4*muT**2 - 5*muT*muL + muL**2) +  2*(muT
& - muL)**2*(2*muT + lambda) -  2*beta*muT*(2*muT + muL + 2*lambda))*MN +
& (muT - muL)*(-8*alpha*muT*(muT - muL) + alpha**2*(4*muT - muL) +  4*(muT
& - muL)**2*(2*muT + lambda) +  beta*(-8*muT**2 + 4*muT*muL - 8*muT*lambda
& + 2*muL*lambda))*MN**2))/ ((muT*(-1 + MN) - muL*MN)*(muL*(2*muT + lambda)
& +  (-alpha**2 + alpha*(4*muT - 2*muL) + 4*muT*(-muT + muL) +
& 2*beta*(2*muT + lambda))*MN +  (alpha**2 - 4*alpha*(muT - muL) + 4*(muT
& - muL)**2 -  2*beta*(2*muT - muL + lambda))*MN**2))
 beta2 = (2*(muT**2*xi*(-(muL*(muT + lambda)) +  (alpha**2 - 2*alpha*(muT
& - muL) - 2*beta*(muT + lambda) +  (muT - muL)*(2*muT - muL + lambda))*MN)
& -  muR*(muT*(-1 + MN) - muL*MN)* (muL*(2*muT + lambda) +  (-alpha**2
& + alpha*(4*muT - 2*muL) + 4*muT*(-muT + muL) +  2*beta*(2*muT
& + lambda))*MN +  (alpha**2 - 4*alpha*(muT - muL) + 4*(muT - muL)**2 -
& 2*beta*(2*muT - muL + lambda))*MN**2)))/ ((muT*(-1 + MN)
& - muL*MN)*(muL*(2*muT + lambda) +  (-alpha**2 + alpha*(4*muT - 2*muL)
& + 4*muT*(-muT + muL) +  2*beta*(2*muT + lambda))*MN +  (alpha**2
& - 4*alpha*(muT - muL) + 4*(muT - muL)**2 -  2*beta*(2*muT - muL
& + lambda))*MN**2))
 lambdaD = (muT*muL*(4*muT*(-muT + muL)*xi +  2*(muT - 2*muT*xi
& + muL*xi)*lambda + lambda**2) +  (alpha**2*muT*(4*muT*xi - lambda) +
& 2*alpha*muT*(2*muT - muL)*(-2*muT*xi + 2*muL*xi + lambda) +  2*beta*muT*(
& -4*muT**2*xi + muT*(2 - 4*xi)*lambda + lambda**2) +  (muT
& - muL)*(8*muT**3*xi + 2*muT*muL*(-1 + 2*xi)*lambda -  muL*lambda**2
& - 4*muT**2*(muL*xi + lambda - xi*lambda)))*MN +  (alpha**2*(-5*muT*muL*xi
& + 2*muL**2*xi + 2*muT*lambda - muL*lambda) +  2*alpha*(muT
& - muL)*(2*muT*muL*xi - 4*muT*lambda + muL*lambda) +  2*(-4*(muT
& - muL)**2*(muT*muL*xi - muT*lambda + muL*xi*lambda) +
& beta*(muT**2*(6*muL*xi - 4*lambda) +  muL*lambda*(-2*muL*xi + lambda) +
& muT*(-2*muL**2*xi + muL*(3 + 5*xi)*lambda - 2*lambda**2))))* MN**2 - (muT
& - muL)*(-4*alpha*(muT - muL)*(2*muT*xi + lambda) +  alpha**2*(4*muT*xi
& - muL*xi + lambda) +  2*(2*(muT - muL)**2*(2*muT*xi + lambda + xi*lambda)
& +  beta*(2*muT*(-2*muT + muL)*xi +  (-2*muT + muL - 4*muT*xi
& + muL*xi)*lambda - lambda**2)))*MN**3 )/((muT*(-1 + MN) - muL*MN)*
& (4*muT**2*(-1 + MN)*MN + (alpha**2 - 2*beta*lambda)*(-1 + MN)*MN +
& 4*muL**2*MN**2 + muL*(lambda + 2*MN*(-alpha + 2*alpha*MN + beta*MN)) +
& muT*(-4*(alpha + beta)*(-1 + MN)*MN + muL*(2 + 4*MN - 8*MN**2))))
 muLD = (xi*(-(muT*muL**2*(2*muT + lambda)) +  muT*muL*(alpha**2 - 4*alpha*muT
& - 4*beta*muT + 4*muT**2 +  2*alpha*muL - 4*muT*muL - 2*beta*lambda)*MN -
& 2*muT*muL*(2*muT**2 - 2*alpha*(muT - muL) - 4*muT*muL +  muL*(beta
& + 2*muL))*MN**2 +  (muT - muL)*(-8*alpha*muT*(muT - muL)
& + alpha**2*(4*muT - muL) +  4*(muT - muL)**2*(2*muT + lambda) +  beta*(
& -8*muT**2 + 4*muT*muL - 8*muT*lambda + 2*muL*lambda))*MN**3)  - muL*(muT*(
& -1 + MN) - muL*MN)* (4*muT**2*(-1 + MN)*MN + (alpha**2 - 2*beta*lambda)*(
& -1 + MN)*MN +  4*muL**2*MN**2 + muL*(lambda +  2*MN*(-alpha + 2*alpha*MN
& + beta*MN)) +  muT*(-4*(alpha + beta)*(-1 + MN)*MN + muL*(2 + 4*MN
& - 8*MN**2))))/ ((muT*(-1 + MN) - muL*MN)*(4*muT**2*(-1 + MN)*MN +
& (alpha**2 - 2*beta*lambda)*(-1 + MN)*MN + 4*muL**2*MN**2 +  muL*(lambda
& + 2*MN*(-alpha + 2*alpha*MN + beta*MN)) +  muT*(-4*(alpha + beta)*(-1
& + MN)*MN + muL*(2 + 4*MN - 8*MN**2))))
 muTD = (muT*muL*(muT - muL*xi)*(2*muT + lambda) +  muT*(-(alpha**2*muT)
& + 2*alpha*(2*muT - muL)*(muT - muL*xi) +  2*beta*muT*(2*muT + lambda) -
& (muT - muL)*(4*muT**2 + muT*muL*(2 - 4*xi) + muL*lambda))*MN +
& (2*alpha*muT*(muT - muL)*(muL + 4*muT*(-1 + xi) - 2*muL*xi) -
& alpha**2*(muL**2*xi + muT**2*(-2 + 4*xi) + muT*(muL - 5*muL*xi)) +  2*(
```

```
& -2*(muT - muL)**2*(2*muT**2*(-1 + xi) - muL*xi*lambda +  muT*xi*(-muL
& + lambda)) +  beta*(4*muT**3*(-1 + xi) -  muT**2*(-1 + 2*xi)*(3*muL
& - 2*lambda) + muL**2*xi*lambda +  muT*muL*(muL*xi + lambda
& - 5*xi*lambda))))*MN**2 +  (muT - muL)*(-4*alpha*muT*(muT - muL)*(-1
& + 2*xi) -  alpha**2*(muT - 4*muT*xi + muL*xi) +  2*(2*(muT
& - muL)**2*(muT*(-1 + 2*xi) + xi*lambda) +  beta*(-(muT*(2*muT - muL)*(-1
& + 2*xi)) +  (muT - 4*muT*xi + muL*xi)*lambda)))*MN**3)/ ((muT*(-1 + MN)
& - muL*MN)*(4*muT**2*(-1 + MN)*MN +  (alpha**2 - 2*beta*lambda)*(-1
& + MN)*MN + 4*muL**2*MN**2 +  muL*(lambda + 2*MN*(-alpha + 2*alpha*MN
& + beta*MN)) +  muT*(-4*(alpha + beta)*(-1 + MN)*MN + muL*(2 + 4*MN
& - 8*MN**2))))
 betaD = (4*beta**2*MN*(muT*(-1 + MN) - muL*MN)* (2*muT*(-1 + MN) + lambda*(-1
& + MN) - muL*MN) +  xi*(-8*alpha*muT*(muT - muL)**2*MN +  4*(muT
& - muL)**3*(2*muT + lambda)*MN +  alpha**2*(4*muT**2*MN + muL**2*MN
& + muT*(muL - 5*muL*MN))) -  2*beta*(4*muT**3*(xi + (-1 + MN)**2)*MN +
& muL*MN*(-(alpha**2*(-1 + MN)*MN) - 4*muL**2*MN**2 +  muL*((-1
& + xi)*lambda + 2*alpha*(1 - 2*MN)*MN)) -  2*muT**2*(2*(-(xi*lambda)
& + alpha*(-1 + MN)**2)*MN +  muL*(1 + MN - 8*MN**2 + 6*MN**3 + xi*(-1
& + 3*MN))) +  muT*(alpha**2*(-1 + MN)**2*MN +  2*muL**2*MN*(-1 + xi - 4*MN
& + 6*MN**2) +  muL*(lambda*(-1 + xi + MN - 5*xi*MN) +  2*alpha*MN*(1
& - 5*MN + 4*MN**2)))))/ (2.*(muT*(-1 + MN) - muL*MN)* (4*muT**2*(-1
& + MN)*MN + (alpha**2 - 2*beta*lambda)*(-1 + MN)*MN +  4*muL**2*MN**2
& + muL*(lambda + 2*MN*(-alpha + 2*alpha*MN + beta*MN)) +  muT*(-4*(alpha
& + beta)*(-1 + MN)*MN + muL*(2 + 4*MN - 8*MN**2))))
 alphaD = (muT*muL*(2*(muT - muL)*xi*(2*muT + lambda) +  alpha*(-2*muT*(-1
& + xi) + lambda)) +  (-(alpha**3*muT) + alpha**2*muT*(muL*(-2 + xi)
& - 4*muT*(-1 + xi)) +  alpha*(2*beta*muT*(2*muT + lambda) +  (muT - muL)*(
& -2*muT*muL*(1 + xi) + muT**2*(-4 + 8*xi) -  muL*lambda)) - 2*muT*xi*
& (2*(muT - muL)**2*(2*muT + lambda) +  beta*(-4*muT**2 - 4*muT*lambda
& + muL*lambda)))*MN +  (alpha**3*(2*muT - muL) - alpha**2*(4*muT**2
& - 5*muT*muL + muL**2)* (2 + xi) + 2*alpha*(4*muT*(muT - muL)**2*(1 + xi)
& +  beta*(-4*muT**2 + 3*muT*muL - 2*muT*lambda + muL*lambda)) -  2*(muT
& - muL)*xi*(2*(muT - muL)**2*(2*muT + lambda) +  beta*(2*muT*(-2*muT
& + muL) + (-4*muT + muL)*lambda)))*MN**2 -  alpha*(muT - muL)*(alpha**2
& - 4*alpha*(muT - muL) + 4*(muT - muL)**2 -  2*beta*(2*muT - muL
& + lambda))*MN**3)/ ((muT*(-1 + MN) - muL*MN)*(4*muT**2*(-1 + MN)*MN +
& (alpha**2 - 2*beta*lambda)*(-1 + MN)*MN + 4*muL**2*MN**2 +  muL*(lambda
& + 2*MN*(-alpha + 2*alpha*MN + beta*MN)) +  muT*(-4*(alpha + beta)*(-1
& + MN)*MN + muL*(2 + 4*MN - 8*MN**2))))

 Else
!
! MN = 0
!
 mu2 = muR - muL*xi
 alpha2   = 2*xi*(-2*muT + muL + (2*muT**2)/(2*muT + lambda))
 beta3    = 2*xi*(muT - muL - (alpha*muT)/(2*muT + lambda))
 beta2    = -2*muR + (2*muT*xi*(muT + lambda))/(2*muT + lambda)
 lambdaD = 4*muT*xi - 2*muL*xi - lambda - (4*muT**2*xi)/(2*muT + lambda)
 muTD    = -muT + muL*xi
 betaD = beta*(-1 + xi) - (alpha**2*xi)/(2.*(2*muT + lambda))
 alphaD = 2*(-muT + muL)*xi + alpha*(-1 + (2*muT*xi)/(2*muT + lambda))
 EndIf
```

The material parameters obtained from Eq. (4.51) for passive damage / closed crack are the following:

```
 muR = muRC
 If(MN > 1.0E-3) Then
 mu3 = (4*xi*MN*(beta*muT*muL -  (muT - muL)*(2*(muT - muL)**2 + beta*(-4*muT
& + muL))*MN))/ ((muT - muT*MN + muL*MN)*(-muL + 2*beta*(-1 + MN)*MN))
 mu2 = -((-(muR*(muT - muT*MN + muL*MN)*(-muL + 2*beta*(-1 + MN)*MN)) +  xi*(
& -(muT*muL**2) + 2*(-2*(muT - muL)**3 + beta*(-2*muT + muL)**2)*
& MN**2))/((muT - muT*MN + muL*MN)*(-muL + 2*beta*(-1 + MN)*MN)))
 alpha2 = (-2*xi*(muT*muL*(-muT + muL) + (alpha - 2*beta)*muT**2*MN +  (muT
& - muL)*(-(alpha*muT) + 4*(muT - muL)**2 + beta*(-6*muT + 2*muL))*
& MN**2))/((muT - muT*MN + muL*MN)*(-muL + 2*beta*(-1 + MN)*MN))
 alpha3 = (-2*xi*(muT*(-alpha + 2*muT - 2*muL)*muL +  (4*beta*muT**2
& - alpha*(2*muT**2 - 3*muT*muL + muL**2))*MN +  2*(beta*(6*muT - 2*muL)
& + alpha*(muT - muL) - 4*(muT - muL)**2)* (muT - muL)*MN**2))/ ((muT
& - muT*MN + muL*MN)*(-muL + 2*beta*(-1 + MN)*MN))
 beta5 = (-4*muT*xi*(muL*(-muT + muL) +  2*((muT - muL)**2 + beta*(-2*muT
& + muL))*MN))/ ((muT - muT*MN + muL*MN)*(-muL + 2*beta*(-1 + MN)*MN))
 beta4 = (4*xi*(beta*muT*muL - (muT - muL)* (2*(muT - muL)**2 + beta*(-4*muT
& + muL))*MN))/ ((muT - muT*MN + muL*MN)*(-muL + 2*beta*(-1 + MN)*MN))
 beta3 = (-2*xi*(muT*(muT - muL)*muL -  2*muT*(-2*beta*muT + (muT - muL)**2)*MN
& -  2*(muT - muL)*(2*(muT - muL)**2 + beta*(-4*muT + muL))*MN**2))/ ((muT
& - muT*MN + muL*MN)*(-muL + 2*beta*(-1 + MN)*MN))
 beta2 = -2*muR - (2*muT**2*xi*(muL + (2*beta - muT + muL)*MN))/ ((muT - muT*MN
& + muL*MN)*(-muL + 2*beta*(-1 + MN)*MN))
 lambdaD = -((lambda*(muT - muT*MN + muL*MN)*(-muL + 2*beta*(-1 + MN)*MN) +
& xi*(-8*muL**3*(-1 + MN)*MN**2 +  muL*(-1 + MN)*(-(muT*(2*muT + lambda))
& +  (alpha**2 + 16*beta*muT - 24*muT**2 - 2*beta*lambda)*MN**2) +  muT*(-1
& + MN)*MN*(-((alpha**2 - 2*beta*lambda)*(-1 + MN)) +  8*muT**2*MN
& - 4*beta*muT*(1 + 3*MN)) +  muL**2*(-2*muT + MN*(2*muT + lambda -
& 4*(beta - 6*muT)*(-1 + MN)*MN))))/ ((muT - muT*MN + muL*MN)*(-muL
& + 2*beta*(-1 + MN)*MN)))
 muLD = -((muL*(muT - muT*MN + muL*MN)*(-muL + 2*beta*(-1 + MN)*MN) +
& xi*(muT*muL**2 + 2*beta*muT*muL*MN -  2*(muT - muL)*(2*(muT - muL)**2
& + beta*(-4*muT + muL))*MN**3))/ ((muT - muT*MN + muL*MN)*(-muL + 2*beta*(-1 + MN)*MN)))
 muTD = -((4*muL**3*xi*(-1 + MN)*MN**2 +  muT*muL*(-1 + MN)*(muT + 2*(beta
& - 5*beta*xi + 6*muT*xi)*MN**2) -  2*muT**2*(-1 + MN)*MN*(2*muT*xi*MN
& + beta*(-1 + MN - 4*xi*MN)) +  muL**2*(-(muT*MN) + xi*(muT + 2*(beta
& - 6*muT)*(-1 + MN)*MN**2)))/ ((muT - muT*MN + muL*MN)*(-muL + 2*beta*(-1 + MN)*MN)))
 betaD = (2*(muT - muL)**3*xi*MN +  2*beta**2*(-1 + MN)*MN*(muT*(-1 + MN)
& - muL*MN) -  beta*(muL**2*(-1 + xi)*MN + 4*muT**2*xi*MN +  muT*muL*(-1
& + xi + MN - 5*xi*MN)))/ ((muT*(-1 + MN) - muL*MN)*(muL - 2*beta*(-1  + MN)*MN))
 alphaD = (alpha*(muT*(-1 + MN) - muL*MN)* (2*(muT*xi + beta*(-1 + MN))*MN
& + muL*(-1 + xi - 2*xi*MN)) +  2*xi*(-4*muT**3*MN**2 + 2*muL**2*(beta
& + 2*muL)*MN**2 -  muT*muL*(muL + 8*beta*MN**2 + 12*muL*MN**2) +
& muT**2*(muL + 12*muL*MN**2 + 2*beta*MN*(1 + 3*MN))))/ ((muT*(-1 + MN)
& - muL*MN)*(muL - 2*beta*(-1 + MN)*MN))
  Else
  mu2= muR - muL*xi
 alpha2  = 2*(-muT + muL)*xi
 beta3   = 2*(muT - muL)*xi
 beta2   = -2*muR + 2*muT*xi
 lambdaD= 2*muT*xi - 2*muL*xi + (-1 + xi)*lambda
 muTD    = -muT + muL*xi
 betaD = beta*(-1 + xi)
 alphaD = alpha*(-1 + xi) + 2*(-muT + muL)*xi
  EndIf
```

Series title, number and report code of publication

VTT Publications 628
VTT-PUBS-628

Author(s)
Kolari, Kari

Title

Damage mechanics model for brittle failure of transversely isotropic solids
Finite element implementation

Abstract

A new continuum damage model, the wing crack damage (WCD) model, was developed for the analysis of brittle failure of transversely isotropic solids. Special attention was paid to the analysis of axial splitting under compression and tensile cracking under tension.

In addition to the WCD model a three-dimensional version of the damage model proposed by Murakami and Kamiya was enhanced and implemented in ABAQUS/Standard FE software.

The proposed WCD model is based on the use of the damage vector. The vector represents both the normal direction of the surface of the plane crack and the size of the damaged area. Damaging induces anisotropy in an originally transversely isotropic material. The evolution equations for damage are motivated by the wing crack growth mechanism. The evolution is based on propagation of pre-existing damage.

The proposed model enables modelling of pre-existing cracks. The feature can be exploited in studying the effect of orientation and size distribution of pre-existing cracks on the failure of materials. The model was implemented in ABAQUS/Standard FE software as a user subroutine.

The unsymmetrical behaviour of cracked materials under tension and compression due to the opening and closure of cracks is taken into account in the proposed model. In the work it was shown that the widely used strain-based crack closure criteria cannot be reliably applied in a two- and three-dimensional stress state. To attain a deformation localisation zone of finite width, a damage rate-dependent damage surface was introduced.

The validity of the proposed model was verified by testing it against five basic structures composed of known natural materials (ice, marble and concrete). The numerical simulations revealed the capability of the model in modelling brittle failure modes of transversely isotropic materials.

ISBN
978-951-38-6995-3 (soft back ed.)
978-951-38-6996-0 (URL: http://www.vtt.fi/publications/index.jsp)

Series title and ISSN	Project number
VTT Publications 1235-0621 (soft back ed.) 1455-0849 (URL: http://www.vtt.fi/publications/index.jsp)	

Date	Language	Pages
March 2007	English, Finnish abstr.	195 p. + app. 7 p.

Name of project	Commissioned by

Keywords	Publisher
failure mechanics, brittle failure, anisotropy, continuum mechanics, damage models, finite element analysis, solid materials, structural analysis, three-dimensional, transversal isotropy, wing crack	VTT P.O. Box 1000, FI-02044 VTT, Finland Phone internat. +358 20 722 4404 Fax +358 20 722 4374

Julkaisun sarja, numero ja raporttikoodi

VTT Publications 628
VTT-PUBS-628

Tekijä(t)
Kolari, Kari

Nimeke

Transversaali-isotroopisen materiaalin haurasmurtuman mallintaminen vauriomekaniikan avulla

Implementointi elementtimenetelmään

Tiivistelmä

Tutkimuksessa on esitetty kaksi vauriomekaniikkaan (Continuum damage mechanics) perustuvaa materiaalimallia: Murakami Kamiyan (MK) malli, sekä uusi ”wing crak damage” -malli (WCD). Molemmat mallit on liitetty ABAQUS-elementtimenetelmäohjelmistoon UMAT-aliohjelmana.

Esitetty uusi WCD-malli on tarkoitettu transversaali-isotrooppisten materiaalien haurasmurtuman mallintamiseen. Erityistä huomiota on kiinnitetty yksiaksiaalisessa puristuksessa tapahtuvan kuormituksen kanssa yhdensuuntaisen halkeamisen sekä yksiaksiaalisessa vedossa tapahtuvan kuormitusta vastaan kohtisuorassa olevan säröytymisen mallintamiseen.

Esitetty WCD-malli perustuu ”vauriovektorin” käyttöön. Vauriovektori edustaa sekä tasomaisen särön normaalin suuntaa että vaurioituneen alueen kokoa. Vaurioitumisen vuoksi transversaali-isotrooppisesta materiaalista tulee anisotrooppista. Vaurion kasvumekanismi simuloi siipisärön (wing crack) kasvumekanismia.

Uusi WCD-malli mahdollistaa materiaalissa ennen kuormitusta olevien alkusäröjen mallintamisen. Piirrettä voidaan hyödyntää tutkittaessa alkusäröjen suunnan ja suuruuden vaikutusta materiaalin vaurioitumiseen.

Halkeilleen materiaalin epäsymmetrinen käyttäytyminen vedossa ja puristuksessa särön avautumisen ja sulkeutumisen vuoksi on otettu huomioon esitetyssä mallissa. Tutkimuksessa on osoitettu, että venymäperusteista sulkeutumiskriteeriä ei voida luotettavasti soveltaa kaksi- ja kolmiaksiaalisessa jännitystilassa.

Esitetyssä mallissa vauriopinta on vaurionopeuden funktio. Siksi muodonmuutosten paikallistumis-vyöhykkeen leveys on äärellinen.

Esitetyn mallin pätevyys on todennettu testaamalla mallia viidessä eri kuormitustapauksessa käyttäen tunnettuja luonnonmateriaaleja (jää, betoni ja marmori). Numeeriset testit osoittivat mallin pätevyyden ja tehokkuuden transversaali-isotrooppisten materiaalien haurasmurtuman mallintamisessa.

ISBN
978-951-38-6995-3 (nid.)
978-951-38-6996-0 (URL: http://www.vtt.fi/publications/index.jsp)

Avainnimeke ja ISSN	Projektinumero
VTT Publications 1235-0621 (nid.) 1455-0849 (URL: http://www.vtt.fi/publications/index.jsp)	

Julkaisuaika	Kieli	Sivuja
Maaliskuu 2007	Suomi, engl. tiiv.	195 s. + liitt. 7 s.

Projektin nimi	Toimeksiantaja(t)

Avainsanat	Julkaisija
failure mechanics, brittle failure, anisotropy, continuum mechanics, damage models, finite element analysis, solid materials, structural analysis, three-dimensional, transversal isotropy, wing crack	VTT PL 1000, 02044 VTT Puh. 020 722 4404 Faksi 020 722 4374

A new continuum damage model, the wing crack damage (WCD) model, was developed for the analysis of brittle failure of transversely isotropic solids. Special attention was paid to the analysis of axial splitting under compression and tensile cracking under tension. The model was implemented in ABAQUS/Standard FE software as a user subroutine.

The proposed method is based on the assumption of pre-existing cracks. The feature can be exploited in studying the effect of orientation and size distribution of pre-existing cracks on the failure of materials. The unilateral response due to crack closure effect is taken into account.

The validity of the proposed WCD model was verified by numerical simulation of five specimens in various loading conditions. The specimens were composed of known transversely isotropic materials like ice and marble, and concrete that was considered an isotropic material. The model was found to be efficient in the analysis of axial splitting and tensile failure modes.

In addition to the WCD model a three-dimensional version of the damage model proposed by Murakami and Kamiya was enhanced and implemented in ABAQUS/Standard FE software.

Julkaisu on saatavana
VTT
PL 1000
02044 VTT
Puh. 020 722 4404
Faksi 020 722 4374

Publikationen distribueras av
VTT
PB 1000
02044 VTT
Tel. 020 722 4404
Fax 020 722 4374

This publication is available from
VTT
P.O. Box 1000
FI-02044 VTT, Finland
Phone internat. + 358 20 722 4404
Fax + 358 20 722 4374

ISBN 978-951-38-6995-3 (soft back ed.)
ISSN 1235-0621 (soft back ed.)

ISBN 978-951-38-6996-0 (URL: http://www.vtt.fi/publications/index.jsp)
ISSN 1455-0849 (URL: http://www.vtt.fi/publications/index.jsp)